
The Formation and Evolution of Massive Galaxies and their Supermassive Black Holes over the past 12 Billion Years

Asa Frederick Leon Bluck, B.Sc. (Hons), M.Sc., PGCE (Oxon), FRAS



**The University of
Nottingham**

Thesis submitted to the University of Nottingham
for the degree of Doctor of Philosophy, February 2011

"You have to know the past to understand the present."

– Carl Sagan

"We are all in the gutter, but some of us are looking at the stars."

– Oscar Wilde

Supervisor: Prof. Christopher J. Conselice
(University of Nottingham)

Examiners: Prof. Alfonso Aragon-Salamanca
(University of Nottingham)
Dr. Scott Chapman
(University of Cambridge)

**Dedicated to my parents, Roger & Penny Bluck
and grandparents, Ruby & Frederick Bluck
and Winifred & Leon Underhill
with all my love**

Abstract

This thesis examines many of the ways in which massive galaxies and their super-massive black holes have changed over the past 12 billion years. In a sense, this is an attempt to write a cosmic history of massive galaxies, and in so doing construct a useful catalogue of changes which can be studied to gain insight into galaxy formation and evolution. In particular, this thesis concentrates on two potential drivers for galactic evolution: external influences from galaxy - galaxy interactions (Chapters 2 - 3); and internal influences from AGN feedback (Chapter 4). We find that both of these mechanisms have a profound impact on massive galaxies throughout their lifetimes.

In Chapter 2 the major merger history of massive galaxies is probed via close pair statistics and computational morphological approaches. We find that there is a monotonic rise in the merger fraction of massive galaxies with redshift out to $z = 3$, which is best parameterised by a simple power law of the form $f_m = f_0(1 + z)^m$, where $f_0 = 0.008 \pm 0.003$ and $m = 3.0 \pm 0.4$. We compute the total number of major mergers that massive galaxies (with $M_* > 10^{11} M_\odot$) experience from $z = 3$ to the present to be $N_m = 1.7 \pm 0.5$. We also note a close accord between morphological and close pair methods at $z < 1.5$ for standard optically defined CAS mergers and $d < 30$ kpc close pairs, probably indicative of both methods tracing the underlying merger activity with similar mass ratio and timescale sensitivities. Further, we provide a series of additional tests to the close pair method.

In Chapter 3 we extend the study of galaxy interactions to minor mergers, and also compute the morphologically determined major merger fractions of very high redshift massive galaxies. We find that high redshift massive galaxies are frequently highly asymmetric with $\sim 1/4$ fitting the CAS definition of a merger at $1.7 < z < 3$. We go on to utilise the extraordinary depth and resolution of the HST GOODS NICMOS Survey

Abstract

to probe the minor merger history of massive galaxies. We find that in total massive galaxies experience $N_m = (4.5 \pm 2.1) / \tau_m$ mergers with galaxies with $M_* > 10^9 M_\odot$ from $z = 3$ to the present, where τ_m is the merger timescale which will vary with mass. From this we compute the total stellar mass increase, due to mergers, of massive galaxies to be $\Delta M_* \sim 3 \times 10^{11} M_\odot$ over the past 12 billion years. This potentially offers a tempting solution for the observed rapid growth of massive galaxies throughout the same epoch.

In chapter 4 we investigate in detail the co-evolution of massive galaxies and their supermassive black holes by constructing a complete volume limited sample of 85 AGN with hard band luminosities $L_X > 2.35 \times 10^{43} \text{ erg s}^{-1}$ residing within host galaxies with masses $M_* > 10^{10.5} M_\odot$ at $0.4 < z < 3$. Using this data we compute the Eddington limiting (minimum) masses, M_E , of the black holes in our sample. By assuming that there is no evolution in the Eddington ratio ($\mu = L_{Bol} / L_{Edd}$) and then that there is maximum possible evolution to the Eddington limit, we quantify the evolution in the M_* / M_{BH} ratio as lying in the range $700 < M_* / M_{BH} < 10000$, compared to a local value of $M_* / M_{BH} \sim 1000$. Furthermore, we find that the active fraction of massive galaxies rises with redshift from $1.2 \pm 0.2 \%$ at $z = 0.7$ to $7.4 \pm 2 \%$ at $z = 2.5$. We calculate the maximum timescales for which our sample of AGN can continue to accrete at their observed rates before surpassing the local galaxy-black hole mass relation. We use these timescales to calculate the total fraction of massive galaxies which will be active above our threshold, finding that at least $\sim 40 \%$ of all massive galaxies will be Seyfert luminosity AGN or brighter since $z = 3$. We find that the energy output due to these objects is sufficient to strip apart every massive galaxy in the universe at least 35 times over. Finally, we use this method to compute the evolution in the X-ray luminosity density of AGN with redshift, finding that massive galaxy Seyferts are the dominant source of X-ray emission in the Universe at $z < 3$.

We conclude in Chapter 5 by summarising these findings and commenting upon the powerful role of both internal and external influences on galaxy formation and evolution over the past 12 billion years.

Acknowledgements

First and foremost I thank my supervisor and friend, Prof. Christopher J. Conselice, for his unwavering support and enthusiasm throughout my doctorate. I am immensely grateful for his advice, encouragement and insight. I also thank Dr. Omar Almaini for acting in many ways as my second supervisor, and offering me much of his time and energies. I appreciate the significant effort, work and productive scientific discussions of my other co-authors: Dr. Amanda Bauer, Mr. Fernando Buitrago, Dr. Rychard J. Bouwens, Dr. Emanuele Daddi, Dr. Mark Dickinson, Dr. Ruth Gruetzbauch, Dr. Carlos Hoyos, Dr. Elise Laird, Ms. Alice Mortlock, Prof. Kirpal Nandra, Dr. Casey Papovich, Dr. Haojing Yan and Dr. Cui Yang. I also thank for excellent suggestions and comments on my research: Prof. Alfonso Aragon-Salamanca, Ms. Emma J. Bradshaw, Dr. Kevin Bundy, Mr. Robert Chuter, Prof. Richard Ellis, Dr. Sebastien Foucaud, Ms. Yara Jaffe, Dr. Steve Maddox, Prof. Michael Merrifield, Dr. Mat Page, Dr. Frazer Pearce and Dr. Samantha J. Penny.

I thank my examiners, Prof. Alfonso Aragon-Salamanca (University of Nottingham) and Dr. Scott Chapman (University of Cambridge), for taking the time to read, study and examine my research for the degree of Doctor of Philosophy, and for making many productive suggestions for improving the work presented here.

I wish to express my heartfelt thanks to all at the University of Nottingham School of Physics and Astronomy who have helped so much in the research I have undertaken and the resulting publications and thesis. Nottingham Astronomy is truly a special place to work and I feel honoured to have had that opportunity. In view of which, I also wish to express my thanks to the school secretary, Ms. Melanie Stretton, for frequently going beyond the call of duty to aid in my affairs.

Acknowledgements

I thank the Science and Technology Facilities Council (STFC) for funding the research presented in this Thesis, and providing a much valued stipend to assist in my studies. All of the work presented here is ultimately funded by STFC studentship grant: ST/F004486/1. I also appreciate generous additional funding from the Institute of Physics, the Onassis Foundation, Gemini Observatory, and the Royal Astronomical Society to attend various conferences, summer schools, and observatory training throughout my doctorate. I also thank Gemini Observatory for allowing me to write the final amendments to my Thesis during the first few months of my employment as a Science Fellow, and thank Inger Jorgensen in particular for her understanding.

I also wish to thank Prof. Andrew Liddle, my MSc supervisor at the University of Sussex, for incredibly detailed supervision and much support leading to me taking up this doctoral course. I am hugely grateful for the level of superb education, support and encouragement I received at my alma maters: the University of Durham, the University of Sussex and the University of Oxford. I particularly single out St. Hild and St. Bede College (University of Durham) and Kellogg College (University of Oxford) for outstanding pastoral support throughout my undergraduate and early postgraduate career. I am also hugely indebted to my former schools, Our Lady of Sion and Broadwater Manor, for opening up my eyes to the wonders of learning and knowledge.

Finally, I personally thank from the bottom of my heart my family and friends, without whom I would have nothing to show for my life, let alone a complete doctoral thesis. In particular, I acknowledge the enormous love, support, help and understanding I have received from my parents, Roger and Penny Bluck, and my grandparents, Winifred and Leon Underhill, and Ruby and Frederick Bluck. If what I have achieved here makes them proud then that is my greatest reward. I also thank my friends, especially: Rob Chuter, Dan Cluett, Andrew Coleman, Chris Conselice, Mark Gordine, Ruth Gruetzbauch, Gavin Hackett, William Jeatt, Chris Kelly, Duncan Lee, Graham Mullard, Katherine Mustafa, Helen Spear, Charlie Thomas and Mark Wegner. You, my friends and family, rock my world!

Contents

List of Figures	iv
------------------------	-----------

List of Tables	vi
-----------------------	-----------

The Formation and Evolution of Massive Galaxies and their Supermassive Black Holes over the past 12 Billion Years

1 Introduction	2
1.1 What is Cosmology?	3
1.2 Galaxies	10
1.2.1 Massive Galaxies	13
1.2.2 Galaxy Formation and Evolution	14
1.3 Supermassive Black Holes	21
1.3.1 Black Hole - Galaxy Relations	24
1.4 Data and Observations	26
1.4.1 The HST GOODS NICMOS Survey (GNS)	26
1.5 Thesis Outline	32
1.6 Published Work, Conference Presentations and Press Releases	33
1.6.1 Published Work	33
1.6.2 Conference Presentations and Invited Talks	35
1.6.3 Press Releases	35
2 The Major Merger History of Massive Galaxies	37
2.1 Introduction	38
2.2 Data and Observations	40
2.3 Close Pair Method	43
2.4 Results	44
2.4.1 Merger Fraction	44

2.4.2	Merger Fraction Evolution	45
2.4.3	Merger Rates	47
2.4.4	Comparison of Structural Mergers and Pair Fractions	48
2.5	Discussion	53
2.6	Summary and Conclusions	56
2.7	Retrospective: Close Pair Errors, Star Formation Rates and Morphology	57
2.7.1	Introduction	57
2.7.2	Updated Error Analysis - The Millennium Simulation	58
2.7.3	Photometric Close-Pairs	63
2.7.4	Comparison with Star Formation Rates and Morphologies	66
3	The Structures and Minor Mergers of Massive Galaxies	74
3.1	Introduction	75
3.2	Data and Observations	78
3.3	Results	79
3.3.1	CAS Morphologies	79
3.3.2	Minor Merger Fraction from Pair Statistics	87
3.4	Discussion	92
3.4.1	Mergers	92
3.4.2	Size Evolution	95
3.5	Summary and Conclusions	97
4	SMBH - Galaxy Co-Evolution	99
4.1	Introduction	101
4.2	Data and Observations	104
4.2.1	Near Infrared Data	104
4.2.2	Spectroscopic and Photometric Redshifts	106
4.2.3	Stellar Masses	108
4.2.4	X-ray Data	109
4.3	Biases and Systematic Errors	112
4.3.1	AGN Contamination in Stellar Masses	113
4.3.2	Photometric Redshifts of X-ray Sources: Systematics	117
4.3.3	Malmquist-type Bias	120
4.3.4	Completeness	122
4.4	Method	124

4.4.1	Detecting AGN	124
4.4.2	X-ray and Bolometric Luminosities	126
4.4.3	Eddington Accretion	128
4.5	Results	130
4.5.1	The Active Fraction	130
4.5.2	SMBH Mass Evolution	133
4.5.3	Accretion Rate - Stellar Mass Dependence	140
4.5.4	Global Properties of AGN	142
4.5.5	Hardness-Mass Dependence	152
4.6	Discussion	153
4.6.1	Evolution in the $M_{BH} - M_*$ Relationship	154
4.6.2	From AGN Lifetimes to Feedback Energy	157
4.7	Summary and Conclusions	158
5	Conclusions	161
5.1	Conclusions	162
5.1.1	Galaxy - Galaxy Interactions	162
5.1.2	Size Evolution	164
5.1.3	The Role of Supermassive Black Holes in Galaxy Evolution	165
5.2	Summary	166
5.3	Future Work	167
5.3.1	Massive Galaxy Formation and Evolution	167
5.3.2	Supermassive Black Holes	169
5.3.3	Final Suggestions	170
Appendices		
A	CAS	173
A.1	Asymmetry	174
A.2	Concentration	175
A.3	Clumpiness	175
B	Data Tables	177
Bibliography		197

List of Figures

1.1	Hubble's law	7
1.2	Hubble's Tuning Fork	13
1.3	Luminosity and Mass Function Plots	15
1.4	2df - Millennium simulation Comparison	17
1.5	Black Hole - Galaxy Scaling Relations	27
1.6	GNS Massive Galaxy Rest Frame UV - Optical Comparison	29
2.1	The Merger Fraction Evolution of $M_* > 10^{11} M_\odot$ Galaxies	46
2.2	Major Merger Rate Evolution	49
2.3	The Redshift Evolution of the Average Time Between Major Mergers	50
2.4	The Evolution of the Derived Merger Fraction through Several Previous Studies Compared to our Results	53
2.5	The Ratio of the Time-scale Sensitivity for the CAS Identified Mergers and the Time-scale for Merging for Galaxies in $20 h^{-1}$ kpc Pairs	54
2.6	The Ratio of the CAS merger Fraction and the Pair Fraction	55
2.7	Millennium Simulation	64
2.8	Photo-z - Spec-z comparison 1	66
2.9	Photo-z - Spec-z comparison 2	67
2.10	SFR Comparison	71
2.11	Aysymmetry vs Star Formation Rate	72
2.12	Star Formation rate vs Pair Number	72
2.13	Asymmetry vs Pair Number	73
3.1	Concentration (C) - Asymmetry (A) Plot	80
3.2	Major Merger Fraction Evolution	84
3.3	Asymmetry (A) vs. Residual Flux Fraction (RFF) Plot	87
3.4	Merger Fraction - Mass Range Plot	93
4.1	The EGS Field	110

4.2	The GOODS Fields	112
4.3	Frequency Histogram of the Ratio of K band flux to X-ray hard band flux for our Volume Limited Sample of AGN	115
4.4	Hard Band Luminosity vs. Redshift for 508 AGN	129
4.5	The Active Fraction Evolution with Redshift	131
4.6	The SMBH Eddington Mass plotted against Stellar Mass of Host Galaxy across Three Redshift Ranges	137
4.7	The Redshift Evolution of the Ratio of Eddington Limiting Mass to Stellar Mass of Host Galaxy (M_E/M_*)	139
4.8	Plots of SMBH Efficiency (μ) and Maximum Time to reach Local Relation (τ_{max})	142
4.9	Accretion Rate - Stellar Mass Dependence	143
4.10	The Contribution to the X-ray Luminosity Function of sub-QSO Massive Active Galaxies	151

List of Tables

B.1	Photometric Pair - Statistical Pair Comparison	178
B.2	Comparisons of Statistical and Photometric Close Pair Numbers, Asymmetry and Star Formation Rates	179
B.3	List of Potential Close Pairs - 1	185
B.4	List of Potential Close Pairs - 2	187
B.5	Close Pair Method Test: Spectroscopy form the Millennium Simulation	188
B.6	AGN Data Source Summary	189
B.7	Average Properties of the AGN Samples	190
B.8	Volume Limited Sample of Active Massive Galaxies at $0.4 < z < 3$.	191

**The Formation and Evolution of
Massive Galaxies and their
Supermassive Black Holes over the
past 12 Billion Years**

Chapter 1

Introduction to the Formation and Evolution of Massive Galaxies and their Supermassive Black Holes

1.1 Philosophical Motivation: What is Cosmology?

A semantic definition of cosmology could be phrased as: the study of the Universe as a whole often through scientific or empirical methods but not necessarily solely constrained to these. But this would be to miss the fundamental point about cosmological endeavour. Perhaps the most profound discovery of mankind is that the Universe had a beginning in time and has since evolved into what it is now from an earlier, simpler, hotter and smaller state. This fundamental point about cosmology is also a truism about existence: things change. If they did not it would be sufficient to simply observe how things are and one would immediately know how they were and will be for all time. To a modern reader this may sound obvious, but it is pertinent to note that it is not at all so. Take for example the ‘cosmologies’ of ancient Greece and Egypt, or even the cosmologies of medieval society or laterday Christianity. These all have a sharp division between the immutable and immortal heavens, and the changeable ephemeral Earth. We now know that this division is, at least in a physical sense, a myth. However, the knowledge to free our thoughts from this dualism between Heaven and Earth was hard won and not at all realised for what it was at the time.

In the 17th Century, Newton and Galileo, among others, described and explained how the laws of nature as we understand them on Earth can be applied to the heavens above to give phenomenally accurate predictions of, for example, the motions of planets around the sun and moons around planets. This naturally suggests that the same ephemerality (or tendency to change) might apply out there in the heavens above us as well as down here on earth. This point was not embraced at the time. Instead, Newton and his contemporaries believed in an eternal, static, and immutable Universe in which objects were defined for all time by deterministic laws which they unchangingly follow. This view held such prevalence across both science and religion that it is easy to forget that it disagrees fervently at its base level with both.

All of the major monotheistic religions have a creation myth associated with them, as do many non-monotheistic religions such as the many polytheistic religions in the ancient world. Now, if there is creation then there is a period of formation (of ‘making’) and thus there is, in a sense, evolution - a period of becoming. Equally, at the heart of Newton’s theories is a principle of causality, a metaphysical assumption that

one thing *causes* another, which implies that things naturally change, albeit via pre-ordained deterministic and knowable laws. Therefore, the idea of a separate eternal reality just above the sky where all is forever as it was and will be has never fit particularly well either natural philosophy (science) or theology (in most religions at least). So it becomes significant and interesting to ask, why was this view so passionately adhered to? One obvious solution is that of timescales. Cosmological objects tend to change on timescales far greater than everyday objects down here on Earth (with a Gyr = 1 billion years often being the usual unit of time used among cosmologists and astrophysicists), and thus it is very difficult to actually perceive changes in the heavens directly within the lifetime of human civilisation. Nonetheless, there are a number of significant counter-examples, such as bright (nearby) supernovae, comets and meteor showers which all suggest change and variability over and above the clockwork mechanics of the standard solar system picture and the static background of distant stars. A thoroughly convincing answer is, therefore, something that is difficult to achieve and is far beyond the scope of this thesis, but I will return to the question periodically by way of highlighting how it is often what is most obvious that is hardest to see about nature. For now, however, it will suffice to look briefly at how this view of unchanging and immutable heavens came to be discarded by scientists.

Albert Einstein is heralded by many as the greatest thinker of all time, but for the purposes of this discussion it will be his blindness to the true nature of his theory of general relativity, and to the Universe itself, that will be of most interest. In seeking to find a reconciliation between Maxwell's electromagnetism and Newton's mechanics, and later universal gravitation, Einstein was forced to consider deeply what was required of a physical theory at quite a philosophical level. He postulated a 'principle of relativity' which states that the laws of physics should be precisely the same everywhere regardless of where, when, what angle etc. an observer happens to be positioned. This is the radical generalisation of the the idea (began with Newton and Galileo) that one can use the same laws to describe the motions of the heavens to those which describe the motions of balls on inclined planes down here on Earth. Of course, this theory led to several startling (and now experimentally and observationally tested) consequences, including the absolute constancy of the speed of light, time dilation, length contraction, black holes and warped spacetime. But it is the role of curved spacetime to describe

gravity that will provide an insight into our present concern, of trying to understand what in fact cosmology is. Einstein related the total curvature of spacetime (roughly $G_{\mu\nu}$) to the total mass-energy ($T_{\mu\nu}$) by the Einstein field equation (e.g. Misner, Thorne & Wheeler 1973):

$$G_{\mu\nu} + \Lambda g_{\mu\nu} = \frac{8\pi G}{c^4} T_{\mu\nu} \quad (1.1)$$

where

$$G_{\mu\nu} = R_{\mu\nu} - \frac{1}{2} g_{\mu\nu} R \quad (1.2)$$

and R is the Ricci scalar, $R_{\mu\nu}$ is the Ricci curvature tensor which is reduced from the Riemann tensor, and $g_{\mu\nu}$ represents the metric of spacetime. c is the speed of light and G is Newton's universal gravitational constant. Λ is the much maligned and disputed cosmological constant (discussed below) which may be a means of explanation to the observed dark energy, resulting in accelerated expansion of spacetime today. What is most important for our present concerns, is the fact that this equation beautifully links spacetime to mass-energy, effectively linking the stage and players together inextricably.

It became rapidly apparent to Einstein that his theory of general relativity led naturally to a dynamical spacetime, where 'matter tells spacetime how to curve, and spacetime tells matter how to move' (Wheeler). In unifying space and time, matter and energy, and finally the effects of mass-energy as curved spacetime, Einstein discovered that the entire fabric of the Universe, that of space and time itself (not just the objects within it), is subject to change and evolution. But this view was philosophically abhorrent to him, and to return to the view of a static, unchanging, immutable spacetime in which objects passively evolve according to universal physical laws, he introduced a mathematically sound yet physically mysterious 'cosmological constant'. This was set to balance the inward force of gravity in the Universe providing a static (non-dynamical, immutable) spacetime. Unfortunately, this was a failure both theoretically and, as it turned out, empirically as observations of distant 'nebulae' and mathematically rigorous checks of the effect of the cosmological constant on a static spacetime both led to the conclusion

that we live in a dynamical spacetime, in a Universe which *evolves* with cosmic time. One of the greatest and most celebrated modern astronomers was Edwin Hubble, whose use of Cepheid variable stars to deduce absolute magnitudes and hence distances to ‘nebulae’ allowed him to discover a fascinating, and at the time beguiling, relation. He noted that the distances to many ‘nebulae’ were vast, often millions of light years away, placing them far outside the Milky Way galaxy, which at the time was thought by most astronomers to be the entire extent of the Universe (Hubble 1926). Moreover, he compared these distances to Doppler redshifts obtained earlier by Vesto Slipher to demonstrate a startling result. Slipher noted that the vast majority of ‘nebulae’ had light Doppler shifted to the red part of the spectrum, indicating that these objects were all moving away from us. Hubble showed that the further the extra-galactic ‘nebulae’ (which we now know as galaxies) were from us the faster their recession velocities (see Fig. 1.1 for a contemporary example). Thus (as in e.g. Sparke & Gallagher 2000):

$$v = H_0 r \quad (1.3)$$

where v is the line of sight recession velocity of a distant galaxy, r is its distance from us, and H_0 is Hubble’s constant, known today to be ~ 70 km/s Mpc $^{-1}$. What this most readily demonstrates is that the Universe is expanding. If we run time backwards we would see the Universe shrink, and if we allow this to go on indefinitely we see that the observable Universe would reach zero size in a finite time. A first estimate of this time is given by $1/H_0$ (assuming no variation in the Hubble parameter). Today we are able to use our detailed knowledge about the constituents of the Universe - matter, dark matter and dark energy, and their relative abundances - to compute the age of the Universe more precisely. This is now known to be ~ 13.7 billion years (e.g. Suyu et al. 2010). Thus, we have profound empirical evidence that we live not only in a dynamical Universe (which changes or evolves over time) but also live in a Universe which is finite, in time at least, and has therefore a beginning about which we can ask meaningful scientific questions.

Even without the direct test of dynamical spacetime performed by Hubble and Slipher, a static unchangeable view of the Universe would already have been in big trouble by the late 1920’s. It was demonstrated by Friedmann and de Sitter (amongst others) that

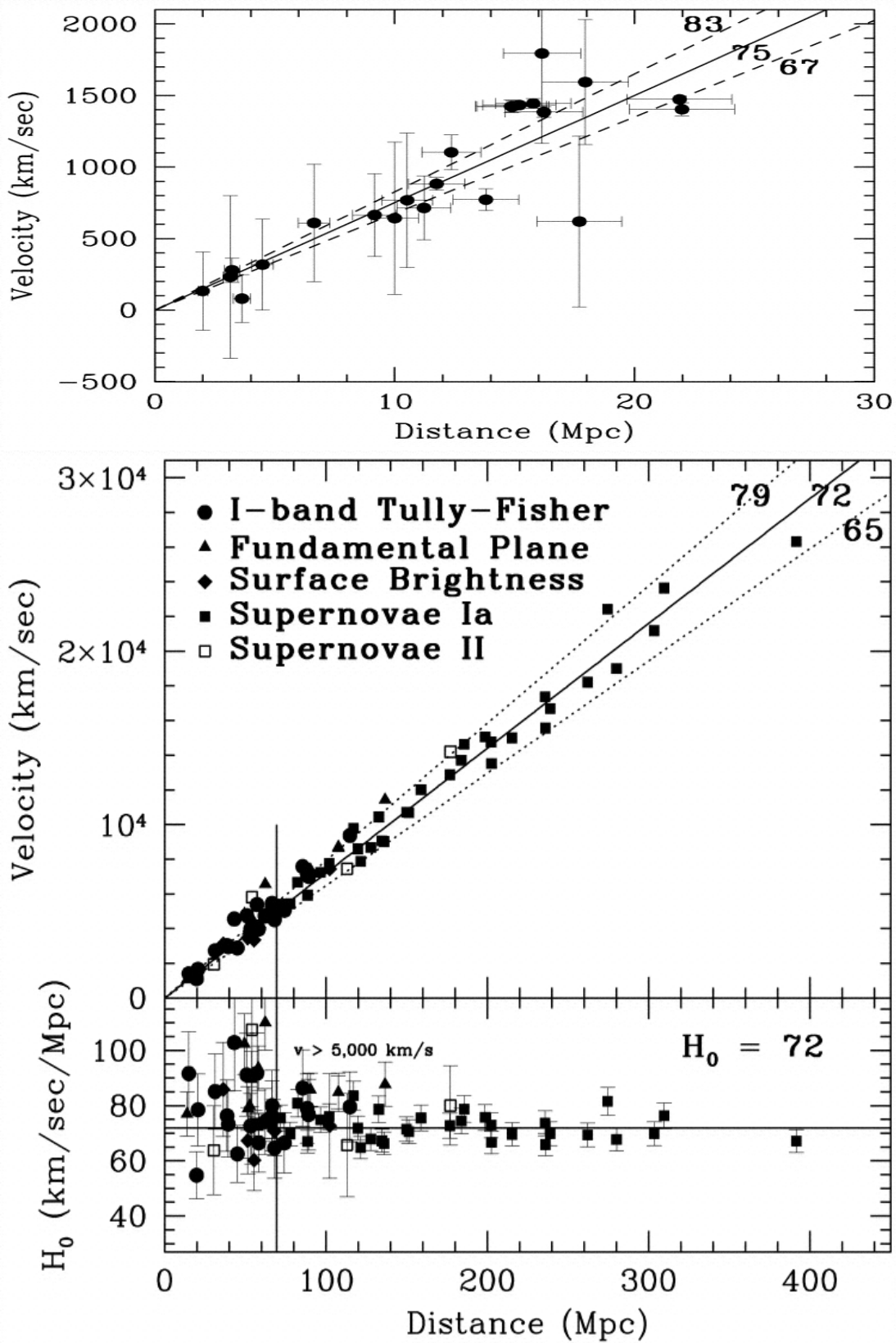


Figure 1.1: Hubble plot for (top) Cepheid determined distances, and (bottom) a variety of distance indicators, including supernovae and the Tully-Fisher relation (as indicated on the plot). These plots are taken from Freedman et al. (2000). The current accepted best value for H_0 is ~ 72 km/s Mpc^{-3} .

Einstein's cosmological constant could not prevent spacetime from either expanding or contracting, as it was an unstable solution, much like trying to get a pen to rest stably on its tip. Moreover, since other empirical tests of relativity were performed (most notably the explanation of the precession of the perihelion of Mercury, Le Verrier 1859, and Eddington's inspired observation of the displacement of a star on the sky due to the curvature in spacetime caused by the sun's gravitational field, Dyson et al. 1920), high confidence in the validity of general relativity was already beginning to emerge. Thus, science was on the verge of accepting once and for all an evolving picture of the Universe and all within it.

In the decades of the 20th century which followed more and more evidence mounted for a picture of the cosmos as a changeable, developing entity. The masses, colours, densities, and even morphologies of galaxies were seen to vary with cosmic time (e.g. Aragon-Salamanca et al. 1993). The chemical composition of the stars and gas regions varied, as did the density and frequency of quasars (e.g. McLure & Dunlop 2004). Perhaps most significantly the size of the Universe dramatically increases with age, and hence the Universe cools. Again, by playing this backwards in time it is easy to see how this implies a much smaller, denser, and hotter Universe in the past. From this model, and detailed application of general relativity and nuclear and atomic physics, the relative abundances of nuclei were accurately and correctly predicted (Suess & Urey 1956). Finally, this kind of cosmology led to the prediction of a Cosmic Microwave Background by Dicke, Gamow and others (e.g. Gamow 1948), a relic of the energy from the Big Bang itself, which was in due course observed, first by Penzias and Wilson and later with purpose built precision satellites, including COBE, WMAP and now PLANCK among many other experiments (see e.g. Bennett et al. 2003). All this combines to make a compelling case for a dynamical spacetime and evolving Universe.

The upshot of all this is that we now know with absolute certainty that the Universe in which we inhabit changes over time, and in a very fundamental sense this is what cosmology is all about. Cosmology is both an observational/ empirical scientific field, and also a more speculative mathematical/ theoretical pursuit in modern science. Ideally these two branches inform and strengthen each other, leading to discovery and

explanation. The jewel in the crown of this bipartisan approach is the current standard cosmological model, known as Λ CDM, short for dark energy - cold dark matter. Add to this the Big Bang theory and inflation, and we have a self consistent, phenomenally predictive and thoroughly tested picture of the Universe. However, it is in many important ways fundamentally flawed. As of the time of writing there is no accepted explanation for dark matter (although many conjectures exist mostly within supersymmetry models for quantum gravity), worse there is almost complete failure in accounting for the dark energy within standard particle physics (with many string theorists reaching for a multiverse solution through anthropic arguments). Furthermore, inflation has many problems of its own (not least the reheating problem) and the Big Bang theory gives us no insight into how the Universe began (or why it exists) in the first place. In many ways, what the standard model of cosmology is, is an empirically formulated procedural method for correctly accounting for the exact observed expansion of the Universe, matching with a vast collection of data from supernovae to the CMB. What it is emphatically not, is a satisfactory scientific explanation of it at present.

To return now to the titular question, given this introductory discussion, *what is cosmology?* In a sense it is history (at the observational/ empirical end) and philosophy (at the mathematical/ theoretical end). Because the Universe is not static and unchanging, and in fact evolves with cosmic time, and due to the finite speed of light, to observe the Universe is to witness history, and to seek coherent explanation of that history is in the purest sense philosophy. Due to the evolving nature of stars, galaxies, and space-time itself it is not sufficient to know how things are now, and in fact it becomes vital to ascertain how things were in the past. By observing how things change (be they galaxies, quasars or gas cloud chemical compositions) we can come to understand the causal reasons for this change, and with this predict the future evolution of the Universe. So, it is at this final juncture, in cosmology's predictive potential, that it returns to be most naturally 'science'. The more we come to know about the detailed history of the Universe and its constituents, the better equipped we shall be to find explanation for the evolution witnessed, and with this the more reliable and robust our predictions about the future will become.

In this thesis I study in detail many of the ways in which massive galaxies and their supermassive black holes have changed over the past 12 billion years of cosmic evolution. Thus, I construct a cosmic history of massive galaxies and their supermassive black holes. To achieve this I combine extremely high resolution and deep images in the near infrared from the Hubble Space Telescope (HST) with deep X-ray imaging from the Chandra X-ray Observatory (CXO), and combine these space based data sets to a wealth of photometry and spectroscopy from ground based instruments, including the Palomar Observatory, the Canada France Hawaii Telescope, Keck, the VLT and Gemini telescopes. The result is an attempt at a thorough description of many of the ways in which massive galaxies and their supermassive black holes have evolved from the early Universe to the present day. From this I suggest several plausible and observationally motivated explanations to the witnessed evolution, which lead to the possibility of predictions for the future.

1.2 Galaxies

For almost a century astronomers have known that there are other galaxies in the Universe than our Milky Way. However, some nearby galaxies had been viewed by the naked eye and through the eye pieces of modest telescopes for several centuries before. They were not realised to be extra-galactic objects containing billions of stars like our own galaxy until the pioneering work of Edwin Hubble (Hubble 1925, 1926) using Cepheid variable stars as distance indicators. However, this explanation as to the the nature of some ‘nebulae’ was first suggested as a possibility much earlier by Thomas Wright and Immanuel Kant in the 1750’s. We now know there to be at least $\sim 10^{11}$ galaxies in the observable Universe (Williams et al. 1996), and these objects vary greatly in size and mass, from $10^6 - 10^{13} M_{\odot}$ and from $\sim 1 - 30$ kpc. A clear and unambiguous definition of the term ‘galaxy’, however, is not immediately apparent. Nonetheless, there are several significant commonalities between these objects suggesting, at least, that they are natural kinds of some sort. Firstly, all galaxies are vast gravitationally bound objects containing at least millions of stars. Additionally, galaxies contain in general a large amount of gas and dust, and presumably planets, comets, asteroids and other low brightness objects such as brown dwarfs, white dwarf

stars and so on, which are much harder to detect than the stellar components.

All of this ‘baryonic’ (read atomic + ionic) component to the mass of galaxies, however, contributes only around 20 % of the total mass of galaxies. Fritz Zwicky in 1933 demonstrated that the velocity dispersion of galaxies in the Coma cluster was far too high to be gravitationally bound in a virialised system by the observable mass (Zwicky 1933), hence, suggesting the existence of some unseen ‘dark’ matter. We now know that many other measurements agree that there is missing mass in galaxies and galactic groups and clusters. Observations of the rotation curves of galaxies (Rubin et al. 1980), gravitational lensing of distant galaxies by nearby galaxy clusters (e.g. Taylor et al. 1998), and X-ray luminosities of X-ray clusters (e.g. Vikhlini et al. 2006) all lead inexorably to the conclusion that much of the mass of galaxies is in some invisible ‘dark’ form. Furthermore, evidence from the baryon acoustic peaks of the temperature power spectrum of the CMB and from the primordial nuclear abundances dictate that this matter be non-baryonic in form (see Hinshaw et al. 2009 for the most up to date WMAP data on the Λ CDM cosmology). One alternative to this view is that the laws of gravitation must be modified on the vast scales of galaxies and galactic clusters (see Milgrom 1983), although more recent measurements of the ‘bullet’ cluster seem to support a particle approach for explaining dark matter (e.g. Markevitch et al. 2004). Constraints from modelling the evolution of large scale structure and from comparing these simulations to galaxy redshift surveys suggest that this non-baryonic dark matter must be non-relativistic, or ‘cold’ (see, for the 2dF survey example, Cole et al. 2005). Therefore, in terms of mass, the most important constituent of a galaxy is in fact this cold dark matter. However, if there were a ‘dark galaxy’ with much mass and little or no electromagnetic emission it is unclear whether this would be justifiably described as a ‘galaxy’ in the common parlance or merely referred to as a dark matter halo.

For the purposes of this thesis we shall operationally define galaxies to be gravitationally bound collections of *at least* many millions of stars, which are expected to contain significant other components including dark matter, interstellar gas and dust, and stellar remnants. One other vital component of most galaxies seems to be a central supermassive black hole (SMBH) which has typically a mass $\sim 1/1000$ that of its host galaxy’s stellar mass component (see e.g. Kormendy & Richstone 1995 and Haring &

Rix 2004) . We shall return to discuss these fascinating objects in much more detail in the next section.

So far the components of galaxies have been discussed, but equally important are the structures that galaxies form. The distribution of galaxies on the sky is not a random pattern. In fact one is much more likely to find a galaxy near another galaxy than in a randomly chosen area of sky. Thus, it has been known for almost as long as we have been able to observe extra-galactic galaxies that these group and cluster together to form immense structures throughout the observable Universe (e.g. Kessler et al. 2009). In a sense galaxies are the building blocks of cosmic large scale structure, the fundamental mass units (or atoms) of clusters and filamentary super-clusters that permeate our Universe. Therefore, galaxies are simultaneously ‘island Universes’ (c.f. Kant), containing often billions of stars gravitationally bound into mostly coherent dynamical systems, and ‘cosmic atoms’ (c.f. Sandage) which are the seeds and constituents of large scale structure.

It is, of course, paramount in any research program to ask ‘why study this?’ and the field of extra-galactic astrophysics is no exception. By way of an answer, on the one hand galaxies are powerful laboratories in which to test the laws of physics on size, mass and energy scales far removed from that of the Earth. On the other hand, they are also fundamental units in cosmology in their own right, and any hope of understanding the evolution of the Universe as a whole must rely on the reductionist appreciation of its constituent base parts, i.e. galaxies. But perhaps the most important reason of all for studying galaxies is that we ourselves evolved to live on a planet orbiting a star which itself is part of, and orbits the centre of, a galaxy. Thus, any serious attempt to appreciate our place in the Universe must address both our place in our galaxy and how our galaxy (and by extension all galaxies) formed and evolved to be as they are today. It is this dual capacity to probe both fundamental physics and cosmology, along with the wonder and audacity to ask how we came to be here, that makes extra-galactic astronomy such an exciting and important field of research in the early 21st Century.

For largely historical reasons, the first attempts to categorise galaxies were morphological in nature, i.e. galaxies were grouped together according to their ‘shape’. Hubble (1922) invented a now much maligned and disputed ‘tuning fork’ approach to cate-

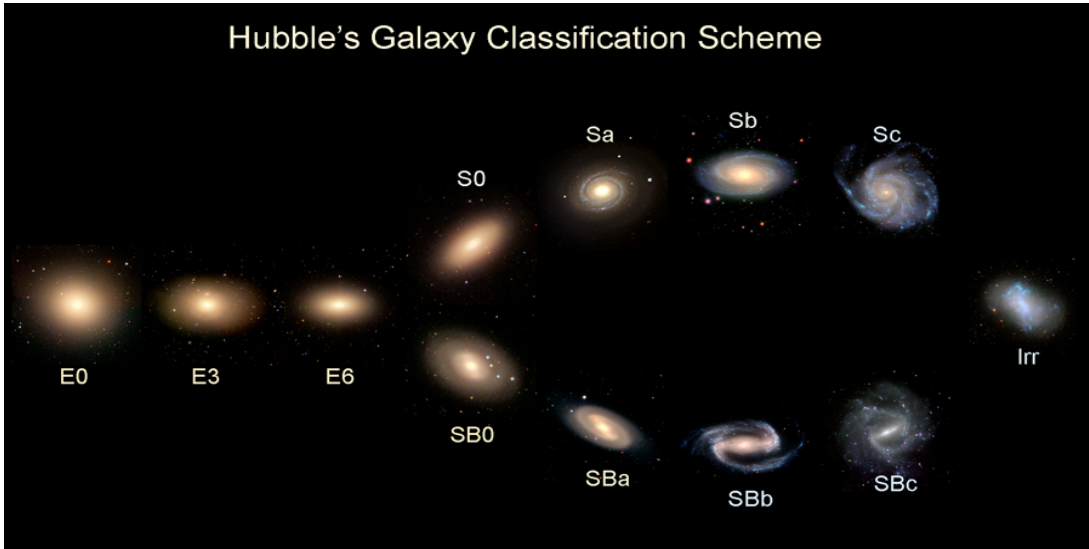


Figure 1.2: Hubble's 'tuning fork' categorisation scheme for galaxies, going from early type spheroidal galaxies (on the left), via lenticulars (at the branching point), to late type disc galaxies with spiral arms (on the right). However, for the purposes of this thesis we shall mostly be interested in the disturbed irregular galaxies (shown at the extreme right end of the diagram) which do not classically fit anywhere in the Hubble scheme. These galaxies are obviously in a state of change, and will provide a tracer for galaxy formation and evolution. Image credit: University of Texas

gorising galaxies ('non-Galactic nebulae') via morphology (see Fig. 1.2). Most galaxies in the local Universe are either elliptical or disc like in shape, with the latter most often having spiral structure. A smaller group of peculiar or irregular galaxies is also observed to exist. Ordinarily one most often find irregular galaxies to be the result of the merging together of two or more galaxies, with peculiar galaxies arising from tidal interactions between galaxies or the cluster potential which can also result in merging. Therefore, observing irregular or distorted galaxies is effectively catching galaxy formation and evolution in the act - it is witnessing change in progress. This means that studying galaxy morphology can be a powerful tracer of merger history, and, hence, galactic formation and evolution. We shall discuss the formation and evolution of massive galaxies in §1.2.2. The type of galaxies studied in this thesis are all very massive (with stellar mass $M_* > 10^{10.5-11} M_\odot$) and we turn next to discuss these objects in the following section.

1.2.1 Massive Galaxies

Most of the galaxies in the Universe are relatively small, and even by mass the vast majority of galaxies' contribution to the observable Universe would come from smaller

systems. This is represented by the steepness of the local stellar mass (and luminosity) function (see Fig. 1.3). Massive galaxies are rare, and contribute only modestly to the total mass and luminosity from galaxies in the Universe, but they are, however, very good tracers of galactic evolution and cosmic history. Due to their high stellar masses, massive galaxies are very often highly luminous objects. This allows them to be seen from Earth, via large telescopes, routinely out to almost the entire distance of the visible Universe (up to $z \sim 4$ or so) at present times. Furthermore, in the dominant paradigm of galaxy formation, small galaxies form from the gravitational collapse of gas clouds in dark matter halos in the very early Universe, which then merge together to form larger structures via hierarchical assembly. Thus, the most massive galaxies in the Universe are most likely those which have undergone the most evolution throughout their lifetimes. The result of which is that massive galaxies are excellent probes of galactic evolution, relatively easy sources to detect at very great distances and, from this, bright beacons of cosmic history.

In this thesis massive galaxies are considered generally to be galaxies with high stellar mass (as often total dynamical mass is unobtainable in practice for high redshift systems) with $M_* > 10^{10.5-11} M_\odot$. At high redshifts this criteria will select the most massive galaxies in existence at these early times, which are likely to be progenitors for large modern day ellipticals, and perhaps brightest cluster galaxies (BCGs).

1.2.2 Galaxy Formation and Evolution

The formation and evolution of massive galaxies is most properly considered within the Big Bang theory paradigm of cosmic evolution. Within the cold dark matter (CDM) picture, simulations suggest that dark matter halos form in the very early Universe out of slight density fluctuations, likely a relic from cosmic inflation (Guth 1981), which increase in size and mass hierarchically out of the merging of smaller halos together to form larger ones as the Universe expands (see e.g. the Millennium Simulation, Harker et al. 2006, Bett et al. 2007). This leads to a complex filamentary large scale structure to the mass distribution of the Universe. The dominant paradigm for galaxy formation and evolution posits that galaxies form within these dark matter halos and merge in line with them. This picture, however, ignores much of the highly complex

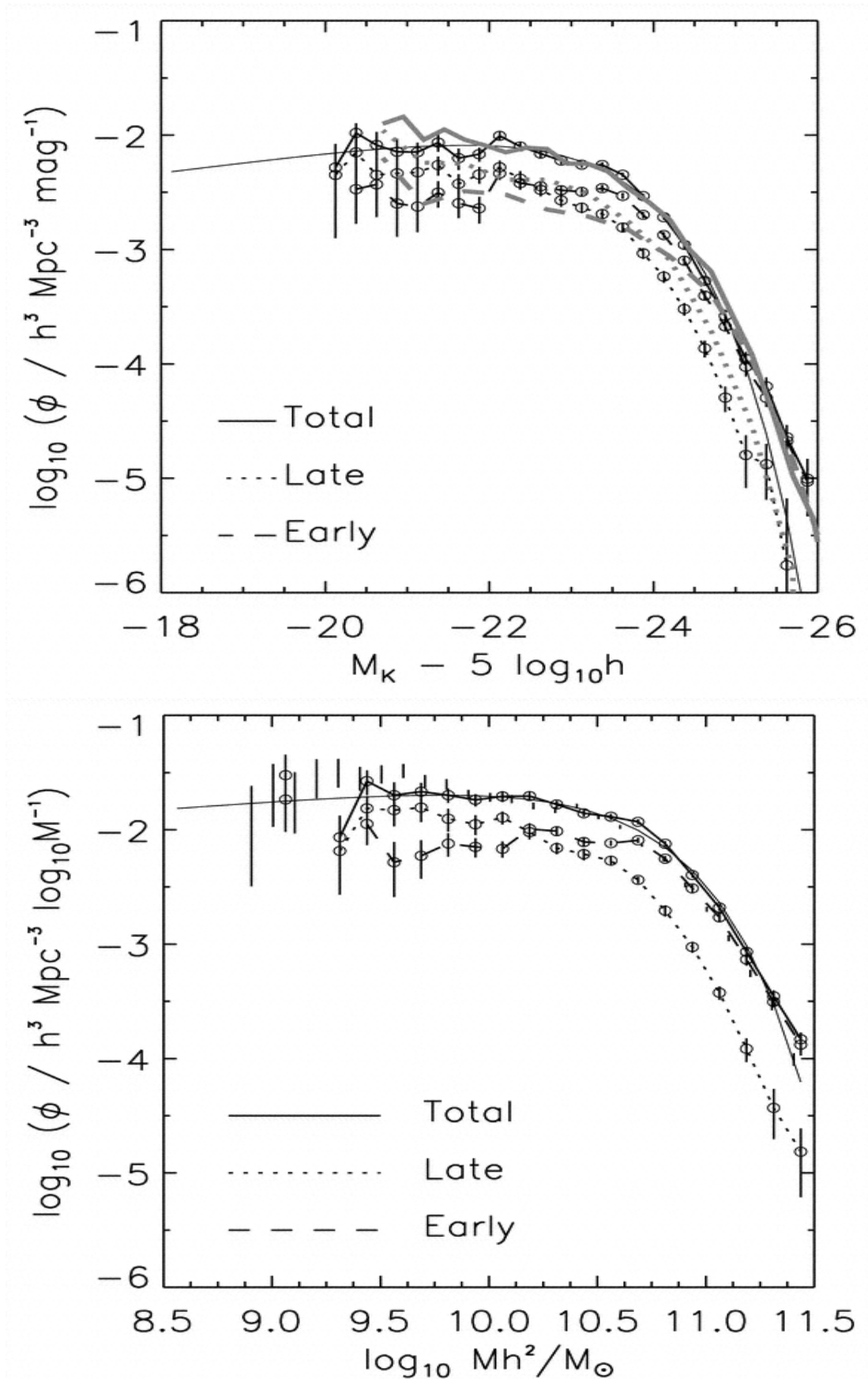


Figure 13: K band luminosity (top) and stellar mass (bottom) functions for the local Universe, taken from Bell et al. 2003. Note that the total number of massive ($M_* > 10^{11} M_{\odot}$) galaxies is much lower than the number of less massive galaxies. However, these massive galaxies are much more luminous and, hence, are easier to detect and study at high redshifts, resulting in these objects

and unpredictable baryonic gas physics that is involved in galaxy formation. Thus, there is likely to be significant departure in the structure and distribution of galaxies when compared to the underlying skeleton of the dark matter distribution. This notwithstanding, the global distribution of galaxies in the local universe as seen from, for example, the 2DF survey shows filamentary structure uncannily reminiscent of that predicted in CDM models (see Fig. 1.4), suggesting that hierarchical assembly in line with CDM evolution is a good first order approximation of the history of galaxy evolution.

A perhaps oversimplified description of galaxy formation is as follows (for a more thorough discussion see e.g. Cole et al. 1994, Sugerman et al. 2000, Krumholz & McKee 2005, Kitzbichler & White 2007, Romano-Diaz et al. 2009). In the very early Universe dark matter begins to clump together under the attractive potential of gravity, due to the slight over- and under-densities left as a relic from inflation. Baryonic matter is well distributed throughout the CDM landscape at this early time and begins to cool via various processes, collapsing to the centre of dark matter halos. Torques are induced via interactions between halos, such as orbiting, merging and close passes. Through conservation of angular momentum, as the baryonic matter cools and collapses it spins faster and is transformed into a disc. These systems are held virialised via high rotational velocities. Slight imperfections in the distribution of matter may lead to orbiting density waves which provoke spiral structure. Thereafter, major and minor merging of galaxies can disrupt this highly structured kinematic system, leading to temporarily irregular shaped galaxies, which may settle into elliptical galaxies, which are held apart (virialised) via the effective pressure of their high velocity dispersions. These ‘early type’ galaxies are usually redder in colour, most probably because they have necessarily experienced more merging, resulting in star bursts (rapid star formation) and the increased depleting of available cool gas to form new stars with. In this picture the fraction of blue (star forming) spiral galaxies will naturally decrease, and the fraction of red (non-star forming) ellipticals will rise with time, and, due to the hierarchical nature of the process, the average (or typical) galaxy mass will increase with cosmic time. Furthermore, since the Universe is expanding, and even the comoving number density of galaxies will presumably decrease with time (due to galaxies merging together to form single systems), the irregular galaxy fraction will also de-

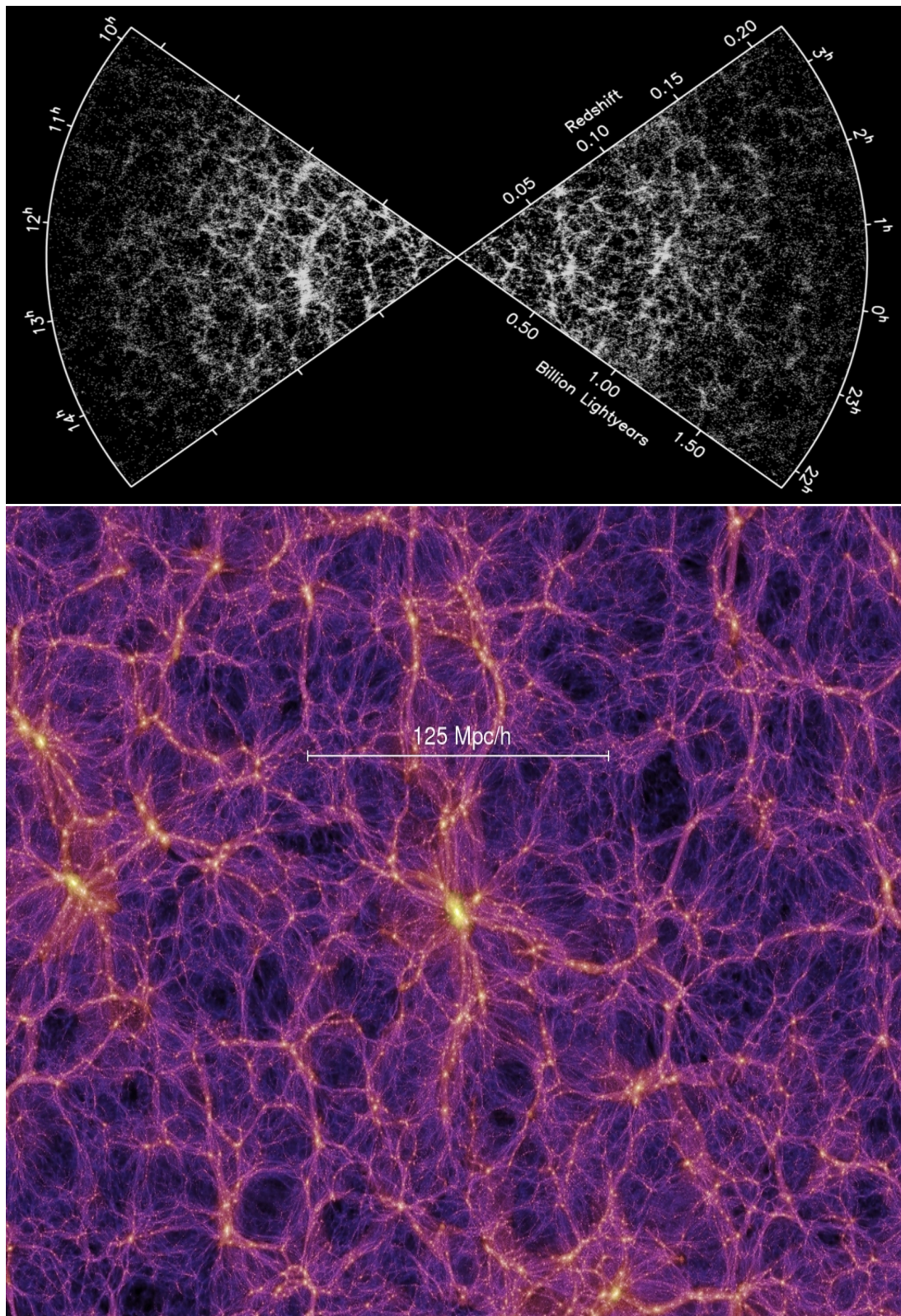


Figure 1.4: A comparison of the distribution of galaxies in the local Universe (top, from the 2df Survey, Cole et al. 2005) and the predicted distribution of dark matter (bottom, from the Millennium simulation, Bett et al. 2007). Note the similar filamentary structure in both images, suggesting that on large scales, to first order at least, galaxies trace the underlying mass distribution of the Universe, which is dominated by cold dark matter.

crease with time. Although the global predictions stated here do hold true, there are still significant issues to be resolved with this picture.

Despite the lauded success of this hierarchical model of galaxy formation, other theories for galaxy formation do exist. The most important and distinct of these is monolithic collapse (see e.g. Madau et al. 1998 and Moore et al. 1999 for discussions from observational and theoretical perspectives respectively). In this paradigm galaxies form via gravitational collapse of baryonic gas clouds in the very early Universe and form a wide spectrum of galaxy masses, sizes and morphologies, due to a combination of gas physics and the underlying gravitational potential of dark matter. Then galaxies grow rapidly quiescent in terms of their interactions with each other, and galaxies predominantly passively evolve with cosmic time thereafter. Principal arguments against this monolithic collapse model include the observation of major merging of massive galaxies throughout cosmic history (see Chapter 2, Patton et al. 2000, Conselice et al. 2007, Rawat et al. 2008, Bluck et al. 2009, Lopez-Sanjuan et al. 2009a/b, Conselice, Yang & Bluck 2009), the dramatic reduction of the peculiar morphology fraction of galaxies with cosmic time (see more in Chapter 3, Schade et al. 1995, Abraham et al. 1996), the close resemblance of the galaxy distribution to the simulated dark matter distribution (Cole et al. 2005, Fig. 1.4), and the observations of star burst galaxies periodically throughout cosmic history which are thought to be triggered by mergers (e.g. Juneau et al. 2005, Conselice, Yang & Bluck 2009). These arguments, however, do not entirely rule out some aspects of the monolithic collapse mechanism, as it is still possible that these processes are secondary evolutionary features. One strong case for monolithic collapse is the recent observations of morphologically undisturbed massive galaxies at very high redshifts (see Conselice & Arnold 2009), where one can construct a persuasive case for there not being enough time for massive galaxies to have formed via hierarchical assembly (merging) and become dynamically cool and morphologically smooth in the few hundred million years allowed since the origin of the Universe.

The debate between hierarchical assembly and monolithic collapse will provide a general backdrop to this thesis, and Chapter 2 and 3 in particular will consider the case for both these paradigms in much detail in light of new data acquired during my PhD from

the HST NICMOS 3 camera. This issue is further complicated by much recent excitement concerning the role of gas inflows towards galaxies as a mechanism for galaxy evolution and possibly formation (e.g. Townsley et al. 2003, Kauffmann et al. 2006). Here much of the baryonic mass of galaxies could be built up by accretion of gas from the intergalactic medium, as opposed to through initial gas cloud collapse or merging with smaller galaxies. It is likely that all three of these formation processes, along with quiescent evolution and star formation, occur and are important for explaining the origin and diversity of massive galaxies in the Universe.

As well as the above mechanisms for galaxies to build up and increase their baryonic and stellar mass, and in this sense ‘form’, there are also both internal and external processes that effect how galaxies evolve over cosmic time. Along with morphology, another powerful tool with which one can examine the nature of galaxies is colour, defined as the difference between the absolute magnitudes of differing wavebands. It has been known for some time that there are more ‘red’ galaxies in denser environments, such as the centres of clusters, than in less dense environments such as the outskirts of clusters, groups, or voids (Butcher & Oemler 1984). Additionally it is known that there was a higher fraction of blue galaxies at early times than in the present day Universe (Oemler 1974). This suggests that there is evolution towards redder colours in galaxies over cosmic time, perhaps in part caused by increased clustering. Intuitively, this is a logical outcome of the standard process of star formation: as galaxies age they use up cool gas to make stars, thus the star formation rate will decline and the stellar populations will age and redden. However, this picture is fundamentally flawed as there should (by this mechanism alone) be plenty of available gas in galaxies to form new stars by the present day (e.g. Bell et al. 2004). Therefore, a fundamental question still to be addressed in extra-galactic astrophysics is: what drives the reddening of galaxies?

Some other process(es) must be responsible for the reddening of galaxies over cosmic time. One of the first candidates explored by astrophysicists was the effect of supernovae feedback on star formation (e.g. Reddish 1975, Couchman & Rees 1986, Thomas & Fabian 1990). As a rule of thumb there is roughly one supernova per 100 stars over the age of the Universe, providing a vast amount of energy which is input

into the interstellar medium of galaxies (e.g. Diehl et al. 2006). Could this energy be responsible for the reddening of galaxies witnessed? There is little doubt today that supernovae explosions will have a profound impact on the interstellar medium, in general heating and blowing away cool gas, needed to form new stars, thus aiding in the production of the red sequence. This is not necessarily, however, the only effect worth considering. Since there are observed relationships between the colour, morphology and environment of galaxies (e.g. Dressler 1980, Butcher & Oemler 1984), whereby the galaxies in the most dense environments tend to be red lenticulars (S0's) or ellipticals, it is likely that there are environmental considerations to the evolution of galaxies as well, for example selecting against blue spiral galaxies in very dense environments.

Processes such as tidal forces from the cluster potential, ram pressure stripping, harassment and strangulation can lead to a reduction of available cool gas and a consequent reduction of star formation rate and ultimately a reddening of galaxies (e.g. Gunn & Gott 1972, Moore et al. 1996, Gnedin & Ostriker 1997, Poggianti et al. 2006). Further, as mentioned above, the major (and possibly minor) merging of galaxies together can also result in an eventual reddening of galaxies through induced star bursts and the rapid depletion of cool gas supplies. This is also likely to have a differential environmental effect, whereby the optimum environments for merging are likely to be intermediate density regions, where the frequency of galaxy close passes (and interactions) is still moderately high, but the velocity dispersion is relatively low compared to in the centre of clusters. Thus, increased integrated merger histories can lead to more kinematically, and hence morphologically, disturbed systems which leads to an evolutionary effect whereby there are less blue spiral galaxies in denser environments than in less dense ones. Furthermore, black holes in the centres of galaxies can generate a colossal amount of energy through the accretion of matter onto their event horizons, also leading to a source of feedback energy on star formation (see §1.3 below).

For the purpose of this thesis the most important formation mechanism considered will be that of merging (see chapters 2 and 3), and the most significant evolutionary mechanism which will be addressed is the role of central supermassive black holes (SMBHs) in massive galaxy evolution (considered in Chapter 4). We turn to an introduction to the nature, and role in feedback on star formation, of SMBHs in massive galaxies in

the next section.

1.3 Supermassive Black Holes

The idea of an object so dense that light could not escape its surface was first suggested by John Michell in his 1783 letter to the royal society (Michell 1784). This idea of a ‘dark star’ was largely ignored until it was reinvented in the early 20th century as a black hole. Black holes were first predicted as an artifact of spacetime in Einstein’s general theory of relativity at the strong field limit, as a solution to the Einstein field equation under the assumption of a point particle and spherical mass by Karl Schwarzschild (Schwarzschild 1916). These objects were not taken seriously astrophysically for some time, until the pioneering work of Chandrasekhar. Chandrasekhar computed that the electron degeneracy pressure of white dwarf stars would not be able to withstand masses greater than 1.44 solar masses, and thus these objects should collapse further, possibly forming black holes (Chandrasekhar 1931, 1935). We now know that there is an intermediary state of Zwicky’s neutron star, where electrons are effectively forced inside protons at this mass limit, to form stars held apart by the degeneracy pressure of neutrons (Baade & Zwicky 1934). However, work by Oppenheimer, Tolman and Volkoff concluded that stars above approximately three solar masses would inevitably collapse into black holes, as neutron degeneracy pressure would be unable to withstand the intense gravitational forces on such massive and compact bodies (Tolman 1939, Oppenheimer & Volkoff 1939).

Therefore, the hunt was on to detect a black hole as this became a vital prediction of both general relativity and our understanding of quantum forces. Detecting black holes directly is tantamount to being impossible given that they emit no light (except possibly through Hawking radiation which will be infinitesimally small for any feasible astrophysical black hole in the Universe today). Consequently, black holes must be looked for indirectly. One early possibility emerged in searching for the evidence of matter being accreted onto a black hole from a companion star. This matter should heat up and radiate energy away, possibly up to $\sim 40\%$ of its rest mass (Thorne 1974), making accretion the most efficient transfer mechanism of matter into radiation short

of matter - anti-matter collision. A particular signature of this process would be a very high emission in X-rays, making X-ray astronomy an attractive field for those astrophysicists keen to probe fundamental physics. The first strong indirect evidence for the existence of a black hole come in observations of the now infamous Cygnus-X1, a strong nearby X-ray source believed to be the result of accretion onto a black hole from a neighbouring star (Bower et al. 1965). Soon, however, a wealth of observational evidence mounted for the existence of roughly solar mass black holes through the motions of stellar binary companions around strong X-ray sources (e.g. Meszaros 1975, Oda 1977, McClintock & Remillard 1986, Cowley et al. 1990). It is now generally accepted that black holes exist and are common at roughly solar masses in our galaxy at least.

Since the early 1990's the possibility of supermassive black holes (SMBHs) residing at the centre of galaxies has been seriously suggested by astronomers. For over a decade now the existence of these central SMBHs have been widely postulated to be a near ubiquitous constituent of massive galaxies (e.g. Kormendy & Richstone 1995, Ferrarese & Merritt 2000, King 2003). These objects are known to vary in mass from a few hundreds of thousands of solar masses to several billion solar masses. They are thought to form from the merging of black holes created in the supernovae explosions of population III stars in the very early Universe, which will fall to the centre of the galaxy, and then slowly accrete matter in the form of cool gas and dust over many billions of years, to become the vast central supermassive black holes we observe to exist in the local Universe. Alternative hypotheses have been suggested for the formation mechanisms of SMBHs. One possibility is that instead of forming from smaller black holes via a merger tree evolution, they form out of the collapse of a relativistic super-giant star, maybe of the order a hundred thousand or more solar masses, which then grows via accretion of matter thereafter (Begelman et al. 2006). What is clear, however, is that the accretion of matter onto SMBHs will occur in all scenarios, and result in both the growth in mass of the black hole and a high degree of electromagnetic emission into the surrounding galaxy and intergalactic medium (IGM) from the accretion disc.

Perhaps the earliest observational evidence for extra-galactic supermassive black holes

were from radio, and later X-ray and optical, observations of quasars, or quasi-stellar objects (QSO's). These objects are point like, high redshift sources of colossal amounts of energy (e.g. Schmidt 1963), and are in fact the most luminous known objects in the Universe, out-shining host galaxies by up to a million times for time periods up to an estimated billion years or so (Silk & Rees 1998, Fabian 1999, and more in Chapter 4, Bluck et al. 2010a). A crucial observational fact about these objects is that they always shine brightly in X-rays, thought to be due to inverse Compton scattering of photons in the corona around SMBH accretion discs, and sometimes (around one in ten) are very bright in radio wavelengths as well, due largely to synchrotron radiation around jets. The current paradigm is that these QSO's are powered by accretion around the central supermassive black holes of some very distant and massive galaxies; with the radio loud QSO's arising from relativistic jets (due to magnetic effects) surging out of some of these accretion discs and their interaction with the interstellar and intergalactic medium. The effect of this colossal outpouring of radiation and energy must have dramatic implications on the evolution of the galaxies in which these supermassive black holes reside. One of the principal aims of this thesis is to examine the role of SHBHs in the evolution of massive galaxies, and to help constrain differing models of SMBH formation and evolution, see Chapter 4 in particular.

Detailed studies of nearby galaxies confirmed the existence of SMBHs via a variety a methods, including through virial estimator techniques, reverberation mapping, and the observation of the motion of stars in the cores (e.g. King 2003, McLure & Dunlop 2002, 2004 and O'Neil et al. 2005). In particular, the evidence for the existence of a SMBH of mass $\sim 4 \times 10^6 M_{\odot}$ at the centre of our Galaxy is overwhelming, with detailed observations of the orbits of stars confirming that the only known object that could be sufficiently massive and compact is a SMBH (e.g. Schodel et al. 2002). Since black holes are fundamental objects, and thus in a sense 'simple' there are only a few parameters with which one needs to accurately define them. A general relativistic black hole can be completely described by just three numbers, its mass, charge and angular momentum (see Heusler 1998). However, the mass and angular rotation speed are in fact the only astrophysically significant properties of black holes (since charged black holes would very rapidly attract matter of opposing charge thus becoming neutral), along with details of their environments, such as accretion discs.

Estimating the rotational speeds of SMBHs themselves is very difficult to achieve due to the fact that we cannot observe the SMBH directly and must deduce the likely rotation via indirect means (such as observation of the accretion disc) and from this construct the motion of the SMBH from theoretical assumptions and a deep knowledge of the inertial reference frame dragging (and hence geometry) in the region of space-time considered. In general, therefore, this fundamental parameter is usually unknown. Mass estimators are much easier to come by, but still require sophisticated techniques and exceptional observational data even in the local Universe. Estimation of the masses of SMBHs in distant galaxies is often very difficult to achieve, but methods based on the Doppler broadening of emission lines from orbiting broad line emitting regions often give rise to the most robust estimates when combined to either direct or indirect estimates of the radius of the source. Direct methods involve measuring the time delay between emission from the accretion disc and re-emission from the broad line emitting region (as in McLure & Dunlop 2002, 2004), with indirect methods making use of the observed correlation between distance from the SMBH and strength of the 3000 Å line (McLure & Jarvis 2002, Willot, McLure & Jarvis 2003, Woo 2008). Additionally lower limits can be placed on SMBH masses through Eddington arguments (e.g. Alexander et al. 2009, and further details in Chapter 4).

Once the existence of SMBHs as a common constituent of galaxies was established, it was natural to look for possible correlations between the global properties of host galaxies and the intrinsic property of mass of the SMBH. Perhaps surprisingly, considering that SMBHs are much less massive ($\sim 1/1000 M_*$) than their host galaxies and vastly smaller (with Schwarzschild radii ~ 1 AU and accretion discs < 1 pc, compared to typical massive galaxy sizes of 10 Kpc or so), close relations were found to exist. We explore the nature of some of these relationships in the next section, and their importance to our understanding of the formation and evolution of massive galaxies.

1.3.1 Black Hole - Galaxy Relations

Kormendy and Richstone (1995) found a correlation between the mass of extragalactic SMBHs and the total optical luminosity of their host galaxies. This landmark discovery opened the possibility of there being other, possibly more fundamental, relationships

between the global properties of host galaxies and the SMBHs that dwell within them. Perhaps the most tightly correlated, and indicative of a fundamental causal connection, is the Gebhardt-Magorrian relation between SMBH mass and the velocity dispersion of the inner spheroidal component of galaxies (Magorrian et al. 1998 and Gebhardt et al. 2000, see Fig 1.5). This is now thought to have the form $M_{BH} \propto \sigma^\alpha$, with $\alpha \sim 4 - 5$. Since velocity dispersion is fundamentally related to total dynamical mass ($M \propto \sigma^2$), this implies that there is a close positive relationship between the total mass of the inner region of galaxies and the mass of their SMBHs.

Furthermore, relationships have been demonstrated to exist between the stellar mass of spheroids, or bulge stellar mass of disc galaxies, and the SMBH mass (Haring & Rix 2004, see Fig 1.5). Although this relationship is not necessarily the tightest or most fundamental, it does prove in practice to be the easiest to probe at higher redshifts. This makes it an ideal choice to study the co-evolution of SMBHs and their host galaxies, using possible evolution in this relationship as a tracer (see Chapter 4).

Taken in aggregate, what do these correlations between the global properties of massive galaxies, and the mass of their central SMBHs tell us? One possibility which must be considered is that these relationships are nothing more than a coincidence. This, however, seems very unlikely given both the tightness of some of these correlations and the potential for variability about these ratios. Nevertheless, until we have an accepted model which gives rise to these empirical trends we must be open to the possibility that these relationships are a transient occurrence. More likely, the relationships discussed here indicate a causal connection between galaxies on large scales and SMBHs on smaller scales. The nature of this causal connection is not immediately apparent, and it is in fact possible that it could be formulated in either direction: i.e. galaxies could dictate the growth and final mass of their SMBHs, or SMBHs could somehow dictate how much galaxies can grow in mass, possibly through AGN feedback on star formation. To have a better idea of which, if either, of these possibilities more closely describes the truth of the situation, it would be hugely advantageous to know when this relationship occurs, and, if it is relatively recent in the history of the Universe, how it changes with cosmic time. One of the major aims of this thesis (in Chapter 4) is to determine empirical limits on the possible evolution of the $M_{BH} - M_*$

relationship with redshift, and from this begin to deduce how SMBHs and their host galaxies evolve together through cosmic time. Ultimately, the question of why these relationships develop will be tentatively addressed through a careful examination of how and when they develop.

1.4 Data and Observations

This thesis draws on data from a variety of ground and space based telescopes looking across the electromagnetic spectrum from the infrared to X-rays. In particular photometry from the Palomar Observatory POWIR Survey is utilised in the near infrared (NIR), along with optical photometry from the Canada France Hawaii Telescope in the EGS field. Hubble Space Telescope imaging in the optical and NIR is utilised via the ACS and NICMOS cameras in the GOODS fields. Additionally, we utilise optical and NIR spectroscopy from the Very Large Telescope, Gemini Observatory and Keck Observatory across both the GOODS and EGS fields. Furthermore, we use the deepest available X-ray imaging from the Chandra X-ray observatory in both the GOODS and EGS fields. A full account of the details of this data is provided as appropriate in each chapter, where it is most relevant.

The main original proprietary data set used in this thesis is the HST GOODS NICMOS Survey, in which a large portion of my PhD has been spent preparing usable catalogs, computing observable quantities (such as stellar masses and rest frame colours), and analysing the data. As such, a more detailed account of this survey and my contribution to it is provided in the next section.

1.4.1 The HST GOODS NICMOS Survey (GNS)

The HST GOODS NICMOS Survey (GNS) is a 180 orbit Hubble Space Telescope survey (P.I. C. J. Conselice) consisting of 60 pointings with the NIC-3 camera in the F160W (H) band in the GOODS North and South fields (see Dickinson et al. 2003 for an overview of GOODS). Each pointing is observed to 3 orbits depth, with each tile

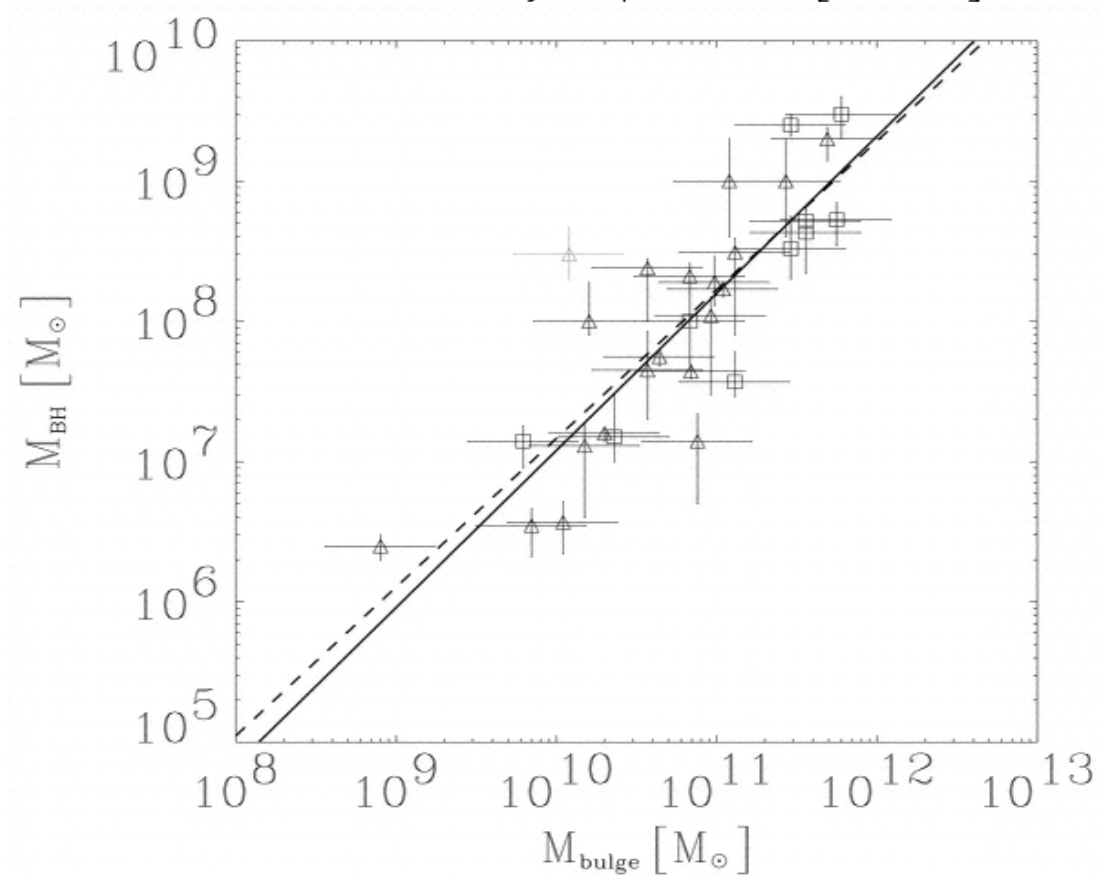
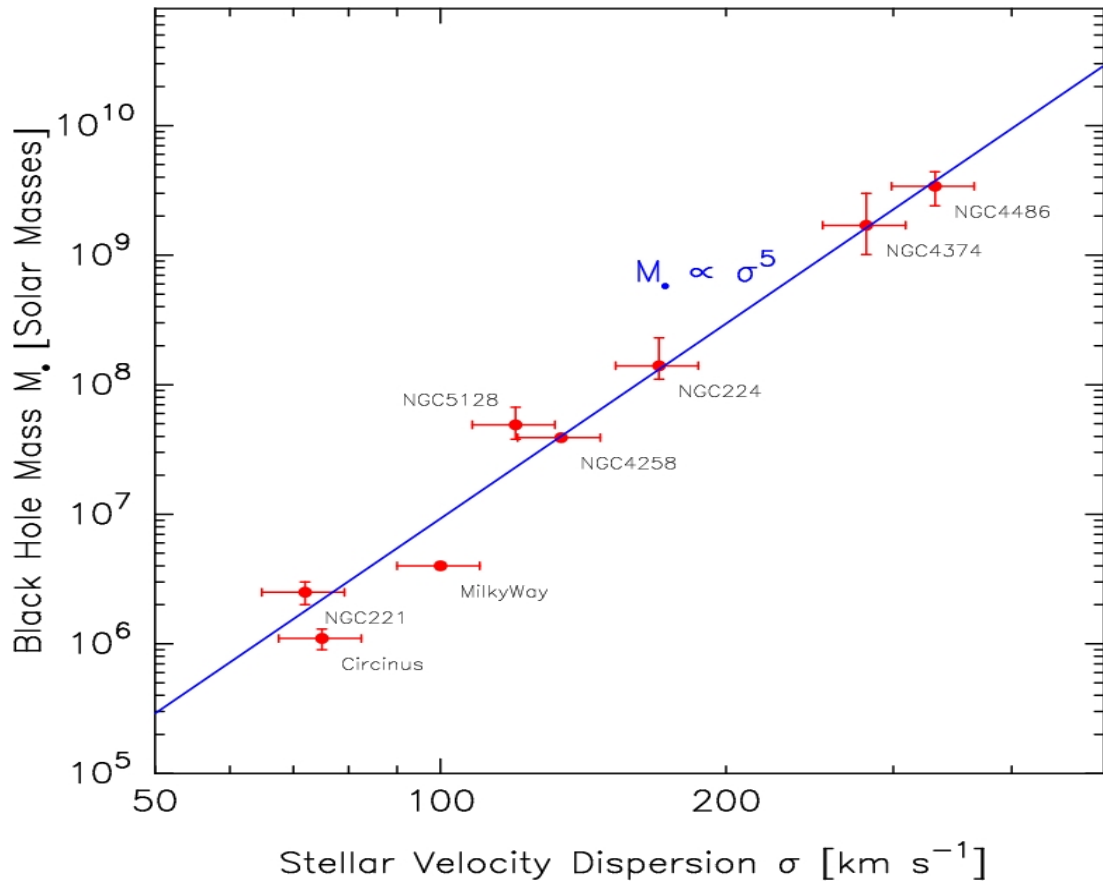


Figure 1.5: The Gebhardt-Magorrian relation (top, Magorrian et al. 1998) and $M_{\text{BH}} - M_{\text{bulge}}$ relation (bottom, Haring & Rix 2004). These relationships suggest that there is some causal connection between host galaxies and the SMBHs which reside at their centres. The nature of this relationship and its evolution with redshift will be discussed at length in Chapter 4.

($51.2'' \times 51.2''$, $0.203''/\text{pix}$) observed in 6 exposures combining to form images with a pixel scale of $0.1''$ and a point spread function (PSF) of $\sim 0.3''$ FWHM (full width half maximum). The pointings are centred around massive galaxies (with stellar masses $M_* > 10^{11} M_\odot$) at $1.7 < z < 3.0$. In total 8298 galaxies are detected, with ~ 100 in the high mass, high redshift range (see Fig. 1.6 for an example comparison between ACS, rest frame UV, and NICMOS, rest frame optical, imaging of high redshift massive galaxies in our sample). Details of the data reduction procedures may be found in Magee, Bouwens & Illingworth (2007). The massive galaxies chosen for study in this sample were selected by a variety of techniques using optical-to-infrared colours (see Yan et al. 2004, Papovich et al. 2006, and Daddi et al. 2007). Full details of the selection, implementation, data reduction and initial analysis (including source detection, photometric redshift and stellar mass determination) of the GNS data set may be found in Conselice et al. (2010). Further details and a preliminary account is found in Buitrago et al. (2008), Bluck et al. (2009), Bluck et al. (2010a), Gruetzbauch et al. (2010, in prep) and Bauer et al. (2010, in prep). Some further details of relevance to this thesis are presented below.

1.4.1.1 Source Counts

Sources are detected in the H band images using the SExtractor package (Bertin & Arnouts 1996). Our detection criterion is based on a 2σ detection above the background noise and the requirement of at least 3 adjacent pixels having values above this threshold also. We measure magnitudes from the MAGAUTO output parameter. This measures flux in a Kron-like elliptical aperture, where the aperture is deduced from the light profile of the galaxy in question. The flux contained within the ellipse is then converted to a magnitude using the mag zeropoint of 25.17. Throughout this thesis every effort is made to ensure consistency between the magnitudes measured and compared to in external data sets. Thus, the MAGAUTO function is precisely the same as utilised in the POWIR (low- z) and GNS (high- z) sample, and, further, when comparing stellar mass we are careful to use the same IMF and fitting techniques. We achieve depths to 5σ of $H_{AB} = 26.8$, which is considerably deeper than the deepest prior near-infrared imaging from the VLT in the GOODS field, of $H_{AB} = 24.5$ (Retzlaff et al. 2010). Stars

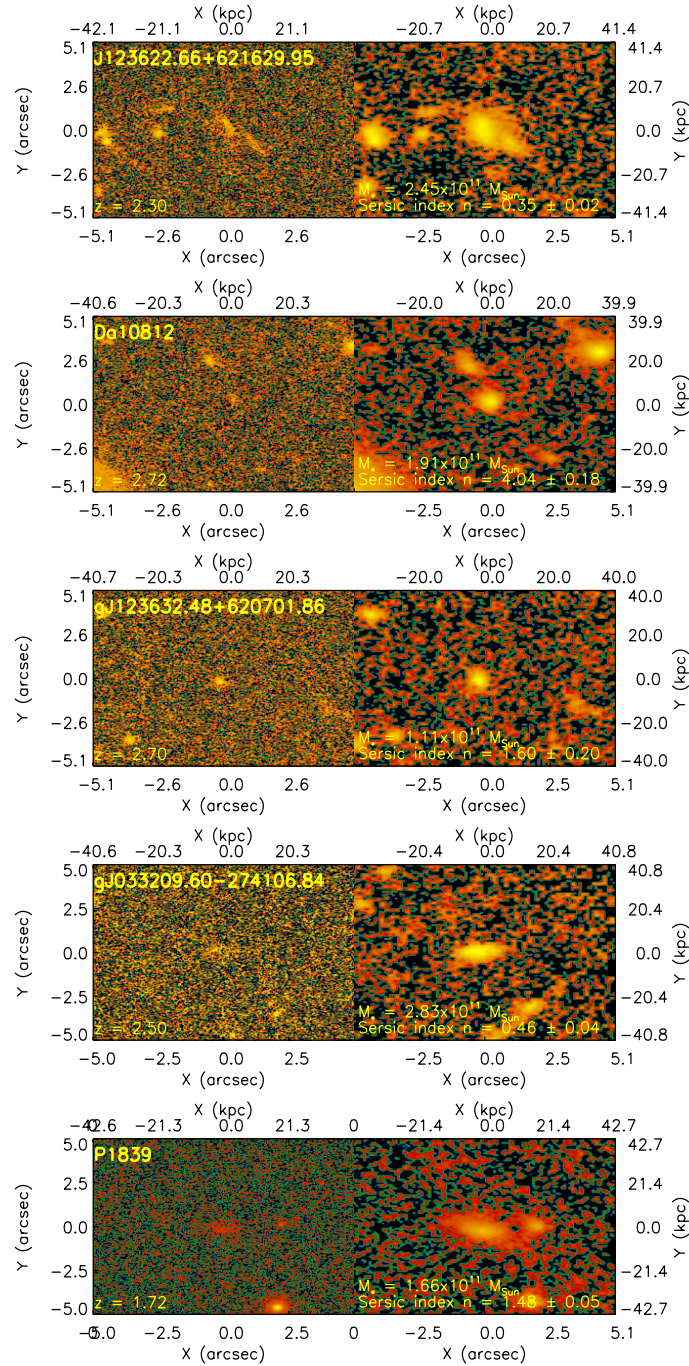


Figure 1.6: Comparison of rest frame UV (ACS, left) to optical (GNS, right) imaging of a sample of very massive ($M_* > 10^{11} M_{\odot}$) galaxies at $1.7 < z < 3.0$. Note that many of these galaxies are much more visible in the rest frame optical GNS imaging than in the ACS imaging. Furthermore, many of these galaxies are extremely compact, with effective radii ~ 1 kpc. Image credit: F. Buitrago, A. Bluck, C. Conselice.

and spurious detections were eliminated from the catalog, and a resulting 8298 galaxies were detected. Particular effort was placed in ensuring that there was an accurate optimal balance of deblending of sources in this resulting GNS catalog. Each pointing was looked at in detail by eye and assessed for quality of fit with the segmentation map.

1.4.1.2 Photometric Redshifts

To obtain photometric redshifts for our galaxy survey, we match the H band GNS imaging to GOODS ACS fields. Photometry was available in the B, V, I and z bands down to a limiting magnitude of $B_{AB} \sim 28.2$. Matching was performed using a $2''$ radius, however the mean separation was significantly less than this. The photometric redshifts were then obtained by fitting template spectra to the BVIZH band photometric data. Two approaches were used, the standard χ^2 minimisation procedure, using HYPERz (Bolzonella et al. 2000) and a Bayesian approach utilising the BPz code (Benitez 2000). The Bruzual & Charlot stellar population synthesis code (Bruzual & Charlot 1993) was used to construct model spectra for the HYPERz method. Full details of this approach can be found in Conselice et al. (2010) and Gruetzbauch et al. (2010).

The Bayesian approach uses similar template fitting but draws on empirical, as opposed to synthetic, templates. Whereas the HYPERz code determines the most likely position of each galaxy in a parameter space of redshift, age, metallicity and reddening, the BPz code also takes into account, as a ‘prior’, how likely it is to find certain types of combinations. Effectively this introduces a weighting to each solution, as well as a simple χ^2 minimisation. Again full details can be found in Gruetzbauch et al. (2010).

To assess the reliability of our photometric redshifts we compare with spectroscopic redshifts available from our sample of galaxies. There are approximately 1000 spec-z’s available out of a total of ~ 8000 galaxies detected in the GNS. To quantify the quality of agreement between redshift measures, we define $\delta z = \Delta z / (1 + z) = (z_{spec} - z_{phot}) / (1 + z_{spec})$. We find good agreement between photometric and spectroscopic redshifts across both codes. In particular, for HYPERz, when considering only high probability sources (with $P > 95\%$), we find $\langle \delta z \rangle = 0.033$, with a scatter of $\sigma_{\delta z} = 0.045$. BPz gives a slightly improved offset of $\langle \delta z \rangle = 0.026$, but a higher degree of

scatter, $\sigma_{\delta z} = 0.058$, for high probability sources. As such, we adopt the photometric redshifts from the HYPERZ code throughout the body of this thesis. Full discussion on the comparison of photo-z's and spec-z's is provided in Gruetzbauch et al. (2010), as well as issues leading to possible systematics in the following Chapters as appropriate (see §4.4 in particular).

1.4.1.3 Stellar Masses and Rest-frame Colours

The stellar masses and rest-frame colours computed for the GNS are measured via multicolour stellar population fitting techniques based on identical catalogs to the photometric redshift measurements. A large set of spectral energy distributions (SEDs) were constructed from Bruzual & Charlot (2003) models, assuming a Chabrier initial mass function (IMF). We consider the star formation history to be exponentially declining, such that:

$$\text{SFR}(t) = \text{SFR}_0 e^{t/\tau} \quad (1.4)$$

where the values for the e-folding time, τ , are randomly populated between 0.01 and 10 Gyrs. Whilst parameters such as age, metallicity and e-folding time are not particularly well fit due to various degeneracies in the codes, our measures of rest-frame colours and stellar masses are accurate. From the width of the probability distribution we estimate errors on our stellar masses to be ~ 0.2 dex. Additional errors from the choice of IMF lead us to a total error of ~ 0.3 dex, or roughly a factor of two. Further considerations, such as the possible effects of AGB stars on the SEDs of galaxies, and their resultant increase in mass uncertainty, are discussed in the data sections of Chapters 2 & 4 in more detail. We, however, conclude that these types of effect do not seriously adversely affect our stellar mass confidence. Throughout this thesis we are careful to compare stellar masses computed via the same models, and using the same IMF.

Rest-frame colours are taken direct from the best fit model SED for each galaxy, with approximate errors, from the probability distribution, of 0.2. Full details of the stellar mass and rest-frame colour determination is provided in Conselice et al. (2010) and

further information in Gruetzbauch et al. (2010). A brief description of the salient details of the GNS data will also be provided in each chapter where appropriate, including considerations of the impact of possible systematic (as well as random) sources of error on photometric redshifts and stellar masses.

1.5 Thesis Outline

Chapter 2 investigates the major merger properties of a population of massive high redshift galaxies, using statistical close pair methods. Comparison is made between differing approaches to determine merger fractions, including morphological (CAS) and close pair techniques. We find that there is a monotonic rise in merger fraction for the most massive galaxies in the Universe out to $z = 3$, best parameterised by a simple power law of the form $f_m \propto (1 + z)^3$. We also deduce the total number of major mergers experienced by massive galaxies since $z = 3$ as being $N_m = 1.7 \pm 0.5$. Further, a series of checks and tests on the close pair method are provided in a retrospective to this chapter.

Chapter 3 investigates the structures, morphologies and minor merger properties of a population of massive high redshift galaxies. We find that approximately 1/4 of all massive galaxies at $1.7 < z < 3$ are in a state of high morphological disturbance, most likely explained by major merging. Moreover, we go on to investigate the minor merger properties of massive galaxies, utilising extremely deep HST H-band data from the GNS, and statistical close pair methods. We find that massive galaxies experience a total of $N_m = (4.5 \pm 2.1) / \tau_m$ mergers with galaxies with stellar masses $M_* > 10^9 M_\odot$ over the past 12 billion years. Where τ_m is the merger timescale, which is thought to vary with stellar mass. This leads to a mass increase of $\Delta M_* \sim 3 \times 10^{11} M_\odot$ from $z = 3$ to the present, assuming an average timescale of $\tau_m \sim 1$ Gyr, which is motivated by N-body simulations.

Chapter 4 investigates the co-evolution of supermassive black holes and their host galaxies over the past 12 billion years. This Chapter brings together X-ray data from the Chandra X-ray Observatory (CXO), near-infrared data from the GOODS NICMOS (GNS) and Palomar Observatory Wide-field Infra-Red (POWIR) surveys, and

spectroscopy from the CFHT, VLT and Keck, to link over 500 bright X-ray sources to their massive host galaxies, and probe the evolution of AGN and galaxies together since $z = 3$. Among the numerous results in this, the largest, section of the thesis are: The local $M_{BH} - M_*$ relation is primarily unchanged with redshift; at least 40% of all massive galaxies will become AGN reaching Seyfert luminosities, or brighter, since $z = 3$; The total energy output from the SMBHs in these galaxies is sufficient to strip apart each galaxy at least 35 times over; and the total X-ray luminosity function (XLF) of the Universe is dominated by AGN in massive galaxies, at all redshifts up to $z = 3$.

Chapter 5 summarises the results and findings of this thesis and presents conclusions concerning the formation and evolution of massive galaxies and their supermassive black holes over the past 12 billion years. A discussion of suggested future work, motivated by the discoveries of this thesis, is also provided.

1.6 Published Work, Conference Presentations and Press Releases

Much of the work presented in this thesis is currently published in peer reviewed journals, or pending publication therein, and has been presented at conferences and with press releases. This section highlights these prior publications for the interested reader to pursue at their leisure.

1.6.1 Published Work

The following is a list of publications that I was involved in during the course of my Ph.D. studies. Much of the work presented in this thesis is published, or pending publication, in the below list:

1. *A surprisingly high pair fraction for extremely massive galaxies at $z \sim 3$ in the GOODS NICMOS survey*

Bluck, Asa F. L.; Conselice, Christopher J.; Bouwens, Rychard J.; Daddi, Emanuele; Dickinson, Mark; Papovich, Casey; Yan, Haojing, 2009, MNRAS, 394, 51L

2. *The structures of distant galaxies - III. The merger history of over 20000 massive galaxies at $z < 1.2$*

Conselice, Christopher J.; Yang, Cui; **Bluck, Asa F. L.**, 2009, MNRAS, 394, 1956

3. *On the co-evolution of supermassive black holes and their host galaxies since $z = 3$*

Bluck, Asa F. L.; Conselice, Christopher J.; Almaini, Omar; Laird, Elise; Nandra, Kirpal; Gruetzbauch, Ruth, 2010, accepted for publication in MNRAS, [arXiv:1008.2162]

4. *The HST GOODS NICMOS Survey: Overview and distant massive galaxy sample and selection*

Conselice, Christopher J.; **Bluck, Asa F. L.**; Buitrago, Fernando; Bauer, Amanda E.; + GNS Team (26 co-authors), 2010, accepted for publication in MNRAS, [arXiv:1010.1164]

5. *Galaxy properties in different environments up to $z \sim 3$ in the GOODS NICMOS Survey*

Grutzbauch, Ruth; Chuter, Robert W.; Conselice, Christopher J.; Bauer, Amanda E.; **Bluck, Asa F. L.**; Buitrago, Fernando; Mortlock, Alice, 2010, accepted for publication in MNRAS, [arXiv:1011.4846]

6. *Probing Stellar Mass Functions over All Galaxy Masses at $z \sim 1 - 3$ in the GOODS NICMOS Survey*

Mortlock, Alice; Conselice, Christopher J.; **Bluck, Asa F. L.**; Bauer, Amanda E.; Grutzbauch, Ruth; Buitrago, Fernando; Ownsworth, Jamie, 2010, submitted to MNRAS

7. *Star-forming properties of a stellar mass selected sample of galaxies to $z = 3$*

Bauer, Amanda E.; Conselice, Christopher J.; Grutzbauch, Ruth; **Bluck, Asa F. L.**; Buitrago, Fernando; Mortlock, Alice, 2010, submitted to MNRAS

8. *The minor and major merger histories and the Kormendy relation of massive galaxies at $z < 3$ in the HST GOODS NICMOS Survey*

Bluck, Asa F. L.; Conselice, Christopher J.; Buitrago, Fernando; Gruetzbauch, Ruth; Hoyos, Carlos; Bauer, Amanda; Mortlock, Alice, in preparation

9. *Structure, activity, and evolution of massive galaxies at $z \sim 1 - 3$ from the GOODS NICMOS Survey*

Weinzirl, Tim; Jogee, Shardha; Conselice, Christopher J., Papovich, Casey; **Bluck,**

Asa F. L.; Buitrago, Fernando; Dickinson, Mark + GNS Team, in preparation

1.6.2 Conference Presentations and Invited Talks

The following is a list of conference presentations and invited talks given over the course of my PhD and based primarily on the research presented in this thesis:

1. AGN Populations and Power Meeting, University of Birmingham, 2010

Talk: ‘The Evolution of Supermassive Black Holes over Cosmic Time’

2. National Astronomy Meeting, University of Glasgow, 2010

Talk: ‘On the Co-evolution of Supermassive Black Holes and their host Galaxies since $z = 3$ ’

3. Invited Talk to Gemini North Observatory, Hilo, Hawaii, 2009

Talk: ‘Extreme Galaxies from the Edge of the Universe II’

4. Invited Public Lecture for International Year in Astronomy, Nottingham, 2009

Lecture: ‘Our Never Ending Universe: What Caused the Big Bang?’

5. Galaxy Evolution and Environment Conference, Kuala Lumpur, Malaysia, 2009

Poster: ‘The Merger History of Massive Galaxies’

6. Invited Talk to Gemini South Observatory, La Serena, Chile, 2009

Talk: ‘Extreme Galaxies from the Edge of the Universe I’

7. Invited Talk to Nottingham Particle Theory Group, 2008

Talk: ‘Can we use Galaxies to Constrain Cosmological Models?’

8. National Astronomy Meeting, Queen’s University, Belfast, 2008

Poster: ‘The HST GOODS NICMOS Survey (GNS): First results’

1.6.3 Press Releases

The following is a list of press releases based on the research presented in this thesis:

1. **New Scientist Article**, 2010:

‘When Black Holes go Rogue, they Kill Galaxies’

2. **Science Now Article**, 2010:

‘Supermassive Black Holes can Kill Whole Galaxies’

3. **RAS Press Release**, from NAM 2010:

‘Connecting Black Holes and Galaxy Death’

4. **RAS Press Release**, from NAM 2009:

‘Hubble Survey Reveals the Formation of the First Massive Galaxies’

5. **Nature News Article**, 2009:

‘Galaxies Collision History Revealed’

Chapter 2

A surprisingly high pair fraction for extremely massive galaxies at $z \sim 3$ in the GOODS NICMOS Survey

The work in this chapter is published as: Bluck et al. (2009)

(with additional excerpts from Conselice, Yang & Bluck (2009))

This Chapter is based on work I led, in collaboration with Christopher J. Conselice¹, Rychar J. Bouwens², Emanuele Daddi³, Mark Dickinson⁴, Casey Papovich⁵, Haojing Yan⁶ and Cui Yang¹.

¹ University of Nottingham, School of Physics and Astronomy, Nottingham NG7 2RD, UK

² Astronomy Department, University of California, Santa Cruz, CA 95064, USA

³ Laboratoire AIM, CEA/DSM-CNRS-Universite Paris Diderot, Irfu/SAp, Orme des Merisiers, F-91191, Gif-sur-Yvette, France

⁴ National Optical Astronomy Observatory, Tucson, AZ 85719, USA

⁵ Astronomy Department, Texas A & M University, TX, USA

⁶ The Observatories of the Carnegie Institution of Washington, Pasadena, CA 91101, USA

Abstract

We calculate the major pair fraction and derive the major merger fraction and rate for 82 massive ($M_* > 10^{11} M_\odot$) galaxies at $1.7 < z < 3.0$ utilising deep HST NICMOS data taken in the GOODS North and South fields. For the first time, our NICMOS data provides imaging with sufficient angular resolution and depth to collate a sufficiently large sample of massive galaxies at $z > 1.5$ to reliably measure their pair fraction history. We find strong evidence that the pair fraction of massive galaxies evolves with redshift. We calculate a pair fraction of $f_m = 0.29 \pm 0.06$ for our whole sample at $1.7 < z < 3.0$. Specifically, we fit a power law function of the form $f_m = f_0(1+z)^m$ to a combined sample of low redshift data from Conselice et al. (2007) and recently acquired high redshift data from the GOODS NICMOS Survey. We find a best fit to the free parameters of $f_0 = 0.008 \pm 0.003$ and $m = 3.0 \pm 0.4$. We go on to fit a theoretically motivated Press-Schechter curve to this data. This Press-Schechter fit, and the data, show no sign of levelling off or turning over, implying that the merger fraction of massive galaxies continues to rise with redshift out to $z \sim 3$. Since previous work has established that the merger fraction for lower mass galaxies turns over at $z \sim 1.5 - 2.0$, this is evidence that higher mass galaxies experience more mergers earlier than their lower mass counterparts, i.e. a galaxy assembly downsizing. Finally, we calculate a merger rate at $z = 2.6$ of $\mathfrak{R} < 5 \times 10^5 \text{ Gpc}^{-3} \text{ Gyr}^{-1}$, which experiences no significant change to $\mathfrak{R} < 1.2 \times 10^5 \text{ Gpc}^{-3} \text{ Gyr}^{-1}$ at $z = 0.5$. This corresponds to an average $M_* > 10^{11} M_\odot$ galaxy experiencing $N_m = 1.7 \pm 0.5$ major mergers between $z = 3$ and $z = 0$, with the bulk of this merging occurring at $z > 1$.

2.1 Introduction

Hierarchical assembly is the established leading theory for the evolution of structure in the universe from the viewpoint of Cold Dark Matter (CDM) theory. This states that larger structures form from the merging of smaller structures. Thus CDM halos grow in size, with the largest structures forming latest in the history of the universe. Galaxies are often thought to form principally in line with halo mergers. If they do, it is likely that merging of smaller galaxies to create more massive ones is the major

factor in the evolution of galaxies over cosmic time. Alternatives to a merger history of massive galaxies include rapid collapse mechanisms, whereby galaxies form over very short time-scales in the early universe, and then do not significantly interact during the rest of their lifetimes.

The aim of this chapter is to address the question: what mechanism drives galaxy evolution with regards to the most massive ($M_* > 10^{11} M_\odot$) galaxies in the universe? We can observationally test this by calculating the merger fraction of massive galaxies at different redshifts. Previous work by Conselice et al. (2007) explores this problem for similar mass galaxies out to $z \sim 1.4$, using morphological techniques. We extend this work using a close-pair method to $z \sim 3$, using data from the GOODS NICMOS Survey.

There are several different ways to locate merging galaxies which roughly relate to the stage of the merger. The most direct method is to look at morphological disturbances in galaxies, e.g. Chapter 3, Bluck et al. 2010b, and Conselice et al. (2003, 2006, 2008 and 2009). In this approach one selects galaxies with asymmetries, or distortions in their morphologies, above a certain threshold, and define these as merging systems. This can be carried out by eye, or via computational methods, e.g. CAS, Gini and M_{20} parameters (see §A, Conselice 2003, 2006, Conselice et al. 2008 and Lotz et al. 2008a). Alternatively, one could also look in principle for secondary features such as an abrupt increase in star formation rate. This is because the merging of gas rich galaxies will often give rise to an increase in star formation, and hence a distinctive spectral signature, see e.g. Lin et al. (2008) and Mathis et al. (2005).

Also one can look for galaxies in close proximity and count the number of galaxies in apparent pairs in a given sample. This pair counting method requires much less angular resolution than the morphological approaches, and can be extended to higher redshifts more directly than the others. The close pair method does not precisely trace merging, however, but rather looks for likely potential future mergers. Thus, to go from a close pair fraction to a merger fraction requires that assumptions be made. Ultimately, the pair count method measures mergers before they happen, the morphological approach measures merging while it happens, and methods involving increased star formation rates trace merging during and after the event.

Merging is already thought to be of paramount importance in driving the rate of star formation, the formation and evolution of supermassive black holes, and as a mechanism for increasing galaxy mass. Further, mergers can be used to trace the formation history of galaxies, probing where, when, and how galaxies form. Conselice et al. (2007) and Rawat et al. (2008) find that massive galaxies ($M_* > 10^{11} M_\odot$) out to $z \sim 1.5$ have an increasing merger fraction with redshift. It has been noted for lower mass systems that there is a levelling off and eventual turn around in the merger fraction at $z < 2$ (see Conselice et al. 2008). In order to probe whether the same levelling off and turn around in the merger fraction occurs for $M_* > 10^{11} M_\odot$ galaxies, it is necessary to explore the merger fraction of these massive galaxies at higher redshift.

Consequently, we have collated a sample of 82 galaxies with $M_* > 10^{11} M_\odot$, selected from the GOODS North and GOODS South fields. These are imaged as part of the GOODS NICMOS Survey (GNS). The GOODS field has the multi-band coverage needed to estimate good photometric redshifts, in addition the depth and angular resolution from NICMOS allows us to resolve significantly fainter objects around the primary targets to distances of a few kpc. Thus, for the first time, we can probe the pair fraction history to $z \sim 3$. We argue that the increase in merger fraction with redshift continues for massive galaxies in our sample out to $z \sim 3$. The merger fraction shows no sign of levelling off or turning around at $2 < z < 3$, unlike for lower mass systems observed by Conselice et al. (2008). Thus, we find that, complimentary to the star formation results of Bundy et al. (2006) and Palpino et al. (2008), the most massive galaxies appear to form by mergers at a higher rate in the early universe than less massive ones.

Throughout this chapter we assume a Λ CDM Cosmology with: $H_0 = 70 \text{ km s}^{-1} \text{ Mpc}^{-1}$, $\Omega_m = 0.3$, $\Omega_\Lambda = 0.7$, and adopt AB magnitude units.

2.2 Data and Observations

The GOODS NICMOS Survey imaged a total of 8298 galaxies in the F160W (H) band, utilising 180 orbits and 60 pointings of the HST NICMOS-3 camera. These pointings are centred around massive galaxies at $z = 1.7 - 3$ to 3 orbits depth. Each tile

(51.2''x51.2'', 0.203''/pix) was observed in 6 exposures that combine to form images with a pixel scale of 0.1'', and a point spread function (PSF) of $\sim 0.3''$ full width half maximum (FWHM). See Magee, Bowens & Illingworth (2007) for details relating to the data reduction procedure. The pointings were chosen and optimised to contain as many high-mass ($M_* > 10^{11} M_\odot$) galaxies as possible. The selection of these is outlined in Conselice et al. (2010). These galaxies consist of high redshift galaxies selected by various optical-to-infrared colour techniques (see Conselice et al. 2010 for a full discussion and Papovich et al. 2006, Yan et al. 2004 and Daddi et al. 2007). A total of 82 galaxies were found with $M_* > 10^{11} M_\odot$, with photometric and spectroscopic redshifts between $z = 1.7$ and $z = 3$. Limiting magnitudes reached are $H_{AB} = 26.5 (10\sigma)$.

There is a wealth of observational data covering the GOODS field. As such, the masses and photometric redshifts of our sample of massive galaxies are calculated using data from the U-band to the H-band (e.g. Giavalisco et al. 2004) and contain K-band photometry which is especially sensitive to established stellar populations and hence stellar mass. Bands omitted are J and H-band initially, added later for final sample. The 4000 Å break is covered for all systems at $1.7 < z < 3.0$ which increases the reliability of the result. We do not use the available IRAC bands, however, due to their large PSF and resultant errors in correctly matching galaxies. The stellar masses were measured utilising standard multi-colour stellar population fitting techniques, producing uncertainties of ~ 0.2 dex. The details of this procedure can be found in, e.g. Bundy et al. (2006) and Conselice et al. (2007). The stellar masses were calculated assuming a Chabrier initial mass function and by producing model spectral energy distributions (SEDs) constructed by Bruzual & Charlot (2003) via stellar population synthesis models parametrised by an exponentially declining star formation history. The model SEDs are then fit to the observed SEDs of each galaxy to obtain a stellar mass. Recent work by Conroy, Gunn and White (2008), however, has suggested that current methods for measuring stellar masses may have greater errors than previously thought (~ 0.3 dex). Although newer methods have been developed utilising different stellar evolution tracks, we find that these newer models do not significantly affect our measured stellar masses, and our stellar masses are accurate to within a factor of a few. For a discussion of this see Trujillo et al. (2007) and Conselice et al. (2008).

Due to the steepness of the stellar-mass function at high masses, Poisson errors in measuring the mass of galaxies may lead to more lower mass galaxies being counted in our high mass sample. These are technically Eddington biases, but may be considered as a form of Malmquist bias. To model this we ran a set of Monte-Carlo simulation based on the stellar mass function for high z galaxies in Fontana et al. (2006). We used intrinsic stellar mass errors of ± 0.3 dex (as estimated by our codes) and allowed a mock sample of galaxies to be re-distributed in stellar mass, according to the steepness of the Fontana et al. (2006) mass function. We found that $\sim 8\%$ of lower mass galaxies systematically infiltrated our higher mass sample. This effect is relatively small and will not significantly affect our results. Moreover, since we go on to note a dramatic increase in the pair fraction of massive galaxies, when compared to less massive ones, this effect cannot be responsible because contamination of lower mass systems would result in the pair fraction of higher mass galaxies being lower (see e.g. Conselice et al. 2007).

Details on the photometric redshift deduction is provided in §1.4.1.2, and e.g. Conselice et al. (2008), with further details provided in the Retrospective provided at the end of this chapter. Additionally to the photometric redshifts, we find seven spectroscopic redshifts from the literature for our sample. Using the GOODS/VIMOS DR1 (see Popesso et al. 2008) we find three matches with $\frac{\delta z}{1+z} = 0.026$, and four spectroscopic redshifts from a compilation of redshifts from the literature (see Wuyts et al. 2008) giving $\frac{\delta z}{1+z} = 0.034$.

We use SExtractor to make catalogs for all detected galaxies in the GNS, removing stars and obviously spurious detections (for a full account see Conselice et al. 2010). Essentially this was done via discounting point-like sources autonomously and checking this by eye. We then carefully check by eye that the deblending is accurate and that we are not artificially merging separate galaxies or splitting individual galaxies into parts. For the massive galaxies studied in this chapter, we put in particular effort to ensure that the sources are extracted accurately. Further, the choice of studying major mergers with stellar mass ratios of at least 1:4 of the primary source (± 1.5 mag.) allowed us to be complete to 5σ . The full completeness calculations are presented in Conselice et al. (2010).

2.3 Close Pair Method

We follow an approach similar to Patton et al. (2000) for calculating major merger fractions for our galaxies based on a close pair method. First we separate our galaxies into two redshift bins, with $1.7 < z < 2.3$ for the first group (containing 44 galaxies) and $2.3 < z < 3.0$ for the second group (containing 38 galaxies). The method for assigning potential pairs is relatively straightforward. We assign any galaxy within 30 kpc, in physical units (taking $H_0 = 70 \text{ km s}^{-1} \text{ Mpc}^{-1}$), of our host galaxy to be a count, if it is within ± 1.5 of the host galaxy magnitude. To calculate a pair fraction we sum up the number of galaxies within 30 kpc of all of our host galaxies and divide by the total number of galaxies. This would be an accurate pair fraction if we had precise redshifts for all of the galaxies in our sample, and included in the summation only those at the same redshift as the host. As we have photometric redshifts only for our host galaxies and potential pairs, we do not know if any particular galaxy within 30 kpc projected on sky is a real pair or just foreground or background contamination.

We correct for contamination by calculating the probability of a close galaxy being a pair by chance from our surface number counts. These number counts are taken around the objects to minimise clustering effects. We then subtract this correction from our running pair total. Specifically we calculate:

$$\text{corr} = \int_{m-1.5}^{m+1.5} \rho(m') \times \pi(r_{30\text{kpc}}^2 - r_{5\text{kpc}}^2) dm' \quad (2.1)$$

Where $\rho(m')$ is the surface density of galaxies in the survey, in the magnitude range ± 1.5 of the magnitude of the host galaxy. $r_{30\text{kpc}}$ and $r_{5\text{kpc}}$ are distances of 30 and 5 kpc from the host galaxy's centre, respectively. Essentially this expression corresponds to calculating how many galaxies in the whole survey are within ± 1.5 of the magnitude of the host galaxy, and dividing this number by the total area of the survey. We then multiply by the area within the annulus marked out by the radii 5 and 30 kpc, which is done to avoid miscounting due to blending with the host galaxy. This gives an expectation value for the number of galaxies one would expect to see within 30 kpc of the host galaxy purely by chance. Although massive galaxies at high redshifts are highly clustered, our correction is based upon the densities of objects centred around

these systems (at radii < 200 kpc). The mean correction is ~ 0.5 but this of course varies with magnitude range considered. The specific value of the correction is then subtracted from the number counts for each host galaxy in turn to obtain a major pair fraction thus:

$$f_m = \frac{1}{N} \sum_{i=1}^{i=N} (\text{counts}_i - \text{corr}_i) \quad (2.2)$$

Where N is the total number of galaxies in the summation. We use the values of ± 1.5 for the magnitude range to select major (1:4) mergers only (where we are complete). Furthermore, we adopt the convention of setting 30 kpc as our pair distance to be in line with Patton et al. (2000) and Bundy et al. (2004). This allows us to make fruitful comparisons, and also follows rough theoretical arguments for the likelihood of a major close pair becoming a major merger in a relatively short (~ 400 Myr) time-scale. This is calculated through N-body simulations by Lotz et al. (2008a,b) and is based on typical group velocity dispersions and the merging of gas rich disk systems for massive galaxies in NFW potentials. Uncertainties in this timescale are significant and can be up to a factor of two or slightly more considering variable initial velocities, gas densities and specific mass ratios of the merging systems. The merger fractions derived via close pair methods at $d = 30$ kpc also have a similar timescale to the merger fractions calculated via CAS methods ($\sim 400 \pm 300$ Myr for $d < 30$ kpc, $\sim 1000 \pm 400$ Myr for CAS). For further discussion on this and the characteristic timescales relevant to these two approaches, see §2.4.4, Chapter 3, Conselice, Yang & Bluck (2009).

2.4 Results

2.4.1 Merger Fraction

We find a pair fraction of $f_m = 0.29 \pm 0.06$ for the whole sample at $1.7 < z < 3.0$. Within the range $1.7 < z < 2.3$ we calculate a pair fraction $f_m = 0.19 \pm 0.07$, and within the range $2.3 < z < 3.0$ we calculate a pair fraction $f_m = 0.40 \pm 0.10$. These are considerably higher values than those found by Conselice et al. (2008) for

similar mass objects at $z < 1.4$. We do not make any correction to transform our pair fractions into merger fractions, unlike Patton et al. (2000) and Rawat et al. (2008). This is because both morphological and close pair methods likely trace merging but have different timescales. A detailed investigation on the differing timescales traced by morphological and pair methods in Conselice, Yang & Bluck (2008) suggests that the timescale for 30 kpc pairs and morphologically selected mergers is very close. Moreover, we go on to calculate the pair fractions for the POWIR survey massive galaxies, to directly compare these values to the GNS massive galaxies (see Fig. 2.1).

N-body simulations from Wetzel et al. (2008) suggest that pair fraction methods may underestimate the number of true major mergers, as pairs at higher separations may also merge. If this is true, it suggests that the real merger fractions may be higher than what we calculate. But, since the calculated merger fractions in this chapter are very high, this will not change the thrust of our conclusions and may even make them stronger. Our results cannot be treated as strict lower limits, however, as other malmquist-like bias could conspire to lead our values to be overestimated. A careful analysis of this possibility is provided in the Retrospective at the end of this chapter. Our pair fractions are plotted alongside lower redshift points from the POWIR Survey, with merger fractions estimated via CAS methods (Conselice et al. 2007) and via close pairs (calculated in this chapter), and with a local universe value calculated in de Propis et al. (2007) based on morphological methods in Fig. 2.1. For a detailed explanation of morphological techniques see Chapter 3.

2.4.2 Merger Fraction Evolution

We plot a fit of the form $f_m = f_0(1+z)^m$ to all POWIR and GNS points (solid line in Fig. 2.1), and find a best fit to the free parameters of: $f_0 = 0.008 \pm 0.003$ and $m = 3.0 \pm 0.4$. Our value of f_0 compares very favourably to the accepted local universe value of the merger fraction for massive galaxies of 0.009 ± 0.002 at $z = 0.05$ (de Propis et al. 2007). The red squares represent POWIR data for $M_* > 10^{11} M_\odot$ galaxies at $z < 1.4$ (Conselice et al. 2007) with merger fractions calculated morphologically. We also fit a power law exponential curve of the form $f_m = a(1+z)^b \exp(c(1+z)^2)$ to all POWIR and GNS points (dotted line in Fig. 2.1) (Carlberg, 1990). We find a best

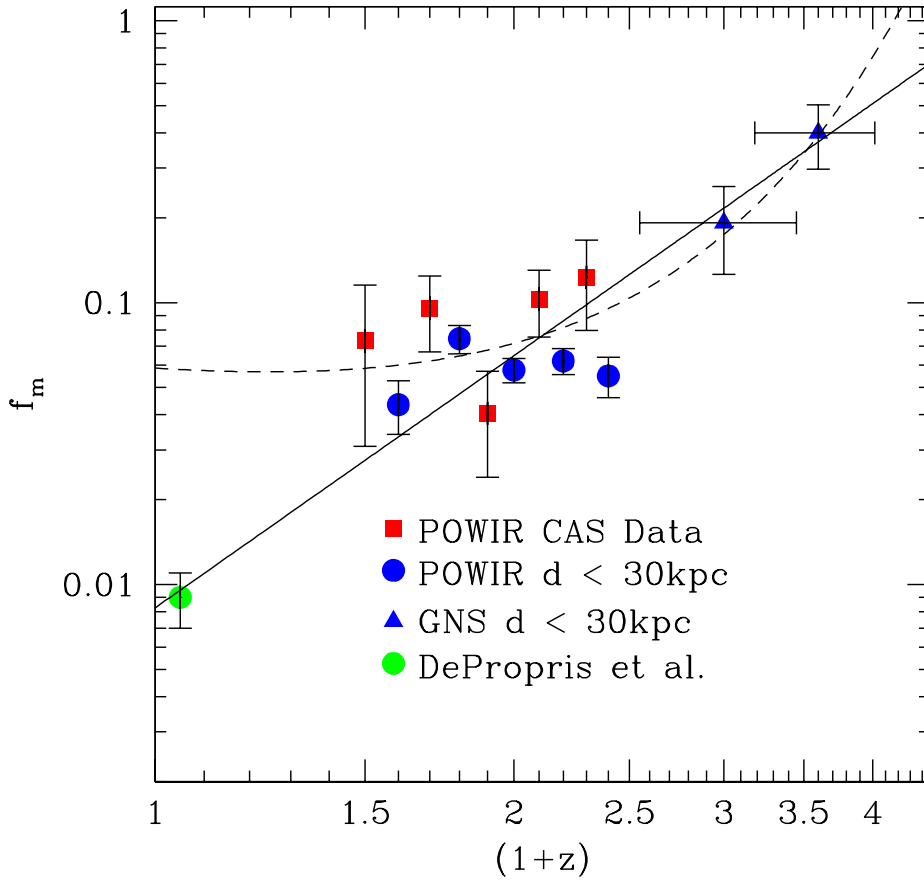


Figure 2.1: The merger fraction evolution of $M_* > 10^{11} M_\odot$ galaxies. The red squares are taken from POWIR data, with merger fractions calculated via CAS morphologies (Conselice et al. 2007). The blue circles are taken from POWIR data, with merger fractions calculated via close-pair methods (this work). Blue triangles are taken from the GNS, with merger fractions calculated via close-pair methods (this work). The green circle represents the local universe value (calculated in de Propriis et al. 2007). Solid line is a best fit power law, to the high z data, of the form $f_m = 0.008(1+z)^3$, with dotted line being a best fit power law exponential, to the high z data, of the form $f_m = 0.008(1+z)^{0.3} \exp(1.0(1+z)^2)$.

fit to the free parameters of: $a = 0.008 \pm 0.002$, $b = 0.3 \pm 0.2$ and $c = 1.0 \pm 0.6$. There is poor agreement, however, between the power law exponential prediction for the local universe value and the de Propriis et al. (2007) point. This parameterisation also shows no sign of turning over at high z , unlike for the lower mass systems in Conselice et al. (2008). As such, this indicates that the merger fraction continues to increase with redshift out to $z \sim 3$, implying that higher mass objects are experiencing relatively more mergers than their lower mass counterparts at high redshift, compared to the lower mass data in Conselice et al. (2008).

2.4.3 Merger Rates

In order to calculate merger rates from our merger fractions we must assume a time-scale (τ_m) over which merging is occurring for galaxies in a major pair. Adopting the simulation results found in Lotz et al. (2008b), we take $\tau_m = 0.4 \pm 0.3$ Gyr for close pairs at $d = 30$ kpc, and $\tau_m = 1.0 \pm 0.4$ Gyr for morphological CAS measurements, for roughly equal mass systems. The timescales are deduced from N-body simulations of massive gas rich disk-like galaxies in NFW potentials, a range of initial velocity separations are considered and the results utilised here are appropriate for the group environment, where our galaxies most probably reside. This is likely to be true because these are the most massive galaxies in the Universe at these redshifts, but no true clusters have formed by $z \sim 2.3$ which is the median redshift of the sample. Errors given take into account variable velocity separations, gas content and mass ratios. We also need to know the comoving number density, $n(z)$, for $M_* > 10^{11} M_\odot$ galaxies at different redshifts. We calculate this using data from Drory (2005) for the GOODS South field. The typical errors of these values are $\pm 20\%$ of the value. It is also important to use the galaxy merger fraction (f_{gm}) as opposed to the merger fraction calculated above. The galaxy merger fraction relates to the merger fraction (f_m) by:

$$f_{gm} = \frac{2 \times f_m}{1 + f_m} \quad (2.3)$$

This gives the number of galaxies merging as opposed to the number of mergers (f_m), divided by the number of hosts in the sample. For a more detailed derivation of this and discussion on its application see Conselice (2006). We calculate the merger rate thus:

$$\mathfrak{R}(z) = f_{gm}(z)n(z)\tau_m^{-1} \quad (2.4)$$

where $n(z)$ is the comoving number density of galaxies and $f_{gm}(z)$ is the galaxy merger fraction (calculated above). We calculate this rate at $z = 2.6$ as $\mathfrak{R} < 5 \times 10^5 \text{ Gpc}^{-3} \text{ Gyr}^{-1}$ and at $z = 0.5$ as $\mathfrak{R} < 1.2 \times 10^5 \text{ Gpc}^{-3} \text{ Gyr}^{-1}$. These rate calculations are, however, notoriously difficult to perform accurately as there are significant errors associated with the calculation of the comoving number density (n), the galaxy

merger fraction (f_{gm}), and the characteristic timescale for a merging system being detected (τ_m). When added in quadrature, the resultant final error on the merger rate is very large. Therefore, unlike for the merger fraction, the major merger rate is consistent with having no redshift evolution. There are two competing variables here: the comoving number density, $n(z)$, which decreases with increasing redshift, and the galaxy merger fraction, $f_{gm}(z)$, which increases with increasing redshift. These appear to combine to roughly negate any redshift evolution of the merger rate $\mathfrak{R}(z)$ (Fig. 2.2).

A useful term may be defined (Γ) which is essentially the characteristic time between mergers that an average galaxy experiences at a given redshift. It is defined as:

$$\Gamma = \frac{\tau_m}{f_{gm}} \quad (2.5)$$

This is plotted in Fig. 2.3. It is clear that Γ evolves with redshift from ~ 1.5 Gyr at $z = 3$ to ~ 12 Gyr at $z = 0$. Further, we fit a curve of the form $\Gamma = \Gamma_0(1+z)^{-p}$, with a best fit to the free parameters of: $\Gamma_0 = 12 \pm 3$ Gyr and $p = 1.6 \pm 0.4$. This represents a steep increase in the time taken for galaxies to merge. We calculate the number of expected mergers (N_m) for a given galaxy between two redshifts using this power law fit. Specifically we calculate:

$$N_m = \int_{t_1}^{t_2} \frac{1}{\Gamma(z)} dt = \int_{z_1}^{z_2} \frac{1}{\Gamma(z)} \frac{t_H}{(1+z)} \frac{dz}{E(z)} \quad (2.6)$$

where $\Gamma(z)$ is the characteristic time between mergers, t_H is the Hubble time, and the parameter $E(z) = [\Omega_M(1+z)^3 + \Omega_k(1+z)^2 + \Omega_\Lambda]^{1/2} = H^{-1}(z)$. Calculating this from $z = 3$ to $z = 0$, we obtained a value of $N_m = 1.7 \pm 0.5$ major mergers per galaxy, with $\tau_m = 0.4$ Gyr.

2.4.4 Comparison of Structural Mergers and Pair Fractions

In this section we look to prior work in Conselice, Yang and Bluck (2009), as well as to the data in this chapter, to compare the effectiveness of morphological or structural approaches to assigning mergers with close pair statistical methods.

One of the results we derive from our measured structural mergers is how the derived

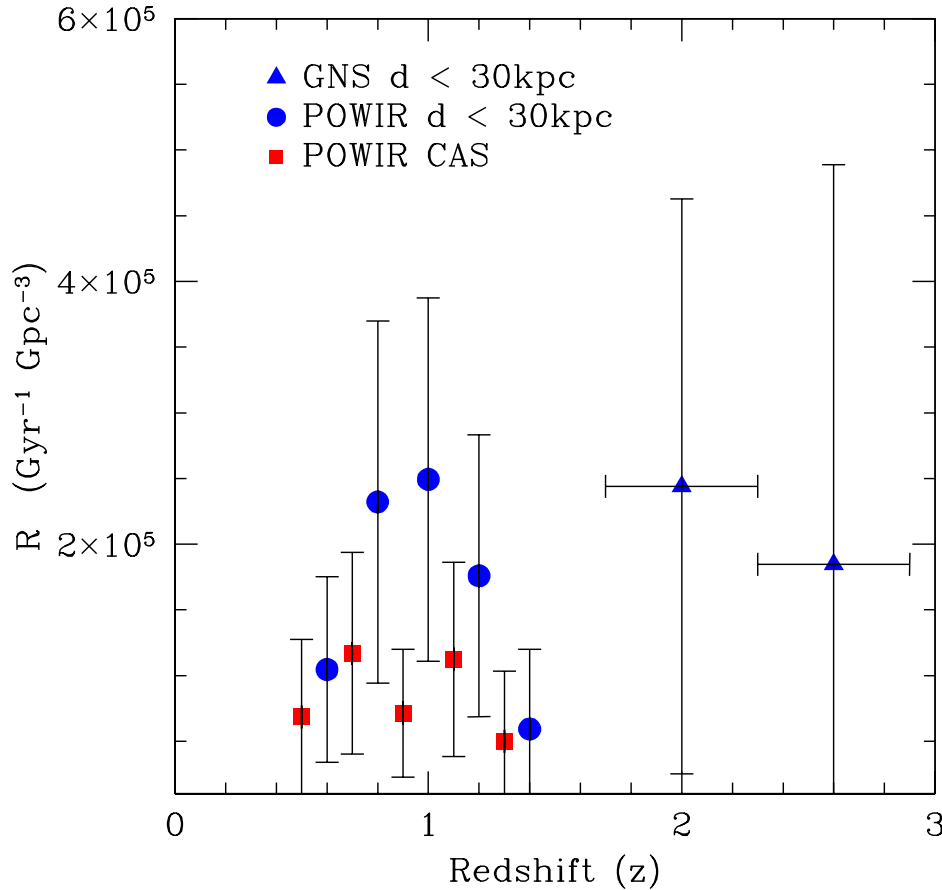


Figure 2.2: The major merger rate, $\mathfrak{R}(z)$, evolution with redshift. Although this is a difficult commodity to constrain due to high composite errors, this is the most directly comparable merger statistic for comparison to models. Red squares are taken from POWIR data with merger fractions calculated via morphological CAS methods, blue circles are taken from POWIR data with merger fractions calculated via close pair methods and the blue triangles are high redshift data taken from the GNS with merger fractions derived from close pair methods.

merger fractions, based on the CAS and other methods (such as Gini/ M_{20}) compare with derived pair fractions for lower mass systems. Fig. 2.4 shows this comparison, with the morphological methods (Conselice, Yang and Bluck 2009 & Lotz et al. 2008a) shown in red, and the pair methods (Kartaltepe et al. 2007; Lin et al. 2008; de Ravel et al. 2008) shown in blue, taken from Conselice, Yang & Bluck (2009). What is immediately clear is that the structural methods, while agreeing quite well with each other, find a higher merger fraction than the pair methodology (at $d < 20$ kpc) for most masses and redshifts in general. However, there appears to be good agreement for the highest mass systems at all redshifts up to $z \sim 1.5$ (at $d < 30$ kpc, see Fig. 2.1). There are several possible reasons for this.

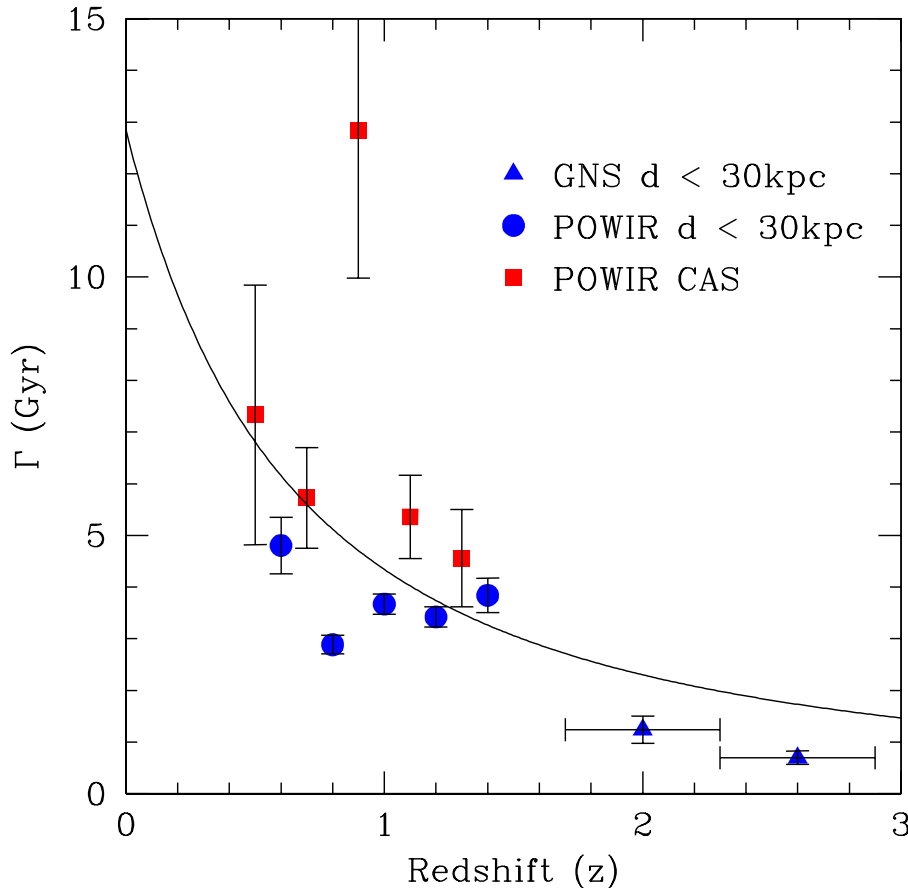


Figure 2.3: The redshift evolution of the average time between mergers $\Gamma = \tau_m / f_{gm}$. Red squares are taken from POWIR data with merger fractions calculated via morphological CAS methods, blue circles are taken from POWIR data with merger fractions calculated via close pair methods and the blue triangles are high redshift data taken from the GNS with merger fractions derived from close pair methods. The solid line is the fit $\Gamma = 12(1+z)^{-1.6}$.

While it is possible that one or both methods have systematics that result in inaccurately measured merger fractions, we first investigate what the time-scales for these methods are. This is an important question as these fractions differing can be partially, or entirely, explained if the time-scales for merging for the two methodologies are different. For example, if the time-scale for a 20 kpc pair to merge is half the time-scale sensitivity for an asymmetric galaxy, then we would expect the pair fraction to be half of the CAS merger fraction if both methods are tracing the same merger process. That is, the merger fraction for a given sample scales as the time-scale sensitivity of the method used to find mergers. Given that the merger rates for the two methods should give the same result, the ratio of the pair fraction to its merger timescale should be equal to the structural merger fraction divided by its time-scale, or:

$$\frac{f_{\text{pair}}}{\tau_{\text{pair}}} = \frac{f_{\text{CAS}}}{\tau_{\text{CAS}}}. \quad (2.7)$$

Time-scales (τ) within the merger process are notoriously difficult to measure and have large uncertainties. Initially, measuring the merger rate from pairs involved dynamical friction calculations (e.g., Patton et al. 2002; Conselice 2006), and typical time-scales for a 20 kpc pair to merge were thought to be $\sim 0.5 - 1$ Gyr with various assumptions. The time-scale calculation for dynamical friction used by Conselice (2006), and in earlier studies are based on isothermal mass distributions and the time-scale can depend highly on the mass of the galaxies, and the characteristic velocity of the system (e.g., Conselice 2006, eq. 7).

Likewise, the time-scales for merging within the CAS system for dark matter dominated galaxies was found to be similar to the dynamical friction time-scales derived from an isothermal profile and a galaxy with mass of $\sim 10^{10} M_{\odot}$. There are however problems with both of these calculations, which have already been alluded to above for the dynamical friction time-scale. The measured time-scales for the CAS method are found by Conselice (2006) to vary between $\sim 0.3 - 0.8$ Gyr, depending on viewing angle and the orbital parameters of the two galaxies in the pair. Also, the simulations used in Conselice (2006) are purely dark matter, and it is desirable to determine the CAS time-scale for systems with stars, star formation, and dust.

New simulations were recently analysed by Lotz et al. (2008b, 2010) in terms of CAS, Gini/ M_{20} , and pair selection for mergers. Lotz et al. (2008b) furthermore utilise simulations that include star formation and dust, and are currently by far the most thorough investigation into merger time-scales using both morphology and the time-scales for mergers to occur within a given separation from $20 h^{-1}$ kpc to $30 h^{-1}$ kpc, and $50 h^{-1}$ kpc.

Lotz et al. (2008b) find a variety of time-scales for their merger simulations depending on the type of merger and the type of galaxy. For their highest resolution simulation (SbcPPx10), they calculate a merger time-scale of $\tau_{\text{CAS}} = 0.94 \pm 0.13$ for the CAS methodology, and a time-scale of $\tau_{\text{pair}} = 0.15 \pm 0.18$ for galaxies to merge within a $20 h^{-1}$ kpc pair. This ratio of time scale, which we denote as $\kappa = \tau_{\text{CAS}}/\tau_{20\text{kpc}}$, is equal to $\kappa = 6.3$ for this model.

Fig. 2.5 shows the histogram for the value of κ for all the models published in Lotz et al. (2008b). What we find is a general distribution, but with all the Sbc models having a ratio $\kappa > 1$. The models shown by the blue hatched histogram in Fig. 2.5 are for the Lotz et al. (2008b) ‘G’ models, which are less gas dominated, and have sub-parabolic orbits which lead to artificially shortened merger time-scales in pairs. As can be seen, while earlier analytical calculations showed that the time-scale for pair merging was similar to the morphological merger time-scale, the simulations by Lotz et al. demonstrate that the time-scales for pairs to merge are shorter than the analytical estimates (at $d < 20$ kpc).

This implies that if the pair method and the structural methods are measuring the same merger process, then the merger fraction derived from pairs should be lower than that derived from structure by an equivalent amount. We denote this ratio as $\kappa' = f_{\text{CAS}}/f_{\text{pair}}$. For the COSMOS field we find that the value of κ' using the data from Kartaltepe et al. (2007) and Conselice, Yang and Bluck (2009), give κ' values from 1.5-3.5, yet the pairs from Kartaltepe et al. (2007) are not selected in the same way our CAS mergers are, i.e., with $M_* > 10^{10} M_{\odot}$.

A better test of the merger criteria time-scale is to determine how the ratio of the CAS merger fraction and the pair fraction change with redshift in the same sample. While it is likely that even within the same sample, the CAS and pair methods will find galaxies in different modes of evolution (e.g. de Propris et al. 2007), it is still instructive to determine this ratio within a well defined sample. We utilise the POWIR data base from the EGS to determine this ratio (e.g. Conselice et al. 2007, 2008b).

Fig. 2.6 shows this ratio for galaxies at separations of < 20 kpc, 30 kpc, and 50 kpc. The values for $f_{\text{m}}(\text{CAS})/f_{\text{m}}(\text{Pair})$, with a pair defined as having a separation of < 20 kpc, range from 12.2 to 2.3, with a average value of 6.2, which perhaps coincidentally is close to the value of κ for the highest resolution model from Lotz et al. (2008b). This implies, at least, that there is no inconsistency between the pair method and structural methods for measuring merger fractions and rates. Moreover, we find that the timescales of $d < 30$ kpc pairs and CAS selected mergers are roughly equivalent for massive galaxies (with $M_* > 10^{11} M_{\odot}$) up to $z = 1.5$ (see Fig. 2.6 and 2.1). In Chapter 3 this analysis will be extended out to even higher redshifts, up to $z \sim 3$, and found to

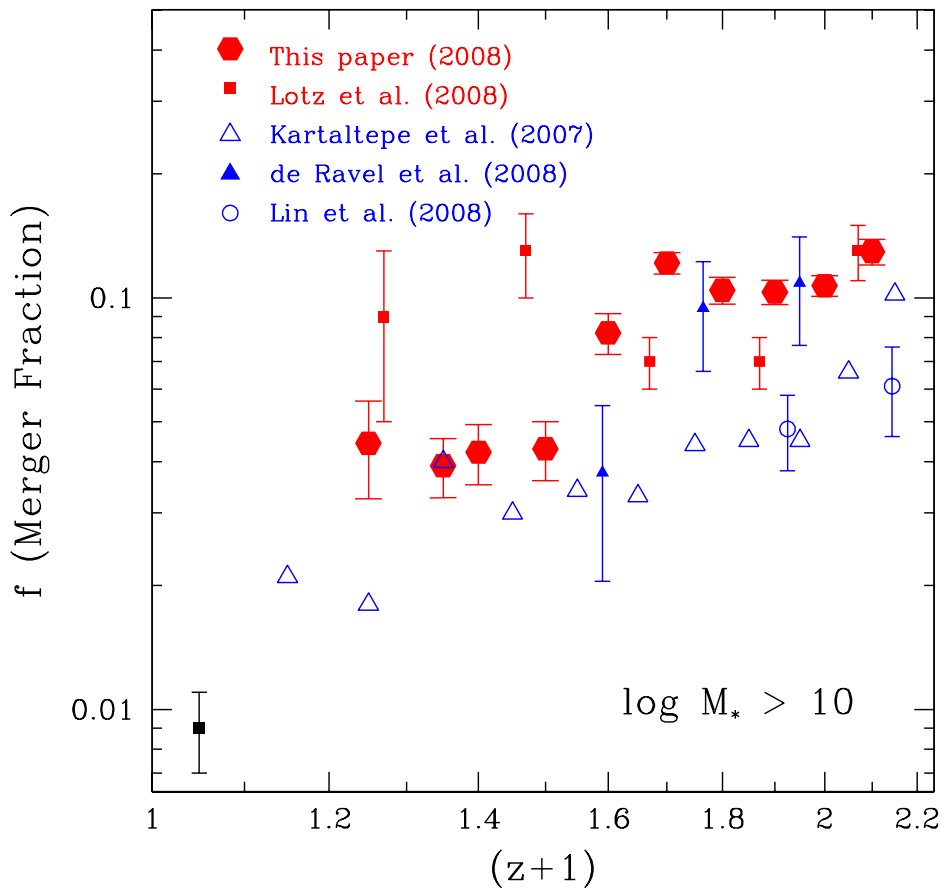


Figure 2.4: The evolution of the derived merger fraction through several previous studies compared to our results. Those systems which are coloured red are those derived through structural methods, either the CAS system (Conselice, Yang & Bluck 2009) or the Gini/ M_{20} method (Lotz et al. 2008a). The blue symbols are the merger fractions derived from ($d < 20$ kpc) pair studies, either kinematic pairs as in Lin et al. (2008) and de Ravel et al. (2008) or photometric pairs from the COSMOS fields (Kartaltepe et al. 2007). In general the morphologically defined mergers give a higher merger fraction than those derived through pairs.

still be true. What this may represent is an optimal distance for measuring close pairs whereby the timescales agree favourably to more direct structural approaches.

2.5 Discussion

Conselice et al. (2008) find that galaxies with masses in the range $8 < \log(M_*/M_\odot) < 9$ and $9 < \log(M_*/M_\odot) < 10$ have a peak in their merger fraction at around $z = 1 - 1.5$, with galaxies with stellar masses $\log(M_*/M_\odot) > 10$ appearing to peak in their merger fraction later, at around $z \sim 2$. In this chapter we have found that for galaxies with $\log(M_*/M_\odot) > 11$ the merger fraction continues to increase out to $z \sim 3$, indicating

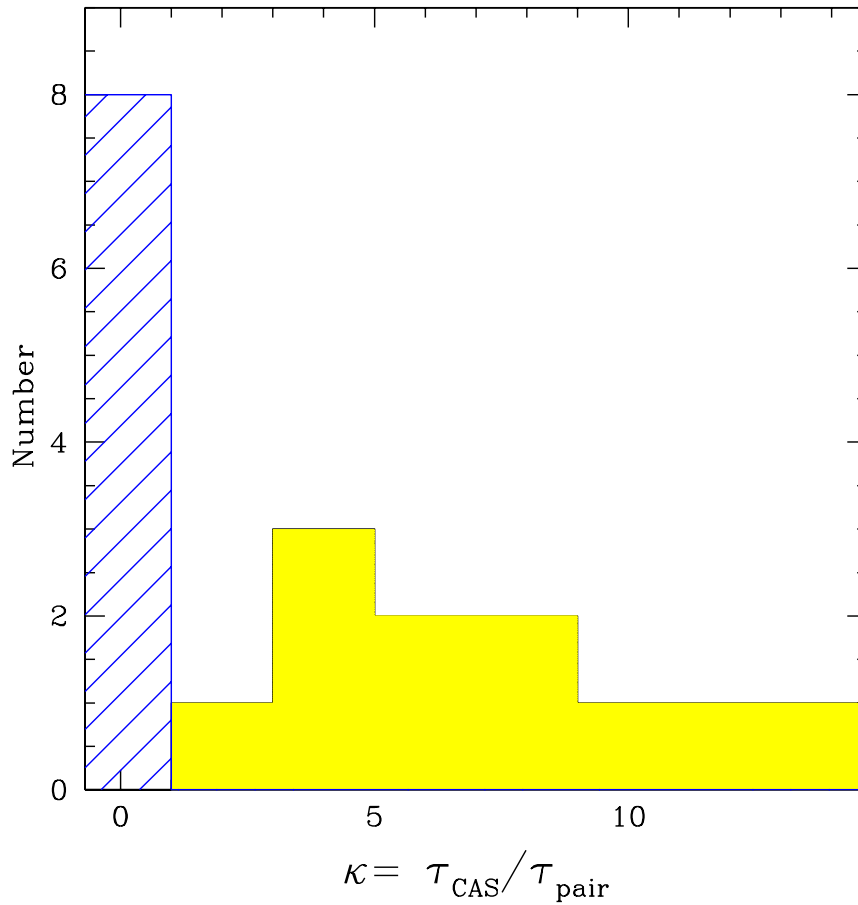


Figure 2.5: The ratio of the time-scale sensitivity for the CAS identified mergers and the time-scale for merging for galaxies in $20 \text{ h}^{-1} \text{ kpc}$ pairs. The blue hatch histogram shows the results for galaxies in sub-parabolic orbits, while the solid yellow show the results for the more realistic Sbc orbital models from Lotz et al. (2008b).

that the peak must occur at $z > 3$. This provides further evidence that more massive galaxies undergo a greater number of major mergers earlier than less massive systems.

This method of calculating pair fractions is based on noting over-densities of galaxies around host galaxies, based on background counts. However, the clustering of galaxies increases with redshift (see Bell et al. 2006). So, this effect may be partly explained by the correlation function of galaxies increasing with redshift. Since the parameters of this function are poorly known observationally, no attempt has been made to correct for this issue. Consequently, our pair fraction results from both the GNS and POWIR surveys may be interpreted as the 2 point correlation function evaluated at 30 kpc for these massive galaxies. This clearly evolves and it is likely true that the actual pair fraction evolves in line with this correlation. Contamination from line of sight projec-

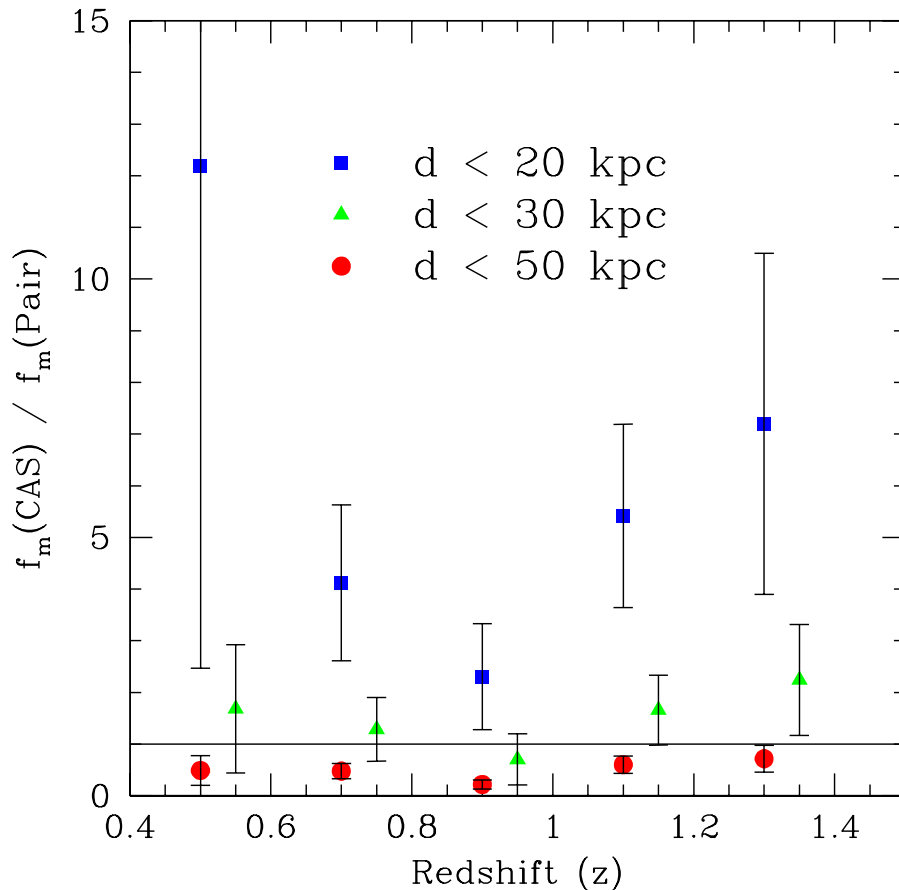


Figure 2.6: The ratio of the CAS merger fraction and the pair fraction, within the same sample of galaxies with $M_* > 10^{11}$ within the EGS and the other POWIR fields (Conselice et al. 2007, 2008b). The blue squares are for those systems with separations of < 20 kpc, the green triangles are for those with separations of < 30 kpc, and the red circles are for systems with separations of < 50 kpc.

tion at scales larger than 30 kpc will be minimised by the fact that we calculate our correction around the galaxies being measured. Further, we have recently acquired morphological CAS measurements on the GNS galaxies as well as the POWIR ones (see Chapter 3). This gives a consistent merger fraction ($f_m \sim 0.3$) to the pair methods. We explore this fully in the following chapter, and elude to the relation between morphological and pair methods in Conselice, Yang & Bluck (2008) and Bluck et al. (2010b), in preparation.

Despite the large errors associated with calculating merger rates, we have demonstrated that there is little or no evolution in the rate of major mergers with redshift. The maximum evolution permitted by the errors (to 2σ) would only amount to increasing the merger rate by a factor of five. This agrees well to predictions from the Millen-

nium Simulation (see Bertone & Conselice 2009). Of greater significance, however, is our calculation of the redshift dependence on the characteristic time between mergers, $\Gamma(z)$. This quantity decreases significantly with redshift. As such, in the early universe ($z \sim 3$) there appears to have been a shorter time between major mergers of massive galaxies than there is today.

2.6 Summary and Conclusions

We derive the major merger fractions for massive ($M_* > 10^{11} M_\odot$) galaxies in the GNS at two redshifts. We find a merger fraction of $f_m = 0.19 \pm 0.07$ at $z = 2.0$ and $f_m = 0.40 \pm 0.10$ at $z = 2.6$. This indicates, when compared to data from Conselice et al. (2007), De Propis et al. (2007), and POWIR pair fractions (also calculated in this chapter) in Fig. 2.1, that there is a strong correlation between merger fraction and redshift for massive galaxies. Furthermore, we fit a function of the form $f_m = f_0(1+z)^m$ to our data, and the data from Conselice et al. (2007) at lower redshifts for $M_* > 10^{11} M_\odot$ galaxies, finding a best fit to the two free parameters of: $f_0 = 0.008 \pm 0.003$ and $m = 3.0 \pm 0.4$. This indicates that the merger fraction for massive galaxies continues to increase out to $z \sim 3$. This implies that more massive galaxies have higher numbers of mergers earlier than less massive ones, since previous work has found that the merger fraction for lower mass galaxies levels off and declines with increasing redshift in the range $z \sim 1 - 2$ (e.g. Conselice et al. 2008).

We find that there is close agreement between CAS selected structural merger fractions and $d < 30$ kpc close pair fractions, for massive galaxies at $z < 1.5$. We argue that this is most probably a result of both methods being sensitive to the underlying merger history, and, moreover sharing a similar mass ratio and timescale sensitivity. We also note that our empirically deduced ratios between close pair and structural merger fractions agree very well to the highest resolution and most realistic available N-body simulations of these processes (see Lotz et al. 2008a,b).

We calculate the major merger rate finding no significant evolution from $\mathfrak{R} < 5 \times 10^5 \text{ Gpc}^{-3} \text{ Gyr}^{-1}$ at $z = 2.6$ to $\mathfrak{R} < 1.2 \times 10^5 \text{ Gpc}^{-3} \text{ Gyr}^{-1}$ at $z = 0.5$. Moreover, a steep evolution is ruled out. We also calculate the evolution of the characteristic time

between mergers $\Gamma(z)$, finding a rapid decrease from ~ 12 Gyr at $z = 0$ to ~ 1.5 Gyr at $z = 3$. This indicates that massive galaxies take much longer between individual mergers in the local universe than at high z , but, since there are more massive galaxies now than there were in the early universe, the comoving rate remains roughly constant. By integrating over the best fit to this curve, we calculate the average number of major mergers an average massive ($M_* > 10^{11} M_\odot$) galaxy experiences from $z = 3$ to the present is $N_m = 1.7 \pm 0.5$.

2.7 Retrospective: Close Pair Errors, Star Formation Rates and Morphology

2.7.1 Introduction

During the course of the Viva Voce examination on this Thesis a number of questions were raised regarding the reliability, or otherwise, of the close pair method presented in this chapter, and indeed used further to identify minor mergers in the following chapter (Chapter 3). Additionally, suggestions were made to investigate whether the galaxies in apparent pairs have higher levels of asymmetry or star formation rates. In particular, reference was made to the large body of work published by Lopez-Sanjuan, Marc Balcells and collaborators on the merger fraction and rate for massive galaxies up to $z \sim 1$ which was published after the results of Chapter 1 (e.g. Lopez-Sanjuan et al. 2009a/b, Lopez-Sanjuan et al. 2010). They find merger fractions up to a factor of 2-3 times lower than that of Conselice, Yang & Bluck (2009) through using a maximum likelihood method, accounting for Malmquist-type biases.

A complete comparison between the approaches presented in this Thesis and the work of Lopez-Sanjuan et al. is beyond the scope of this section, however, the author acknowledges here that there is some debate in the field as to the correct methodology for assigning close pairs and indeed deducing merger fractions from these. The methods presented in this thesis draw a close parallel to the work of Patton et al. (2000) and are by far the most commonly used methods (see e.g. Patton et al. 2000, Conselice et al. 2003, Bundy et al. 2004, Rawat et al. 2008, Conselice 2009, Jogee et al. 2009). It is

also pertinent to note that the Lopez-Sanjuan - Balcells team have not computed pair and merger fractions for $z > 1.5$ galaxies, which this Thesis centres around, and thus no direct comparison between the results can be made here. Nonetheless, at $z = 0.6$ both approaches give a merger fraction of ~ 0.08 (see Fig. 1.1 and Lopez-Sanjuan et al. 2009a). This notwithstanding, the efficacy of the close pair method will be tested in this section in a variety of ways, with the intention of better understanding the errors intrinsic to the method, possible systematic effects and its relation to other indicators such as elevated star formation rates and asymmetries.

This section has three goals:

1. Compare model statistical close pair fractions to model spectroscopic close pair fractions in the Millennium Simulation.
2. Look at photometric close pairs as both a sanity check and as a means to identify future targets of interest for spectroscopic follow up.
3. Explore possible relationships between star formation rate (SFR), asymmetry (A) and close pair fraction (f_m).

Each of these are looked at in turn throughout this section.

2.7.2 Updated Error Analysis - The Millennium Simulation

The aim of this sub-section is to compare the merger fraction results obtained by the statistical close pair methods presented in this Thesis with spectroscopic close pair methods for a set of model galaxy catalogs constructed from the Millennium Simulation. In particular, we use light cone views developed by Kitzbichler & White (2006) constructed from semi-analytic galaxy catalogs in the Millennium Simulation produced by De Lucia & Blaizot (2007). The techniques used, and full details of the models are provided in these references. For the purposes of this section it should suffice to comment that the views were a set of six pencil beam light cone observations through an extended Millennium simulation, whereby $500 h^{-3} \text{ Mpc}^3$ blocks were added together with a small angular shift to avoid exact repetition. The full prescriptions for assigning galaxy luminosities and masses from halo masses are beyond

the scope of this Thesis, but are presented (for the interested reader) in detail in De Lucia & Blaizot (2007) and references therein. Effectively the catalogs from De Lucia & Blaizot (2007) provide the fundamental characteristics of the galaxies, such as stellar mass, luminosity, location in the model coordinates system, and the tables from Kitzbichler & White (2006) provide the direct observational components, such as RA and Dec, observed (spectroscopic) redshifts and apparent K band magnitudes.

We selected eight areas of the Kitzbichler & White (2006) views, with equal (0.01 square degree) areas which provide our eight unique runs. This was chosen organically to contain roughly equal high redshift massive galaxy numbers to our GNS sample, and to keep to a minimum the computational overheads that go with very large numbers of total galaxies visible in the view. The average number of $M_* > 10^{10.5} M_\odot$ galaxies at $1.7 < z < 3$ in each run is 60 (comparable to the 82 used in the GNS sample). The average number of galaxies visible at all redshifts and stellar masses in each view is ~ 32000 . This provides ample numbers to gain meaningful statistics on the differences between spectroscopic and statistically deduced close pair fractions, from model data. We were forced to choose slightly lower stellar mass cuts than used in the GNS ($\lg[M_*] > 11$) due to the intrinsic underpopulation of very massive galaxies (and halos) at high redshifts inherent in the Millennium simulation, see e.g. Bertone et al. (2009) for a discussion on this issue. However, the mass and redshift parameter space is broadly similar and should provide a decent first formal test to the efficacy of the close pair method.

For each run we selected two samples: a high stellar mass, high redshift galaxy catalog containing only $M_* > 10^{10.5} M_\odot$ galaxies at $1.7 < z < 3$; and a large catalog containing all galaxies viewed in the light cone and restricted area utilised regardless of mass or redshift. We then ran our close pair codes (exactly as presented in §2.3) and further ran an additional set of three spectroscopic close pair codes (corresponding to massive galaxies with pairs within 30 kpc, with magnitudes ± 1.5 of the host galaxy magnitude, and velocity differences of $\Delta v < 500$ km/s, 1000 km/s and 1500 km/s respectively) utilising the observed (spectroscopic) redshifts available for all objects in the view from the Kitzbichler & White (2006) catalogs. Explicitly we compute the spectroscopic pair fractions as:

$$f_{pair} = \frac{N_{pair}(< 30kpc, +/- 1.5mag, \Delta V < X)}{N_{host}} \quad (2.8)$$

Where N_{pair} gives the total number of galaxies in the model with companions within 30kpc of the host, and within +/-1.5 of the host galaxy's K-band magnitude, with a velocity difference from the model observed spectroscopic redshift of $X = 500$ km/s, 1000 km/s and 1500 km/s. The statistical pair fraction is computed as in eq. 2.3 where the corrections for our statistical method are computed exactly as in eq. 2.1 in §2.3 with these corrections being taken around the objects in question (at radii < 200 kpc in physical units). The results are presented in Table B.5, which can be found in Appendix B.

Graphs showing and comparing the spectroscopically and statistically deduced pair fractions are presented in Fig. 2.7. We find that our statistical close pair method gives values which are in general lower than $\Delta v < 1500$ km/s spectroscopic close pairs and higher than $\Delta v < 500$ km/s. We also note that in all but one case (run 4) our statistical methods are slightly higher in value than the $\Delta v < 1000$ km/s spectroscopic close pairs. Quantitatively, we calculate a mean difference of: +0.075+/-0.04 between statistical and spectroscopic close pairs (with $\Delta v < 500$ km/s); +0.029+/-0.021 between statistical and spectroscopic close pairs (with $\Delta v < 1000$ km/s); and -0.018 +/- 0.23 between statistical and spectroscopic close pairs (with $\Delta v < 1500$ km/s). The errors presented here are taken as the standard deviation about the mean difference in values.

Care must be taken when taking these raw results and attempting to transform these into updated errors on the statistical method. Since the environmental data on our sample of high redshift high stellar mass galaxies (presented in Grutzbauch et al. 2010) places these objects as primarily in groups, as opposed to field or cluster galaxies, this would seem to suggest that velocity dispersions ought to be less than ~ 500 km/s. This is, unfortunately, not ideal when utilising the Millennium Simulation as the smoothing length inherent to the halo merger trees results in there being very few galaxies in close pairs with low ($\Delta v < 500$ km/s) relative velocities for artificial reasons. As such, the exact velocities cannot be entirely trusted at small distances, which is the area of interest for this study. A full quantitative analysis of the effects of the smoothing length in the Millennium Simulation on over populating close pairs with higher velocities

is beyond the scope of this Thesis. Nonetheless, it can be seen that the $\Delta v < 500$ km/s spectroscopic close pairs scale less well with both the statistical method and the higher velocity difference spectroscopic methods, and we tentatively suggest that this is ultimately a result of the smoothing scale length in the Millennium Simulation.

If we consider the $\Delta v < 1000$ km/s spectroscopic close pair as the real values for close pairs (which is often used in the literature), then we witness a relatively small offset of $+0.029 \pm 0.021$, which is smaller than the average statistical random errors for our high redshift data (± 0.07). It is also interesting to note that this effect is comfortably within 2σ of indicating no intrinsic bias at all. Whether or not the $\Delta v < 1000$ km/s spectroscopic close pair is itself entirely representative of the true pair fraction is not considered here, but it is recommended that this is looked into further in the future. What is established here is that there is broad agreement between spectroscopic and statistical close pair methods when applied to the model data of the Millennium Simulation. There is a hint of a small possible bias for the statistical method to overestimate the spectroscopic method at $\Delta v < 1000$ km/s, but this is only visible at the 2σ level and contributes a significantly smaller shift than the random errors on our data at high redshifts. It is also not at all clear as to what Δv is best to choose in this comparison. Thus, we do not modify our results in the previous sections in light of this analysis, but we do give an updated error estimate in light of this and other issues at the end of this subsection. We do, however, note that our methods give close accord with spectroscopic methods at $\Delta v < 1000$ km/s, and broadly correlate with the spectroscopic methods at all relative velocity limits probed here (see Fig. 2.7 and Table B.5).

The variation in measured pair fraction for each of the differing spectroscopic and statistical methods can be quantified as the standard deviation about the mean of the runs. These vary from $\sigma = 0.04 - 0.06$ across all of the methods, with the spectroscopic close pair method at $\Delta v = 500$ km/s giving the highest variance, possibly due to the adverse effect the smoothing length of the Millennium Simulation has at these low velocities. Since all of the methods have similar variance here this is most naturally interpreted as cosmic variance across the Millennium Simulation. Whether there is greater or less variance in the real Universe than that witnessed in the Millennium Simulation cannot be judged without a greater sample of different areas of sky probed

to high redshifts than currently possessed or available. However, as a first estimate the effect on the error of the statistical pair fractions used throughout this chapter due to cosmic variance may be estimated to be ~ 0.05 (the mean variance of the eight runs), which is similar to the statistical error on our high redshift sample. Thus we tentatively suggest that the observed variance can be explained by small number counting errors, not global cosmological effects, and do not take these into account further. If greater cosmic variance is witnessed to that expected merely via counting error (either in future models or real world data) this view will have to be revised.

Unfortunately, the mechanics of the Millennium Simulation's semi-analytics makes it impossible to use for probing the merger timescales directly. There is neither sufficient resolution nor sophisticated enough gas physics implemented to trust the timescales between close pairs becoming mergers, thus, this is not explored further here. The most realistic models to date are implemented by Lotz et al. (2008a/b, 2010). These are based on gas rich disk mergers (Sbc models), and are computed via N-body simulations. The values they obtain are used throughout Chapter 2 and 3, but it is acknowledged that uncertainty in the initial relative velocities remain an unrestricted source of error in these analyses at the present time.

Future planned spectroscopic study, as well as even more detailed and realistic N-body simulations, will come to better constrain this difficult issue in time. For now, adopting average group relative velocities of typically $\Delta v \sim 300 - 400$ km/s and looking principally at gas rich disks have yielded workable values of the merger timescale (τ_m). In light of the uncertainty in this issue, however, in the following Chapter the majority of the analyses are performed in a timescale independent manner, and where possible timescales are factored out of the equations until the final values are stated to make it easy for researchers in the future to implement new timescales into our analyses, when these are better constrained than at present.

To better acknowledge the true errors on the total number of mergers, given both the small systematic offset between spectroscopically and statistically determined close pair fractions, and the uncertainties in the timescale, τ_m , we have recomputed these here in a timescale independent manner. Assuming that the $\Delta v < 1000$ km/s spectroscopic close pair fraction in the Millennium Simulation can be treated as a true

close pair fraction, and noting that we have effectively used a mean timescale between the CAS and close pair methods of $\langle \tau_m \rangle = 0.8$ Gyr, we can recompute the total number of major mergers from $z = 3$ to the present. We find that an average massive ($M_* > 10^{11} M_\odot$) galaxy will experience $N_m = 1.35_{-0.6}^{+0.4} / \tau_m$ mergers over the past 12 billion years, with objects within a stellar mass ratio of $\sim 1 : 4$.

By way of conclusion, we have noted a close agreement between spectroscopically and statistically computed model pair fractions in the Millennium Simulation, especially at commonly used velocity differences of $\Delta V < 1000$ km/s. There is a hint of possible bias whereby statistical methods may slightly overestimate the true spectroscopic pair fractions, but this is only evident at the 2σ level and moreover corresponds to a shift significantly less than the random counting errors for our high mass and high redshift sample. Thus, no significant modification to the results are required or implemented here. The broad observed agreement between these approaches, and small offsets in values when applied to model data, lend an important positive check on the methods used throughout this Thesis. Further investigation here, however, is strongly recommended, and real-world spectroscopic follow up is essential to fully establish the validity of the method. A first step toward this goal is presented in the following section, by selecting possible future targets of interest.

2.7.3 Photometric Close-Pairs

Although the close pair method presented in this chapter is statistical in nature, and does not rely on finding pairs at similar redshifts (as in the spectroscopic close pair methods described above), looking at the differences in photometric redshifts of identified potential (statistical) pairs can provide both a useful sanity check and a means to identify systems that could be interesting to follow up with spectroscopy in the future. In this sub-section we compute photometric redshifts for the entire sample of galaxies imaged by the GNS, compute photometric close pair fractions, and provide a set of tables which present salient information on the potential close pairs, as well as other information about the host galaxies such as star formation rate (SFR) and asymmetry (A), see Tables B.1, B.2, B.3 and B.4 in Appendix B.

The methods used to compute photometric redshifts are presented in §1.4.1.2. Also full

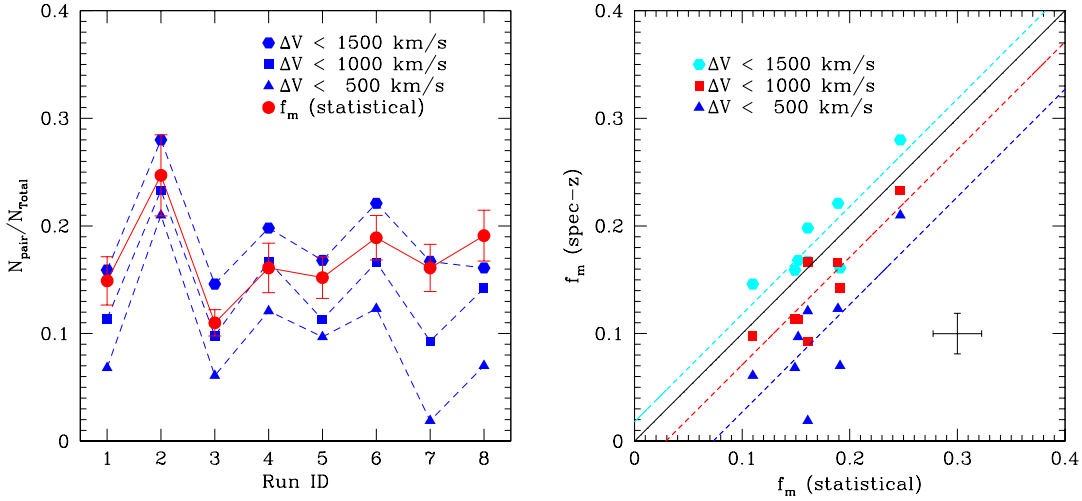


Figure 2.7: Left panel is a comparison of spectroscopic and statistically deduced model pair fractions across the eight runs performed on the Kitzbichler & White (2006) views of the De Lucia & Blaizot (2007) galaxy models drawn from the Millennium Simulation. Right panel presents spectroscopically confirmed close pairs at varying velocity differences as a function of the statistically deduced pair fraction. Red error bars (left plot) are Poisson errors on the statistical counting. Black error bar (right plot) represents the average counting error on all methods. These errors do not take into account cosmic variance, systematic effects or biases as this is in part what these plots aim to address. The solid black line indicates the one-to-one relation. The cyan, red and blue dashed lines indicate best fits to the $\Delta v = 1500$, 1000 and 500 km/s close pair fractions respectively, assuming a constant one-to-one gradient and varying the intercept only. Explicitly $f_m(\text{spec-z}) = f_m(\text{statistical}) - c$, where $c = -0.018$ for 1500 km/s, $+0.029$ for 1000 km/s, and $+0.071$ for 500 km/s.

details are presented in Grutzbauch et al. (2010) with further discussion in Conselice et al. (2010). Briefly, two methods were used: HYPERz and BPz, both functioning via fitting template spectra to the BVizH HST bands we possess for the data. A comparison of our photometric redshifts with the available spectroscopic redshifts within the sample is presented in Fig. 2.8, for both methods used. In total we have 906 spectroscopic redshifts and ~ 8000 photometric redshifts. In Fig. 2.9 we present the scatter as $\delta z = \Delta z / (1+z)$ as a function of apparent magnitude, and also plot explicitly the fraction of catastrophic outliers (those with $|\delta z| > 0.3$) as a function of H-band magnitude. It was concluded that HYPERz gives the superior result and we utilise this for the remainder of this subsection (please see full details in Grutzbauch et al. 2010).

Errors on the photometric redshifts were computed via Monte-Carlo simulation, utilising the intrinsic scatter ($\delta z = 0.02$) and its dispersion ($\sigma_{\delta z} = 0.06$). We then allowed the fraction of catastrophic outliers ($f_{\text{outlier}} = 0.2$) to be randomly shifted from $\delta z = 0.3$ to 1. The resultant 1σ errors are found to be $\sigma_z = 0.15(1+z)$.

We compute the photometric close pair fractions for our sample of massive galaxies

for 1, 2, 3 and 4 σ differences in redshift between the host and potential companion, and present these results in Table B.1. For all the massive ($M_* > 10^{11} M_\odot$) galaxies we produce a comparison table between photometric close pairs at the 3 σ detection threshold and statistical pair fractions computed previously in this chapter (see Table B.2). For those galaxies with photometric close pairs at the 3 σ detection level we additionally provide two more tables displaying the characteristics of the pairs (Tables B.3 and B.4), where some of these galaxies may be candidates for actual close pairs. The tables provide details on the RA, Dec, photometric redshift and H-band magnitude for both the host galaxies and their potential pairs. In the future it would be interesting to investigate some of these candidate pairs with spectroscopy, and in so doing come to give a real-world test similar to the model test for the close pair method demonstrated in the previous subsection. At present due to lack of spectral data for our sample of pairs this cannot be done, and what follows in the rest of this section are some more general and statistical comments.

We note that the photometric close pair fractions may be interpreted as upper limits to the true pair fraction at the certainty level of the difference between host and companion redshift, to within the Poisson statistical counting error. We can thus compute upper limits to the pair fraction robustly. At $1.7 < z < 2.3$ we can state that $f_m < 0.37$ to 3 σ , and at $2.3 < z < 3.0$ we can state that $f_m < 0.64$ to 3 σ . These upper limits are calculated by taking the uncorrected pair fraction for massive galaxies in our sample having pairs with redshifts less than 3 σ away from the host galaxy and adding to this value the 3 σ counting error. The statistically deduced pair fractions in these redshift ranges are ~ 0.2 and ~ 0.4 respectively, comfortably lower than the robust upper limits. This is at least indicative of there being no fundamental inconsistency between the methods (also see Table B.1 for raw data). However, a more thorough examination will have to wait until spectroscopic follow up has been performed on some of the galaxies with potential real pairs in Tables B.3 and B.4 which are possible actual close pair candidates with redshifts compatible to within 3 σ . For a direct comparison between raw pair counts within 30 kpc for ± 1.5 mag objects, photometric close pairs with redshifts within 3 σ , and corrected statistical pair counts please see Table B.2 in Appendix B.

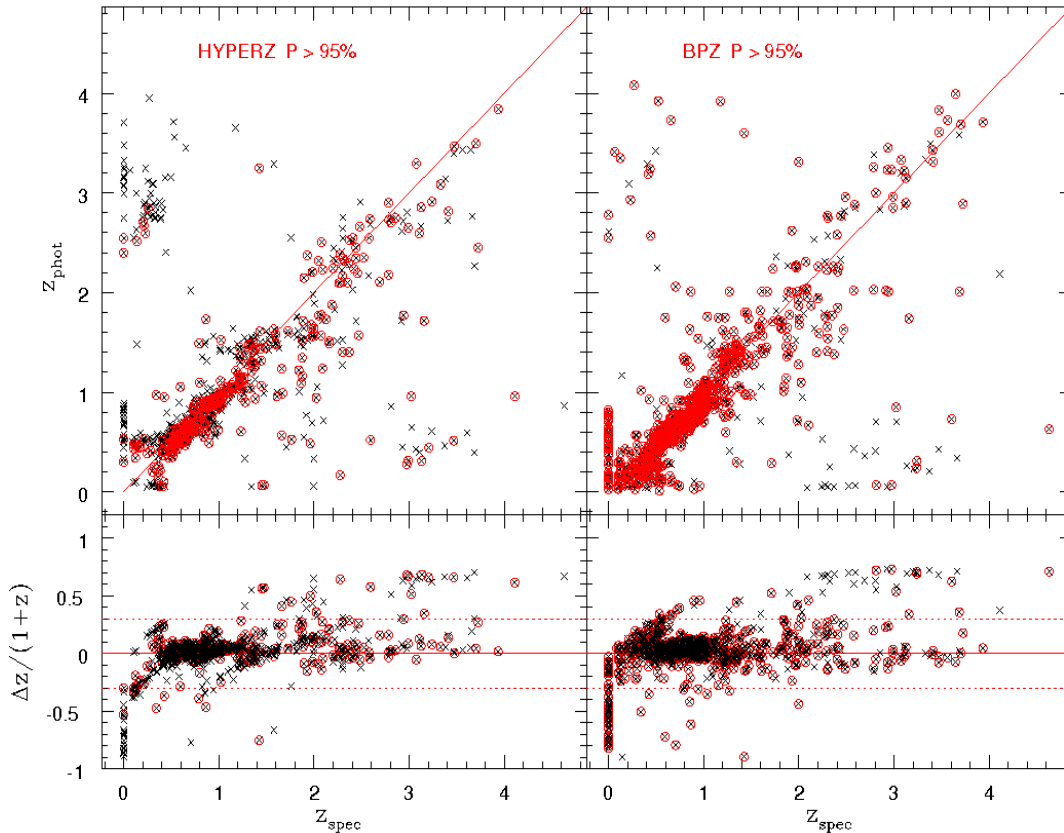


Figure 2.8: Photo-z - Spec-z comparison 1: Reliability of photometric redshifts. Top panels: photometric vs. spectroscopic redshifts using HYPERZ (left) and BPZ (right). Photometric redshifts with a high probability of $P > 0.95$ are circled in red. Bottom panel: $\Delta z / (1+z)$ ($=\delta z$) dependence on redshift. Black symbols show all redshifts, red symbols high probability redshifts only. The dashed lines show the limit for catastrophic outliers at $|\delta z| > 0.3$

2.7.4 Comparison with Star Formation Rates and Morphologies

There is a multitude of data available across the GOODS fields, and in this sense no GOODS survey is an island. For consistency within the GNS data heretofore we have considered only HST imaging, except in the original massive galaxy sub-set where we add a host of groundbased photometry (including the K-band where available). In this section the aim is to broaden this approach, including star formation data from the UV (HST ACS) and $24 \mu\text{m}$ (MIPS). This is not an extensive examination of multi-wavelength analysis and in fact merely represents a start to this process within the GNS. Much future work can be done in this area and the author encourages all who are interested to obtain the freely available GNS data (see Appendix B) and continue in this line of study.

Star formation rates are computed in two different ways: through UV emission with

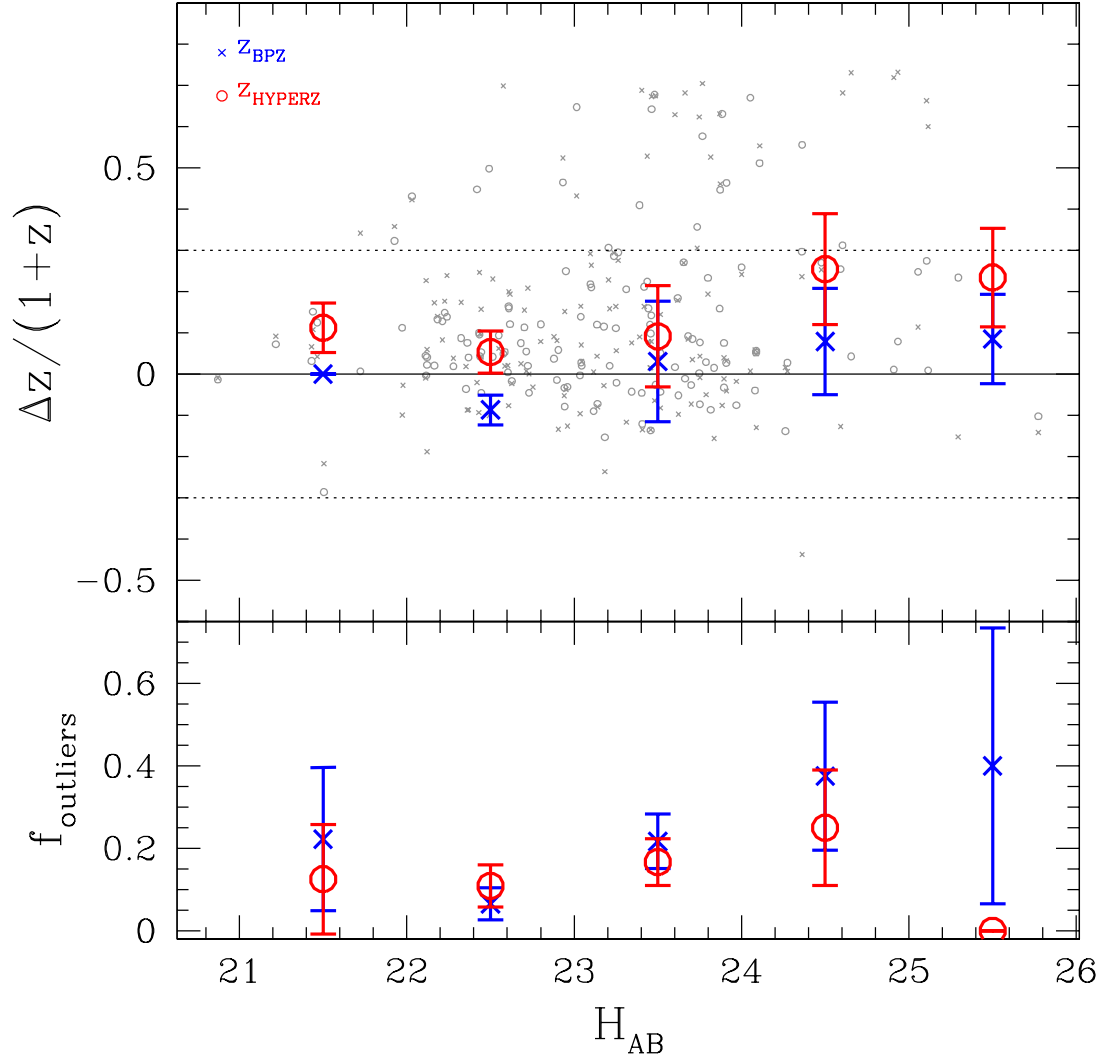


Figure 2.9: Photo-z - Spec-z comparison 2: Dependence of $\Delta z / (1+z)$ on magnitude. Top panel: $\Delta z / (1+z)$ vs H-band magnitude for HYPERz (red circles) and BPz (blue crosses). Median values in each magnitude bin (bin size 1 mag) are plotted as big symbols with errorbars representing the scatter in each bin. The dashed line shows the limits for catastrophic outliers. Bottom panel: Fraction of catastrophic outliers $|\delta z| > 0.3$ as a function of H-band magnitude. For this plot only the redshift range $1.7 < z < 3$ is used.

SED slope correction and through the $24 \mu\text{m}$ flux. The star formation rates were not computed as a part of this Thesis and are in fact presented in detail in a forthcoming, submitted, paper (Bauer et al. 2010). It is beyond the scope of this thesis to provide a full detailed description of all of the steps taken to deduce SFRs through these methods, and the interested reader is directed to Bauer’s work. What follows here is a brief description of the essential details for each method in turn.

As a primary star formation rate indicator we use UV light, which we determine from both observed optical and modelled spectral energy distributions (SEDs). UV lumi-

nosity is closely related to the level of ongoing star formation as the UV continuum luminosity is produced by short-lived O and B stars primarily. However, these methods are strongly affected by dust extinction. In fact inferring the level of dust reddening from photometric properties remains a major challenge to understanding the star formation properties of galaxies at all redshifts. To address this issue an SED correction is applied. UV star formation rate (SFR_{UV}) is calculated from the observed optical ACS z-band flux density which corresponds to a rest-frame wavelength of 2125 Å- 3400 Å, at $z = 1.5 - 3$. A simple K-correction is applied as $\log(1+z)$ (as in Kim et al. 1996; Daddii et al. 2004) and the Kennicutt (1998) conversion to SFR is applied:

$$SFR_{UV}(M_{\odot}yr^{-1}) = 1.4 \times 10^{-28} L_{\nu}(ergs^{-1}Hz^{-1}). \quad (2.9)$$

As a check, a different approach is used by fitting model SEDs to the multi-wavelength GOODS data for our sample of galaxies, which are then used to give synthetic estimation of the UV emission at 1600 Å, and 2800 Å, which are also transformed to UV SFRs via the above formula. Good agreement is found between these two methods (see Bauer et al. 2010). For the purposes of this analysis the SED fit technique was used. To obtain reliable SFRs from the rest-frame UV a dust correction must be applied, and this is certainly not trivial (see e.g. Meurer et al. 2009). Meurer et al. demonstrate a correlation between rest-frame UV slope, β , and dust attenuation for a sample of relatively nearby starburst galaxies (where $F_{\lambda} \sim \lambda^{\beta}$). From the best fit synthetic models we calculate the slope, β , and apply the Calzetti et al. (2004) law to deduce the dust correction. As a sanity check it is noted in Bauer et al. (2010) that there is broad agreement between the uncorrected UV SFR added to the 24 μm SFR and the SED corrected UV SFR (see Fig. 2.10). Less than 10 % of data points lie beyond 2 σ of the one-to-one line. However, there is a tendency for the FIR method to have higher values than the UV + SED correction method. This is possibly indicative of the SED correction method underestimating the dust attenuation for some systems.

For the FIR method, a total SFR is obtained by adding together the uncorrected UV star formation rate to the 24 μm deduced SFR. The $SFR_{24\mu m}$ is computed from the monochromatic luminosity at rest-frame 24 μm to which the Alonso-Herrero et al. (2006) calibration is applied. The assumption here is that the 24 μm emission is re-

radiated star light from young short-lived O and B stars by dust. If a significant fraction of this emission is in fact not re-radiated young star light then this method can overestimate the true SFR, possibly also offering an explanation to the higher values observed via the FIR method to the SED corrected UV method.

We compare the star formation rates via both of these methods in Fig. 2.11 to the asymmetry (A) of the galaxies, for all objects with detected UV and/or 24 μm emissions. Please see Appendix A for detailed description of the derivation of the A parameter. For now it should suffice to comment that A is a measure of the total global asymmetry of a galaxy, with high values generally being thought to be indicative of merger activity. We find no evidence here of a correlation between SFR (deduced via both methods) and global asymmetry, A. We do not conclude, however, that there is no relationship between SFR and A, only that with our data errors and the limitations of measuring SFR especially at high redshifts we cannot report any here.

Furthermore, we go on to compare SFR (deduced via both methods) with corrected statistical close pair fraction in Fig. 2.12. Again no correlation is noted here. This is not surprising as the statistical close pair numbers are merely probabilities of close pairs, and have large errors per galaxy. Finally, we compare global asymmetry to corrected statistical close pair fraction in Fig. 2.13. No correlation is witnessed here either. Simulations in Narayanan et al. (2009) find elevated star formation rates for merging systems, but we do not witness this effect here, with mergers identified either through pair fractions or morphologies.

Star formation rates, asymmetry and close pairs are all frequently used to measure merger activity, but a lack of correlation between these indicators is not necessarily an indication that any one, or all, of these methods are intrinsically flawed. This is because the time-frames of the methods are different, and frequently poorly constrained. Furthermore, SFR activity may be a result of other processes than merging alone. Essentially, the close pair method looks for probable future mergers, whereas the asymmetry approach looks for merging up to some time after the event, and SFR insofar as it is incited by merging will be most evident during the event itself and for a short time afterwards. These differing time-frames may offer a partial explanation to what is witnessed here. Additionally large errors in the statistical pair method per galaxy,

as well as in the star formation rates may be simply obscuring any underlying correlation. For now we can only conclude with any certainty that there is no evidence for correlation between SFR, close pair numbers and asymmetries here at high redshift for massive galaxies, not that there is any strong evidence for no correlation. The implication, however, is that if our results can be believed, the highly star forming, highly asymmetric, and highly clustered massive galaxy populations may be primarily distinct sets at high redshifts. If this is true, then much mobility between these sets must occur as close pairs transform into star bursts incited by merging and then later into the irregular or disturbed galaxies detected through morphological methods. This remains an open question. Much future work will ensue on this issue, which will be further informed by radio fluxes, sub-mm fluxes, X-ray fluxes and deeper high resolution NIR data from the CANDELS survey.

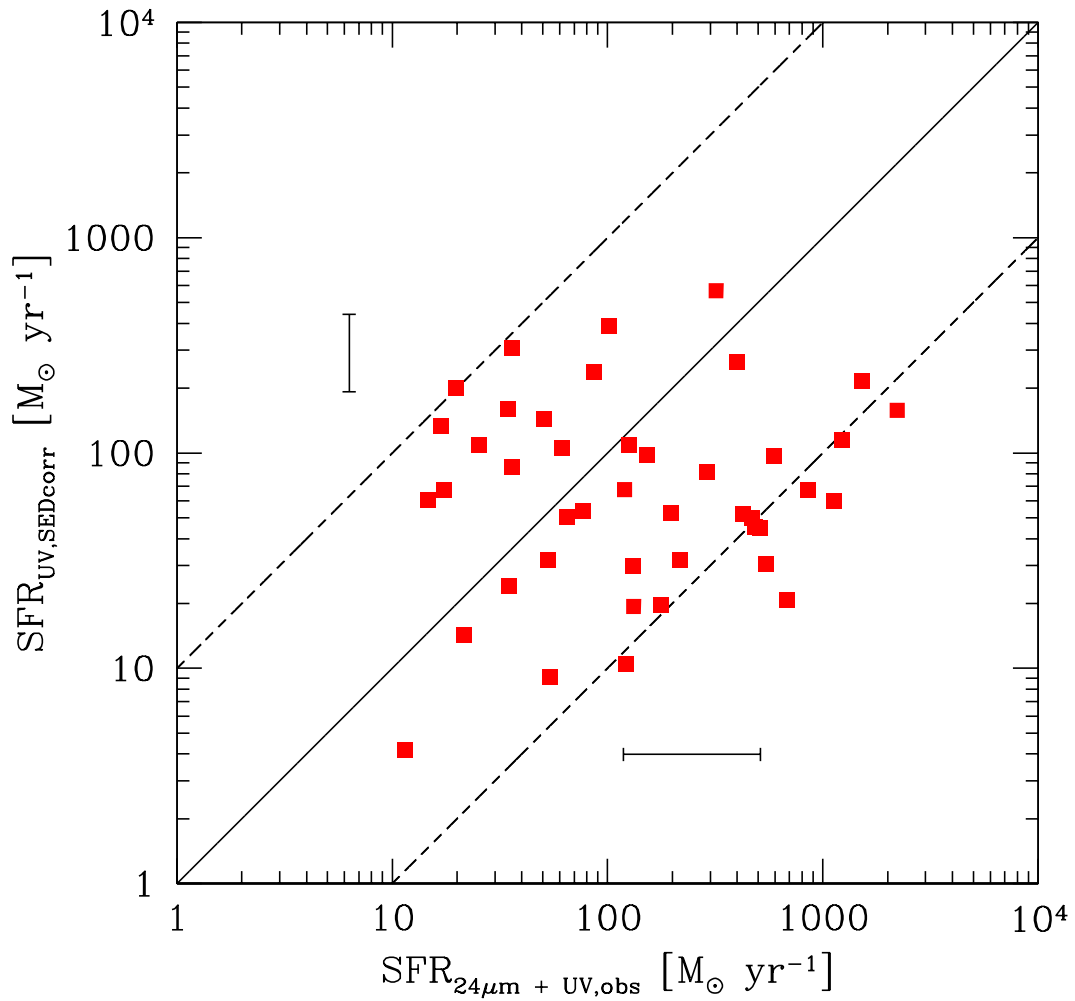


Figure 2.10: Comparison of UV SED corrected star formation rate to $24 \mu m$ + UV observed star formation rate. The solid black line is the one-to-one correlation, with the dotted lines indicating discrepancies of a factor of 10 in either direction. The horizontal error bar is the mean 1σ error on the $24 \mu m$ + UV observed star formation rate, and the vertical error bar is the mean 1σ error on the UV SED corrected star formation rate.

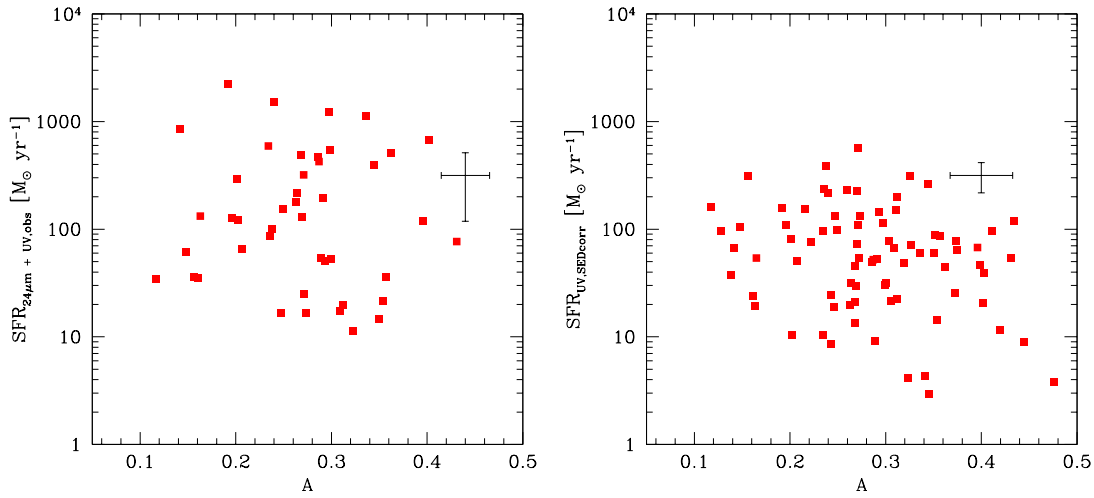


Figure 2.11: Aysymetry vs Star Formation Rate. Left plot shows $24 \mu\text{m} + \text{UV}$ observed star formation rates in comparison to asymmetry, A . Black error bar is the mean 1σ error on the data points taken from the CAS code for A , and from the errors of the SED fitting for SFR. Right plot shows UV deduced SFR corrected for dust attenuation via SED fitting, with the black error bar being the mean 1σ error on the data points from the SED fitting and dust correction.

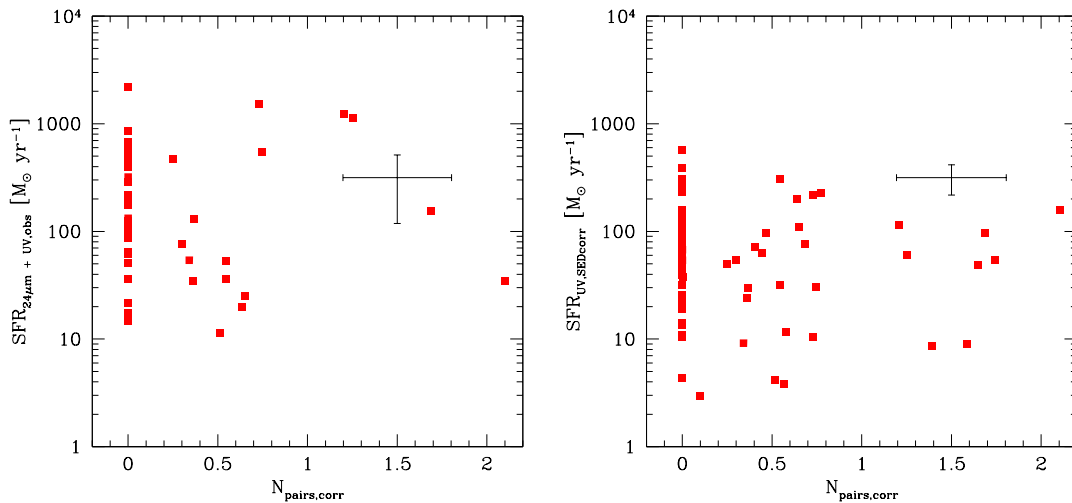


Figure 2.12: Star Formation rate vs Pair Number. Corrected statistical pair number (which can be interpreted as the probability of a pairing) vs star formation rate, for (left panel) $24 \mu\text{m} + \text{UV}$ observed star formation rate and (right panel) UV SED corrected star formation rate. The black error bars are mean 1σ errors on the pair numbers and star formation rates respectively.

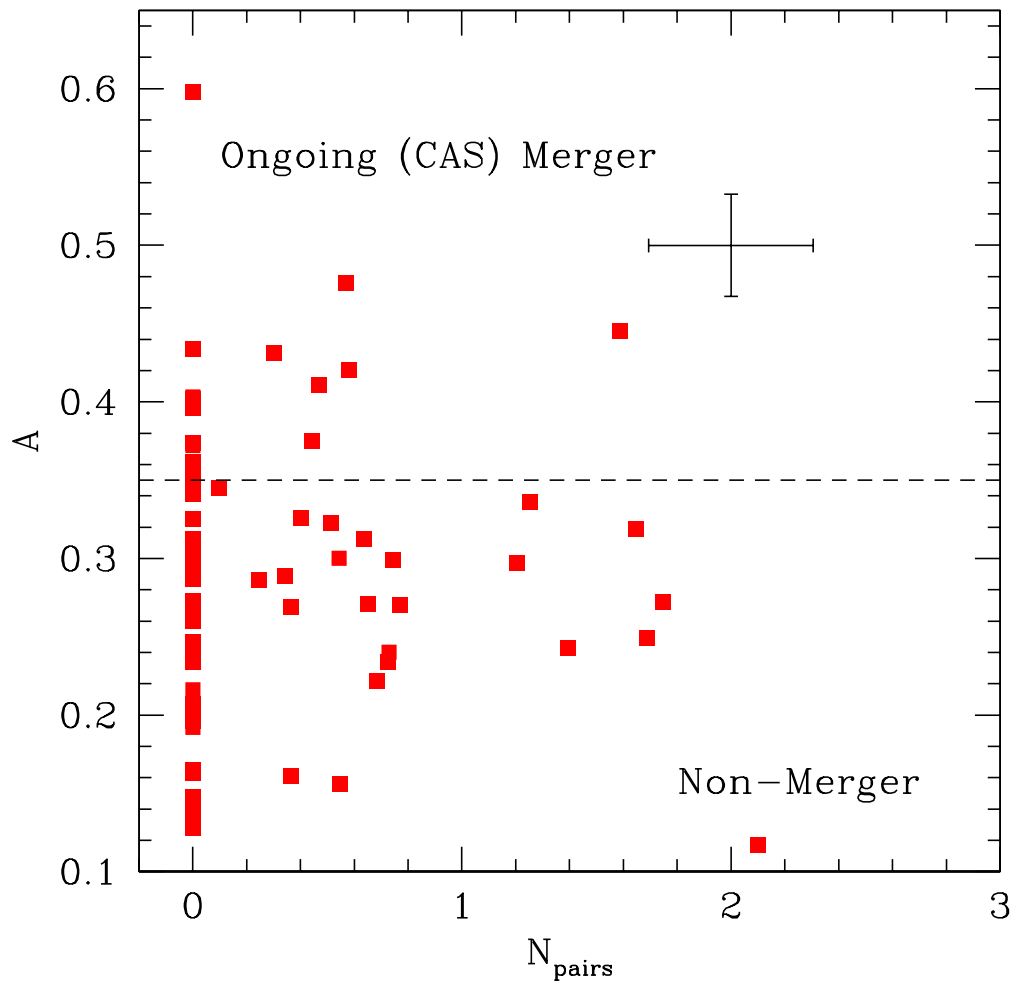


Figure 2.13: Asymmetry vs Pair Number. The black error bar represents the mean 1σ error on the data points. The black dotted line indicates the CAS cutoff for a major merger.

Chapter 3

The structures, minor and major merger histories of massive galaxies at $z < 3$ in the Hubble Space Telescope GOODS NICMOS Survey

The work in this chapter is in preparation for publication as: Bluck et al. (2010b)

This Chapter is based on work I led, in collaboration with Christopher J. Conselice¹, Fernando Buitrago¹, Ruth Gruetzbauch¹, Carlos Hoyos¹, Amanda Bauer¹ and Alice Mortlock¹.

¹ University of Nottingham, School of Physics and Astronomy, Nottingham NG7 2RD, UK

Abstract

We investigate the structures, morphologies, and the major (up to 1:4 by mass) and minor (up to 1:100 by mass) merger history of a population of massive ($M_* > 10^{11} M_\odot$) galaxies at high redshifts ($z = 1.7 - 3$). We utilise extremely deep and high resolution HST H-band imaging from the GOODS NICMOS Survey (GNS), which corresponds to rest frame optical wavelengths at the redshifts probed. We find that massive galaxies at high redshifts are often morphologically disturbed, with a CAS deduced merger fraction $f_m = 0.22 \pm 0.05$ at $z = 1.7 - 3$. We find close accord between close pair methods (within 30 kpc apertures) and CAS methods for deducing merger fractions at all redshifts, up to $z = 3$. This suggests that both methods trace the underlying merger evolution and, moreover, have a similar timescale sensitivity. We also find a correlation between the residual flux fraction (RFF) from GALFIT fitting of our population of galaxies and their global asymmetry (A). We deduce the total minor + major merger history of massive galaxies with $M_* > 10^9 M_\odot$ galaxies, and note that this scales roughly linearly with mass and magnitude range. We compute the total number of mergers to be $(4.5 \pm 2.1) / \tau_m$ from $z = 3$ to the present (where τ_m is the merger timescale which is expected to vary as a function of mass), corresponding to an average mass increase of $(2.79 \pm 1.6) \times 10^{10} M_\odot$ over the past 12 Gyrs due to merging. We postulate that the size evolution observed elsewhere throughout the literature may possibly be explained, partially or entirely, by this merging.

3.1 Introduction

The cold dark matter paradigm for structure formation in the Universe leads naturally to a hierarchical picture of galaxy growth, whereby large objects form from the merging together of smaller objects. As such, observing galaxies in a state of merging becomes desirable both as a probe of galaxy evolution and as a critical test to the Λ CDM cosmological model (see e.g. Bertone & Conselice 2009). Many studies have probed to date the merger history of massive galaxies, in particular, up to high redshifts ($z < 3$) see Chapter 1 and e.g. Patton et al. (2000), Conselice et al. (2003), Rawat et al. (2008), Conselice, Yang & Bluck (2009), and Bluck et al. (2009).

At low to intermediate redshifts ($0 < z < 1.4$) close pair methods and morphological approaches find close accord in estimating the major merger history of massive galaxies (see Chapter 1 and Conselice, Yang & Bluck 2009). At the highest redshifts, studies have concentrated primarily on close pair methods, as opposed to morphological approaches, due to restrictions on the resolution of imaging of very high redshift objects. These studies find rough agreement in identifying a positive evolution of the major merger fraction with redshift, with a best estimate for the most massive galaxies (with $M_* > 10^{11} M_\odot$) of evolution such that $f_m \propto (1 + z)^{3.0+/-0.4}$, with no sign of this monotonic increase in merger fraction with redshift abating at higher redshifts (see e.g. Bluck et al. 2009). For lower mass systems there is an observed peak to the merger fraction history at $z \sim 1 - 2$, as seen in e.g. Conselice et al. (2007), but to date no similar peak is observed for the most massive galaxies in the Universe (with $M_* > 10^{11} M_\odot$), even out to $z = 3$. This disagrees with predictions from semi-analytical interfaces with the Millennium Simulation, where a turn around in merger fraction is expected for massive galaxies by $z \sim 2$. The under-population of massive galaxies in the Millennium Simulation is a well known problem, and this is possibly the root cause of this discrepancy. Interestingly, however, the merger rates computed in Bluck et al. (2009) agree comfortably with that predicted from the Millennium simulation (Bertone & Conselice 2009). Obviously, at some point the merger fraction plot must turn over but this has yet to be observed or constrained.

The total number of major mergers that massive galaxies experience since $z \sim 3$ has been estimated assuming a merger timescale based on N-body simulations (see e.g. Lotz 2008a,b), and a parameterisation of the merger history (see Bluck et al. 2009 and Conselice, Yang & Bluck 2009). Current best estimates for massive galaxies suggest that the total number of major mergers ($\sim 1:4$ by stellar mass) experienced since $z = 3$ by the most massive galaxies in the Universe (with $M_* > 10^{11} M_\odot$) is currently $N_M = 1.7 +/- 0.5$ (see Chapter 2 for further details). This implies that there is on average a mass increase of less than a factor of two or so due directly to major merging over the past 12 billion years of massive galaxy evolution. Additionally, there is a growing mass of evidence to suggest that over the same time period massive galaxies grow in size by up to a factor of five by building up stellar matter in their outer regions, suggesting a volume increase of at least a factor of 50 (see e.g. Carasco et al. 2010, van Dokkum et

al. 2010, Cimatti et al. 2008, Buitrago et al. 2008, Trujillo et al. 2007). To some extent spectroscopic measures of the velocity dispersions of a very small subset of these high redshift massive galaxies are beginning to confirm that they are extremely dense and compact (e.g. van Dokkum et al. 2009).

If this growth in size is a real effect, and remains as dramatic as described currently in the literature, then a crucial question to address is: *how do these massive galaxies grow so much in size whilst growing so little in mass?* If the major merger histories are correct, and the size evolution is correct, then we are expected to believe in a meteoric growth of 50 times or so in volume during a period of very modest (factor of two or so) growth in mass due to major merging. Thus, it seems unlikely that the most obvious candidate for driving galaxy growth (that of major merging) can ultimately be responsible. So, it becomes necessary to explore other possibilities, e.g. alternative external influences such as minor mergers (this chapter, and Naab et al. 2009) and intrinsic evolution via, for example, AGN ‘puffing up’ scenarios (Fan et al. 2008, Bluck et al. 2010a and Chapter 4).

In order to investigate the role of minor mergers and structural evolution in massive galaxies, we combine a variety of different techniques and approaches. In this chapter we analyse the structural and morphological properties, and minor merger fraction histories, of a sample of 82 massive ($M_* > 10^{11} M_\odot$) galaxies imaged in the rest frame optical as part of the HST GOODS NICMOS Survey at $1.7 < z < 3$. In particular, we compute the morphological CAS parameters (Conselice et al. 2003) for the sample and use this to obtain an independent merger fraction for our high redshift sample of massive galaxies to the close pair derived merger fraction in Chapter 2. We go on to compare the Asymmetry (A, Conselice et al. 2003) of our massive galaxies with the residual flux fraction (RFF, Blakeslee et al. 2006) from their GALFIT fitting (first performed for our GNS galaxies in Buitrago et al. 2008). Furthermore, we exploit the exceptional resolution and depth of the HST GNS by using statistical close pair methods to investigate the high mass end of the minor merger history for these objects, constructing a minor merger history.

Throughout the chapter we assume a Λ CDM Cosmology with: $H_0 = 70 \text{ km s}^{-1} \text{ Mpc}^{-1}$, $\Omega_m = 0.3$, $\Omega_\Lambda = 0.7$, and adopt AB magnitude units.

3.2 Data and Observations

The HST GOODS NICMOS Survey images a total of 8298 galaxies in the F160W (H) band, utilising 180 orbits and 60 pointings of the HST NICMOS-3 camera. These pointings are centred around massive galaxies at $1.7 < z < 3.0$ to 3 orbits depth. Each tile ($51.2'' \times 51.2''$, $0.203''/\text{pix}$) is observed in 6 exposures that combine to form images with a pixel scale of $0.1''$, and a point spread function (PSF) of $\sim 0.3''$ full width half maximum (FWHM). The total area of the survey is $\sim 43.7 \text{ arcmin}^2$. Limiting magnitudes reached are $H_{AB} = 26.8$ (5σ), see Conselice et al. (2010). We are complete down to $M_* = 10^{9.5} M_\odot$ at $z = 3$ to 5σ . The wealth of observational data available in the GOODS field allowed us to utilise data from the U to the H band in the determination of photometric redshifts. These are computed via a neural network approach, where spectroscopic redshifts in the field are used to train our codes. Multi-colour stellar population fitting techniques were utilised to estimate stellar masses to an accuracy of $\sim 0.2 - 0.3 \text{ dex}$. These use Bruzual and Charlot (2003) models, and assume an exponentially declining star formation history, with a Chabrier initial mass function (IMF). See §1.4, Buitrago et al. (2008), Bluck et al. (2009), Gruetzbauch et al. (2010) and a complete account in Conselice et al. (2010) for full details on the sample selection, source extraction, data catalogs, and determination of photometric redshifts, rest-frame colours and stellar masses. The issue of thermally pulsating AGB stars in model SED fits for massive high redshift galaxies was explored in detail in Conselice et al. (2008) and Bundy et al. (2007) and found not to be a significant problem for our stellar mass determination, perhaps increasing the errors to $\sim 0.3 \text{ dex}$, at the upper end of our initial estimation.

A discussion of more robust error estimates on stellar masses can be found in Chapter 2, where it is concluded, through Monte-Carlo simulation, that systematic errors arising out of Poisson errors from the steepness of the stellar mass distribution (Edgington bias) do not result in a significant infiltration of lower mass objects. Further discussion on the use of the SExtractor package to produce galaxy catalogs is also provided in Bluck et al. (2009) and in Conselice et al. (2010), with special concern for deblending accuracy and removal of stellar objects and spurious detections. In essence point like (non-extended) sources were removed and later objects without galaxy-like

colours were removed. This is, of course, vital to achieve well when utilising close pair statistics approaches. For our sample of massive galaxies, each image was looked at carefully by eye and the source extraction parameters were deduced organically from optimising deblending accuracy.

3.3 Results

3.3.1 CAS Morphologies

Morphology is one of the oldest methods used for analysing the properties of galaxies (see back to e.g. Hubble 1926). The need for automated (computational) approaches not subject to subjective observer biases and assumptions has been profoundly lacking throughout much of the history of astronomy, as well as the need for a way to categorise the morphologies of galaxies in a model independent way. One of the recent attempts to address these problems is the CAS (concentration, C, asymmetry, A, clumpiness, S) structural parameters designed by Conselice et al. (2003). These offer a physically motivated, non-parametric, and computational scheme to uniquely position galaxies in a 3-dimensional structural space dependent on the concentration, asymmetry and clumpiness of their light profiles.

At present, at high redshifts the clumpiness parameter (S) becomes incalculable due to high background noise and surface brightness dimming effects, and due to the limitations of the resolution of our images (of $\sim 0.3''$). As such, we constrain our analysis here to the C - A plane (or concentration - asymmetry plane), where these parameters require less high resolution and are in general affected much less by redshift effects. C and A are defined in detail in §A and in Conselice, Yang & Bluck (2009), as well as early definitions in Conselice et al. (2003). For the purposes of this chapter it should be sufficient to comment that A is a measure of the total global asymmetry of a galaxy, based on minimising the total residual left from subtracting a 180 degree rotation from the original galaxy image. A high numerical value of A indicates a large global asymmetry. C is a probe of the concentration of the light distribution and in particular is constructed from the logarithm of the ratio of the radii at which 80 % and 20 % of

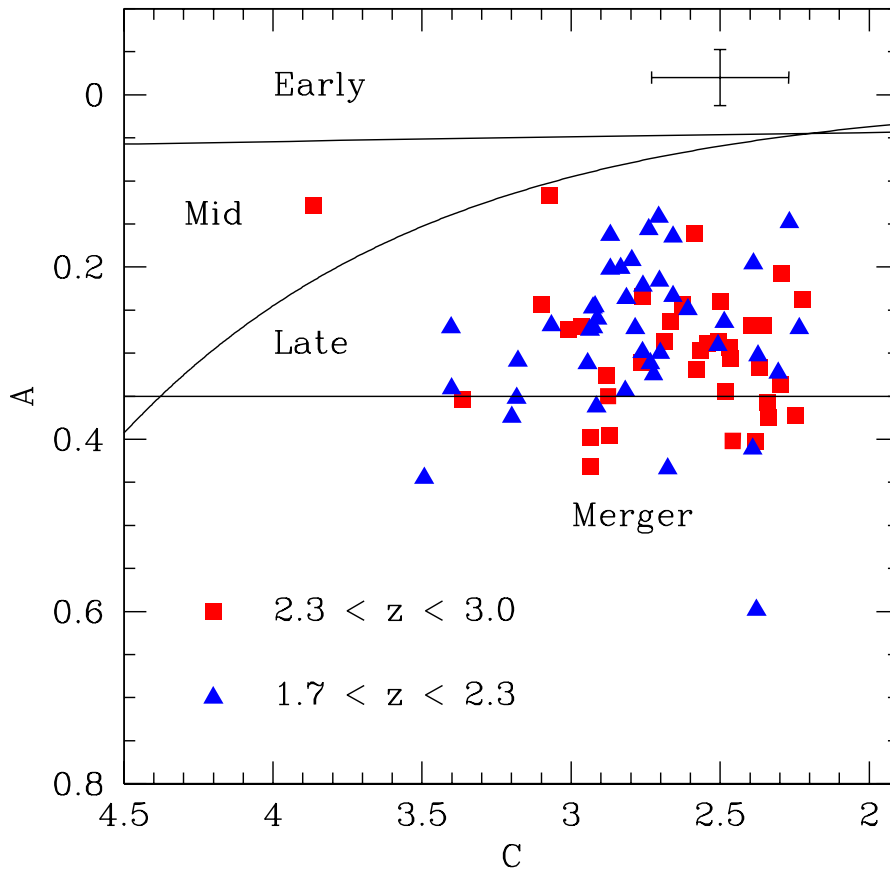


Figure 3.1: Asymmetry (A) plotted against Concentration (C) for the 82 massive ($M_* > 10^{11} M_\odot$) galaxies in our sample at $1.7 < z < 3$. The data is divided via redshift, as described on the plot, and the regions where different morphologies reside at $z = 0$ are also marked on the plot. The placing of almost all non-merging galaxies in the ‘late type’ regime is most probably an effect of all of these galaxies having some morphological disturbance (most likely via minor and sub-major merging), and should not be taken too seriously as a morphological classification, since these lines are drawn for $z = 0$ galaxies. The error bar displayed represents the average 1σ errors on the C and A parameters from the CAS code (Conselice et al. 2003).

the light of the entire galaxy (to the Petrosian radius) is contained. Higher values of C indicate more concentrated light profiles.

We plot where our massive galaxies lie in $C - A$ space in Fig. 3.1. Different morphologies of galaxies separate convincingly in the 3-dimensional $C - A - S$ space, with the most significant division for this chapter being the region where major merging galaxies tend to reside. In the next section we explore the CAS determined major merger history of massive galaxies.

3.3.1.1 Major Merger Fraction from Morphology

The classic rest frame optical definition for a CAS selected merger is (see Conselice 2003; Conselice, Yang & Bluck 2009):

$$A > 0.35 \quad \text{and} \quad A > S \quad (3.1)$$

That is, a merging system will have an asymmetry in excess of $A = 0.35$, and furthermore an asymmetry in excess of its clumpiness, S . This selection has a proven track record of cleanly finding major mergers, in the local Universe at least (see Conselice 2003, de Propris et al. 2007). At higher redshifts there are some additional complications (see Conselice, Yang & Bluck 2009 for a full discussion). Ultimately, the effect of limitations in the resolution of imaging with the HST NIC-3 camera (FWHM $\sim 0.3''$) significantly reduces our sensitivity to the high frequency clumpiness signal in very distant galaxies, in practice setting all S values more or less to zero. This means that the second criteria is irrelevant in practice as if $A > 0.35$ it is always greater than S at high z . This ensures that the asymmetry is a global property of the galaxy and not a result of, for example, clumpy star formation.

Furthermore, because we observe rest frame V to B band with our HST NICMOS H-band images at $z = 1.7 - 3$, we are probing the visible light and hence stellar population of the galaxies in question, not predominantly star formation as in many other high redshift studies, which frequently view similar high mass high redshift objects in optical light, which corresponds to rest frame UV. Thus, we have very high resolution imaging (from HST) and additionally see the established stellar population (not star formation) via observing in the near infra-red, making the HST GNS an ideal survey with which to probe the structures and morphologies of high redshift massive galaxies. Another high redshift effect may be to lower the observed asymmetry due to increased background noise, however, our own analysis through simulations of this effect are at best inconclusive. We find that there is perhaps a slight systematic trend to underestimate asymmetry (A) values at high redshifts even once care has been taken to compare equivalent rest-frame wavelengths. Nonetheless, it is conceivable that this effect is partially lost in the high scatter inherent from the random errors, i.e. the random errors

increase over the systematics. However, to be secure in our conclusions it is advisable to treat our A values as potential lower estimates at high redshifts, whereas to measure an A value *higher* than its true value at high redshifts would be very difficult to achieve. This is intuitive because the low spacial frequency light that A is most sensitive to is smoothed by surface brightness dimming. Nonetheless, if later studies come to suggest a reversal of this trend whereby asymmetry is overestimated at high z this would have a significant impact on our morphological results. Future work on interpreting CAS at high redshift is needed, but what follows in this chapter is a cautious first attempt, motivated and bolstered by early successes in simulation, and tethered by comparison to other tested methods, i.e. close pairs. In the future these methods can be applied to WFPC3 images from the HST with greater reliability and the potential to compare across different wavebands. We do not explore the morphologies of the HST ACS images, even though they are of higher resolution than our NICMOS imaging, for two reasons. First the ACS imaging is all in the rest-frame UV for our redshift objects and hence not representative of the underlying established stellar population's light profiles, hence, not appropriate for commenting on global asymmetry. And secondly, many of our galaxies are barely even visible in the ACS, showing up as point sources or very faint extended sources only. This point emphasizes the need to near infrared study of massive high redshift galaxies due to the lack of information acquirable in the observed optical and rest-frame UV. For now, our NICMOS imaging is the best available for this task.

We identify 18 out of 82 massive galaxies that fit the empirical definition of a CAS selected morphologically determined major merger, resulting in a total major merger fraction of $f_M(\text{CAS}) = 0.22 \pm 0.05$ at $1.7 < z < 3$. We further divide this redshift range up into two as in Bluck et al. (2009) to derive a merger fraction of $f_M(\text{CAS}) = 0.18 \pm 0.065$ (8 out of 44 galaxies) at $1.7 < z < 2.3$, and $f_M(\text{CAS}) = 0.26 \pm 0.08$ (10 out of 38 galaxies) at $2.3 < z < 3$. The errors are calculated by adding Poisson counting statistics to the maximum and minimum values of these fractions, given the CAS code 1σ errors, which are themselves based upon the accuracy of ascertaining the minimum centre for rotation. These values are plotted alongside the close pair derived merger fractions for the same galaxies, and the close pair + CAS merger fractions for lower redshift galaxies (from the POWIR Survey, see Conselice et al. 2007) in Fig. 3.2. Here

we add our latest morphologically determined merger fractions to the merger fraction history plot of Chapter 2 (Fig. 2.1), noting that there is close agreement (to within the 1σ errors) between CAS and close pair ($d < 30$ Kpc) major merger fractions at all redshift ranges probed, including at $z \sim 3$. This is most probably indicative of both approaches being sensitive to the underlying major merger history, with similar detection/merging timescales (see §2.4.4, Conselice, Yang & Bluck 2009 for a detailed discussion of this issue).

Furthermore, we witness no significant rise in merger fraction from morphologies, of $\sim 8 \%$ (with $\sim 1 \sigma$ significance) between our two highest redshift ranges, and note that this is smaller than the observed $\sim 2 \sigma$ increase observed in Chapter 2 through close pair methods for the same galaxy population. It is possible that at our highest redshift range we are experiencing a selection effect to effectively smooth our galaxies' light profiles, thus underestimating A . To know whether this is indeed the reason for this slight discrepancy we shall have to wait for even deeper and higher resolution rest frame optical space based or adaptive optics (AO) ground based imaging of distant massive galaxies, which will come in due course with planned WFC3 surveys, the JWST, and future 30 metre telescopes with advanced AO capabilities. For now it is sufficient to note that broadly speaking there is agreement between close pair and CAS methods of determining merger fractions, and that in both schemes there is a very high chance (4σ rise in f_m from $z = 0$ to $z = 3$ in both CAS and close pair methodologies) that the major merger fraction of massive galaxies was considerably higher at high redshifts than in the local Universe (as shown in Fig. 3.2).

3.3.1.2 A link between Asymmetry (A) and GALFIT Residual Flux Fraction (RFF)

Another procedure for defining the structures and morphologies of galaxies, from a parametric standpoint, is Sersic index fitting through, e.g., GALFIT (Peng et al. 2002). In this section we look for a possible link between the error in GALFIT fitting, the residual flux fraction (RFF), and the global asymmetry (A) of massive high redshift galaxies. Since GALFIT assumes a symmetric light profile one may expect that a poor GALFIT fit would be correlated with the total global asymmetry of the galaxy in ques-

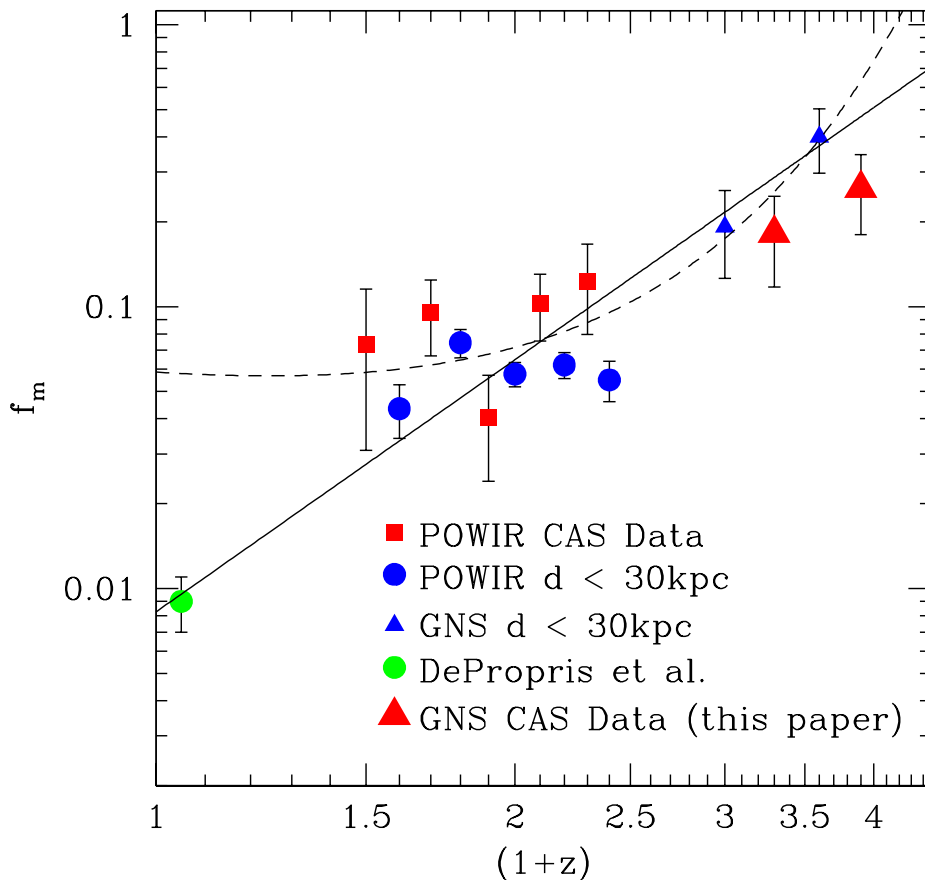


Figure 3.2: The major merger (f_m) evolution with redshift for massive ($M_* > 10^{11} M_\odot$) galaxies. This plot is taken from Bluck et al. (2009), where the major merger history of massive galaxies is probed using statistical close pair methods (at all z) and CAS morphologies (at $z < 1.5$). In this chapter we add the CAS morphology determined major merger fractions for the two highest redshift ranges, up to $z = 3$ (large red triangles). There is generally good agreement between CAS selected mergers and statistically determined close pairs (with $d < 30\text{ kpc}$) at all redshifts. Further, both methods agree that there is a rise in merger fraction with redshift, which is parameterised here by a simple power law best fit (solid line, with exponent = 3 ± 0.5) and power law exponential (dotted line), see Chapter 2 (Fig. 2.1) for further details on the fits. All displayed error bars are 1σ Poisson errors on the statistical counting.

tion. We investigate whether this is indeed the case for high redshift massive galaxies. Furthermore, a positive correlation here would serve as a useful sanity check on the basic reliability of both approaches, and be indicative of their potential complementarity in studying high redshift massive galaxies.

Our sample of massive galaxies have previously had their light profiles fitted with a Sersic index approach using the GALFIT package (see Peng et al. 2002). Early results concerning the size evolution of massive galaxies and crude morphological divisions between discs and spheroids in our sample, as well as details on the fitting techniques

used are presented in Buitrago et al. (2008). Specifically, the Sersic index and effective radii are obtained from fitting the the following formulae for the intensity of light at radii, r ,

$$I_r = I_e \text{dex} \left(-b_n \left[\left(\frac{r}{r_e} \right)^{1/n} - 1 \right] \right) \quad (3.2)$$

where I_e is the intensity of light at the effective radii, n is the Sersic index (with a value of $n = 4$ being equivalent to de Vaucouleurs' (1948) formula for an elliptical galaxy, and a value of $n = 1$ giving rise to an exponentially declining surface brightness profile appropriate for a disc like object). r_e is the circularised effective radius, given by $r_e = a_e(1 - \epsilon)^{1/2}$, where ϵ is the ellipticity and a_e is the semi major axis of the best fit ellipse to the galaxy light profile at the effective radius, r_e . b_n is a constant to be fit to the light profile.

The best fit Sersic profile is constructed via minimising the residuals, which are defined as the difference between the HST F160W (H) band image and the model fit. We quantify the residual flux fraction (RFF, see Blakeslee et al. 2006 and Hoyos et al. 2010), which is a proxy for 'badness of fit', as:

$$\text{RFF} = \frac{(\sum |Res| - 0.8 \times \sigma_{image})}{FLUX_{A_{2e}}} \quad (3.3)$$

where the summation is performed over the total area within the ellipse fit of the galaxy at two effective radii, A_{2e} . $|Res|$ is the absolute (modulus) value of the residual image, and $FLUX_{A_{2e}}$ is the total flux within the the area of the ellipse at two effective radii for the observed image. σ_{image} is defined as:

$$\sigma_{image} = \left(\sigma_{Bkg}^2 + \frac{F}{g} \right) \quad (3.4)$$

where g is the effective gain, F is the flux value from the model for each pixel, and σ_{Bkg} is the standard deviation of the background (noise) from the observed H band images.

The RFF statistic computes the fraction of light, present or absent in the residual image, which is not explained by empirical errors in the Sersic model (for more details

see Hoyos et al. 2010). This effectively equates to a measure of how poor each fit is. Since this type of fitting assumes an intrinsically symmetric profile to the light distribution of galaxies, it may be expected that it would not perform well on more asymmetric galaxies (or those with a high A value, as defined in §3.3.1). To investigate the possibility of a correlation here between poorness of GALFIT fitting (RFF) and asymmetry (A) in high mass high redshift galaxies, we plot these variables against each other in Fig. 3.3.

We find that there is a correlation between RFF and A , whereby galaxies with higher asymmetries tend to have worse fits from the GALFIT analysis. In fact we find that the mean value of A rises with 3σ significance from low to high RFF values, taking the errors as standard error on the mean and incorporating into this the intrinsic errors from the RFF and A methods. A best fit, least squares, simple power law to the unbanned data is found to be:

$$A = (0.28_{+/-0.13}) \times (1 + \text{RFF})^{1.6_{+/-0.7}} \quad (3.5)$$

This implies that asymmetry in the light profile of massive galaxies at high redshifts may be a significant impediment to the use of Sersic profile fitting for some systems. In these cases a non-parametric fit (such as CAS) will be superior, since it makes no underlying assumptions about the spatial symmetry of the galaxy light profile. Furthermore, this relation opens the possibility to potentially identify likely candidates for mergers via high RFF values. For example, we find that galaxies with $\text{RFF} > 0.05$ are ~ 4 times more likely to be mergers (as defined by CAS, see §3.3.1.1) than those with $\text{RFF} < 0.05$. From a KS test this represents a 3σ significant rise from low to high bins of RFF in A . However, there remains a high degree of scatter around the line of best fit, indicative of there being other reasons for poor GALFIT fits of high redshift massive galaxies than pure asymmetry through major merging or other morphological disturbance. This is most probably explained by the errors inherent in measuring CAS and the RFF, as very few galaxies lie further than 2σ from the best fit line.

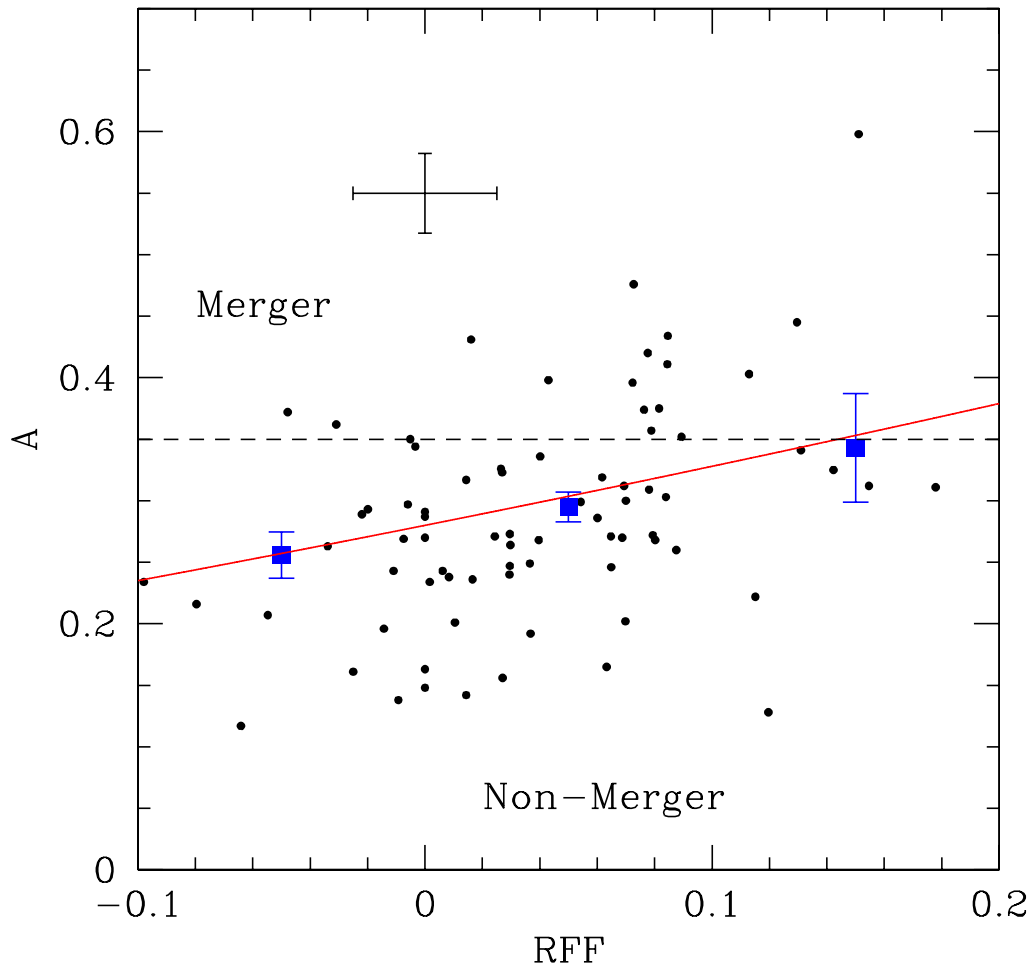


Figure 3.3: Asymmetry (A) vs. Residual Flux Fraction (RFF) from GALFIT Sersic index fitting, for our sample of massive ($M_* > 10^{11} M_\odot$) galaxies at $z = 1.7 - 3$. The black dots are the unbinned data, with the black error bar representing average 1σ errors on RFF and A . The blue squares represent mean values of A , in the RFF ranges $-0.1 - 0$, $0 - 0.1$, and $0.1 - 0.2$, with their corresponding error bars being 2σ errors on the mean in each case. The solid red line is a best fit simple power law to the unbinned data, which is defined in §3.3.1.2.

3.3.2 Minor Merger Fraction from Pair Statistics

Most probes of the merger histories of massive galaxies are considerably limited by constraints due to the depth of the imaging used. This is especially the case at higher redshifts. For this reason almost all merger histories in the literature (at least all those which extend beyond $z \sim 0.5$) are restricted to ‘major’ mergers. Although this definition varies from paper to paper, it is common to use difference such as ± 1.5 magnitudes ($\sim 1:4$ by mass) for close pairs, as in chapter 2 and Bluck et al. (2009), which corresponds to a similar mass regime for which CAS is most sensitive (see also Con-

selice, Yang & Bluck 2009 for a discussion of this). Due to the exceptionally deep HST NICMOS imaging we have acquired in the GNS, we are in a position to go much deeper, down to + 3.5 magnitudes at $z = 3$ and + 4.5 magnitudes at $z = 2.3$. This allows us to probe a mass range of up to a factor of ~ 100 , looking specifically at galaxies with masses $10^9 M_\odot - 10^{11.5} M_\odot$ around massive galaxies with $M_* > 10^{11} M_\odot$. Thus, in a sense, we can probe the minor merger history of massive galaxies as well as the major merger history.

We define the merger fraction, f_m , (in exact analogy to the major merger fraction of Chapter 2) to be:

$$f_m = \frac{1}{N} \sum_{i=1}^{i=N} (\text{counts}_i - \text{corr}_i) \quad (3.6)$$

where

$$\text{corr} = \int_{m-1.5}^{m+m^+} \rho \times \pi (r_{30kpc}^2 - r_{5kpc}^2) dm' \quad (3.7)$$

and N is the total number of massive galaxies in the sample at each redshift range, counts_i is the number of galaxies within the magnitude range $m - 1.5$ to $m + m^+$, contained within the annulus of 5 to 30 kpc ($h = 0.7$) around each massive host galaxy. We use $m - 1.5$ as the lower limit to our integral to assure that we count virtually all mergers down to the upper limit $m + m^+$. There are very few, if any, galaxies which are greater than 1.5 magnitudes brighter than the massive galaxies we probe at high redshifts, given that there are extremely few galaxies with $M_* > 10^{11.5} M_\odot$ at $z > 1.7$.

The value corr is the background correction, which we compute from the surface number density, ρ , of galaxies within the magnitude range under consideration, from our GNS survey. The fact that we take our surface number densities from the same survey (around the objects being studied at radii < 200 kpc), which is centred around massive galaxies at high redshifts, reduces the risk of our results being unduly affected by differential redshift projection effects due to the increased clustering of massive galaxies at high redshifts. This surface number density is then converted to an expectation value for the total number of close pairs one would measure by line of sight contamination, via multiplying over the area of sky contained within the annulus of 5 to 30 Kpc around

each massive host galaxy. We adopt this annulus method, as opposed to a simple circle approach, to avoid effects from the contamination of the light profiles of the merging galaxies by the host galaxy’s brightness (as in Chapter 2). Since these massive galaxies are extremely compact (see Buitrago et al 2008) we find an inner radii of 5 kpc to be more than sufficient to remove this effect.

We vary m^+ from 1.5 to 6.5 in increments of 1.5 (covering a mass ratio up to $M_{*host}/M_{*pair} \sim 100$), probing the major to minor merger fractions, and also probe an ultra-major merger fraction ($> 1:2$ by mass) of $m^+ = 0.5$. The results of this are plotted in Fig. 3.4. The vertical dotted lines indicate the completion limits for each redshift range probed from the GNS (see Conselice et al. 2010 for full details on deducing our mass and magnitude completion thresholds). Essentially we compare our number counts of galaxies at differing magnitudes to those of the much deeper HDF, and conclude that our limits are where these curves cease to agree closely. An early estimate (which continues to be fairly close to the actual value) is from the integration time calculator of the HST NICMOS-3 camera in H-band, setting a 5σ detection limit for our total integrated exposure times. As a sanity check we note that the merger fraction vs. magnitude range plot levels off at the completion limits as one would expect. We, therefore, witness a rise in merger fraction with magnitude range out to the completion limits. We note that the major and minor pair systems are in general different populations, with only $\sim 15\%$ of major mergers also being identified with minor merging. We also present a rough guide to the masses of objects included, at the top of Fig. 3.4. This is computed by assuming a mass-to-light ratio of $\sim 2.5 : 1$ ($H_{AB} : \lg(M_*)$), and a mean stellar mass for host galaxy of $M_* \sim 10^{11} M_\odot$.

We fit the merger fraction dependence on magnitude range, up to the respective completion limits (of + 3.5 at $z = 3$ and + 4.8 at $z = 2.3$). At $2.3 < z < 3$ we find the merger fraction dependence on magnitude range to be:

$$f_m(\delta H_{AB}) = (0.12 + / - 0.07) \times (1.5 + \delta H_{AB})^{0.91 + / - 0.35}, \quad (3.8)$$

at $1.7 < z < 2.3$ we find a slightly steeper dependence of:

$$f_m(\delta H_{AB}) = (0.04+/-0.03) \times (1.5 + \delta H_{AB})^{1.24+/-0.37}. \quad (3.9)$$

Assuming a mass-to-light ratio, the above equations may be converted to the merger fraction dependence on mass range (δm_*). We use a mass-to-light ratio of 2.5 : 1 ($H_{AB} : \lg(M_*)$), and take $\delta m_* = 11.5 - \log(M_*[M_\odot])$. Thus, at $2.3 < z < 3$ we find a merger fraction dependence on mass range for massive galaxies of:

$$f_m(M_*) = (0.28+/-0.17) \times \delta m_*^{0.91+/-0.35} \quad (3.10)$$

and at $1.7 < z < 2.3$ we find a merger fraction dependence on mass range for massive galaxies of:

$$f_m(M_*) = (0.12+/-0.09) \times \delta m_*^{1.24+/-0.37}. \quad (3.11)$$

This gives a prescription for deducing the probable total number of minor mergers from extrapolation of these trends, via the following methodology. The total number of mergers, within a given mass and redshift range, is given by calculating the double integral:

$$N_m = \int_{M_1}^{M_2} \int_{t_1}^{t_2} \frac{1}{\Gamma(z, M_*)} dt dM_* \quad (3.12)$$

$$= \int_{M_1}^{M_2} \int_{z_1}^{z_2} \frac{1}{\Gamma(z, M_*)} \frac{t_H}{(1+z)} \frac{dz}{E(z)} dM_* \quad (3.13)$$

where,

$$\Gamma(z, M_*) = \frac{\tau_m(M_*)}{f_{gm}(z, M_*)} \quad (3.14)$$

and

$$f_{gm}(z, M_*) = \frac{2 \times f_m(z, M_*)}{1 + f_m(z, M_*)}. \quad (3.15)$$

$\Gamma(z, M_*)$ is the characteristic time between mergers, t_H is the Hubble time, $f_m(z, M_*)$ is the merger fraction, $f_{gm}(z)$ is the galaxy merger fraction (i.e. the number of galaxies merging, not the total number of mergers), $\tau_m(M_*)$ is the merger timescale (which we assume to be redshift invariant), and the parameter $E(z) = [\Omega_M(1+z)^3 + \Omega_k(1+z)^2 + \Omega_\Lambda]^{1/2} = H^{-1}(z)$.

We construct a rough minor merger fraction dependence on redshift by extrapolating a line of best fit to the merger fraction (derived at $\log(M_*) \sim 9$) from our two redshift points, finding:

$$f_{gm}(z)|_{M_* > 10^9 M_\odot} = 0.20 + / - 0.11 \times (1+z) \quad (3.16)$$

By integrating between the redshift limits probed in our survey ($z = 1.7 - 3$) in eq. 3.13 we find that an average massive ($M_* > 10^{11} M_\odot$) galaxy will experience on average $N_m = (1 \pm 0.4 / \tau_m(M_*)[\text{Gyrs}])$ mergers with galaxies with $M_* > 10^9 M_\odot$ over the redshift range $z = 1.7 - 3$, and a total of $N_m = (4.5 \pm 2.1) / \tau_m(M_*)[\text{Gyrs}]$ mergers with $M_* > 10^9 M_\odot$ galaxies from $z = 3$ to the present, via extrapolation of the trend. This value should be taken with more caution as we do not probe directly the $z = 0 - 1.7$ minor merger history. We factor the merger timescale $\tau_m(M_*)$ out of our calculations (assuming that it is redshift independent) as this is poorly known for the mass range of galaxies probed in this chapter. However, as a rough guide, Lotz et al. (2008, 2010) suggest that this might be ~ 0.4 Gyr for 3:1 mass mergers, and ~ 1 Gyr for 9:1 mass mergers from N-body simulations. This appears to be roughly a logarithmic dependence of timescale on stellar mass, suggesting that at 1:100 $\tau_m \sim 2 - 3$ Gyrs.

In order to calculate the stellar mass increase due to these major and minor mergers, we must compute an average mass increase per merger. This is computed via the weighted mean from fits to the merger fraction dependence on mass range (Fig. 3.4 and eqs. 3.10 and 3.11). Thus:

$$\frac{\langle \Delta M_* \rangle}{N_m} = \frac{1}{z} \sum_{i=0}^{i=z} \left(\frac{\int_{M_1}^{M_2} M_* f_m(z, M_*) dM_*}{\int_{M_1}^{M_2} f_m(z, M_*) dM_*} \right) \quad (3.17)$$

where we take the average redshift value of $f_m(z, M_*)$ from $z = 0 - 3$, integrated over our mass range of $10^9 - 10^{11.5} M_\odot$. We find $\langle \Delta M_* \rangle / N_m = (6.2 \pm 2.5) \times 10^{10} M_\odot$.

In the redshift range probed directly by the GNS ($z = 1.7 - 3$), this corresponds to an average massive galaxy experiencing a mass increase of $\langle \Delta M_* \rangle = (6.2 + / - 3.2) / \tau_m(M_*) [\text{Gyrs}] \times 10^{10} M_\odot$. This leads to a total stellar mass increase over the past ~ 12 Gyrs ($z = 3 - 0$) from extrapolation, due to $M_* > 10^9 M_\odot$ mergers, with massive ($M_* > 10^{11} M_\odot$) galaxies, of $\langle \Delta M_* \rangle = (2.8 + / - 1.6) / \tau_m(M_*) [\text{Gyrs}] \times 10^{11} M_\odot$. A good first order approximation to the actual value of $\tau_m(M_*)$ will be to take its value at our average mass of merger of $\sim 5 \times 10^{10} M_\odot$, i.e ~ 1 Gyr from N-body simulations in Lotz et al. (2010). When compared to the major merger stellar mass increase, computed in Bluck et al. (2009), of $(1.7 + / - 0.5) \times 10^{11} M_\odot$, this suggests that minor mergers contribute a similar amount or slightly less stellar mass than major mergers from $z = 3$ to the present, with a minor merger stellar mass increase of $\sim 10^{11} M_\odot$. It is still, however, possible that ultra-minor mergers of massive galaxies with $M_* < 10^9 M_\odot$ galaxies will be so numerous that they will significantly effect the mass increase of massive galaxies, although this seems very unlikely given the trends and analyses presented in this chapter, and the longer timescales they will experience due to larger differences in mass ratio.

3.4 Discussion

3.4.1 Mergers

In this chapter we have utilised several different methods to probe the structures and evolution of massive galaxies over cosmic time. First, it is important to acknowledge that there are massive galaxies at $z > 2$, but their properties are somewhat different to local massive galaxies. The most prominent difference is that these massive galaxies tend to have smaller effective radii for their masses and hence higher surface brightness than more local equivalents. We find that $\sim 1/4$ of all massive galaxies (with $M_* > 10^{11} M_\odot$) are highly morphologically disturbed at $1.7 < z < 3$, and in fact fit the rest frame optical definition for a CAS selected merger (see §3.3.1). This implies that major merging is an important factor in the evolution of massive galaxies, and qualitatively supports a hierarchical approach to galaxy formation. Moreover, we find remarkable accord between ($d < 30$ kpc) close pair fractions and CAS merger fractions at all

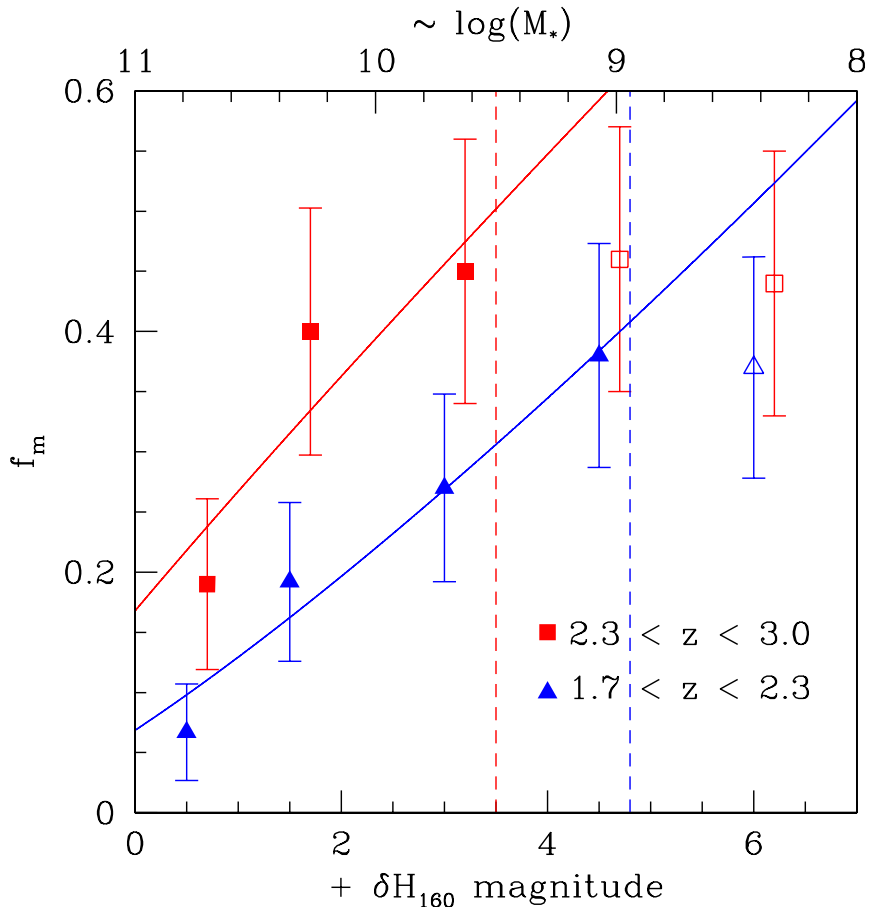


Figure 3.4: The Merger Fraction (f_m) as a function of magnitude range ($+\delta H_{160}$) and stellar mass sensitivity threshold ($\log(M_*)$) for massive galaxies (with $M_* > 10^{11} M_\odot$). The data points are separated into two redshift ranges as displayed on the plot. The error bars displayed are 1σ Poisson errors on the statistical counting. The vertical dotted lines indicate the completeness limits for each redshift range, respectively. Solid symbols indicate merger fractions computed where we are complete, and open symbols indicate merger fractions computed where we are incomplete. The solid lines are best fit simple power law functions to the merger fraction dependence on mass/magnitude range for each redshift range (see §3.3.2 for further details).

redshifts, up to $z = 3$ (see Fig. 3.2). This strongly suggests that both approaches trace the underlying major merger activity in massive galaxies, and, furthermore, implies that the timescales involved in each approach must be similar (also see §2.4.4 and Conselice, Yang & Bluck 2009 for a discussion of this effect at lower redshifts). To understand this further, it is pertinent to note that close pair approaches trace merging *before* the event, and CAS selected morphological methods trace merging during and *after* the event. Thus, what does it mean to suggest that the timescales are roughly equivalent?

If close pair methods accurately trace merger activity in massive galaxies, they work by

making use of a probability distribution. In order for two galaxies to merge they must be close in six dimensional phase space. Now, with a close pair approach one only measures directly two spatial dimensions, and correct for the third spacial dimension via computing the expectation value for the number of galaxies in a given area of sky, based on surface number density of the survey in question (see §3.3.2). Therefore, no direct knowledge is acquired concerning the relative velocity of the two galaxies. Consequently, one must assume a spread of plausible velocity differences in order to compute merger timescales, and, hence, whether or not any given close pair will actually merge (see e.g. Lotz et al. 2008a,b and 2010), as a merger timescale less than the Hubble time will define in principle a *future* merger via the close pair method. However, in general, the higher the initial separation, the larger the merger timescale, and the lower the probability that the two galaxies will merge. Also, at very large apertures for the close pair methods, one will simply recover the background correction and hence the merger fraction will tend to zero. To bring all of this together, what this means is that there should be an optimal aperture size to utilise, and we suggest here that this is ~ 30 kpc for massive galaxies. The reason for this is that there is close accord with CAS, at all redshifts, suggesting that the number of close pairs at this distance correlates closely to the actual number of major mergers.

Due to the exceptional depth and resolution of our HST GNS imaging, and because we observe galaxies in the rest frame optical (V-band) we have high confidence in our morphological (CAS) methods. Moreover, this allows us to extend the work performed in Chapter 2 on the major merger fraction and evolution of massive galaxies via close pair methods, to their minor merger fraction evolution (see §3.3.2). As commented on above, there is a close accord between 30 kpc pairs and actual mergers, and in view of this we adopt the same aperture to detect minor mergers, though note that the timescales will be different here due to the unequal mass distribution. We find that the total merger fraction scales roughly linearly with magnitude (and hence stellar mass) range, with an exponent $\sim 0.9 - 1.3$ across the redshifts probed in this chapter.

From this we compute the total number of mergers a massive galaxy ($M_* > 10^{11} M_\odot$) will experience with other galaxies with $M_* > 10^9 M_\odot$, finding this to be $N_m \sim 4.5 / \tau_m$, where τ_m is the merger timescale, thought to vary between $\sim 0.4 - 2$ Gyr through-

out our mass range sensitivity (see Lotz et al. 2010), with mass ratios closer to unity having shorter timescales than systems with mass ratios higher or lower than this (also see Lotz et al. 2010). This corresponds to a total mass increase of $\Delta M_* \sim 3 \times 10^{11} M_\odot$ from $z = 3$ to the present. When compared to the total mass increase due to major mergers computed in Chapter 2 of $\Delta M_* \sim 2 \times 10^{11} M_\odot$ from $z = 3$ to the present, this suggests that minor mergers are similarly significant to major mergers in the mass increase of massive galaxies, contributing $\sim 1/3$ of the total mass difference over the past 11.5 Gyrs. Whilst it is possible that mergers with galaxies with $M_* < 10^9 M_\odot$ may be so numerous that they could still contribute even more significantly to the total mass increase, this possibility does seem extremely unlikely, especially considering the fact that as the mass difference between merging galaxies increases, so does the merger timescale. Finally, by way of comparison, this level of mass increase agrees favourably with studies of the evolution of the mass function of massive galaxies from $z = 3$ to the present, see e.g. Mortlock et al. (2010, in prep.).

By way of comparison to other means of galaxy mass increase, we compare our merger driven stellar mass increase to the stellar mass increase observed in Dickinson et al. (2003) from the Hubble Deep Field - North. Dickinson et al. find that massive galaxies can grow by up to a factor of ten in mass between $z = 3$ and the present. This suggests that star formation may result in as much, or even more, stellar mass growth to that of merging in the major and sub-major regime (explored in this chapter). This type of mass increase would lead our population of galaxies to end up as the most massive galaxies in the Universe by present times, some of which doubtless becoming brightest cluster galaxies (BCGs). It is most probable that our population of massive galaxies will move from group to cluster environments over cosmic time and moreover end their lives at the centre of these clusters as very bright, very massive systems.

3.4.2 Size Evolution

Numerous studies over the past five years have found increasingly compelling evidence for dramatic size evolution of massive galaxies over the past ten or so billion years (e.g. Carasco et al. 2010, van Dokkum et al. 2010, Cimatti et al. 2008, Buitrago et al. 2008, Trujillo et al. 2007). It is currently widely argued that massive galaxies may grow

in size by up to a factor of five since $z = 3$, resulting in a colossal volume increase of at least a factor of 50. Whilst there are still concerns that some (or all) of this apparent size evolution may be driven by inaccurate Sersic fitting of massive galaxies at high redshifts, due to a number of factors including surface brightness dimming effects, a wealth of evidence from simulation, and observational attempts to break the degeneracies inherent in former approaches, are coming to establish the validity of this result. If this size evolution is real (and not an artifact from our Sersic fitting), then it becomes of vital importance in contemporary astrophysics to address the question: *What drives the size increase of massive galaxies over cosmic time?*

Naab et al. (2009) and Khochfar & Silk (2006) have both argued from a theoretical standpoint for merger driven size evolution of massive galaxies. We have, in this chapter, also computed the merger history of massive galaxies with $M_* > 10^9 M_\odot$ galaxies (see §3.4.1). Thus, there are ~ 4.5 mergers predicted from $z = 3$ to the present, which may go some way to explaining the observed size evolution of massive galaxies. In fact, arguments presented in Naab et al. (2009) suggest that a mass increase due to minor and major mergers of a factor of three (as predicted in this chapter), could lead to size evolution of up to a factor six in radii. The more mergers there are the greater the size evolution, thus a mass increase of a given magnitude will be more effective at increasing the size of the resultant galaxy if it is imparted in a series of minor mergers rather than one major mergers. Thus it is the relatively high fraction of mass imparted by minor mergers which is most useful for increasing a massive galaxy's size. The minor and major merger history witnessed in this work is large enough to explain the entire growth witnessed in massive galaxies across the past 12 billion years (e.g. Trujillo et al. 2007, Buitrago et al. 2008) according to recent theoretical estimation (Naab et al. 2009). From this, it seems most plausible that the size evolution of massive galaxies is predominantly driven by merging. It is, however, worth considering other contributive factors, such as the effect of the enormous outpouring of energy from supermassive black holes in the nuclei of massive galaxies over this same period of cosmic history (see Bluck et al. 2010a, Fan et al. 2008 and Chapter 4). It may yet prove probable that it is a combination of passive evolution, major and minor merging, and AGN 'puffing up' which causes the size evolution of massive galaxies. This work, however, implies that merging by itself could be responsible, assuming the validity of

the arguments presented in Naab et al. (2009) and the right gas fractions and mass ratios of the mergers, which are yet to be fully empirically deduced.

3.5 Summary and Conclusions

In this chapter we have studied in detail the structures, morphologies, minor mergers and evolution of a population of 82 extremely massive ($M_* > 10^{11} M_\odot$) galaxies at very high redshifts ($1.7 < z < 3$). We find that massive galaxies at high redshifts are frequently morphologically disturbed, with $\sim 1/4$ meeting the criteria for a CAS selected major merger (see §3.3.1). Furthermore, we note that close pair methods (with $d < 30$ kpc) to deduce major mergers find close accord with morphological CAS determined major mergers at all redshifts, up to $z = 3$, indicative of both approaches being sensitive to the underlying merger history, and, moreover, having similar mass ratio and timescale sensitivities (see §2.4.4 and §3.4.1 for a discussion).

We note that the ‘poorness’ of GALFIT fitting (RFF) is positively correlated with the global asymmetry of the galaxy (A) for high redshift massive galaxies, see §3.3.1.2. Moreover, we find that galaxies with GALFIT fits defined as ‘poor’ ($RFF > 0.1$) are over 4 times more likely to be highly asymmetric systems (with $A > 0.35$) than those galaxies with ‘good’ ($RFF < 0.1$) fits, which suggests that Sersic index fitting can be used to select likely major merger candidates through analysis of the RFF. However, the high degree of scatter about this correlation should provide a cautionary reminder that there are most likely other reasons for ‘poor’ GALFIT fits than solely global asymmetry (A) at high redshifts.

We go on to investigate the minor merger properties of our sample of massive galaxies, down to a mass sensitivity threshold of $M_* = 10^9 M_\odot$. In order to achieve this we utilise extremely deep and high resolution H band imaging from the HST GOODS NICMOS Survey, which corresponds to rest frame optical wavelengths at the redshifts probed in this chapter ($z = 1.7 - 3$). We deduce that there are in total $N_m = (4.5 \pm 2.1) / \tau_m$ mergers from $z = 3$ to the present, which leads to massive galaxies growing in mass by a factor of ~ 3 due to all mergers, with $1/3$ of this mass increase being driven by minor mergers with galaxies of mass $M_* = 10^9 - 10^{10.5} M_\odot$. We go on to suggest

that the size increase over cosmic time of massive galaxies could be driven by these mergers, noting that the number of mergers we compute for massive galaxies (and their resultant approximate threefold mass increase) could correspond to a size increase of up to a factor of six via the Naab et al. (2009) model.

In conclusion, we find that massive galaxies are more asymmetric at high redshifts, have many more minor and major mergers at early times than late times, and grow in mass threefold from $z = 3$ to the present due to merging alone. We also suggest that the size evolution of massive galaxies seen elsewhere must be partly (or possibly entirely) driven via this galaxy merging.

Chapter 4

On the co-evolution of supermassive black holes and their host galaxies since $z = 3$

The work in this chapter is published as: Bluck et al. (2010a)

This Chapter is based on work I led, in collaboration with Christopher J. Conselice¹, Omar Almaini¹, Elise Laird², Kirpal Nandra¹ and Ruth Gruetzbauch¹.

¹ Centre for Astronomy and Particle Theory, School of Physics and Astronomy, University of Nottingham, Nottingham NG7 2RD, UK

²Astrophysics Group, Imperial College London, Blackett Laboratory, Prince Consort Road, London SW7 2AZ, UK

Abstract

To investigate the evolution in the relation between galaxy stellar and central black hole mass we identify a population of 508 X-ray selected AGN (Active Galactic Nuclei) at $0.4 < z < 6$ residing within host galaxies with stellar masses in the range $10^{10} M_{\odot} < M_{*} < 10^{12} M_{\odot}$. From this sample we construct a volume limited complete sample of 85 AGN with host galaxy stellar masses $M_{*} > 10^{10.5} M_{\odot}$, and specific X-ray luminosities $L_X > 2.35 \times 10^{43} \text{ erg s}^{-1}$ at $0.4 < z < 3$. We calculate the Eddington limiting masses of the supermassive black holes (SMBHs) residing at the centre of these galaxies, and observe an increase in the average Eddington limiting black hole mass with redshift. While the black hole mass and Eddington ratio ($\mu = L_{bol}/L_{Edd}$) are degenerate, if we assume that the local $M_{BH} - M_{*}$ relation holds at all redshifts we find that the mean Eddington ratio μ rises from 0.056 ± 0.010 at $z = 0.7$ to 0.087 ± 0.011 at $z = 1.25$, with no significant evolution thereafter to $z = 3$.

Alternatively, by assuming that there is no evolution in μ and then that there is maximum possible evolution to the Eddington limit, we quantify the maximum possible evolution in the M_{*}/M_{BH} ratio as lying in the range $700 < M_{*}/M_{BH} < 10000$, compared with the local value of $M_{*}/M_{BH} \sim 1000$. We furthermore find that the fraction of galaxies which are AGN (with $L_X > 2.35 \times 10^{43} \text{ erg s}^{-1}$) rises with redshift from $1.2 \pm 0.2 \%$ at $z = 0.7$ to $7.4 \pm 2.0 \%$ at $z = 2.5$. We use our results to calculate the maximum timescales for which our sample of AGN can continue to accrete at their observed rates before surpassing the local galaxy-black hole mass relation. We use these timescales to calculate the total fraction of massive galaxies which will be active (with $L_X > 2.35 \times 10^{43} \text{ erg s}^{-1}$) since $z = 3$, finding that at least $\sim 40\%$ of all massive galaxies will be Seyfert luminosity AGN or brighter during this epoch. Further, we calculate the energy density due to AGN activity in the Universe as $1.0 (\pm 0.3) \times 10^{57} \text{ erg Mpc}^{-3} \text{ Gyr}^{-1}$, potentially providing a significant source of energy for AGN feedback on star formation. We also use this method to compute the evolution in the X-ray luminosity density of AGN with redshift, finding that massive galaxy Seyfert luminosity AGN are the dominant source of X-ray emission in the Universe at $z < 3$.

4.1 Introduction

One of the major unresolved questions in observational astrophysics is the role of supermassive black holes (SMBHs) in the evolution of galaxies. For over a decade the existence of SMBHs in the centre of massive galaxies has been established (e.g. Kormendy & Richstone 1995), but the impact they have on their host galaxies is still hotly debated. In the local Universe relations between the mass of the SMBH and the luminosity of the host galaxy have been discovered (Kormendy & Richstone 1995), as well as tighter relations between the SMBH mass and velocity dispersion, and hence mass, of the hosting bulge or spheroid (Ferrarese & Merritt 2000, Marconi & Hunt 2003, Haring & Rix 2004). These relationships indicate a causal link between galaxies and the SMBHs that reside within them. However, the nature of this interdependence and its origin remain open issues in the field. A classic crucial question is: which evolves first, the host galaxy or its SMBH? This fundamental ‘chicken and egg’ question can be resolved by measuring the masses of SMBHs at higher redshifts and investigating whether they follow the local $M_{BH} - M_*$ relationship, and if not, quantifying how they differ from it.

SMBHs are thought to be a near ubiquitous component of massive galaxies (e.g. Ueda et al. 2003, Barger et al. 2005) although the exact fraction of massive galaxies that contain SMBHs is still unknown, especially at higher redshifts. One probe of the evolution of SMBHs is to look at the X-ray luminosity function (XLF) and examine how it evolves with redshift (Ueda et al. 2003, Hasinger et al. 2005, Barger et al. 2005, Aird et al. 2009). These studies demonstrate that there is a steep positive evolution of the XLF with redshift out to $z \sim 1.2$, followed by a less steep decline with redshift thereafter at even higher z . Studies disagree on whether there is evolution in the fundamental shape of the XLF, but all agree that there is evolution in the X-ray luminosity density with redshift. As such, SMBHs are known to be dynamic objects, subject to effects from the evolution of their host galaxies. In order to probe the evolution of AGN over cosmic time one must be careful to compare populations that are fundamentally linked. With XLF studies one considers a range of X-ray luminosities and quantifies the evolution within this range, often ignoring the characteristics of the underlying host galaxy population. In this chapter, we restrict our sample of AGN to those with

optical - NIR detected host galaxies with well determined redshifts and stellar masses, allowing us to link objects at different redshifts for comparison via the stellar masses of their host galaxies.

Measuring the mass of a SMBH, however, is not trivial. Often the most robust methods involve a virial mass estimation technique (see e.g. McLure & Dunlop 2002), whereby one acquires detailed spectroscopy of the central most region of a galaxy and use the assumption of a virialised system to estimate the SMBH mass from the broadening of spectral lines. The mass contained within a radius R is $M(< R) \sim R\sigma^2/G$. The value of σ can be deduced directly from the FWHM (full width half maximum) of any broad line emission (most commonly H_β). More challengingly, the radius at which the broad line emitting region resides must be known in this method. This can be deduced from the time delay between line emission from the accretion disc and re-emission from the broad line emitting region, in orbit around the disc. Thus, $R \sim c\tau$, where τ is the time delay. This is only possible to measure in nearby systems with any accuracy, due to the high resolution required in this method. Fortunately, an empirical relationship has been demonstrated to exist (e.g. McLure & Jarvis 2002, Willott, McLure & Jarvis 2003, Woo et al. 2008) between the monochrome luminosity of the 3000 Å line and the radius of the broad line emitting region. Nonetheless, even this method requires good spatial resolution, and a bright (most often quasar) source for anything but the most local AGN (active galactic nuclei).

In order to estimate the SMBH mass of a distant Seyfert-luminosity active galaxy, one may employ Eddington arguments by setting the outward radiative force equal to the inward force of gravity. Essentially this method gives a minimum value to the black hole mass given the luminosity of its accretion disc (see e.g. Alexander et al. 2009). Essentially $M_{BH} \propto \mu L_{Bol}$, with μ being a constant term related to the efficiency of the SMBH. In the local Universe, at $z < 0.2$, $\mu \sim 0.05$ (see e.g. Marconi et al. 2009), implying that the average SMBH in the local Universe is accreting matter at $\sim 5\%$ of the Eddington maximum. The bolometric luminosity of the accretion disc may be calculated by employing a measured X-ray specific luminosity and utilising a spectral energy distribution. Naturally, these Eddington based methods are less reliable for calculating the mass of the central black hole because they contain an efficiency

degeneracy. Therefore, one can trace the evolution of the black hole mass only with assumptions about the evolution of the efficiency and vice versa. However, for representative AGN at intermediate to high redshifts ($z > 1$) the Eddington method is often the only method for calculating SMBH masses for more than a few galaxies as it does not depend on obtaining very high resolution spectroscopy which frequently cannot be obtained, especially for lower luminosity AGN.

In this chapter we calculate the Eddington limiting (minimum SMBH) mass for 508 X-ray active galaxies with known stellar masses and spectroscopic or photometric redshifts, taken from the GOODS and Extended Growth Strip fields. We utilise deep X-ray data from the Chandra X-ray Observatory (hereafter Chandra) and optical to near infrared data from the Hubble Space Telescope (HST) NICMOS and ACS cameras, the Palomar Observatory and a host of other ground based observatories, including the CFHT, VLT and Keck observatories. We construct from this data set a volume limited sample of 85 ‘Seyfert’ galaxies with specific hard band luminosities $L_X > 2.35 \times 10^{43} \text{ergs}^{-1}$ and host galaxy stellar masses in the range $10^{10.5} M_\odot < M_* < 10^{12} M_\odot$ (selected to be not point like), where we are complete to $z = 3$. We use this sample to probe the evolution of the $M_{BH} - M_*$ relationship with redshift, and to compute the total active fraction (at bright ‘Seyfert’ luminosities) of massive galaxies over the past 11.5 billion years.

This chapter is structured as follows: §4.2 outlines the sources of our data and measures of photometric redshifts and stellar masses, §4.3 outlines the major sources of random and systematic error or biases affecting this work, and what we have done to parameterise and minimise their effects. §4.4 outlines our methods, including explanation of how we deduce lower limits to black hole masses. §4.5 presents our results in detail, as well as presenting a novel method for calculating AGN lifetimes. §4.6 encompasses a discussion of our results, with §4.7 summarising our conclusions. Throughout the chapter we assume a Λ CDM Cosmology with: $H_0 = 70 \text{ km s}^{-1} \text{ Mpc}^{-1}$, $\Omega_m = 0.3$, $\Omega_\Lambda = 0.7$, and adopt AB magnitude units.

4.2 Data and Observations

We utilise near-infrared and optical data from the GOODS ACS and NICMOS galaxy Surveys (ACS, Dickinson et al. 2003; GNS, Conselice et al. 2010), the Palomar Observatory Wide-field Infra-Red (POWIR) galaxy Survey (Conselice et al. 2007, 2008, and Davis et al. 2007), and complementary surveys based in the GOODS field and Extended Growth Strip (EGS). Additionally, we compare these observations to X-ray catalogs from the Chandra Deep Field North / South (CDF-N/S, Alexander et al. 2003, Luo et al. 2008), and the AEGIS-X survey (Laird et al. 2009). In so doing we construct two samples: an ‘AGN’ sample where we are not complete (with all NIR galaxy - X-ray source matches within a $1.5''$ radius for hard band X-ray luminosities $L_X > 10^{42}$ erg s $^{-1}$ in galaxies with stellar masses $M_* > 10^{10} M_\odot$; and a volume limited sample of ‘Seyfert’ galaxies (defined to be not-point-like AGN with hard band X-ray luminosities $L_X > 2.35 \times 10^{43}$ erg s $^{-1}$ in host galaxies with stellar masses $M_* > 10^{10.5} M_\odot$) where we achieve completion to $z = 1.5$ in the EGS field and $z = 3$ in the GNS fields. In general we use the first, and larger, sample to probe intrinsic AGN properties, and the volume limited sample to probe the redshift co-evolution of SMBHs and their host galaxies in the ‘Seyfert’ luminosity regime.

4.2.1 Near Infrared Data

We utilise the POWIR survey in the EGS field to obtain redshifts and stellar masses for a large sample of galaxies and, after matching with Chandra data, our sample of AGN hosts out to redshifts of $z = 1.5$. The POWIR Survey obtained deep K and J band imaging over ~ 1.52 deg 2 in the EGS (see Fig. 4.1 for an illustration). Limiting magnitudes reached in the K band are typically 22.5 - 23 (5σ) over the entire area. In total $\sim 20,000$ galaxies were imaged between $z = 0.4$ and $z = 2$. Photometric redshifts were calculated for these galaxies using optical (CFHT) + NIR (Palomar) imaging in the BRIJK bands (see Conselice et al. 2008 for a detailed discussion of these, and §4.2.2 for further details). From this stellar masses were estimated by fitting spectral energy distributions with Bruzual & Charlot (2003) stellar population synthesis models, with varying star formation histories. Resulting stellar mass errors are $\sim 0.2 - 0.3$

dex (see Conselice et al. 2007 and §4.2.3 for further details). We are complete down to $M_* = 10^{10.5} M_\odot$ at $z = 1.5$. For full details on the selection, photometry, redshift and stellar mass calculations see Conselice et al. (2007 and 2008) and §4.2.2 and 4.2.3. Also see §4.3.2 for a discussion of possible sources of systematic errors on photometric redshifts and stellar masses.

We utilise data from the ultra-deep ‘pencil beam’ HST GOODS ACS and GNS surveys to obtain masses and photometric redshifts for galaxies at high redshifts ($1.5 < z < 3$) in the GOODS North and South fields (see Fig. 4.2). We use published masses and photometric redshifts (see Dickinson et al. 2003, Giavalisco et al. 2004) for the large AGN sample, but restrict for our volume limited sample the area probed to that covered additionally by the GNS, where we have much deeper imaging in the H-band and higher mass completion. The GOODS NICMOS Survey images a total of ~ 8000 galaxies in the F160W (H) band, utilising 180 orbits and 60 pointings of the HST NICMOS-3 camera (see Fig. 4.2 for a depiction of the pointings). These pointings are centred around massive galaxies at $1.7 < z < 3$ to 3 orbits depth. Each tile ($51.2'' \times 51.2''$, $0.203''/\text{pix}$) is observed in 6 exposures that combine to form images with a pixel scale of $0.1''$, and a point spread function (PSF) of $\sim 0.3''$ full width half maximum (FWHM). The total area of the survey is $\sim 43.7 \text{ arcmin}^2$. Limiting magnitudes reached are $H = 26.5$ (10σ). We are complete down to $M_* = 10^{10} M_\odot$ at $z = 3$, to 10σ . The wealth of observational data available in the GOODS fields allows us to utilise data from the U to the H band in the determination of photometric redshifts (see §4.2.2 for further details). Multi-colour stellar population fitting techniques were utilised to estimate stellar masses to an accuracy of $\sim 0.2 - 0.3$ dex (see §4.2.3 for further details and §4.3.2 - 4.3.2 for a discussion on the errors involved in computing stellar masses for AGN at high redshifts). A selection bias is introduced due to our pointings being selected to maximise the number of massive galaxies imaged, whereby we witness higher surface densities of massive galaxies in the GNS than expected from imaging to a similar depth a randomly chosen area of sky. Where necessary we take account of this bias in our analyses (see e.g. §4.5.1).

Details of the techniques used for the GNS in constructing catalogs, photometric redshifts and stellar masses may be found in Buitrago et al. (2008), Bluck et al. (2009),

Gruetzbauch et al. (2010) and a more full account in Conselice et al. (2010), as well as further information in §4.2.2 - 4.2.3. A discussion of more robust error estimates on stellar masses can be found in Chapter 1 and Bluck et al. (2009), where it is concluded, through Monte-Carlo simulation, that systematic errors arising out of Poisson errors from the steepness of the stellar mass distribution (Eddington biases) do not result in a significant infiltration of lower mass objects. Further discussion on the use of the SExtractor package to produce galaxy catalogs is also provided in Bluck et al. (2009), with special concern for deblending accuracy and removal of stellar objects and spurious detections. Possible sources of systematic bias on stellar masses and photometric redshifts, and their effect on our results, are addressed in detail in §4.3.

4.2.2 Spectroscopic and Photometric Redshifts

We utilise both spectroscopic and photometric redshifts for the galaxies we study in both the EGS and GNS fields. The only field which has extensive available spectroscopy, however, is the EGS. The Keck EGS spectra were acquired with the DEIMOS spectrograph as part of the DEEP2 redshift survey (Davis et al. 2003). Target selection for the DEEP2 spectroscopy was based on the optical properties of the galaxies detected in the CFHT photometry, with the basic selection criteria being $R_{AB} < 24.1$. DEEP2 spectroscopy was acquired through this magnitude limit, with no strong colour cuts applied to the selection. About 10,000 redshifts are measured for galaxies within the EGS. The sampling rate for galaxies that meet the selection criteria is 60%.

This DEIMOS spectroscopy was obtained using the 1200 line/mm grating, with a resolution $R \sim 5000$ covering the wavelength range 6500 - 9100 Å. Redshifts were measured through an automatic method comparing templates to data, and we only utilise those redshifts measured when two or more lines were identified, providing very secure measurements. Roughly 70% of all targeted objects result in secure redshifts.

We utilise photometric redshifts computed by our group within the EGS (e.g. Bundy et al. 2006; Conselice et al. 2007, 2008). Within the EGS, photometric redshifts are based on the optical + near infrared imaging, in the BRIJK bands, and are fit in two ways, depending on the brightness of a galaxy in the optical. For galaxies that meet the spectroscopic criteria, $R_{AB} < 24.1$, we utilise a neural network photometric

redshift technique to take advantage of the vast number of secure redshifts with similar photometric data. Most of the $R_{AB} < 24.1$ sources not targeted for spectroscopy should be within our redshift range of interest, at $z < 1.5$.

The neural network fitting is done through the use of the ANNz (Collister & Lahav 2004) method and code. To train the code, we use the ~ 5000 secure redshifts in the EGS, which have galaxies spanning our entire redshift range. The training of the photometric redshift fitting was in fact only done using the EGS field, whose galaxies are nearly completely selected based on a magnitude limit of $R_{AB} < 24.1$. We then use this training to calculate the photometric redshifts for galaxies with $R_{AB} < 24.1$. The agreement between our photometric redshifts and our ANNz spectroscopic redshifts is very good using this technique, with $\delta z/(1+z) = 0.07$ out to $z \sim 1.4$. The agreement is even better for the $M_* > 10^{10.5} M_\odot$ galaxies where we find $\delta z/(1+z) = 0.025$ across all of our four fields (Conselice et al. 2007).

For galaxies which are fainter than $R_{AB} = 24.1$ in the EGS we utilise photometric redshifts using Bayesian techniques, and the software from Benitez (2000). The priors we use is the distribution of magnitudes for the differing morphological types as a function of redshift, obtained from the Hubble Deep Field - North data (Benitez 2000). In short, the code not only determines the best fit redshift and spectral type, but takes into account how likely it is to find a galaxy of that spectral type and redshift at the given redshift. For an object to have a photometric redshift we require that it be detected at the 3σ level in all optical and near-infrared (BRIJK) bands, which in the R-band reaches $R_{AB} \sim 25.1$. We optimised our results, and correct for systematics, through the comparison with spectroscopic redshifts, resulting in a redshift accuracy of $\delta z/(1+z) = 0.17$ for $R_{AB} > 24.1$ systems. These $R_{AB} > 24.1$ galaxies are, however, only a very small part of our sample. Furthermore, all of these systems are at $z > 1$.

The redshifts for the GOODS sample were derived using the HST ACS and ground based NIR imaging, for the whole GOODS area, and the HST GNS + ACS space based data for the volume limited sub-sample. Most of these sources were chosen through multiple selection methods, namely the BzK, IERO and DRG selection (see Conselice et al. 2010, in prep. for a full description). However, in the volume limited case only mass selection was applied (see Fig. 4.2). Our photometric redshifts, which

we use for these massive galaxies, are determined via standard techniques similar to that used in the POWIR data described above (see §1.4.1.2, Gruetzbauch et al. 2010 and Conselice et al. 2010). Additionally, we find seven spectroscopic redshifts from the literature for our sample of massive galaxies. Using the GOODS/VIMOS DR1 (see Popesso et al. 2008), we find three matches with $\delta z/(1+z) = 0.026$, and four spectroscopic redshifts from a compilation of redshifts from the literature (see Wuyts et al. 2008) giving $\delta z/(1+z) = 0.034$. Please see Conselice et al. 2010, for full details on the determination of photometric redshifts and stellar masses for the GNS sample. Some further discussion is also given in §1.4.1.

4.2.3 Stellar Masses

For the POWIR survey in the EGS field, stellar masses were derived from spectroscopic and photometric redshifts and Palomar Observatory and Canada France Hawaii Telescope obtained BRIJK wavebands by fitting spectral energy distributions with Bruzual & Charlot (2003) stellar population synthesis models, with varying star formation histories. A Chabrier initial mass function (IMF) was assumed. Full details of this method and its intrinsic errors are provided in Conselice et al. (2007 and 2008). The errors on the stellar masses were estimated to be $\sim 0.2 - 0.3$ dex, taking into account issues regarding the reliability of photometric redshifts, the effects of AGB stars on the analysis, and Eddington bias. Additional errors from the choice of IMF for the stellar mass codes would lead to a factor of two or so uncertainty (see Conselice 2007).

For the full GOODS field (non-volume limited sample), stellar masses were derived from a combination of groundbased NIR imaging, and space based (ACS) optical imaging. These were taken from the literature (see Giavalisco et al. 2004).

For the GNS, volume limited sample, stellar masses were calculated from photometric redshifts and the HST ACS (BViZ) and NICMOS (H) wavebands. The exact same Bruzual & Charlot (2003) models and Chabrier IMF were used as with the POWIR sample. Full details of the techniques used and error analyses performed are provided in Conselice et al. (2010) and further details in Gruetzbauch et al. (2010). Errors on these stellar masses are also estimated to be ~ 0.3 dex, with possible additional errors on top from the choice of IMF. More details on the computation of stellar masses are

provided in §1.4.1.3.

The effect of possible systematic bias on the determination of stellar masses for high redshift AGN host galaxies is discussed in detail in §4.3.1 and §4.3.2. Here systematic errors arising from the contamination of AGN light in the galaxy SED, and from systematic photometric redshift errors (and catastrophic outliers) for high redshift AGN host galaxies are considered.

4.2.4 X-ray Data

The X-ray data used in this chapter all originates from the Chandra X-ray Observatory, with pointings in the GOODS North / South and EGS fields (see Fig. 4.1 and 4.2 for a graphical representation of the fields). The AEGIS-X survey covers a $\sim 0.64 \text{ deg}^2$ area on the sky with on-axis limiting fluxes of $5.3 \times 10^{-17} \text{ erg cm}^{-2} \text{ s}^{-1}$ in the soft (0.5 - 2 KeV) band and $3.8 \times 10^{-16} \text{ erg cm}^{-2} \text{ s}^{-1}$ in the hard (2 - 10 KeV) band. The AEGIS-X survey is complete for 54 % of the total survey area covered in the hard band down to $2.1 \times 10^{-15} \text{ erg cm}^{-2} \text{ s}^{-1}$. This corresponds to a X-ray luminosity of $2.35 \times 10^{43} \text{ erg s}^{-1}$ at $z = 1.5$, which is the redshift limit we use for the POWIR survey. Thus, we are complete in X-ray sources above our luminosity threshold for our volume limited sample, with $L_X > 2.35 \times 10^{43} \text{ erg s}^{-1}$ at $z < 1.5$, for a reduced area of the total EGS field. We restrict our volume limited sample to those galaxies and X-ray sources which reside within the fraction of the survey's area where we are complete to these limits. The total area of our volume limited sample is approximately 1/2 of the total AEGIS-X area (corresponding to $\sim 1/4$ of the total EGS POWIR field area, see Fig. 4.1). See Laird et al. (2009) for further details on this survey.

The X-ray data we use to compare with the GOODS North galaxy catalogs comes from the Chandra Deep Field North 2 Ms X-ray source catalog (which along with the Chandra Deep Field South is the deepest ever X-ray image taken to date). This covers $\sim 460 \text{ arcmin}^2$ of sky and reaches on-axis soft band (0.5 - 2 KeV) fluxes of $2.5 \times 10^{-17} \text{ erg cm}^{-2} \text{ s}^{-1}$ and on-axis hard band (2 - 8 KeV) fluxes of $1.4 \times 10^{-16} \text{ erg cm}^{-2} \text{ s}^{-1}$. This survey is complete for 28.5 % of the total survey area down to a hard band flux of $4.5 \times 10^{-16} \text{ erg cm}^{-2} \text{ s}^{-1}$, which corresponds to a luminosity limit of $L_X = 2.3 \times 10^{43} \text{ erg s}^{-1}$ at $z = 3$, where we limit our GOODS data in redshift for the volume limited

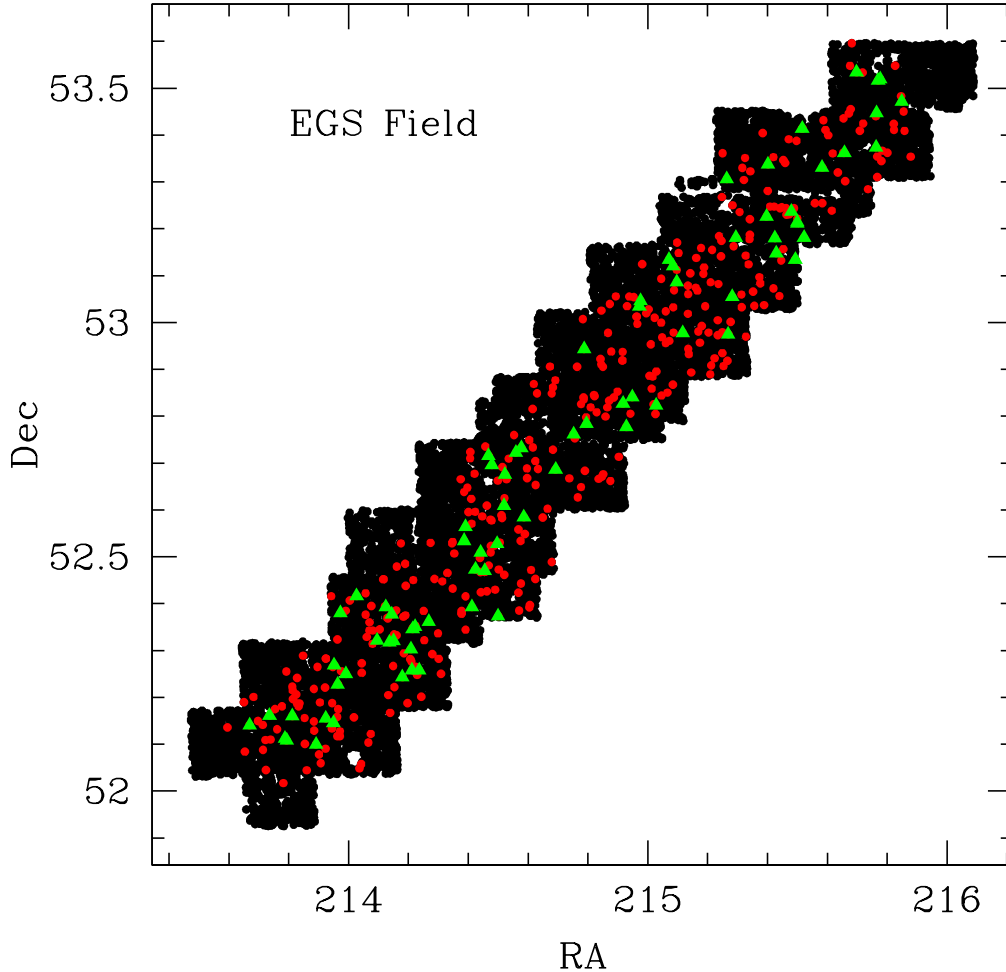


Figure 4.1: The EGS field. Black dots/ region indicate the location of $M_* > 10^{10} M_\odot$ galaxies at redshifts ($0.4 < z < 1.5$). Note that there are ~ 16000 galaxies displayed here. The red circles are massive galaxies with secure X-ray counterparts within a $1.5''$ radius of their positional centre, with hard band luminosities $L_X > 10^{42} \text{ erg s}^{-1}$, which form our low and intermediate redshift AGN sample. The Chandra (AEGIS-X) survey covers an area approximately 1/2 the size of the POWIR survey, which can be visualised by looking for where the red points generally reside. The green triangles indicate bright ‘Seyfert’ luminosity AGN with $L_X > 2.35 \times 10^{43} \text{ erg s}^{-1}$ at $0.4 < z < 1.5$, residing within massive galaxies with $M_* > 10^{10.5} M_\odot$, where we are complete for a reduced area of this survey ($\sim 1/4$ the entire EGS area). The criteria to select the region of completion for the Chandra AEGIS-X survey is roughly given by setting the off-axis angle $\text{OAA} < 7.02'$. This marks out a complex area due to varying depths, angles of pointing, and repeat observations, and hence we do not display it here. However, as a guide to the region of completion, where the green triangles reside we are complete to the above stated limits.

sample. This leads us to detect all X-ray sources above our luminosity threshold ($L_X > 2.35 \times 10^{43} \text{ erg s}^{-1}$) at $z < 3$ within the reduced area, to which we restrict our volume limited sample. See Alexander et al. (2003) for a comprehensive review of the CDF-N data acquisition and properties.

To compare with our GOODS South galaxy catalogs we use the CDF-S 2 Ms X-ray source catalog. Here an area of $\sim 436 \text{ arcmin}^2$ of sky is imaged in X-ray hard and soft bands. Limiting on-axis fluxes achieved are: soft band (0.5 - 2 KeV) $1.9 \times 10^{-17} \text{ erg cm}^{-2} \text{ s}^{-1}$ and hard band (2 - 10 KeV) $1.3 \times 10^{-16} \text{ erg cm}^{-2} \text{ s}^{-1}$. This survey is complete for 22 % of the total survey area down to fluxes of $4.5 \times 10^{-16} \text{ erg cm}^{-2} \text{ s}^{-1}$. This corresponds to $L_X = 2.3 \times 10^{43} \text{ erg s}^{-1}$ at $z = 3$, where we limit our sample. This leads us to detect all X-ray sources above our luminosity threshold ($L_X > 2.35 \times 10^{43} \text{ erg s}^{-1}$) at $z < 3$ within the reduced area, to which we restrict our volume limited sample. For more details relating to the CDF-S data see Luo et al. (2008).

Our volume limited sample within the highest redshift range, taken from the GOODS North and South fields, has an area of $\sim 2/3$ that of the total GNS field, which corresponds to $\sim 1/9$ of the area of the entire GOODS North and South fields. (See Table 1 for a summary of the data and the areas of completion).

Positional uncertainties are of the order 1 arcsec in size for all of the X-ray data used, making it possible to place a strict 1.5 arcsec aperture limit on confirming an X-ray detected galaxy through matching with NIR imaging (from the GNS and POWIR surveys). Additionally, we imposed checks to determine how sensitive our detection of AGN is to the exact aperture limits we use, finding very few additional detections (~ 5 %) by expanding the limits up to 2.5 arcsecs, and very little loss (~ 2 %) by reducing the limit to 1 arcsec. We also use the criterion of ensuring each detection is unique, to avoid possible confusion. In fact, no AGN - galaxy matches had to be rejected for this reason using an aperture of 1.5 arcsecs.

We present in Table B1 (in Appendix B) a summary of the key surveys utilised in this chapter, which indicates their areas, depths and the reduced areas used to construct volume limited samples. In the table, A_T is the total area of the survey(s) in question, $A_{vol.lim.}$ is the area of the volume limited sub-sample of the survey where there is completion to the mass limits and redshifts indicated (for the NIR + optical surveys),

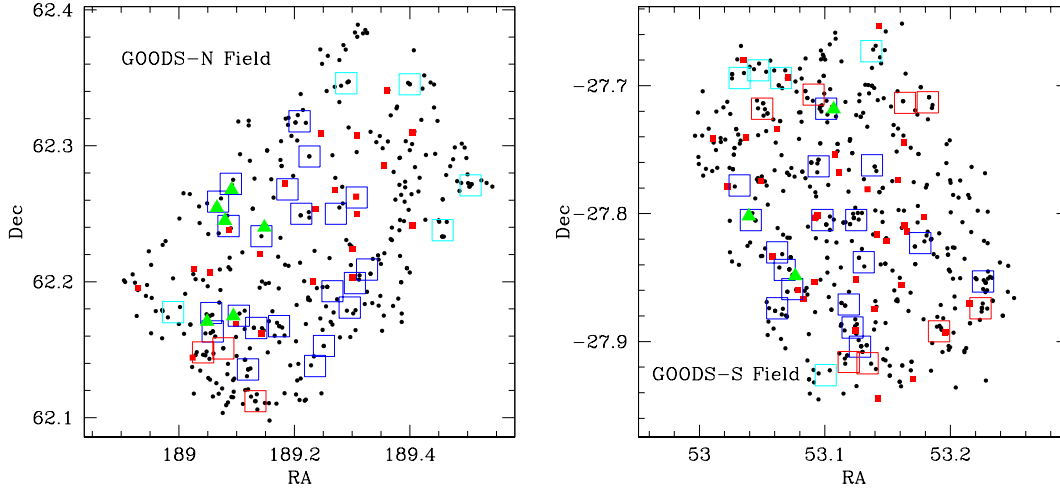


Figure 4.2: Left plot is the GOODS North field; right plot is the GOODS South Field. The black dots indicate the location of $M_* > 10^{10} M_\odot$ galaxies at high redshifts ($1.5 < z < 3$) throughout the entire GOODS field. Small red squares depict those high redshift massive galaxies within the GOODS field with secure X-ray counterparts within a $1.5''$ radius of their positional centre, with hard band X-ray luminosities $L_X > 10^{42}$ erg s $^{-1}$, which form our high redshift AGN sample. The large green triangles indicate bright ‘Seyfert’ luminosity AGN with $L_X > 2.35 \times 10^{43}$ erg s $^{-1}$ residing within massive galaxies with $M_* > 10^{10.5} M_\odot$, where we are complete for a reduced area of this survey ($\sim 1/9$ the entire GOODS area). The square boxes represent the pointings of the HST GOODS NICMOS Survey (GNS), and these are colour coded via Chandra depth. The blue boxes have total Chandra completion to a depth of $L_X > 2.35 \times 10^{43}$ erg s $^{-1}$ at $z = 3$ across their entire area, the cyan boxes have partial completion to this limit, whereas the red boxes are totally insensitive to this threshold. As such, our volume limited sample is restricted to the blue box regions (where all of our sample of ‘Seyfert’ galaxies reside).

and to a threshold hard band X-ray luminosity of $L_X > 2.35 \times 10^{43}$ erg s $^{-1}$ at the redshift limit indicated for each X-ray survey. M_L is the mass limit completion cutoff for the volume limited sample. The quoted depths are given for hard band fluxes (in the case of the X-ray data) and magnitudes in the wavebands indicated (for the NIR + optical surveys). Please see above (§4.2) for full details on the specifics of each survey, and §4.4 for further details on the construction of our volume limited sample.

4.3 Biases and Systematic Errors

Biases and systematic errors are likely an important aspect in our analysis and we have to address these issues very carefully. Not only do we have to deal with issues such as intrinsically inaccurate stellar masses and photometric redshifts (from random errors), but also, we have the added complication that our sources are AGN and emit light in the optical and NIR which can make quantities such as stellar masses and

photometric redshifts systematically less accurate. Some of these systematics include contamination of the AGN in creating higher stellar masses due to the possibly bright point source, as well as creating a galaxy SED which is not entirely stellar. Another issue is that the Chandra X-ray Observatory data is not uniform across its field of view, resulting in less sensitive detections in the outer regions of the field.

We also may detect slightly fewer AGN above our flux limits due to the randomly distributed torus opening angles of accretion discs in our survey. In part this issue will be mitigated by the fact that we utilise the hardest X-ray bands (and hence most penetrating X-ray emission) for our study but this effect is still likely to make our measures of active fractions and luminosity densities lower limits as discussed throughout this chapter. Studies in the local Universe, utilising data from the Swift and INTEGRAL surveys, still find very few Compton thick sources (i.e. those most likely to have edge on accretion discs to our line of sight) even up to energies of ~ 200 KeV (see Ueda et al. 2003 and Steffen et al. 2003). This suggests that missing AGN due to certain torus opening angles will still be a significant issue even though we use the deepest and hardest available X-ray bands to probe our sources. Additionally, these surveys find that those highly obscured AGN have lower luminosities than their less obscured counterparts. This is, however, not a significant problem for the results and conclusions in this chapter because we consider our active fractions and total energy outputs to be minima for this and other reasons, as is explained in detail in the relevant sections. Finally, to derive an Eddington limited black hole mass, we must have some idea of the bolometric luminosity of the AGN. We explore each of these issues in turn throughout this section.

4.3.1 AGN Contamination in Stellar Masses

Since we are working with galaxies that can host bright AGN, we must deal with the fact that some light in the optical-NIR spectral energy distributions of these galaxies may originate from light coming from the AGN. A few methods and tests were used to ensure that this is not a significant problem. The first is that our sample does not include any objects that are point sources, as these were removed before the analysis of stellar masses in both the POWIR data (Conselice et al. 2007; 2008) and the GNS

samples (Conselice et al. 2010). Secondly, in terms of stellar masses, these were measured using only galaxy SEDs, and we find no cases for our sample where the SED is not well fit by standard star formation histories. Regardless, the stellar masses are measured in such a way that the uncertainty in the stellar masses takes into account the range of best fit masses, and this uncertainty increases if the SED is not well fit by a limited number of models, giving a wider range of calculated stellar masses for our library of star formation histories (see Bundy et al. 2006; Conselice et al. 2007; Bundy et al. 2008).

Moreover, we examine the SEDs for our sources in other ways, specifically by taking the ratio of the K-band luminosity to that of the hard band X-ray luminosity to determine the possible extent of AGN contribution to the optical SED. The K-band represents, roughly, rest frame R band at $z \sim 1$ and rest frame V band at $z \sim 2$. In general one would expect the light to be dominated by the underlying stellar population (rather than AGN) at these wavebands (see e.g. Mushotzky et al. 2008). Furthermore Mushotzky et al. (2008) and McKernan (2010) analyse the correlation between infrared light and X-ray hard band luminosity for samples of low redshift AGN, concluding that there is a very steep dependence (suggesting AGN contamination on the galaxy SED) but only for infrared fluxes taken from the very centre of the galaxies in question. Since we disregard point sources, selecting only extended galaxy-like objects, we reduce this possible systematic somewhat. This notwithstanding, we run our own analyses of the ratio between K-band luminosity and X-ray hard band luminosity to be assured of the reliability of our stellar mass estimates. If this ratio is very low, it might imply that the source has an SED which is dominated by the AGN, leading to an overestimate of the stellar mass of the host galaxy.

We find that the mean νf_ν (K band) / νf_ν (2-10KeV) ratio is 3.4 (with a median value of 2.9) for our volume limited sample of ‘Seyfert’ galaxies, suggesting that the majority of light in the K band is from stellar light, not AGN. For example, for QSOs one would expect this ratio to be less than 1.5 - 2 (see Green et al. 2009). The percentage of objects with νf_ν (K band) / νf_ν (2-10KeV) < 1.5 is less than 15%, and for all other objects the light in the K-band must be dominated by stellar light, minimising any contributive uncertainty from the AGN in the stellar mass determination. A frequency

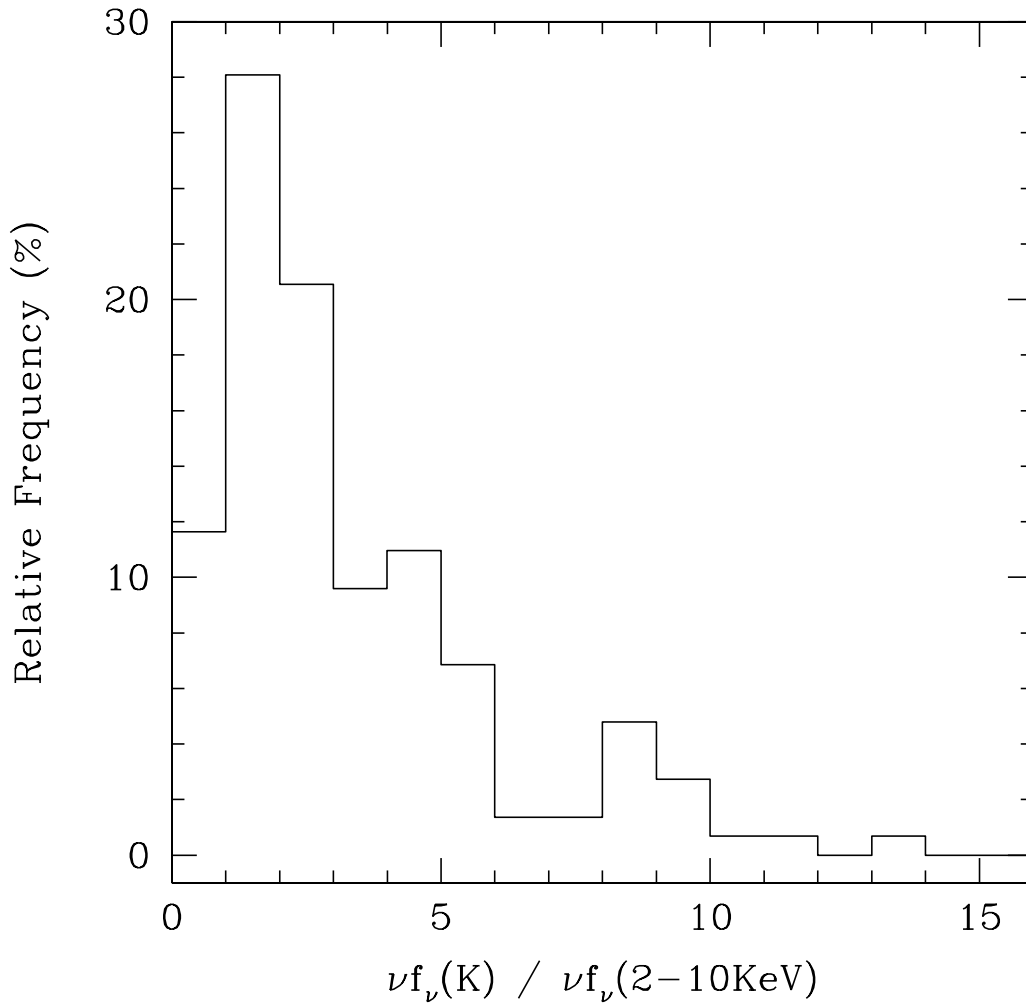


Figure 4.3: Frequency histogram of the ratio of K band flux to X-ray hard band flux for our volume limited sample of active galaxies. The higher the value of this ratio, the less affected our measure of stellar mass will be by contamination of light from the AGN. The mean value for galaxies in our sample is 3.4 (median 2.9), implying that less than a 1/3 of the light in the K band will have been contributed from the AGN on average across our sample (assuming a globally flat spectrum). Therefore, the majority of the light emitted will be from the host galaxy within this frequency range. Nevertheless, there remains a fraction of $\sim 15\%$ of AGN with $\nu f_{\nu}(\text{K band}) / \nu f_{\nu}(2-10\text{KeV}) < 1.5$ where significant infiltration of AGN light on the galaxy SED is possible. The implications of which are discussed in §4.3.1.

histogram of the νf_ν (K band) / νf_ν (2-10KeV) ratio is presented in Fig. 4.3. As mentioned before, and as described in Bundy et al. (2008), we do not find within the stellar mass fits a population of galaxies which are not well fit by the stellar population synthesis models which we use. As described in Bundy et al. (2008), when examining the minimum χ^2 for these fits, the galaxies with AGN have a slightly higher value than those which are not, yet the fraction with $\chi^2 > 10$ is only 10%. Furthermore, there is no correlation between the χ^2 value and the luminosity of the X-ray AGN (Bundy et al. 2008), a further indication that the light from these galaxies is not dominated by the non-thermal AGN component.

Taken in aggregate, the fact that we discard point sources, select objects to be galaxy like in terms of colour, fit SEDs with low χ^2 values to all our galaxies, observe a mean νf_ν (K band) / νf_ν (2-10KeV) ratio of 3.4 (implying that less than 1/3 of the K band light can be from the AGN on average, assuming a globally flat spectrum), and have good agreement between our photometric redshifts and the spectroscopically confirmed redshifts in our sample (see Bundy et al. 2008, and §4.3.2) gives us high confidence in calculating stellar masses for our sample of active galaxies, at $z < 1.5$ at least.

At $z > 1.5$ we still select galaxies to be extended sources with galaxy like colours, and note that all are fit well by star formation history SEDs with low χ^2 to the data. Nevertheless, we have no spectroscopically confirmed redshifts at $z > 1.5$ within our X-ray selected volume limited sample, so we cannot compare these with our photometric redshifts directly. However, previous studies comparing spectroscopic and photometric redshifts at high z find that there is a probable systematic offset whereby photometric redshifts underestimate the true spectroscopic redshifts (see Bundy et al. 2008, Aird et al. 2009, and §4.3.2 for a thorough discussion). Therefore, the stellar masses in our highest redshift bin must be taken with more caution, with X-ray luminosities systematically lowered due to this effect.

However, we find that the mean hard band X-ray luminosity of our volume limited sample of massive galaxies rises with redshift, an effect in opposition to the systematic lowering of photometric redshifts for high redshift AGN host galaxies (discussed in more detail in §4.3.2 below), which leads to general confidence in the trend of our

results despite this possible bias. Furthermore, our computed X-ray luminosities will be minima for this regime (due to the systematic underestimation of the redshifts of the sources), and in the later discussions in this chapter we consider them as such, computing further minimum and maximum quantities, such as the mean maximum lifetime of AGN in our sample. We turn to sources of systematic error on photometric redshifts and hence stellar masses and X-ray luminosities in the next section.

From our discussion above it is evident that there is, however, a population of galaxies for which AGN contamination in the SED of the galaxy could lead to a systematic overestimation of the galaxy's stellar mass. This effect is in opposition to the systematic underestimation of stellar masses and X-ray luminosities for AGN at high redshifts, due to underestimating photometric redshifts (discussed briefly above, and in more detail in §4.3.2 below). To model this first effect, we restrict our sample to those active galaxies with νf_ν (K band) / νf_ν (2-10KeV) > 1.5 and note that this leads to no significant deviation in the mean stellar masses of host galaxies calculated (to within 1 σ) and thus no significant departure for the latter derived quantities under discussion in this chapter. Thus, the dominant bias in our results must be in underestimating stellar masses and X-ray luminosities due to our photometric redshift estimates being systematically lowered for AGN at high redshifts. It is to this effect we turn to in the next section.

4.3.2 Photometric Redshifts of X-ray Sources: Systematics

One of the major issues with measuring photometric redshifts for X-ray sources is that these X-ray sources could have SEDs which are contaminated by the AGN, producing inaccurate photometric redshifts. For our lower redshift data in the EGS field this has been extensively investigated by Bundy et al. (2008), who find a $\delta z = dz/(1+z) \sim 0.11$ for the whole sample of X-ray selected galaxies, and no evidence of additional systematic offsets out to $z \sim 1$. At higher redshifts than this, Bundy et al. (2008) note that there is a systematic offset whereby photometric redshifts underestimate the true spectroscopic redshifts for X-ray luminous AGN. This effect is most prominent for QSO luminosity sources with $L_X > 10^{44}$ erg s⁻¹, which are predominantly excluded from our sample due to selecting against point sources, and objects without galaxy like

colours. In fact less than 10 % of our sample of AGN are in this luminosity regime and none are point-like. However, as seen by Bundy et al. (2008), there is still an observed modest systematic offset for ‘Seyfert’ type AGN with $L_X > 10^{43}$ erg s⁻¹ at $z > 1$ in the EGS field. In fact ~ 15 % of these sources at $1 < z < 1.5$ lie outside the spectroscopic - photometric redshift dispersion of $\delta z \sim 0.11$.

For our high redshift data in the GOODS-N/S fields at $2 < z < 3$ the effects of this systematic trend in photometric redshifts underestimating the actual spectroscopic redshifts for AGN is potentially much more significant. Aird et al. (2009) investigate the reliability of photometric redshifts for AGN in the GOODS fields finding that there is accord between spectroscopic and photometric redshifts out to $z \sim 1.2$ for their sample, in agreement with Bundy et al. (2008). At redshifts higher than this they describe a systematic tendency for the photometric redshifts to be too low in value, which leads to a catastrophic failure in the photometric redshift codes for these objects. None the less, Aird et al. (2009) also note that the worst affected photometric redshifts are for QSO sources with $L_X > 10^{44}$ erg s⁻¹, of which we only have a few in our sample. With these X-ray luminous sources removed, they find a $\delta z = dz/(1+z) \sim 0.13$ for the remaining galaxies. However, there remains a small systematic bias, leading to an underestimation of the redshifts of lower luminosity AGN at $z = 2 - 3$.

We investigate this issue with Monte-Carlo simulations of how uncertainties in photometric redshifts lead to uncertainties in our results. In our random (Gaussian) error analyses we assume a $\delta z = dz/(1+z) \sim 0.2$ for all of our redshifts which is higher than that found by both Aird et al. (2009) and Bundy et al. (2008). Since there are no outliers in the spec-z - photo-z plane (with $\delta z > 0.2$) for AGN in our sample at $z < 1$, we have high confidence in our X-ray luminosities and stellar mass estimates in this redshift range, to within the random error margins intrinsic to calculating stellar masses and luminosities, as plotted in the latter figures of this chapter. We ran a standard symmetric random Monte-Carlo simulation to deduce the errors of stellar masses, X-ray luminosities and Eddington masses arising from random errors of $\delta z = 0.2$ on the photometric redshifts. These are incorporated into our confidence claims.

In our intermediate ($1 < z < 1.5$) and higher ($1.5 < z < 3$) redshift ranges we minimise systematic effects by actively selecting against QSOs, but acknowledge that some

bright point sources probably still remain to some level. It is pertinent here to note that these additional errors are in one direction only, i.e. they systematically lower our photometric redshift from its true value. This, therefore, gives us a minimum redshift and, hence, a minimum X-ray luminosity for our higher redshift AGN, leading to a minimum estimate of the Eddington limiting mass. Additionally this effect will systematically lower the stellar masses of the host galaxies measured, leading to us effectively deducing a minimum stellar mass of very high redshift and X-ray luminous host galaxies. Since much of the analyses of this chapter concern maxima and minima values of quantities such as the lifetime of AGN, the luminosity density due to AGN, and the fraction of active galaxies, we can proceed adequately with this limitation. Moreover, perhaps one of the most significant trends we observe in this chapter is a modest rise in average X-ray luminosity (and, hence, Eddington limiting mass) with redshift. This trend is in the opposite direction to the systematic bias lowering our photometric redshifts, and thus X-ray luminosities, so we retain confidence in this result despite the possible systematics.

This notwithstanding, we ran a further set of Monte-Carlo simulations to investigate possible asymmetric effects of this systematic bias on the measures of stellar masses, X-ray luminosities and the Eddington limiting masses of SMBHs in our sample. As discussed above, no biases are expected for the lowest redshift bin ($z < 1$), and all random errors quoted can be considered free from systematic additions here. For the two higher redshift ranges we consider systematic deviations to lower redshifts. For the intermediate redshift range we consider the spec- z - photo- z plot in Bundy et al. (2008), noting that $\sim 15\%$ of active galaxies have their photometric redshifts systematically lower than their actual spectroscopic redshifts. We allowed 15% of our sources to experience a random systematic shift to higher redshift up to the limit of the outliers in this redshift range, assuming a Gaussian distribution of outliers between the limit of $\delta z = 0.2$ and the maximum outliers location. From this Monte-Carlo analysis we recompute stellar masses, X-ray luminosities and (minimum) Eddington masses for the SMBHs and host galaxies in our sample finding that there is a systematic bias to lower photo- z 's of $\delta z = 0.09$ leading to a systematic lowering of stellar masses of 0.14 dex, subdominant to the random errors (estimated conservatively to be ± 0.3 dex in Bundy et al. 2008 and Conselice et al. 2010).

For our highest redshift range we have no spectroscopically confirmed redshifts within our volume limited sample. Nonetheless, we have analysed those active galaxies within the redshift range with spectroscopic redshifts that lie outside the volume limited sample and find no significant offset between their photometric and spectroscopic redshifts. This was done for a very small sample, however, and we defer to the more comprehensive test of this bias in Aird et al. (2009). Aird et al. (2009) find that at $z > 1.2$ there is a significant systematic lowering of photometric redshifts compared to spectroscopically confirmed ones. We model this effect by allowing all sources in our volume limited sample at this high redshift range to be randomly distributed between the limit $z_{spec} = z_{phot}$ to the location of the lowest outlier. This leads to a systematic lowering of photo- z 's of $\delta z = 0.28$ leading to a systematic shift in stellar mass of $\delta M_* = -0.38$ dex (downwards). Here the systematic effect of miscalculating photometric redshifts to be lower than their actual values for AGN at high redshifts comes to dominate over the random errors inherent in measuring photometric stellar masses for high redshift galaxies.

In all of the redshift ranges the errors deduced from random and systematic error analysis through Monte-Carlo simulation come to dominate for the X-ray luminosities and Eddington masses, over the intrinsic errors in their fluxes. This is to say that the errors on photometric redshifts are always more significant than those on the fluxes for our sources. The errors in photometric redshifts and stellar masses, deduced from a combination of random and asymmetric Monte-Carlo simulations (described above), lead to errors in the Eddington limiting black hole mass which range from: $+/- 2 \times 10^6 M_\odot$ at $z = 0.4 - 1$, $+3.2 - 3 \times 10^6 M_\odot$ at $z = 1 - 1.5$ and $+6 - 4 \times 10^6 M_\odot$ at $z = 1.5 - 3$. The Eddington mass is a lower limit to the mass of the SMBH, given its bolometric luminosity. To compute this we use a bolometric luminosity chosen to be a minimum from the literature and our own analyses (see §4.4.3), thus ensuring that our measured Eddington masses are indeed minimum masses.

4.3.3 Malmquist-type Bias

Due to the steepness of the X-ray luminosity function, there is a potential to transform apparently random errors in X-ray luminosity into systematic errors as there are more

lower luminosity sources in the Universe than higher ones. Since in this chapter we seek to place reliable minimum values on the outpouring of energy by AGN, this is of paramount importance to address. The effect of this Eddington bias would be to introduce into our high luminosity sample AGN which have intrinsic X-ray luminosities lower than that of the lower limit of the sample population intended to be studied. To address this issue we ran a further set of Monte-Carlo simulations, the results of which follow in this section.

We take our number counts of AGN at varying luminosities and redshifts to be roughly representative of the distribution in the Universe, around our completion limit of $L_X = 2.35 \times 10^{43} \text{ erg s}^{-1}$. At luminosities considerably lower than our completion threshold this would certainly not be the case, but given random errors in luminosity due to photometric redshift errors (calculated in the previous section) of $\sim 2 - 4 \times 10^{43} \text{ erg s}^{-1}$ (varying with redshift) and the mean value of our Seyfert sample of $\sim 8 \times 10^{43} \text{ erg s}^{-1}$ this is a reasonable first attempt, and will at least provide a check as to the possible importance of Eddington bias in our study.

We ran a set of random Monte-Carlo simulations allowing all X-ray luminosities in our AGN sample to be varied randomly by up to 2σ of the mean symmetric X-ray luminosity errors computed in the previous section. We then redefine our Seyfert sample and quantify the differences in mean X-ray luminosity. This was repeated 50 times and averages were taken. The resultant (error shifted) population systematically rose in size due to more lower luminosity systems moving up in brightness than higher luminosity systems moving down, simply due to their relative frequencies. In fact the new mean increase was $\sim 10 \%$. Quantitatively, the net mean shift in X-ray luminosity witnessed was $\delta \langle L_{X,obs} \rangle = +0.60 \pm 0.26 \times 10^{43} \text{ erg s}^{-1}$ (at 2σ) to the mean X-ray luminosity of the Seyfert sample. The error presented here is the standard deviation of the mean difference between initial mean X-ray luminosity and recalculated X-ray luminosity (after the random error shift). Thus, the average Seyfert galaxy in our volume limited sample would have its X-ray luminosity overestimated by up to $\langle \delta L_X \rangle = -0.30 \pm 0.13 \times 10^{43} \text{ erg s}^{-1}$ (at 1σ) were this effect not taken into account.

This systematic error is considerably lower than the average random error from photometric redshift uncertainty of $\pm 3.2 \times 10^{43} \text{ erg s}^{-1}$. Furthermore, the other systematic

effect of underestimating the true X-ray luminosity of our AGN due to systematically underestimating the photometric redshifts of high redshift AGN is vastly more significant with values up to $6 \times 10^{43} \text{ erg s}^{-1}$ at $z > 2$ (this is considered in some detail in the previous sub-section). Therefore, we conclude that this Malmquist-type bias is not a significant source of error in our analysis, and is in fact sub-dominant to both the random errors and the primary systematic error (which is oppositely orientated and of tenfold significance) of underestimating X-ray luminosities due to underestimating high redshift photometric redshifts for AGN. We, therefore, do not include these malmquist-type errors further in our analysis, and note that our minimum values for the active fraction and release of energy of bright Seyfert AGN are robust lower limits, given that the dominant sources of systematic error remaining will only serve to raise the values presented in this study. Furthermore, the large random errors and dominant systematic effects are taken in to account throughout this chapter and factored in to the confidence claims made.

4.3.4 Completeness

In order to probe possible trends of SMBH evolution with redshift we must be extremely careful to be complete in both X-ray luminosity for the AGN, and stellar mass of the host galaxy, within whatever redshift range and survey area we choose to investigate. Thus, it is essential to obtain an optimal compromise between depth, area, stellar mass and X-ray luminosity threshold. In this study we are complete to $L_X > 2.35 \times 10^{43} \text{ erg s}^{-1}$, and $M_* > 10^{10.5} M_\odot$, for the reduced area of the EGS and GNS fields we restrict our redshift analysis to. Thus we effectively probe high redshift counterparts to local Universe ‘Seyfert’ luminosity AGN in average massive elliptical galaxies. The higher mass galaxies probed in our sample may also be progenitors for brightest cluster galaxies (BCGs) in the local Universe. The areas to which we achieve completion are approximately 1/2 of the AEGIS-X field (1/4 of the total EGS POWIR field) and 2/3 of the GNS field (1/9 of the total GOODS ACS North and South fields), corresponding to the regions where the Chandra X-ray data is deepest, and the off axis angle of the Chandra pointings are minimised (see Table B1, and Figs. 4.1 and 4.2). We also may miss active galaxies due to their accretion discs having torus opening

angles oriented so that light must travel through the Compton thick accretion disc to reach us. In part this is reduced by us using exclusively the hard Chandra bands in our analysis where we will be least sensitive to this obscuration, however, it is likely that some active galaxies will be missed due to this effect. In fact, as seen by Ueda et al. (2003) and Steffen et al. (2003), there are relatively few Compton thick sources detected in the local Universe, even when probed with energies up to ~ 200 KeV. Thus, for this and other reasons (including our use of a minimum bolometric correction, see §4.4.2) our measures of the total active fraction of massive galaxies, and our estimates of the energy output due to AGN must be considered as lower limits, as discussed in the later sections of this chapter.

In probing the possible evolution in the $M_{BH} - M_*$ relationship at higher redshifts we have been careful to achieve an optimal compromise between minimising various biases, and performing a detailed error analysis of those remaining. The lower the luminosity cut we utilise for our volume limited sample the smaller the area that the X-ray surveys are complete to. Additionally, the brighter the X-ray sources, the higher the contamination of optical light will be on the SED of the galaxy from the AGN and the greater the systematic lowering of the photometric redshifts, leading to less robust stellar mass estimates of the host galaxy (c.f. §4.3.1 - §4.3.2). Taking both of these issues seriously, we have found a suitable compromise. We probe a range of X-ray luminosities for which we are complete out to $z \sim 3$ for a significant fraction of the area of the two main surveys we investigate (EGS and GNS) whilst still being populated by AGN with low (on average $< 1/3$) stellar mass contamination from the AGN. Additionally, there remain reasonably small biases due to the systematic offset of photometric redshifts, which we model and factor into our error calculations. As such, we select bright (non-QSO) ‘Seyfert’ galaxies with $L_X > 2.35 \times 10^{43} \text{ erg s}^{-1}$ and in practice $L_X < 5 \times 10^{44} \text{ erg s}^{-1}$ for our volume limited sample. Within this order of magnitude range in X-ray luminosities we are complete in X-ray sources out to $z \sim 3$ and furthermore have strong estimates of host galaxy stellar masses, which will not be dominated by contamination from the AGN, or unreasonably disturbed by the systematics involved in measuring photometric redshifts for high redshift AGN. The remaining random and systematic errors and biases are modelled through Monte-Carlo simulations (see §4.3.2) and factored into our plots and confidence calculations on our

claims.

4.4 Method

4.4.1 Detecting AGN

The purpose of this chapter is to explore the co-evolution of supermassive black holes and their host galaxies for a statistically significant number of AGN out to very high redshifts ($z \sim 3$). In order to achieve this we have combined two large galaxy catalogs (see §4.2.1): the POWIR survey in the EGS field which amasses over 20,000 galaxies at intermediate redshifts ($0.4 < z < 1.5$); and the GNS which images over 8,000 galaxies as part of an ultra-deep ‘pencil beam’ high redshift ($1.5 < z < 3$) galaxy survey. We combine these galaxy surveys with the deepest available X-ray data from the Chandra X-ray Observatory overlapping these original galaxy survey fields. We select AGN in this study on the basis of high X-ray fluxes. For all detections we use the same two criteria for determining whether or not a given galaxy has an active SMBH at its centre. A given galaxy is deemed ‘active’ if:

1. There is a unique Chandra X-ray detection within a 1.5 arcsec radius of the NIR positional centre of the galaxy.
2. The hard band X-ray luminosity is $L_X > 10^{42} \text{ erg s}^{-1}$.

This ensures that it is most likely that the X-ray source is associated with the host galaxy, and that the X-ray activity is most probably the result of accretion onto a central SMBH, as opposed to being due to stellar formation. Typical X-ray luminosities for massive galaxies without AGN vary widely due to differing star formation rates, but even those with very high star formation rates are expected to have $L_X < 10^{42} \text{ erg s}^{-1}$, with average non-AGN massive galaxies having $L_X \ll 10^{42} \text{ erg s}^{-1}$ (see e.g. Reddy et al. 2005). Galaxies in both the EGS and GNS fields are selected to be galaxy-like in terms of their colours, and to be extended sources. This effectively selects against QSOs where stellar mass estimates would be significantly compromised by the AGN, leaving us with a sample of (sub-QSO) active galaxies, for which we can estimate

stellar masses. With this criteria we identify a total of 436 AGN from the EGS field and 72 AGN from the GOODS North and South fields, giving in total 508 AGN with photometric and spectroscopic redshifts in the range $0.4 < z < 6$. This is our large sample, and suffers from not being volume limited. Thus, we cannot use this sample directly to probe evolutionary traits. However, this sample can be used to investigate intrinsic AGN properties.

In order to study any possible evolution in SMBH mass or luminosity with redshift it is important to construct a volume limited sample, where selection effects are adequately addressed. Out to $z = 3$ for the GNS and $z = 1.5$ for the EGS, we are complete for the entire areas of our surveys (EGS and GNS) down to galaxy stellar masses of $M_* = 10^{10.5} M_\odot$, and complete down to specific X-ray luminosities of $L_X > 2.35 \times 10^{43} \text{ erg s}^{-1}$ for approximately 1/4 of the EGS area (1/2 of the AEGIS-X area) and 2/3 of the GNS area (1/9 of the total GOODS area). The redshift limits are due to the constraints on the depths of both the NIR galaxy surveys and Chandra X-ray surveys used (see §4.2.1 and §4.2.4 for further details), and our desire to construct a sample where we are 100 % complete (to at least 5σ).

In addition to the criteria for selecting an ‘active’ galaxy (above) we impose the following criteria to select our subset volume limited sample of principally ‘Seyfert’ luminosity AGN:

1. The hard band X-ray luminosity is $L_X > 2.35 \times 10^{43} \text{ erg s}^{-1}$.
2. The stellar mass of the host galaxy is $M_* > 10^{10.5} M_\odot$.
3. The redshifts of active galaxies are at $0.4 < z < 1.5$ for EGS sources and $1.5 < z < 3$ for GNS sources.
4. The active galaxy lies within the area of the survey to which the above limits on stellar mass and X-ray luminosity lead to 100% completion (at 5σ), to $z = 1.5$ for the EGS and $z = 3$ for the GNS.

We use this subset to investigate the evolution of AGN over cosmic time. Since we discard point sources, and objects without galaxy like colours, we in principle select

against QSO's (thus ensuring we have high confidence in our stellar mass determinations, see §4.3.1 and §4.3.2 for further discussion on this point) and are left with X-ray bright sub-QSO AGN (where we achieve source completion) which we henceforth describe as being 'Seyferts', due to their comparable X-ray luminosities.

Fig. 4.4 illustrates the redshift, luminosity and host galaxy mass cuts we have made to construct a volume limited sample from our larger AGN sample. Red points are those discarded due to our redshift limits, blue points are those discarded due to our luminosity threshold, green points are those discarded due to the host galaxy stellar mass cuts, magenta points are discarded for lying outside of our completion area, and black points are those included in our volume limited sample. This leaves 85 'Seyfert' galaxies with which we probe the co-evolution of SMBHs and their host galaxies at $z < 3$. A table displaying the co-ordinates and other derived quantities (such as stellar mass of host galaxy and Eddington mass of SMBH) for our volume limited sample is provided in Table B3 (in Appendix B).

4.4.2 X-ray and Bolometric Luminosities

In order to calculate the bolometric luminosity we must first compute the specific X-ray luminosity in the waveband used. Throughout these calculations we use the hard band flux, because it is much less affected by accretion disc and galactic absorption and obscuration than the soft band. In fact the X-ray hard band corresponds to a rest frame X-ray band of roughly 4 - 20 KeV at $z \sim 1$, and 6 - 30 KeV at $z \sim 2$. Furthermore, star formation makes a larger contribution to the soft band than to the hard band, rendering the latter preferable to use in probing high- z AGN. The specific luminosity of the X-ray source is calculated via standard techniques as:

$$L_X = 4\pi f_X D_L^2 \times K_{corr} \quad (4.1)$$

where D_L is the luminosity distance, defined here as:

$$D_L = \frac{c(1+z)}{H_0} \int_0^z \frac{1}{E(z')} dz', \quad (4.2)$$

where f_X is the flux of the source, z is the redshift of the AGN, and $E(z) = [\Omega_M(1+z)^3 + \Omega_k(1+z)^2 + \Omega_\Lambda]^{1/2}$. The K correction that we apply assumes an intrinsic X-ray spectrum of the form $f_\nu \propto \nu^{-0.7}$, as favoured by the literature (e.g. Alexander et al. 2003). This results in a K correction $\propto (1+z)^{0.3}$.

The specific X-ray luminosity must then be converted to a total bolometric luminosity by assuming a spectral energy distribution, or conversion factor. Since we are interested in computing minimum black hole mass estimates from the Eddington limit method, we should also be careful to apply a minimum bolometric correction. In the literature (e.g. Elvis et al. 1994, Elvis et al. 2002, Hopkins, Richards & Hernquist 2007, Vasudevan & Fabian 2007 and 2009) it is established that there is a broad range of possible bolometric corrections, ranging from ~ 15 to 200 or so appropriate generally for AGN. By selecting the extreme low end of the distribution of bolometric corrections computed across the literature, we effectively choose a minimum bolometric correction, which will give rise to a minimum SMBH mass through the Eddington limit method. As such, we may provide a robust lower limit for the masses of a sample of SMBHs by adopting the minimum bolometric correction factor of 15 in all cases.

As an additional check on the reliability of this correction, if we adopt the form $f_\nu \propto \nu^{-1}$ for the total all wavelength spectral profile of our AGN, as often seen in the literature (e.g. Alexander et al. 2008), we may compute a value for the bolometric correction ignoring Compton IR and UV bumps in the SED. From this we calculate the Bolometric luminosity (L_{Bol}) from the specific X-ray luminosity (L_X), using the range of the hard band fluxes ($X_1 - X_2$) and a reasonable estimate of the total spectral range ($\nu_{min} - \nu_{max}$). Specifically we calculate:

$$L_{Bol} = \left(\frac{\ln \frac{\nu_{max}}{\nu_{min}}}{\ln \frac{X_2}{X_1}} \right) L_X \sim 15 L_X \quad (4.3)$$

where we use 10^{-5} - 100 KeV for the spectral range, and adopt the limits of the hard band in each Chandra survey for the frequency limits. This gives a bolometric correction of ~ 15 in each case, which is at the extreme low end of the distribution of bolometric corrections computed across the literature (discussed above). As such, since we are attempting to provide a robust lower limit for the masses of a sample of SMBHs, we adopt this minimum bolometric correction of 15 in all cases.

In the future more use could be made of the multi-wavelength coverage in the GOODS field to ascertain more reliable global spectral shapes, and hence bolometric corrections, utilising data from the radio to the X-ray. In particular, use of IRAC mid IR data as well as various radio bands would help. But it is noted here that our intention is to compute a robust minimum black hole mass, and this is ensured utilising the bolometric correction adopted here as a hard minimum from the literature and our own analyses.

4.4.3 Eddington Accretion

In order to determine minimum SMBH mass estimates from our minimum bolometric luminosities we adopt an Eddington limiting method. We follow an approach outlined in detail, for example, in Krolik (1999) and references therein. By setting the outward radiative force equal to the inward force of gravity, we obtain a theoretical minimum mass given the assumption of spherical accretion of Hydrogen gas. Specifically we use:

$$L_{Edd} = \frac{4\pi cGM_{BH}\mu_e}{\sigma_T} = 1.51 \times 10^{38} \frac{M_{BH}}{M_\odot} \text{ergs}^{-1} \quad (4.4)$$

Where σ_T is the Thompson cross section of an electron and μ_e is the mass per unit electron. By substituting the observed bolometric luminosity into this above equation and rearranging we obtain an expression for the minimum Eddington mass (M_E):

$$\frac{M_E}{M_\odot} = \frac{L_{Bol}(\text{ergs}^{-1})}{1.51 \times 10^{38}}. \quad (4.5)$$

The actual mass of the SMBH will be related to the Eddington minimum mass via a simple relation:

$$M_{BH} = M_E/\mu \quad (4.6)$$

where

$$\mu = L_{Bol}/L_{Edd}. \quad (4.7)$$

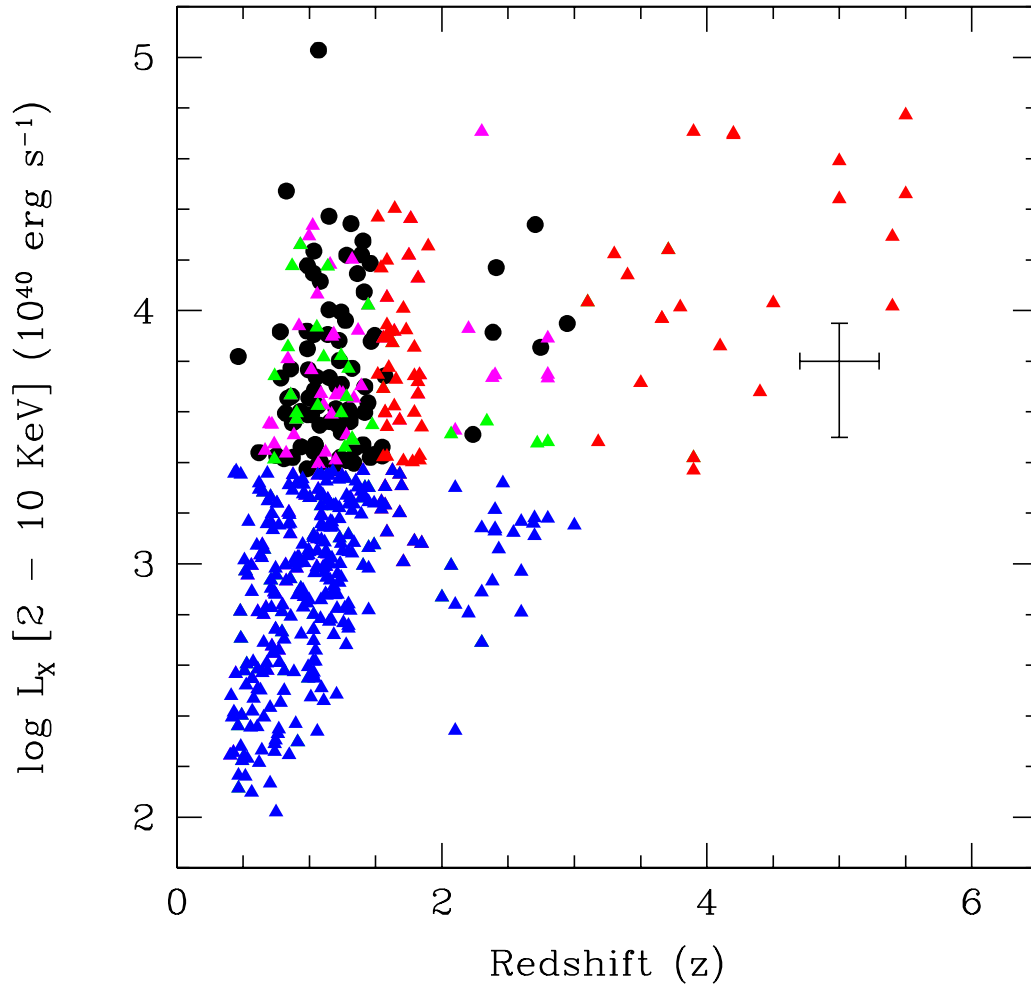


Figure 4.4: Hard band luminosity vs. redshift for the 508 AGN detected in this chapter. Red points indicate those AGN excluded from our volume limited sample due to our redshift cuts, blue points are disregarded due to our X-ray Luminosity limits, green points are disregarded for some analyses due to our host galaxy stellar mass cuts, and magenta points are removed due to lying in areas of the X-ray surveys that are not complete to our luminosity threshold. The remaining black points constitute our volume limited sample of 85 AGN with $L_X > 2.35 \times 10^{43} \text{ erg s}^{-1}$, $M_* > 10^{10.5} M_\odot$ at $0.4 < z < 3.0$, within the most sensitive regions of the Chandra surveys.

This is such that the Eddington mass (which can be computed directly from the bolometric luminosity) is equal to μM_{BH} , where μ is effectively the efficiency of the SMBHs accretion: the fraction of the bolometric luminosity to the Eddington maximum. If $\mu = 1$, the SMBH is at the limit at which it can hold onto its accretion disc. If, for example, $\mu = 0.1$, this implies that the SMBH is radiating at 10% of its Eddington limit. In the local Universe the average value of μ is found to be between 0.01 and 0.05 (e.g. Marconi et al. 2004).

The mass accretion rate of a SMBH may be calculated by:

$$\dot{M} = \frac{dM_{BH}}{dt} = \frac{L_{Bol}}{c^2\eta} \quad (4.8)$$

Where η is the efficiency of mass transfer into electromagnetic radiation. If $\eta = 1$, there is 100% transfer of mass into radiation. The parameter η is restricted in value via theoretical arguments, and may in fact vary from 0.07 - 0.36 (see Thorne 1974), with an expected mean of $\eta = 0.1$ which is not predicted to evolve with redshift (Elvis et al. 2002). This has been observationally confirmed in a variety of studies, including Yu & Tremaine (2002), Elvis et al. (2002) and Marconi et al. (2004).

In this chapter we factor μ out of our mass estimates, plotting μM_{BH} ($= M_E$) instead, and display the local relation as a function of μ . We take $\eta = 0.1$ at all redshifts in line with the latest local Universe observations and theoretical arguments (Thorne 1974, Elvis et al. 2002), but note that this may provide an additional source of uncertainty in our results if η is permitted to evolve with redshift. We are now in a position to derive lower bounds on the SMBH masses ($M_E = \mu M_{BH}$) and actual mass accretion rates (\dot{M}) for the 508 AGN we have detected, and utilise the volume limited sample of 85 ‘Seyfert’ galaxies to probe possible evolution over cosmic time. In the following section we investigate how these properties vary as a function of stellar mass of host galaxy, and as a function of redshift. A table displaying the Eddington masses, X-ray hard band luminosities, stellar mass of host galaxies, and redshifts of our volume limited sample is provided in Table B3. The average properties of both the full AGN sample, and volume limited ‘sefvert’ sample are given in Table B2. Both tables may be found in Appendix B.

4.5 Results

4.5.1 The Active Fraction

The fraction of a given population of galaxies that are X-ray active above a certain luminosity threshold can prove an interesting probe of both galactic evolution and SMBH formation. In this section we define ‘active’ to be X-ray activity with hard band X-ray luminosities $L_X > 2.35 \times 10^{43} \text{ erg s}^{-1}$, where we are complete to $z = 3$. We derive the

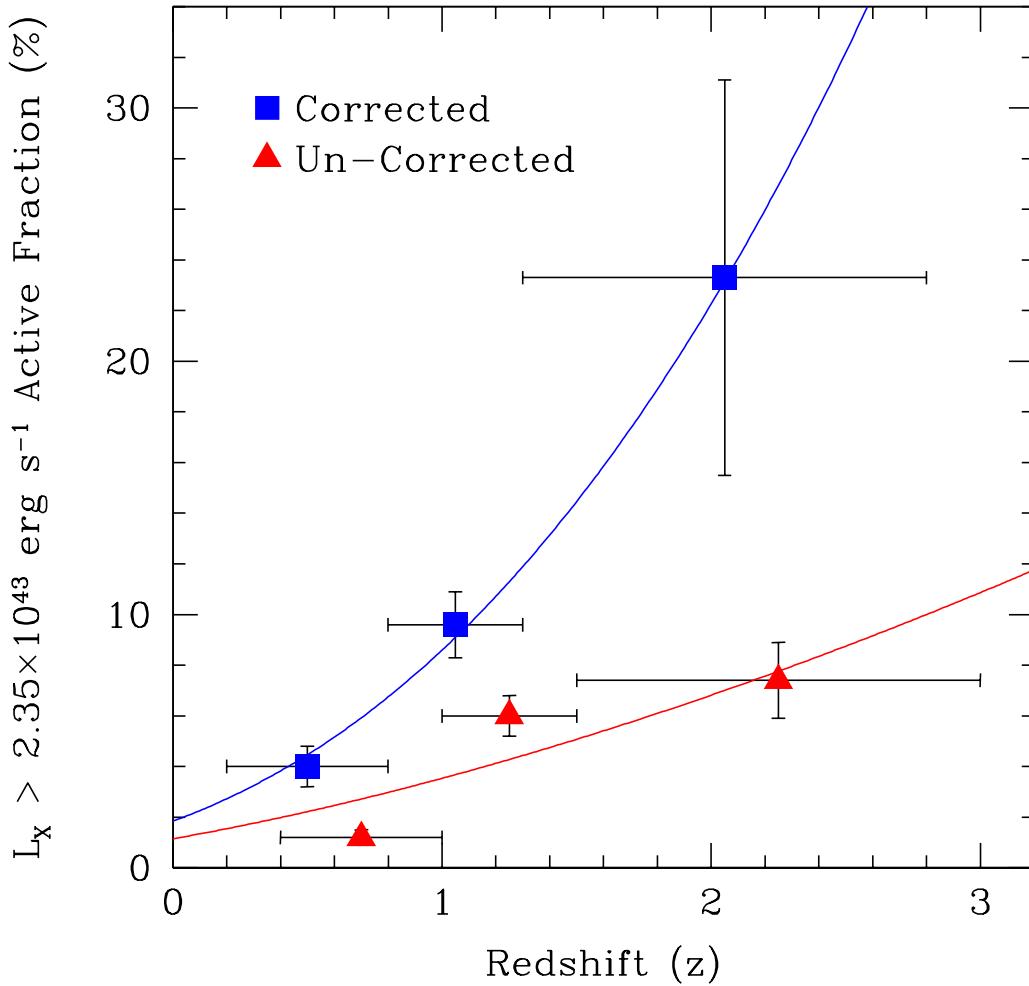


Figure 4.5: The active fraction evolution with redshift. Red triangles indicate active fractions calculated directly from our galaxy sample (§4.5.1), with blue squares being minimum corrected active fractions taking into account the maximum amount of time any given galaxy will remain active ($L_X > 2.35 \times 10^{43} \text{ erg s}^{-1}$) and the time interval within the redshift range probed (see §4.5.4.2 for more details). The blue squares are shifted slightly to the left for clarity. The solid lines indicate a best fit power law to the data, with exponents of 1.6 ± 0.3 for the explicit (un-corrected) active fraction evolution, and 2.5 ± 0.2 for the corrected active fraction evolution.

active fraction of massive galaxies by simply computing the fraction of galaxies within the area, redshift, and mass range of our volume limited sample, from the NIR surveys, that have X-ray luminosities above this threshold, as seen by matching to the Chandra surveys. We note here that this will give a sub-QSO active fraction, since point like sources and sources without galaxy like colours are removed from our galaxy catalogs prior to matching, allowing us to compute reliable stellar masses and photometric redshifts (see §4.2 and §4.4.1 for further details). The fractions we compute must be considered as lower limits due to the possibility of missing active galaxies with torus

opening angles that lead to very high obscuration even in the hard band probed.

At $0.4 < z < 1.0$, for galaxies with $M_* > 10^{10.5} M_\odot$, we find 23 ‘Seyfert’ galaxies (with $L_X > 2.35 \times 10^{43} \text{ erg s}^{-1}$) in our sample. This is out of a total of 1939 detected galaxies in this stellar mass and redshift range, and within the area covered to completion by both surveys (see Fig. 4.1 for clarification). Thus, we find $1.2 \pm 0.2 \%$ of these galaxies to have an active galactic nucleus with $L_X > 2.35 \times 10^{43} \text{ erg s}^{-1}$. This is found to evolve with redshift, such that at $1.0 < z < 1.5$ within the same luminosity and mass range we find a total of 53 Seyfert galaxies out of a total number of 889 detected galaxies in this redshift and stellar mass range, and within the area covered to completion by both surveys. Thus, we find $6.0 \pm 0.8 \%$ of these galaxies to be active with $L_X > 2.35 \times 10^{43} \text{ erg s}^{-1}$ at $z \sim 1.25$.

For the higher redshift points we use a mix of the Chandra Deep Field North/ South and GNS, where the Chandra data covers the totality of the area probed. At $1.5 < z < 3$, for $M_* > 10^{10.5} M_\odot$, we find a total of 9 ‘active’ galaxies, as defined above. This is out of a total population of 121 galaxies in this redshift and stellar mass range, and within the area covered to completion in both surveys (see Fig. 4.2 for clarification). Therefore, we find an active fraction of $7.4 \pm 2.0 \%$ in our high redshift sample. Thus, there is evidence of evolution, whereby the fraction of AGN above our luminosity threshold is larger at higher redshifts in our sample. In fact the active ($L_X > 2.35 \times 10^{43} \text{ erg s}^{-1}$) fraction rises with a 3σ significance between the first two redshift bins, with no significant observed evolution (within the errors) thereafter.

These fractions are considerably lower than the ones deduced in Yamada et al. (2009) for high mass galaxies ($M_* > 10^{11} M_\odot$) for lower X-ray luminosities. They find 33 % of their high mass galaxies to have specific X-ray luminosities within the range $L_X = 10^{42} - 10^{44} \text{ erg s}^{-1}$. It is pertinent to note, however, when comparing the results in Yamada et al. (2009) on the active fraction of massive galaxies to the active fractions presented in this chapter, that we probe a much higher luminosity regime with $L_X > 2.35 \times 10^{43} \text{ erg s}^{-1}$ used as our selection, where we are far more complete in X-ray sources out to high redshifts. However, our results agree with the active fraction of comparable mass ($M_* > 10^{11} M_\odot$) galaxies at $z \sim 1$ of 5 % calculated in Conselice et al. (2007) using similar X-ray luminosity limits to this chapter.

In Fig. 4.5 we plot the observed active fraction evolution with redshift, and add to this the true (corrected) active fraction evolution (calculated in §4.5.4.2). We note that both the active fraction and corrected active fraction rise with redshift across all redshift ranges probed (except possibly in the highest uncorrected redshift bin). We find a best fit simple power law to the active fraction evolution with redshift of $f(L_X > 2.35 \times 10^{43} \text{ erg s}^{-1}) = (1.2 \pm 0.3)(1+z)^{(1.6 \pm 0.3)}$. But note here that it is not a particularly good fit to the data, partially as there is an apparent levelling off at high redshifts.

4.5.2 SMBH Mass Evolution

4.5.2.1 The Local $M_{BH} - M_*$ Relation

As described in the introduction to this chapter (§4.1), relations have been found to exist between the global properties of galaxies and the SMBHs that reside within their cores (see also §1.3.1). In particular, Kormendy & Richstone (1995) find a relation between the luminosity of host galaxies and the mass of the SMBHs that reside within them. Furthermore, relations have also been demonstrated to exist between the stellar mass of host galaxies (or bulge mass for disc galaxies) and the mass of their central SMBHs. The most recent and accurate of these relations is found in Haring & Rix (2004) to be:

$$\begin{aligned} \log(M_{BH}/M_\odot) &= (8.20 \pm 0.10) \\ &+ (1.12 \pm 0.06) \times \log(M_*/10^{11}M_\odot) \end{aligned} \quad (4.9)$$

This approximates closely to $M_*/M_{BH} \sim 1000$ for local ($z < 0.1$) Universe AGN, which we use frequently throughout this chapter as an approximation (see also Haring & Rix 2004). Treu et al. (2007) explore the possible evolution in the $M_{BH} - \sigma$ relation concluding that there is up to a factor of 2 difference in expected mass whereby SMBHs are more massive than expected from the local scaling relations for their host galaxy properties by $z \sim 0.4$. We investigate this further, via novel techniques, out to $z \sim 3$.

The purpose of this section is to test whether or not this local $M_{BH} - M_*$ relation holds at higher redshifts. To test this we have computed Eddington limiting masses

for our volume limited sample of 85 ‘Seyferts’ at $z < 3$, with reliable stellar mass estimates from optical + NIR data (see Table B3). We plot the Eddington limiting (minimum) mass for the SMBH against stellar mass of the host galaxy in three redshift ranges, $0.4 < z < 1.0$, $1.0 < z < 1.5$ and $1.5 < z < 3.0$ (see Fig. 4.6). The error bars included represent average composite 1σ errors on the data, derived from Monte-Carlo simulations (see §4.3.2 for details). For the mass points we make no assumption about the value of the Eddington ratio, μ , but plot as lines where the local $M_{BH} - M_*$ relation would lie with varying values of μ from 0.01 to 1.

4.5.2.2 Evolution: Assuming a Constant $M_{BH} - M_*$ with redshift

In this section we follow an approach similar to that of Babic et al. (2007) who investigate the Eddington ratios of SMBH accretion discs through assuming a constant $M_{BH} - M_*$ relationship with redshift, but expand this from $z < 1$ to $z < 3$, increasing the number of sources studied. Furthermore, by linking AGN to their host galaxies, we also compute the maximum allowable departure from the local $M_{BH} - M_*$ relationship at high redshifts. Within this subsection we restrict our analyses to the volume limited sample of ‘Seyfert’ galaxies where we are complete to $z = 3$, and redshift selection biases are adequately removed.

In order to interpret our μM_{BH} vs M_* points in Fig. 4.6 we must make assumptions about either the Eddington fraction, μ , or evolution in the $M_{BH} - M_*$ relation. As such, mean values of μ are calculated across our three redshift ranges, from low to high z , after assuming that the local $M_{BH} - M_*$ relation is the same at all redshifts, giving: $\mu = 0.056 \pm 0.01$ at $z = 0.4 - 1$, $\mu = 0.087 \pm 0.011$ at $z = 1 - 1.5$, and $\mu = 0.081 \pm 0.019$ at $z = 1.5 - 3$. In comparison, Panessa et al. (2006) find that massive galaxies in the local Universe have a mean value of $\mu < 0.01$ across a wide range of X-ray luminosities (larger than the range probed in this chapter), and Vasudevan et al. (2009) find a mean value of $\langle \mu \rangle = 0.034$ at comparable X-ray luminosities to our sample. Furthermore, we compute an average value for μ for local Universe AGN, within our X-ray luminosity and stellar mass of host galaxy ranges based on data from O’Neil et al. (2005), finding $\langle \mu \rangle = 0.03 \pm 0.015$.

Thus, from an analysis of the mean alone our results suggest some modest increase in

μM_{BH} vs M_* with redshift. This represents a 3σ significant rise in the mean Eddington ratio with redshift between our first two redshift bins, assuming a constant $M_{BH} - M_*$ relation at all redshifts, followed by an apparent levelling off from the intermediate to high redshift bin - where the two highest redshift bins have $\langle \mu \rangle$ equivalent to within 1σ . This may be interpreted as a rise in μ with redshift, requiring no further evolution in the local $M_{BH} - M_*$ relation. If this is so, we are witnessing modest evolution in the Eddington fraction, μ , with redshift from ~ 0.03 in the local Universe to ~ 0.09 at $z = 1 - 1.5$, representing a rise with significance $\sim 3\sigma$ between $z = 0$ and $z = 1.5$ (from Kolmogorov-Smirnoff, KS, test), with no significant further evolution thereafter out to $z = 3$.

4.5.2.3 Evolution: Assuming Constant μ with Redshift

Conversely, we can investigate the maximum allowed evolution in the $M_{BH} - M_*$ relation, assuming no evolution in μ , for our population of ‘Seyfert’ galaxies within our volume limited sample. Since μ is intimately related to the total available fuel for an AGN from cool gas, it is natural to expect it will rise at higher redshifts. Thus, a limit can be placed on evolution in the local relation by setting μ equal to its measured mean value at $z = 0.4 - 1$ of 0.056, because at redshifts higher than $z = 0.4 - 1$, μ is likely ≥ 0.056 due to there being, on average, more available gas as fuel for the SMBHs. Therefore, assuming that there is no evolution in μ with redshift allows us to compute the maximum possible evolution allowable in $M_{BH} - M_*$ from our observed evolution in $\mu M_{BH} - M_*$. From this we compute the maximum evolution in the local ratio M_*/M_{BH} as evolving from 1000 at $z = 0$ (Haring & Rix 2004) to 700 +/- 100 at $z \sim 1.5$, less than a factor of 2. It should be stressed that this is a maximum possible departure from the local Universe $M_{BH} - M_*$ relation at 3σ confidence to lower values. Some, or all, of this observed departure from the local $M_{BH} - M_*$ relation could in fact be driven by evolution in μ , therefore requiring no further evolution in the local relationship.

Crucially, evolution such that $M_*/M_{BH} > 1000$ in the early Universe is unrestrained in this analysis. We can, however, place an upper limit on evolution to higher, as well as lower, values of M_*/M_{BH} by assuming that $\mu = 1$ in the high redshift Universe.

This leads to a maximum positive evolution of approximately a factor of 11 ± 1.5 (assuming no super-Eddington accretion), indicating that $700 < M_*/M_{BH} < 11000$ at $z < 3$. The implication of this is that either SMBHs and their host galaxies grow principally together, or else there is dramatic evolution in μ and SMBHs thus grow after their host galaxies are assembled.

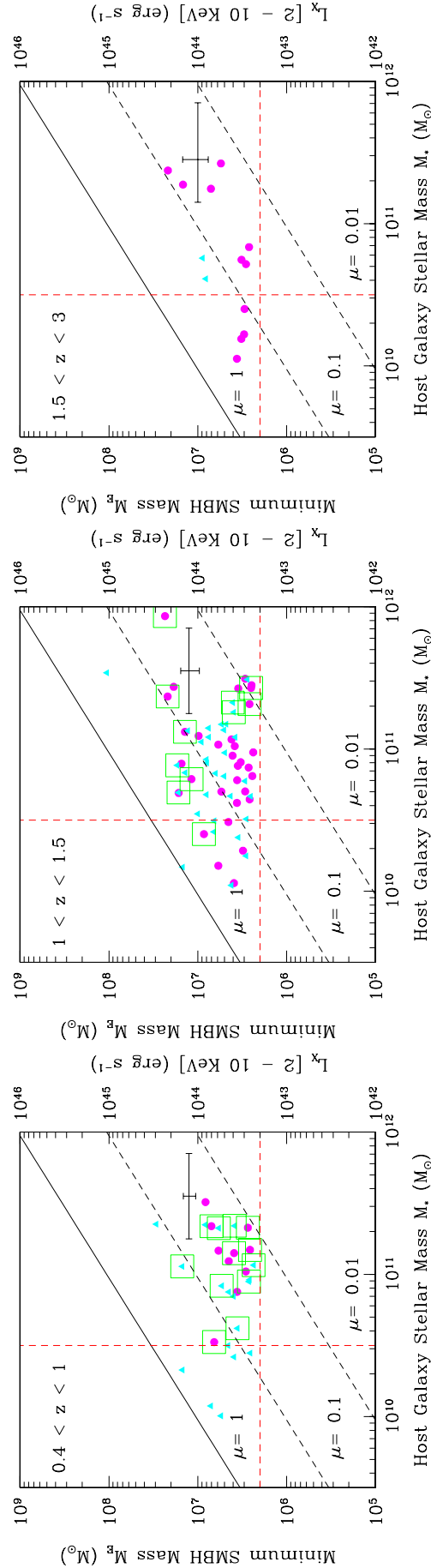


Figure 4.6: The SMBH Eddington limiting (minimum) mass ($M_E = \mu M_{BH}$) plotted against stellar mass (M_*) of the host galaxy across three redshift ranges from left to right, $0.4 < z < 1.0$, $1.0 < z < 1.5$ and $1.5 < z < 3.0$. The error bars represent average 1σ errors based on the composite errors in redshift, stellar mass of the host galaxy, and the hard band X-ray flux from Monte-Carlo simulation (see §4.3.2). We also apply a minimum bolometric correction to ensure that our Eddington masses are true minimum black hole masses (see §4.4.2). We plot the X-ray luminosity on the right of each plot for direct comparison to the data. The solid line is the local relation taken from Haring & Rix (2004), with $\log(M_{BH}) \sim \log(M_*) - 3$. The dashed lines indicate where the local relation would lie for differing values of μ in order to compare our data without making prior assumptions about the μ value. Magenta circles indicate hard X-ray sources with $H > 0.5$, cyan triangles indicate relatively soft X-ray sources with $H < 0.5$ (see §4.5.5 for definition). The green boxes indicate objects with spectroscopically confirmed redshifts. The dotted red lines indicate our luminosity and mass cuts for our volume limited sample, where we are complete across all of the redshift bins for the areas probed. Points that lie below the luminosity threshold of our volume limited sample are removed from these plots for clarity.

4.5.2.4 The High Accretion Fraction

Our mean analysis (above) is somewhat compromised by the fact that at the lower mass end of the host galaxy mass function only AGN with high μ values are visible above our luminosity threshold. This likely drives the apparent flatness of our μM_{BH} vs M_* plots compared to the local relation of Haring & Rix (2004) (plotted in Fig. 4.6 as a solid line), as galaxies with low stellar masses must have high values of μ to be visible in the Chandra observations, whereas this restraint is considerably relaxed for the highest mass galaxies in our sample.

To get a better handle on this potential source of bias, we compute the fraction of Seyferts with $\mu > 0.1$ ($f(\mu > 0.1)$) in each redshift bin, assuming that the local $M_{BH} - M_*$ relation is valid at all z . We obtain for ascending z , $f(\mu > 0.1) = 0.16 \pm 0.03$ at $z = 0.4 - 1$, 0.21 ± 0.02 at $z = 1 - 1.5$ and 0.22 ± 0.07 at $z = 1.5 - 3$. This suggests a hint of a modest (2σ significant) rise (from a KS test) in the fraction of galaxies with $\mu > 0.1$ between $z = 0.4$ and $z = 1.5$, from the un-binned data. There is then no significant evolution from $z = 1 - 1.5$ to $z = 1.5 - 3$. This potential levelling off may be related to the fact that the total X-ray luminosity from AGN peaks around $z \sim 2$ for Seyferts in the Universe (see e.g. Barger et al. 2005, Hasinger et al. 2005, Aird et al. 2009), implying that there should be a similar peak in μ around the same redshift, which is consistent with our results. Interestingly, there is also a peak in the average luminosity of sub-mm galaxies (see Chapman et al. 2003) and star formation rates of massive galaxies (see Bauer et al. 2010, in prep.) at similar redshifts to this.

In conclusion to this section, our results are consistent with no evolution in the $M_{BH} - M_*$ relation with redshift, providing there is mild and plausible evolution in the Eddington ratio, μ , implying that SMBHs and host galaxies grow together throughout cosmic history. Nevertheless, there is a rise in AGN activity represented by an increase in the mean value of the Eddington ratio, μ , out to $z \sim 3$, and a rise in the active fraction of galaxies (seen in §4.5.1) out to $z \sim 3$ as well.

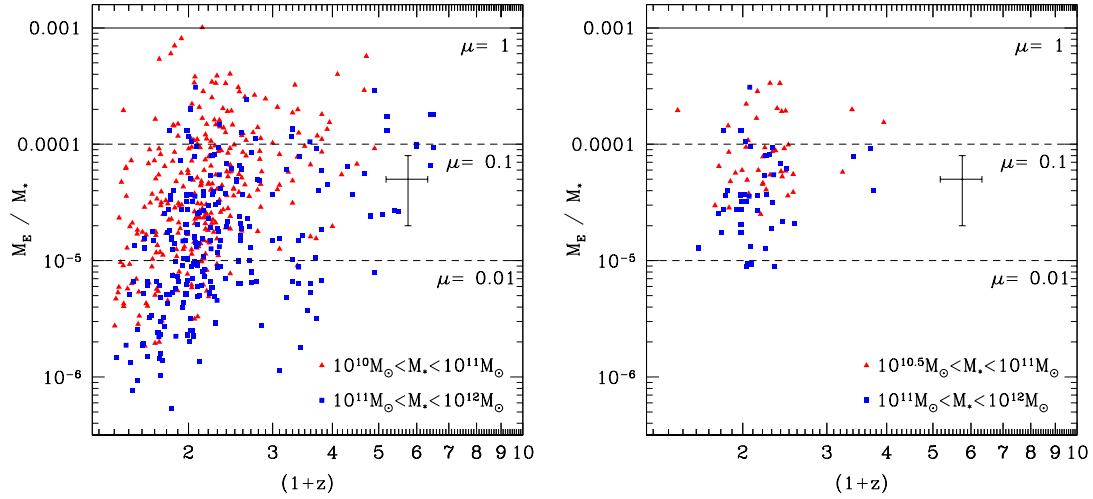


Figure 4.7: The redshift evolution of the ratio of Eddington limiting mass to stellar mass $M_E/M_* = \mu M_{BH}/M_*$. Left plot is for all 508 AGN detected and right plot is for the volume limited sample of 85 ‘Seyferts’. Red triangles indicate low mass ($M_* < 10^{11} M_\odot$) host galaxies, with blue squares indicating high mass ($M_* > 10^{11} M_\odot$) host galaxies. The average 1σ error is plotted in each plot (derived through Monte-Carlo simulation). The solid line represents the local relation of Haring & Rix (2004), with $M_{BH}/M_* \sim 0.001$. The dashed lines show where the local relation would lie for varying values of μ . Note the selection effect whereby lower mass galaxies have higher $\mu M_{BH}/M_*$ ratios at all redshifts. The mean $\mu M_{BH}/M_*$ ratio and dispersion of this also varies with redshift in the left hand plot due to selection effects, leading to higher values and lower dispersions at high z .

4.5.2.5 Stellar Mass Dependence on μ ?

Fig. 4.7 shows the evolution of $\mu M_{BH}/M_*$ with redshift for the whole sample of 508 detected AGN (left) and the volume limited sample of 85 ‘Seyferts’ (right). On the left hand plot there is an apparent evolution in both the mean value of $\mu M_{BH}/M_*$ and the dispersion around the mean. This is largely due to a selection effect driven by the X-ray luminosity limit of the sample. The right hand plot does not show this trend to the same extent because it is volume limited. Nonetheless, there is a tentative rise observed in the mean $\mu M_{BH}/M_*$ value in our volume limited sample from our low redshift bin ($z = 0.4 - 1$) to our intermediate redshift bin ($z = 1 - 1.5$) at $\sim 2\sigma$ confidence (from KS test), with no significant evolution seen thereafter out to the highest redshift range ($z = 1.5 - 3$).

Conversely, if we attempt to fit the volume limited data it becomes clear that our results are consistent with no global evolution in $\mu M_{BH}/M_*$, and we can rule out a steep departure from the local relation at high redshifts, provided there is no dramatic evolution in μ in opposition to the evolution of the $M_{BH} - M_*$ relation. This seems plausible

because the degree of scatter in $\mu M_{BH}/M_*$ is roughly equivalent across all redshift ranges (when the number of points is taken into account), most probably indicative of there being high variety in μ values even out to high redshifts.

In both plots, however, there is a clear separation to 3σ confidence (from KS test) between low mass $M_* < 10^{11} M_\odot$ (red points) and high mass $M_* > 10^{11} M_\odot$ (blue points) host galaxies. This trend may be largely driven by the fact that low mass host galaxies must have relatively high values of μ in order to be detected above our luminosity threshold.

To investigate this further we plot μ vs M_* on the left hand plot of Fig. 4.8, assuming here the validity of the local $M_{BH} - M_*$ relation at all z . The values of μ show a significant decline with increasing stellar mass of host galaxy. The solid line represents the luminosity limit in our sample, and the values of μ are calculated assuming that the local relation holds at all redshifts. Points below the solid line cannot be seen with our X-ray depth. There does, none the less, appear to be a slight dearth of points with high μ at the high stellar mass end. This is most likely partially explained as a feature caused by the lack of very massive galaxies in our sample at high redshifts. In this plot we probe the high end of the distribution in μ and, due to the steepness of the mass function, there are more galaxies populating the low mass end and, hence, it is natural to think that they will reach higher values of μ , simply because there are more of them to randomly populate the plane. Thus, we make no claims regarding possible Eddington ratio, μ , dependence on the stellar mass of host galaxy in this chapter.

4.5.3 Accretion Rate - Stellar Mass Dependence

The local $M_{BH} - M_*$ relation implies that more massive host galaxies will contain more massive SMBHs in their cores. These may in turn accrete at higher rates corresponding to larger Eddington limiting luminosities compared to lower mass systems. Thus, it is natural to expect that there may be a relation between the accretion rate of SMBHs and the mass of their host galaxies. We investigate this possibility here. Since we witness no strong evolution in the local $M_{BH} - M_*$ relation with redshift, with a maximum departure of less than a factor of two to higher SMBH masses for their host galaxy's mass, we investigate the possible dependence of accretion rate on stellar mass across

all of the redshift ranges probed.

We calculate the accretion rate for our sample of AGN as described in §4.4.3 (eq. 4.8). Here we assume a mass to radiation conversion factor of $\eta = 0.1$ (as in e.g. Alexander et al. 2008), in line with common local Universe estimates, theoretical arguments and global X-ray background measures (see Yu and Tremaine 2002, Elvis et al. 2002 and Marconi et al. 2004). We acknowledge, however, that in this part of the analysis our results are subject to some re-evaluation if the value of η is found to vary with redshift and/or mass of the SMBH. We plot these values against their host galaxies' stellar masses in Fig. 4.9. The faint black dots represent the data, with the average 1σ error on the points from Monte-Carlo simulations also plotted in black. The blue squares represent the mean of the data in each redshift range, with the 2σ error on the mean plotted alongside them. The solid red line indicates the best fit power law function to the un-binned data, with $dM_{BH}/dt = 1.8(+/-0.9) \times 10^{-11} M_*^{0.9+/-0.3}$. There is a high degree of dispersion around the best fit line, and we consequently do not use this fit for any further analysis. The high scatter in both plots is most likely due to varying Eddington ratios (μ) at similar host galaxy stellar mass.

Our principal result here is that there is a high degree of scatter in the $\dot{M} - M_*$ plot over and above the intrinsic error for all of our detected AGN (left Fig. 4.9) and for our volume limited sample (right Fig. 4.9). Quantitatively, $\sim 30 \%$ of data points lie beyond 2σ of the best fit line. This notwithstanding, there appears to be a population of very highly accreting SMBHs present only at the high stellar mass end of the total distribution. This is more or less what one would expect, as in the local relationship one finds higher mass SMBHs in higher mass galaxies and, furthermore, more massive SMBHs may accrete at higher rates before shutting themselves off. Quantitatively, we find a modest increase in mean accretion rate with mass for the whole sample: from $0.0054 \pm 0.0005 M_\odot \text{ yr}^{-1}$ for $M_* < 10^{11} M_\odot$ to $0.011 \pm 0.0015 M_\odot \text{ yr}^{-1}$ for $M_* > 10^{11} M_\odot$. For the volume limited case we find that the average accretion rate rises from $0.17 \pm 0.02 M_\odot \text{ yr}^{-1}$ for $M_* < 10^{11} M_\odot$ to $0.26 \pm 0.06 M_\odot \text{ yr}^{-1}$ for $M_* > 10^{11} M_\odot$. From a KS test, the accretion rates of AGN separated via stellar mass, so as to be higher or lower than $M_* = 10^{11} M_\odot$, form distinct populations to a 3σ confidence level in the total sample, with a weaker hint of evolution at the 2σ confidence level for

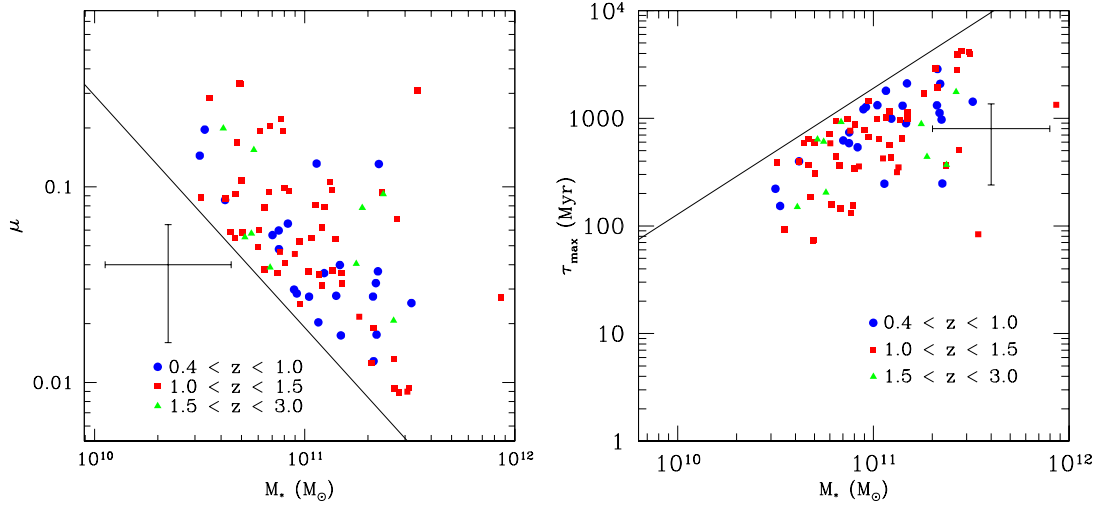


Figure 4.8: Plots of SMBH efficiency μ (left) and maximum time to reach local relation τ_{max} (right) as a function of the stellar mass of host galaxy, for our volume limited sample of 85 ‘Seyfert’ galaxies. μ is calculated assuming the local $M_{BH} - M_*$ relation does not evolve with redshift. τ_{max} is computed by taking $\mu = 1$, thus assuming Eddington accretion, as lower values of μ will lead to lower values of τ . The solid line in both plots indicates the luminosity threshold of our volume limited sample. Differing colour and shape points indicate the different redshift ranges being considered, as stated on the plots. In both plots the black error bars represent average 1σ errors on the individual data points.

the volume limited sample.

4.5.4 Global Properties of AGN

4.5.4.1 AGN Lifetimes

A critical parameter for understanding the evolution of SMBHs is the timescale for which they accrete matter before shutting off. Much work has been performed on constraining the lifetimes of AGN, most commonly for QSOs (e.g. Haehnelt, Natarajan & Rees 1998, Kauffmann & Haehnelt 2000, Yu & Tremaine 2002, McLure & Dunlop 2004, Martini 2003). These studies find rough accord with theory in predicting that the lifetime of QSOs are in the range $10^6 - 10^9$ yrs. The large range in possible values for t_Q are indicative of a great deal of uncertainty in the field. This is in part because robust estimates of the QSO lifetime, t_Q , are often dependent on the Eddington fraction, μ , which to determine directly requires independent measures of the SMBH mass to the AGN X-ray luminosity, which frequently proves extremely difficult to achieve for all but the most local active galaxies.

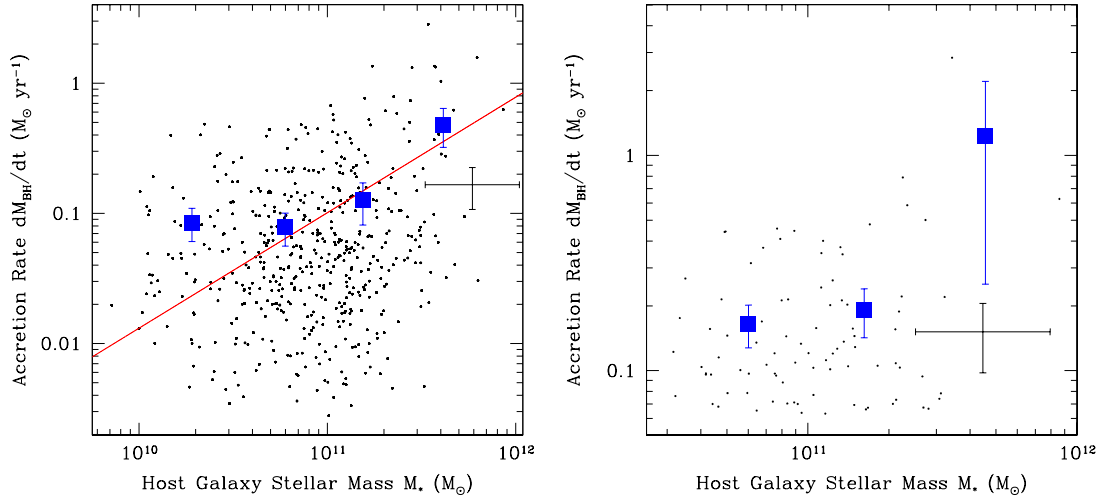


Figure 4.9: On the left is the accretion rate ($dM_{BH}/dt = L_{Bol}/\eta c^2$) plotted against stellar mass of host galaxy for all of our detected 508 AGN. We use $\eta = 0.1$ for all points here to be in line with local Universe values. On the right is the accretion rate (dM_{BH}/dt) plotted against stellar mass of host galaxy for our volume limited sample of 85 ‘Seyfert’ galaxies. Blue squares represent the mean value of the accretion rate in each redshift range, with 2σ errors on the mean plotted alongside them. The black error bars in both plots represent the average 1σ errors on the individual data points. The solid red line is a best fit line to the data with $dM_{BH}/dt = 1.8(+/-0.9) \times 10^{-11} M_*^{0.9+/-0.3}$. Note that very highly accreting AGN are only found at the high stellar mass end in both plots.

Measurements of the probable range of lifetimes allowable from the data for lower luminosity AGN, such as Seyfert galaxies, have also been estimated. Constraints on these measures give $t_S \sim 10^7 - 10^8$ yrs, perhaps shorter than their brighter QSO counterparts (see Martini 2003 for a detailed review). In this section we aim to expand this prior work on AGN lifetimes to more modest X-ray luminosities, looking specifically at ‘Seyfert’ luminosity galaxies over a wide range of redshifts. Furthermore, we propose a novel technique for placing an upper limit on the lifetime of AGN by utilising the local $M_{BH} - M_*$ relation, and assuming that no galaxy can end up lying above the local relation by $z = 0$.

From the accretion rate and measured value of μM_{BH} for each SMBH we calculate the maximum time (τ_{max}) that a SMBH can remain accreting at its current rate before it lies above the local relation, by assuming that it is accreting with an Eddington fraction $\mu = 1$. Values of μ less than this will lead to shorter timescales as this will imply that the actual SMBH mass is closer to the local limit. Further, we also assume that any increase in mass of the host galaxy (i.e. through major mergers) will result in proportional growth of the central SMBH through corresponding black hole merging.

Thus we can write for the maximum time:

$$\tau_{max} = \frac{M_{BH}(z=0) - M_{BH}(z=z')}{\dot{M}} \approx \frac{M_*/1000 - M_E}{\dot{M}} \quad (4.10)$$

$$= \frac{M_*}{1000\dot{M}} - \frac{\eta\sigma_{Tc}}{4\pi G\mu_e} = \frac{M_*}{1000\dot{M}} - 3.75 \times 10^7 \text{ yrs} \quad (4.11)$$

Where \dot{M} is the accretion rate of the SMBH, $M_{BH}(z=0) \approx M_*/1000$ (from the local $M_{BH} - M_*$ relation of Haring & Rix 2004), which is the SMBH's expected mass from the value of its host galaxy's mass at $z=0$, $M_{BH}(z=z')$ is the measured minimum black hole mass at each redshift (z') where $\mu = 1$, M_* is the stellar mass of the host galaxy, and M_E is the Eddington minimum mass. Since M_E and \dot{M} are both proportional to the total bolometric luminosity of the AGN, L_{Bol} , the ratio M_E/\dot{M} is a constant. This constant represents the minimum correction to the lifetime of AGN considering the SMBH's current minimum mass and actual accretion rate. Effectively, the ratio M_E/\dot{M} is the minimum physically allowable time to construct a black hole of a given mass. It is a constant because higher accretion rates would lead to lower timescales, but higher accretion rates also imply a higher minimum Eddington mass which would require a proportionally longer time to form. The combination of this is that the correction factor is constant.

τ_{max} indicates the maximum amount of time that any given AGN can maintain its current level of accretion, at its current X-ray luminosity. This quantity is plotted against stellar mass on the right of Fig. 4.8. One interesting thing to note is that there are some AGN which may continue accreting for a maximum of only a few 100's of Myr at their current rate, with an average maximum lifetime of $\sim 0.9 \pm 0.1$ Gyr in each redshift range. This value of τ_{max} implies that $t_{AGN} < 10^9$ yr for most systems, which agrees favourably with previous independent measures (using differing techniques), and theoretical expectation (see e.g. McLure & Dunlop 2004 and Martini 2003 for a comprehensive review of previous work in the field). Moreover, we can use information about τ_{max} to determine the minimum fraction of galaxies that are likely to accrete above our luminosity threshold throughout the time elapsed in the redshift range probed. This will provide a corrected minimum active galaxy fraction within each redshift range.

4.5.4.2 Corrected Active Fraction

If we assume the cosmological principle and conclude that a snapshot of, for example, Fig. 4.6 were taken in a few hundred Myrs time it would look primarily unchanged, then, from the maximum timescales τ_{max} , we must also conclude that many of the galaxies on the plot will no longer be visible as they must have ceased accreting at that rate so as to not end up higher than the local $M_{BH} - M_*$ relation. Therefore, we deduce the minimum fraction of galaxies that will at some point be visible above our luminosity limit ($L_X > 2.35 \times 10^{43} \text{ erg s}^{-1}$) within the time allotted by a specific redshift range. This is a minimum value because we likely miss some active galaxies within our luminosity range due to very high obscuration along the line of sight for some galaxies as a result of torus opening angles aligned perpendicular to us, and further because we apply the inverse of the maximum lifetime of AGN as calculated in the previous section as a correction factor. We shall call the corrected minimum active fraction f_{true} , which is defined as:

$$f_{true}^{z1-z2} = \frac{t_{z2} - t_{z1}}{\langle \tau_{max} \rangle} f_{obs}^{z1-z2} \quad (4.12)$$

Where f_{obs} is the observed AGN fraction as defined in §4.5.1, $\langle \tau_{max} \rangle$ is the average value of τ_{max} (defined above) in the redshift range being considered, and t_z is the age of the Universe at redshift z , such that $t_{z2} - t_{z1}$ is the time interval between redshifts $z1$ and $z2$.

The total fraction of galaxies expected to have X-ray luminosities above our threshold, therefore, varies with redshift range: At $0.4 < z < 1.0$ it is $4.0 \pm 0.8 \%$, at $1.0 < z < 1.5$ it is $9.6 \pm 1.3 \%$ and at $1.5 < z < 3.0$ it is $23.3 \pm 2.2 \%$. These values may be taken as estimates of the total fraction of massive galaxies expected to reach bright ($L_X > 2.35 \times 10^{43} \text{ erg s}^{-1}$) Seyfert level X-ray luminosities in each of the given redshift ranges for massive galaxies, with $M_* > 10^{10.5} M_\odot$. Naturally, these values are in general higher than the direct measures of AGN fractions calculated in §4.5.1, because the maximum timescales are shorter than the length of time between the redshift limits of each bin. However, both measures of AGN fraction rise with redshift out to $z \sim 3$.

This corrected fraction is plotted in Fig. 4.5 alongside the uncorrected AGN fraction

evolution. The solid blue line represents the best simple power law fit to the data. Explicitly this fit is: $f(L_X > 2.35 \times 10^{43} \text{ erg s}^{-1}) = (1.16 \pm 0.4)(1+z)^{2.5 \pm 0.2}$.

4.5.4.3 The Total Number of Active Galaxies since $z = 3$

A question that has remained contentious, despite several conjectures and studies, is how many galaxies undergo an active phase in their development over the age of the Universe? It is clear that this question will depend on several factors, including the luminosity threshold at which one chooses to define a galaxy as being ‘active’, the lifetime of AGN within this range, the stellar mass range of host galaxies considered, perhaps the environment in which the host galaxy resides, as well as numerous other (frequently ill defined) issues. We are in a position to place a minimum constraint on this question for $M_* > 10^{10.5} M_\odot$ galaxies (from the volume limited subset of the GNS and POWIR NIR surveys), and a definition of active as $L_X > 2.35 \times 10^{43} \text{ erg s}^{-1}$ (from matching with the deepest available chandra X-ray data), since $z = 3$, utilising the maximum lifetimes and apparent active fraction evolution defined and calculated in previous sections (§4.5.1 and §4.5.4.1). This study will provide new limits on the total active fraction out to high redshifts, for ‘Seyfert’ luminosity AGN in massive galaxies.

From our calculations of the average maximum lifetime of an AGN in our sample, and our fitting of the active fraction evolution, we calculate the fraction of $M_* > 10^{10.5} M_\odot$ galaxies that will be AGN (with $L_X > 2.35 \times 10^{43} \text{ erg s}^{-1}$) since $z = 3$. We define the parameter, Γ_{AGN} , in analogy to the characteristic time between galaxy mergers (discussed in Chapters 2 and 3) which may be expressed as:

$$\Gamma_{AGN}(z) = \frac{\langle \tau_{max} \rangle}{f_{AGN}(z)} \quad (4.13)$$

where, f_{AGN} is the observed fraction of AGN at redshift z ($f_{AGN} = 1.2(1+z)^{1.6}$ from §4.5.1), and $\langle \tau_{max} \rangle \sim 0.9 \text{ Gyr}$ is the mean maximum lifetime of AGN over all of the redshifts being considered (i.e. $z = 0 - 3$), and we find no evidence of significant evolution of τ_{max} with redshift. Thus, Γ_{AGN} must be interpreted as a maximum, with its inverse a minimum AGN rate. This is because the apparent active fraction is a minimum and the computed mean lifetime is a maximum. The significance of this

parameter only becomes apparent (unlike Γ for mergers) when we consider the time integral of its inverse. Here, the minimum total fraction of AGN (F_{AGN}) which will accrete with L_X greater than some limit between z_1 and z_2 , may be found by:

$$F_{AGN} = \int_{t_1}^{t_2} \Gamma_{AGN}^{-1}(z) dt = \int_{z_1}^{z_2} \Gamma_{AGN}^{-1}(z) \frac{t_H}{(1+z)} \frac{dz}{E(z)} \quad (4.14)$$

where $\Gamma_{AGN}(z)$ is defined above, t_H is the Hubble time, and $E(z) = [\Omega_M(1+z)^3 + \Omega_k(1+z)^2 + \Omega_\Lambda]^{1/2} = H^{-1}(z)$. Calculating this function from $z = 0$ to $z = 3$, utilising the power law parameterisation $f_{AGN} = 1.2(1+z)^{1.4}$ and taking $\langle \tau_{max} \rangle = 0.9$ Gyr (see §4.5.4.1), we find that $F_{AGN}(z < 3) = 0.41 \pm 0.06$, implying that at least $\sim 40\%$ of all $M_* > 10^{10.5} M_\odot$ galaxies will have been AGN, accreting with hard band X-ray luminosities $L_X > 2.35 \times 10^{43}$ erg s $^{-1}$, over the past ~ 12 Gyrs (since $z = 3$). We note again here that this value is a minimum, and the likelihood is that the true fraction will be higher, perhaps much higher. However, this provides a lower limit to the fraction of massive galaxies which will have undergone an active phase (at bright ‘Seyfert’ X-ray luminosities) since $z = 3$, and can be used to compute further interesting results.

4.5.4.4 The Energy Output of Active Galaxies since $z = 3$

When considering the role of AGN in galaxy formation and evolution, a crucial quantity to know is the total energy released by AGN over their lifetimes. This quantity will impact on the feedback mechanisms involved in the co-evolution of SMBHs and their host galaxies, as well as contributing to our understanding of the X-ray background of the Universe. Almost all previous studies of this quantity have involved probing the evolution of the X-ray luminosity function (XLF) with redshift (e.g. Hasinger et al. 2005, Barger et al. 2005), or equivalently studying the comoving space density evolution of active galaxies with redshift (e.g. Ueda et al. 2003). These studies agree that there is a steep rise in the comoving X-ray luminosity density in the Universe with redshift out to $z \sim 1.5$, with a less steep decline thereafter. This compares well with our results in §4.5.2, where we note a tentative rise in $\mu M_{BH} (\propto L_X)$ with redshift out to $z \sim 1.5$, with a possible flattening off thereafter.

In this section we compute the energy output due to sub-QSO AGN per massive ($M_* >$

$10^{10.5} M_{\odot}$) galaxy in the Universe, by combining the maximum lifetimes of our sample of AGN, the minimum total active fraction of massive galaxies since $z = 3$, and the mean minimum bolometric luminosity of our AGN. Therefore, we can compute the energy released from AGN per massive galaxy as:

$$E_{AGN} = F_{AGN} \times \langle L_{Bol} \rangle \times \langle \tau_{max} \rangle \quad (4.15)$$

where F_{AGN} is the minimum total fraction of galaxies that will be active, with $L_X > 2.35 \times 10^{43} \text{ erg s}^{-1}$, since $z = 3$, $\langle L_{Bol} \rangle$ is the mean minimum bolometric luminosity of our sample of AGN, and $\langle \tau_{max} \rangle$ is the mean maximum lifetime of our sample of AGN, which is $\sim 0.9 \text{ Gyr}$. Since the term F_{AGN} contains a $\langle \tau_{max} \rangle^{-1}$ term, the $\langle \tau_{max} \rangle$ terms in E_{AGN} cancel, yielding an estimate of the true total energy output due to AGN per massive galaxy in the Universe per mean bolometric luminosity. Thus, our value for E_{AGN} is a lower limit to the total energy output due to AGN in massive galaxies, since we use a minimum bolometric correction. Furthermore, this must still be considered a minimum even if we were to use actual bolometric corrections as it does not take into account energy absorbed through Compton thick accretion discs, the host galaxy's interstellar medium (ISM), the local environment, and the intergalactic medium (IGM). Computing this, we find that $E_{AGN} = 1.4 \pm 0.25 \times 10^{61} \text{ erg per } M_* > 10^{10.5} M_{\odot} \text{ galaxy since } z = 3$. This corresponds to an average AGN luminosity density of $L_{AGN} = 1.0 \pm 0.3 \times 10^{57} \text{ erg Mpc}^{-3} \text{ Gyr}^{-1}$

Furthermore, using the Virial Theorem, we can define the binding energy of a galaxy (V_{Gal}) as:

$$V_{Gal} \sim M_{Gal} \times \sigma^2 \quad (4.16)$$

where σ is the velocity dispersion of the galaxy, and M_{Gal} is the total dynamical mass of the galaxy. Assuming an average velocity dispersion of 250 km/s and an average dynamical mass of $10^{11.5} M_{\odot}$ for our galaxies, we find a binding energy of $V_{Gal} = 3.95 \times 10^{59} \text{ erg}$. We define the ratio (r) between these energies such that:

$$r = \frac{E_{AGN}}{V_{Gal}} \sim 35 \quad (4.17)$$

Therefore, the total energy output due to ‘seifert’ level SMBH accretion since $z = 3$ is at least 35 times greater than the binding energy of all $M_* > 10^{10.5} M_\odot$ galaxies in the Universe. This minimum compares very favourably with prior theoretical and observational estimates of the energy emitted in forming a SMBH of $E_{SMBH} \sim 100 V_{Gal}$, found for example in Silk & Rees (1998) and Fabian (1999).

4.5.4.5 The Luminosity Density of Active Galaxies out to $z = 3$ - Explicit and Galaxy Methods

We calculate the comoving X-ray luminosity density evolution for massive galaxies explicitly from the total X-ray luminosities emitted by massive galaxies in our surveys and the total volume to which we are complete. Specifically, we compute the X-ray luminosity density of AGN (ρ_{AGN}) by summing over the survey area and redshift range of our volume limited sample, which is explicitly computed by:

$$\rho_{AGN}(z_1 - z_2) = \frac{1}{V_S} \sum_{j=0}^{j=A_S} \sum_{i=z_1}^{i=z_2} L_X(i, j) \quad (4.18)$$

where,

$$V_S = \frac{A_S}{4\pi} \left(\frac{\pi}{180} \right)^2 V_C \quad (4.19)$$

and

$$V_C = \frac{4}{3} \pi (D_M^3|_{z=z_2} - D_M^3|_{z=z_1}) \quad (4.20)$$

with

$$D_M|_z = D_H \int_0^z \frac{1}{E(z')} dz'. \quad (4.21)$$

Where V_S is the total comoving volume of our surveys to which we achieve mass and luminosity completeness at $M_* > 10^{10.5} M_\odot$ and $L_X > 2.35 \times 10^{43} \text{ erg s}^{-1}$. A_S represents the fraction of each survey’s area to which we are complete, and V_C is the total comoving volume of the Universe between redshifts z_1 and z_2 , computed for a

flat spacetime in a Λ CDM cosmology, as defined in the introduction to this chapter (§4.4.1). $D_M|_z$ is the transverse comoving distance for a flat spacetime out to redshift z , where D_H is the Hubble distance (c/H_0) and $E(z) = [\Omega_M(1+z)^3 + \Omega_k(1+z)^2 + \Omega_\Lambda]^{1/2} = H^{-1}(z)$.

We compute the evolution in the X-ray luminosity density with redshift, finding values of: $7.3 (+/-2.6) \times 10^{38} \text{ erg s}^{-1} \text{ Mpc}^{-3}$ at $z = 0.4 - 1$; $3.1 (+/-1.5) \times 10^{39} \text{ erg s}^{-1} \text{ Mpc}^{-3}$ at $z = 1 - 1.5$; and $5.4 (+/-2) \times 10^{39} \text{ erg s}^{-1} \text{ Mpc}^{-3}$ at $z = 1.5 - 3$. The lower two redshift ranges are in very good agreement with values computed from XLF studies for similar X-ray luminosity ranges to the ones we probe here, as found in Aird et al. (2009). This suggests that the vast majority of the energy contribution to the XLF comes from the most massive galaxies in the Universe at redshifts $z = 0.4 - 1.5$. These values are plotted against the total X-ray luminosity density of all sources in Fig. 4.10.

At $z > 1.5$, however, we obtain a value for the X-ray luminosity density of massive galaxies that exceeds the total X-ray luminosity density computed for all galaxies across all X-ray luminosity ranges in Aird et al. (2009). This disagreement is most likely caused by the fact that the GNS (which we use exclusively to probe high redshifts, $z > 1.5$, due to its high depth) is centred around massive galaxies at high redshifts, thus introducing a systematic bias to observe higher X-ray densities than average in the Universe due to us having higher than representative massive galaxy densities. We estimate our GNS field to be 1.6 times more dense in massive galaxies than the entire (not mass selected) GOODS field (Conselice et al. 2010; Mortlock et al. 2010 in prep.). Once this is taken into account this disparity vanishes (see Fig. 4.10).

In principle this bias can be corrected for by computing the X-ray luminosity density for massive galaxies from a galaxy comoving number density approach, combining the energy output per galaxy and fraction of active galaxies (computed in §4.5.4.3 and 5.4.4) to the comoving number density evolution of massive galaxies from unbiased fields.

From this approach, the average X-ray luminosity density, for the entire redshift range probed ($z = 0.4 - 3$) is $1.5 +/- 0.6 \times 10^{39} \text{ erg s}^{-1} \text{ Mpc}^{-3}$, but this varies with redshift as the active fraction and mean luminosity also vary. i.e the X-ray luminosity density at $z = 0.4 - 1$ it is $6.1 +/- 2.5 \times 10^{38} \text{ erg s}^{-1} \text{ Mpc}^{-3}$, at $z = 1 - 1.5$ it is $4.3 +/- 1.7 \times$

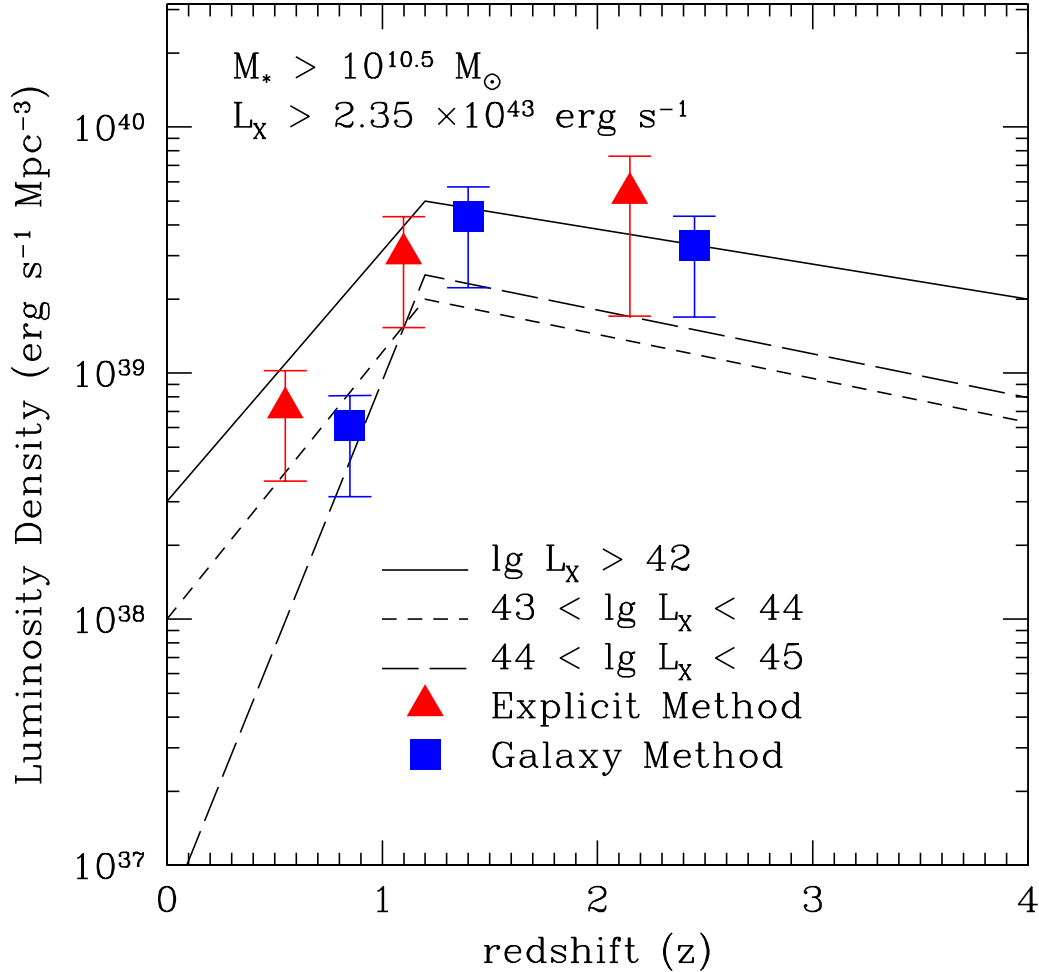


Figure 4.10: The contribution to the X-ray luminosity function of sub-QSO massive galaxies across three redshift ranges, $z = 0.4 - 1$, $z = 1 - 1.5$, and $z = 1.5 - 3$. Our results are broadly consistent with X-ray active sub-QSO massive galaxies being the dominant source of X-ray radiation in the Universe, contributing the majority of the total X-ray luminosity density in each redshift range. Red triangles have luminosity densities computed via an explicit method computing the total X-ray luminosity within a given volume surveyed (see §4.5.4.5 for more details). Blue squares have luminosity densities computed via convolution with the comoving number densities of massive galaxies which agree (to within 1σ) with the explicit method in the lower two redshift ranges, with more significant departure in the highest redshift range due to the fact that the GNS is selected to maximise the density of massive galaxies at $z > 1.7$ in the GOODS field (see §4.5.4.6 for more details). The lines plot are approximate best fit X-ray luminosity functions to the deepest Chandra surveys (CDF-N/S) constructed from data in Aird et al. (2009), where we reproduce only the most relevant luminosity ranges here.

$10^{39} \text{ erg s}^{-1} \text{ Mpc}^{-3}$, and at $z = 1.5 - 3$ it is $3.3 \pm 1.2 \times 10^{39} \text{ erg s}^{-1} \text{ Mpc}^{-3}$. These values compare remarkably well to the calculation from the explicit method above for the lower two redshift ranges, and to calculations of the emissivity from XLF studies in Aird et al. (2009) in particular for all redshift ranges. These values are plotted in Fig. 4.10 alongside those calculated from the explicit method.

We find a rise in X-ray luminosity density with redshift out to $z \sim 1.5$, followed by a levelling off, or probable turn around thereafter. Moreover, we find estimates of the emissivity for AGN with $43.5 < \log L_X < 45$ with a peak value of $\sim 4 \times 10^{39} \text{ erg s}^{-1} \text{ Mpc}^{-3}$ in very close accord with Aird et al. (2009). It is pertinent to note that our estimates of this value are constructed from an independent methodology, and the fact that these different approaches agree is indicative of our ability to place definite precision constraints on the energy outpourings of AGN out to high redshifts, for modest luminosity Seyferts as well as QSOs on a galaxy population basis. Additionally, the corroboration between different methods obtaining comparable results lends further reliability to our estimates of the maximum timescales of AGN in our sample, and the minimum value of the total AGN fraction since $z = 3$. These results also suggest that massive galaxies are the dominant source of X-ray emission in the Universe across all of the redshift ranges probed, $z = 0.4 - 3$, since their contribution to the XLF is almost sufficient to account for its entire magnitude at each redshift.

4.5.5 Hardness-Mass Dependence

The hardness of an X-ray source can prove to be an interesting probe of various aspects of the nature of the AGN. In particular, it can reveal the level of absorption experienced and, hence, is coupled to the $n(\text{H})$ column density around AGN. We investigate here whether there are correlations between the hardness of our X-ray sources and the masses of the host galaxies in which these sources reside. We define hardness, H , as:

$$H = \frac{f_H - f_S}{f_H + f_S} \quad (4.22)$$

where f_H is the hard band flux and f_S is the soft band flux. We crudely define hard X-ray sources as those with $H > 0.5$, and soft X-ray sources as those with $H < 0.5$.

As we look to higher redshifts both the hard and soft bands will become effectively harder. However, for the purposes of this analysis, that effect is not a particularly great problem since at all rest-frame energies probed in this chapter, softer bands will be more prone to absorption than harder bands, and, hence, this hardness ratio will still divide our sample amply between those with high and low levels of absorption. From Fig. 4.6 it is apparent that hard X-ray sources fall systematically below their softer counterparts in units of μM_{BH} . This might be expected as the harder X-ray sources must have experienced greater absorption due to higher $n(H)$ column densities. This effect, however, is small and our results remain primarily unchanged even if we exclude the hard X-ray sources. We have minimised this effect by choosing to use the hard band X-ray data from Chandra where absorption is reduced.

An additional trend may also be noted whereby the harder sources tend to be more biased towards the high stellar mass end of these plots, in the lower two redshift ranges. In the highest redshift range selection effects conspire to lead us to detect predominantly hard X-ray sources and to our measure of hardness being skewed to harder sources generally. To test this we compare the hardness of X-ray sources with the stellar mass of their host galaxies for our lower redshift points.

We ran a KS test finding that the mean mass of host galaxies with a soft X-ray source was $8 \times 10^{10} M_{\odot} \pm 1.5 \times 10^{10} M_{\odot}$, with the mean mass of galaxies with a hard X-ray source being $1.1 \times 10^{11} M_{\odot} \pm 1.5 \times 10^{10} M_{\odot}$, across the lowest redshift ranges. This represents a 97 % chance that the masses of the host galaxies for the hard and soft X-ray sources come from different underlying populations, a significance of $\sim 2 \sigma$.

4.6 Discussion

In this section we give a summary of our results and discuss them in the context of galaxy formation and evolution, and in particular the role of AGN within the evolution of galaxies at $z < 3$.

4.6.1 Evolution in the $M_{BH} - M_*$ Relationship

It is difficult to disentangle the SMBH mass from measures of the Eddington limiting (minimum) SMBH mass, without knowing something about the Eddington ratio, μ . As such, we have retained this source of error within our data and chosen to plot μM_{BH} ($= M_E$) as opposed to M_{BH} in all plots, making no assumption about the actual value of μ , and instead representing this degeneracy by showing the relative position of the local $M_{BH} - M_*$ relation as a function of μ (solid and dotted lines) in Figs. 4.6 and 4.7. We have noted some tentative evidence for evolution in the $\mu M_{BH}/M_*$ ratio with redshift, signifying either a possible departure from the local relationship at higher redshifts, or evolution in the mean value of μ . If we assume that the local relation remains valid at high redshifts then this corresponds to an observed evolution in μ .

The fact that we observe a higher fraction of AGN with $\mu > 0.1$, and a higher mean value of μ , at higher redshifts is probably indicative of the amount of cool gas available in the centre of galaxies decreasing over cosmic time, since the μ ratio is directly related to the available fuel for the SMBH. Where there is unlimited fuel in the form of cool gas at the centre of galaxies, and excellent supply routes to get this fuel into the black hole, one would expect the accretion luminosity to tend towards the Eddington limiting luminosity, giving $\mu = 1$. With a reduction in fuel or supply route efficiency (e.g. through obstruction from outflows) one would expect a lowering in the Eddington ratio. Since galaxies in general decrease their cold gas content over cosmic time due to supernovae (SNe) and AGN feedback, merging, and environmental effects (such as tidal and ram pressure stripping), it is natural to expect a reduction in the mean value of μ over cosmic time (see respectively Brighenti & Mathews 2003, Ciotti & Ostriker 2001, Bluck et al. 2009, Conselice, Yang & Bluck 2009, and Roediger & Hensler 2005).

If evolution in μ exists then there is no requirement for further evolution in the $M_{BH} - M_*$ relation. Thus, our results are consistent with the view that SMBHs and their host galaxies largely co-evolve, increasing their mass in proportion to one another. However, if we take the converse view that there is no evolution in μ then we must conclude that the $M_{BH} - M_*$ relation evolves such that SMBHs had masses higher than expected from the local relation, with regards to their host galaxy's mass, at higher

redshifts. Given that the mean value of μ is expected to rise with redshift in general for massive galaxies, we can quantify the maximum possible evolution in the local $M_{BH} - M_*$ relation by setting μ to be constant at its low redshift value and permitting only evolution in $M_{BH} - M_*$ to account for the observed evolution in $\mu M_{BH} - M_*$. Quantitatively this corresponds to a maximum evolution in the ratio M_*/M_{BH} of less than a factor of two, from ~ 1000 at $z = 0$ to ~ 700 at $z = 2.5$.

This type of evolution to lower M_*/M_{BH} values at higher redshifts seems unlikely as it would imply either that SMBHs lose mass (which is ruled out on theoretical grounds) or else that galaxies grow in size more rapidly than their central black holes. This is also very unlikely as we have observed a sharp decline in merging and star formation rate with redshift (see e.g. chapters 1 and 2 and Bauer et al. 2010) for massive galaxies at redshifts $z < 3$, and moreover SMBHs are expected to grow due to merging in line with their host galaxies. Therefore, we prefer to interpret our results as evolution with redshift of the Eddington ratio, μ , further implying that the available fuel for SMBHs declines over cosmic time, which is explicable within the current paradigm of galaxy evolution. As galaxies evolve they experience feedback from AGN and SNe which both remove the availability of cold gas, and furthermore merging and environmental effects may also contribute to this reduction in cool gas content of galaxies. As such, older galaxies have less available fuel at their centres for their SMBHs and, hence, they accrete at lower fractions (μ) of the Eddington maximum.

One other possibility is that the evolution in μ is dramatic, and thus the local $M_{BH} - M_*$ relationship evolves such that SMBHs were *less* massive than expected for their host galaxies' masses. We can quantify this maximum positive evolution in the M_{BH}/M_* ratio as being \sim a factor of 10, by setting $\mu = 1$, its maximum limit assuming sub-Eddington accretion. Thus, we conclude that either SMBHs evolve more or less in proportion to their host galaxies, or else there is dramatic evolution in μ leading to SMBHs growing later in mass than their host galaxies, through accretion of cool gas.

By way of comparison to the body of literature on the subject of possible evolution in the $M_{BH} - M_*$ relationship with redshift, it is pertinent to note that a wide variety of methods and luminosity ranges have been used and studied, leading to quite a diverse set of conclusions. For example, Borys et al. (2005) find that SCUBA galaxies have

SMBHs which are systematically lower than expected from the local relation for their stellar mass by up to a factor of 50 or so (via Eddington methods), and Alexander et al. (2008) also deduce that for SMGs (sub millimetre galaxies) SMBHs are also smaller than expected for their host galaxy's mass by a smaller factor of 3 or so (via virial methods). However, Jahnke et al. (2009) find that type-1 AGN galaxies from the COSMOS survey fit closely onto the local $M_{BH} - M_*$ slope of Haring & Rix (2004) out to $z \sim 2$. Conversely, recent studies by Merloni et al. (2010) and Declari et al. (2010a,b) using virial estimators of SMBH masses in QSO's both conclude that there is evolution in the local $M_{BH} - M_*$ relation with redshift such that M_*/M_{BH} was lower at high z , by up to a factor of 7 (Declari et al. 2010a,b) or 3 (Merloni et al 2010) by $z = 3$.

Our results are for lower luminosity AGN, principally bright Seyferts, than the majority of studies discussed above, and we rule out positive evolution in the M_*/M_{BH} ratio of greater than a factor of 2, but we do not particularly well constrain evolution to higher values (noting that this must be less than a factor of ~ 10). Despite the inconsistency in luminosity ranges probed and methods used for deducing SMBH masses, there is very broad agreement between all of these approaches that the local $M_{BH} - M_*$ relationship is not departed from by more than roughly one order of magnitude (or a factor of 10) in either direction by $z = 3$. Our study particularly favours a close adherence to the local relationship of Haring & Rix (2004) for bright Seyfert galaxies out to $z = 3$, providing there is not drastic positive evolution in the Eddington ratio, μ , with redshift. If this type of drastic increase in μ does occur then we are forced to conclude that SMBHs in Seyfert galaxies form their mass after their host galaxies, in apparent contradiction to the results for QSO's in Merloni et al. (2010) and Declari et al. (2010a,b), but in accord with the conclusions based on studying SMGs in Borys et al. (2005) and Alexander et al. (2008). Nevertheless, we feel that the most natural conclusion from our results is that SMBHs and their host galaxies evolve principally together, in proportion to one another, preserving the local relation out to $z = 3$, in agreement with Jahnke et al. (2009), as this would require only mild and plausible evolution in μ with redshift.

4.6.2 From AGN Lifetimes to Feedback Energy

We observe that the fraction of AGN above our luminosity threshold ($L_X > 2.35 \times 10^{43} \text{ erg s}^{-1}$) rises with redshift, and that the true fraction, calculated via considering the maximum amount of time a given AGN can continue accreting at its current rate before surpassing the local relation, also rises with redshift. This result reflects the rising mean Eddington ratio with redshift, assuming the validity of the local $M_{BH} - M_*$ relation at all redshifts. Together this may all be interpreted as AGN activity in the Universe rising with redshift, and possibly levelling out at $z \sim 1.5 - 3$ where there is an optimum synergy between the mass of SMBHs and available fuel at the centre of each galaxy. This is consistent with conclusions based on probing the X-ray luminosity function (XLF), in e.g. Ueda et al. (2003), Barger et al. (2005), Hasinger et al. (2005) and Aird et al. (2009), who all find a similar rise and then peak in X-ray luminosity within a similar redshift range.

We have constructed a novel method for estimating the maximum lifetimes of Seyfert luminosity AGN. Using the timescales calculated from considering the maximum accretion permitted before a given AGN will rise above the local $M_{BH} - M_*$ relation, we have calculated the total fraction of $M_* > 10^{10.5} M_\odot$ galaxies which will be active, with $L_X > 2.35 \times 10^{43} \text{ erg s}^{-1}$, since $z = 3$. We find that at least 40% of all massive galaxies will reach Seyfert level luminosities from accretion onto their central SMBHs. Perhaps all massive galaxies will undergo an active period in their evolution since $z = 3$, but currently we can only be sure that at least a significant fraction will obtain this level of X-ray activity.

Moreover, we have computed the energy density due to seyfert luminosity AGN residing within massive galaxies in the Universe as $\rho_{AGN} = 1.0 \pm 2.5 \times 10^{57} \text{ erg Mpc}^{-3} \text{ Gyr}^{-1}$, noting that this corresponds to an average massive galaxy producing at least a factor of ~ 35 times its binding energy in AGN emission. Further, we compute the X-ray luminosity density from this method and note that it rises with redshift from $6.1 \pm 2.5 \times 10^{38} \text{ erg s}^{-1} \text{ Mpc}^{-3}$ at $z = 0.4 - 1$ to $4.3 \pm 1.7 \times 10^{39} \text{ erg s}^{-1} \text{ Mpc}^{-3}$ at $z = 1 - 1.5$, with a slight reduction to $3.3 \pm 1.2 \times 10^{38} \text{ erg s}^{-1} \text{ Mpc}^{-3}$ at $z = 1.5 - 3$, in very close accord to other, alternative, XLF based methods, including Aird et al (2009). In fact in Fig. 4.10 we compare the total X-ray luminosity density in the Uni-

verse at various redshifts (found in Aird et al. 2009) to the contribution provided by sub-QSO massive Seyfert luminosity galaxies (this chapter), finding that the majority of the X-ray luminosity density of the Universe is provided by this population at all redshifts up to $z = 3$.

It has been known for some time that the energy outpourings of AGN will be greater than the binding energy of their host galaxies (see e.g. Silk & Rees 1998, Fabian et al. 1999), but in this chapter we have constrained this empirically per galaxy, as opposed to per AGN. We now know that not only will active galaxies have a greater energy output by their AGN than their total binding energy by some large factor (up to 100 fold according to Fabian et al. 1999), but that the energy released by AGN (even primarily in the Seyfert regime) is at least 35 times greater than the binding energy of all massive ($M_* > 10^{10.5} M_\odot$) galaxies in the Universe. However, it is clear that the crucial question still to be answered is, what fraction of this energy couples to the galaxy? What we measure is the energy that escapes the galaxy to be later detected by us, whereas what matters for considerations of AGN feedback on star formation (and as a possible driver for size evolution) is what magnitude of energy couples to the galaxy itself through radiative or momentum driven processes. To improve these minima, apply them to average mass galaxies, and develop a deeper understanding of the coupling of AGN emissions to galaxy evolution, we shall have to wait for next generation X-ray telescopes and surveys, as well as the JWST.

4.7 Summary and Conclusions

In this chapter we have detected 508 X-ray selected AGN at $0.4 < z < 6$ across the EGS and GOODS North and South fields, using the criteria set out in §4.4.1. We have constructed a volume limited sample of 85 galaxies with $L_X > 2.35 \times 10^{43} \text{ erg s}^{-1}$ and $M_* > 10^{10.5} M_\odot$ at $0.4 < z < 3$, with which we probe the co-evolution of SMBHs and their host galaxies over the past 12 billion years. We adopt an Eddington limit method to obtain minimum mass estimates for the SMBHs residing at the centre of these active galaxies and compare these values to stellar masses of the host galaxies as a function of redshift (see §B for data tables). We find an active fraction of $1.2 \pm 0.2 \%$ at $0.4 <$

$z < 1$, which rises to $6.0 \pm 0.8 \%$ at $1 < z < 1.5$, with a further modest rise to $7.4 \pm 2.0 \%$ at $1.5 < z < 3$.

We probe the $\mu M_{BH} - M_*$ relation across three redshift ranges (see Fig. 4.6) and find that this relation appears in general lower in value, and less steep, than the local $M_{BH} - M_*$ relation. We interpret these differences as lying with our inability to detect low mass host galaxies accreting with small values of μ and, further, interpret the offset between the local $M_{BH} - M_*$ relation and our measured $\mu M_{BH} - M_*$ relation as a modest evolution in μ . In particular, we measure the fraction of high accreting SMBHs, accreting with $\mu > 0.1$ (assuming the local relation's validity at $z > 0$), to rise from $\sim 17\%$ at $z = 0.6$ to $\sim 22\%$ at $z \sim 2.5$ (representing a 2σ evolution).

We calculate accretion rates for our sample of AGN and plot the results of this in Fig. 4.9. We find that there is a high degree of scatter in the accretion rate across all redshifts and stellar masses. Nonetheless, we identify a population of galaxies with very high accretion rates which are only found in high stellar mass galaxies. Moreover, we find that higher mass host galaxies contain higher accreting AGN to a 3σ significance. This is to be expected because more massive galaxies are predicted to contain more massive SMBHs which may accrete at a higher rate.

Further, we calculate maximum timescales at which AGN in our sample can continue to accrete at their current rate, noting that many of these timescales are quite short, with maximum values \sim a few 100 Myrs, and an expectation value of $\langle \tau_{max} \rangle \sim 0.9$ Gyr. From this we calculate the true corrected fraction of ‘Seyfert’ luminosity AGN in each redshift range, observing that it also rises with redshift.

Perhaps our largest contribution in this chapter is computing a minimum fraction of galaxies at $M_* > 10^{10.5} M_\odot$ that will contain ‘Seyfert’ luminosity AGN at some point over the past 12 Gyrs (since $z = 3$). We find that at least $\sim 40\%$ of all massive galaxies will at some point during their evolution between $z = 3$ to the present be active with $L_X > 2.35 \times 10^{43} \text{ erg s}^{-1}$. We also compute the X-ray luminosity density evolution due to massive galaxies, with Seyfert luminosities and brighter, from our sample of AGN, finding a close agreement with the latest estimates of the total X-ray luminosity density evolution from distinct X-ray luminosity based methods (e.g. Aird et al. 2009). This suggests that the majority of the X-ray luminosity function is generated by massive

sub-QSO massive galaxies.

Moreover, we use this total active fraction at ‘Seyfert’ luminosities to compute the average energy output due to AGN per galaxy, and note that this is at least 35 times greater than the binding energy of an average massive galaxy. This is consistent with several previous studies in the literature (e.g. Silk & Rees 1998, Fabian 1999). We extend this prior work quoting this minima empirically and for each massive galaxy in the Universe, as opposed to each AGN. The impact of this much energy being released into the galaxies, as well as into the surrounding large scale environments, might have a profound influence on galaxies’ formation and evolution through AGN feedback. But a crucial question remains: how much of this energy couples to the host galaxy through radiative or momentum driven processes, actually causing the feedback on star formation?

In conclusion, we have provided tentative evidence for the necessity of redshift evolution in μ to account for our data trends: μ may evolve with redshift to higher values, indicating that galaxies at higher redshifts were more rich in the cold gas used as fuel by the SMBH. Furthermore, we note a significant increase in the AGN fraction with redshift which is also indicative of overall AGN activity rising with redshift, as seen previously in many studies of the evolution of the X-ray luminosity function (e.g. Barger et al. 2005, Hasinger et al. 2005). Thus, there is most probably a rise in AGN luminosity out to $z \sim 1.5 - 2$, with a possible levelling off thereafter to $z = 3$, driven perhaps by an optimal balancing of available fuel and mass of SMBHs. Our results are consistent with no change in the local $M_{BH} - M_*$ relation, providing there is modest and plausible evolution with redshift in μ . Furthermore, we place a maximum limit on possible evolution in the M_*/M_{BH} ratio of less than a factor of two to lower values, and less than a factor of ten to higher values, for massive galaxy ‘Seyfert’ luminosity AGN. Therefore, we suggest that SMBH masses and their host galaxy stellar masses evolve together, in direct proportion to one another, or else there is a dramatic increase in the Eddington ratio with redshift and, thus, SMBH masses are built up after their host galaxies.

Chapter 5

Conclusions, Summary, and Future

Work: How do Massive Galaxies

Change with Age?

5.1 Conclusions

This thesis concentrates on several of the many ways in which massive galaxies and their supermassive black holes change over cosmic time. Ultimately, the purpose of this research is to begin to write a history of massive galaxies, including when and how they form, what the major changes that they experience are, what the role of galaxy - galaxy interactions are in the evolution of massive galaxies, and, finally, how supermassive black holes shape the galaxies they inhabit. To begin to address these questions, a plethora of data across the electromagnetic spectrum (X-ray - IR) from ground and space based telescopes has been utilised, including the HST GOODS NICMOS Survey (GNS), which images to unprecedented depth and area a region of the GOODS field in the rest frame optical at $z \sim 2$. What follows in this section is a list of primary conclusions from this work. More detailed conclusions on the individual work is provided at the end of each research chapter (Chapters 2 - 4).

5.1.1 Galaxy - Galaxy Interactions

In Chapter 2 (also see Bluck et al. 2009) the major merger history of massive galaxies (with $M_* > 10^{11} M_\odot$) is explored over the past 12 billion years (up to $z \sim 3$). The principal discovery here is that the merger fraction for extremely massive galaxies continues to rise monotonically with redshift out to at least $z = 3$. In particular, we find that the merger fraction of massive galaxies scales with redshift as $f_m \sim (1+z)^3$. This implies that these objects were in a state of rapid assembly at high redshifts. If galaxies form primarily in line with hierarchical assembly, via the merging of dark matter halos, then this high merger fraction implies that many of the largest halos at high redshifts are highly interacting, and, thus, in a sense, forming. For lower mass galaxies we have seen that the merger fraction peaks at lower redshifts ($z < 2$, see Chapter 2 and Conzelice et al. 2007a). Therefore, we witness a version of downsizing whereby the peak in merger activity for massive galaxies occurs earlier than that of smaller galaxies. This forms a close analogy to the star formation rate downsizing observed in the local Universe, whereby the specific star formation rates of lower mass galaxies are frequently higher than their high mass counterparts. Although these effects may seem in appar-

ent contradiction to a naive interpretation of hierarchical assembly, these trends can be explained largely within this paradigm. This is because within hierarchical assembly the galaxies that form first are in the densest regions of space, thus they rapidly merge, often forming quite large systems by fairly early times; whereas those small galaxies we witness at low redshifts must have formed in lower density regions where merger activity must have been slower, and, therefore, it may persist to later times, and even to the present day. For further discussion of this issue, and the impact of the work performed in Chapter 2 on testing the Λ CDM model through galaxy observations please see Bertone & Conselice (2009).

Another issue considered in Chapter 2 and in Chapter 3 (also see Bluck et al. 2009 and Bluck et al. 2010b), is the methodology of assigning the definition ‘major merger’ to a galaxy - galaxy system. The two principal approaches utilised were morphological (CAS) and statistical (close pair) in nature. We find a close accord between these two methods at apertures at $d < 30$ kpc, and for the standard optical definition of a CAS selected major merger ($A > 0.35$ & S, see Chapters 2 and 3). This implies that both methods trace the underlying merger activity, and, moreover, share a similar mass range and timescale sensitivity. This is estimated by N-body simulations to be a mass range of $\sim 1:4$ by stellar mass, and a timescale of ~ 0.5 Gyrs (see Lotz et al. 2008a, 2010). In Chapter 3 this work is extended out to $z = 3$, where we conclude that $\sim 1/4$ of all massive galaxies at high redshifts are highly morphologically disturbed and, furthermore, fit the definition for a CAS defined major merger, in close agreement to the conclusions from pair statistics in Chapter 2. This lends further credence to our claims in Chapter 2 that massive galaxies form early and are in a high state of growth by $z > 2$.

At the end of Chapter 2 we estimate that there are $N_m = 1.7 \pm 0.5$ major (1:4 by stellar mass) mergers between massive galaxies (with $M_* > 10^{11} M_\odot$) between $z = 3$ and the present, which will correspond to a mass increase of $\Delta M_* \sim 2 \times 10^{11} M_\odot$. At the end of Chapter 3 we deduce that the total number of mergers with $M_* > 10^9 M_\odot$ galaxies which an average massive galaxy experiences over the past 12 Gyrs is $N_m = 4.5 \pm 2.1$, assuming an average merger timescale $\tau_m \sim 1$ Gyr. This gives rise to a mass increase of $\Delta M_* \sim 3 \times 10^{11} M_\odot$. Therefore, we suggest that major mergers

dominate over minor mergers in the formation and evolution of massive galaxies from $z = 3$ to the present, since they contribute the majority of the total stellar mass increase.

Throughout Chapter 1 and parts of Chapter 2 we have established the importance of both major and minor merging in massive galaxy formation and evolution over the past 12 billion years. In particular, we note a total mass increase of \sim a factor of three during this time period, and consider in the following subsection (§5.1.2) the role this might have in driving the size, and volume, increase of massive galaxies over cosmic time.

5.1.2 Size Evolution

One of the most exciting and highly disputed discoveries of recent times in astrophysics, is the dramatic size evolution of massive galaxies over the past 12 billion years or so (see e.g. Bluck et al. 2010b, Carrasco et al. 2010, Cimatti et al. 2008, Buitrago et al. 2008). A mass of evidence from a variety of approaches is beginning to establish a growth of up to a factor of five in the average radii of massive galaxies from $z = 3$ to the present. If this growth is real, it becomes of vital importance in contemporary astrophysics to explain the cause and principal driver for it. It seems that purely passive evolution (through e.g. exponentially declining star formation rates) cannot account for this magnitude of growth by itself. Thus, theoretical ideas for explaining this are usually concentrated on two methods - merging and AGN ‘puffing up’ scenarios (see e.g. Khochfar & Silk 2006, Fan et al. 2008, Naab et al. 2009). In this thesis the role of merging and AGN activity has been thoroughly explored over the past 12 billion years for massive galaxies. Therefore, we are in an excellent position to comment on the likelihood of each of these methods to account for the size evolution.

Throughout Chapter 3 the major merging evolution is probed via morphological methods, and the minor merger history is explored via close pair methods utilising the exceptionally high resolution and depth of the GNS (see §5.1.1). The ~ 4.5 mergers, and average mass increase of $\sim 3 \times 10^{11} M_{\odot}$ deduced in this work could offer a partial explanation to the observed size evolution of these massive systems. According to the theoretical analysis of Naab et al. (2006) a threefold mass increase, as witnessed in Bluck et al. (2010b), can give rise to an increase in radius of up to a factor of six,

which is almost exactly what is observed in e.g. Buitrago et al. (2008). Thus, by itself, the merging of these systems may be able to account for the observed size increase in the literature. However, the size increase permitted through merging is a maximum allowed, assuming the ‘right’ mass ratios and gas fractions. Therefore, there remains the possibility that other factors contribute, as well as major and minor merging, to the growth of massive galaxies over the past 12 billion years. The most likely among those remaining are all driven via AGN feedback mechanisms. It is to this we turn to in the final section of these conclusions (§5.1.3)

5.1.3 The Role of Supermassive Black Holes in Galaxy Evolution

Chapter 4 (and Bluck et al. 2010a) examine the co-evolution of supermassive black holes and their host massive galaxies over the past 12 billion years. One of the most important and intriguing relationships in contemporary astrophysics is the $M_{BH} - \sigma$ relation, relating supermassive black hole mass to the global velocity dispersion of the host galaxy bulge or spheroid. The nature, and fundamental cause, of this relation is currently unknown, and the need to find an explanation for it is undisputed in the field today. In this thesis we have used Eddington methods to estimate lower limits to the mass of supermassive black holes, and have compared these to the stellar masses of their host galaxies (a rough proxy for velocity dispersion / total mass, where at high redshifts these more fundamental parameters are difficult and often impossible to determine with current instruments). Our results are consistent with the local $M_{BH} - M_*$ relation being in place up to $z = 3$, providing there is not dramatic evolution with redshift in the Eddington ratio (μ). This further implies that supermassive black holes and their host galaxies most probably increase in mass together, in proportion to one another, and, thus, in a sense *co-evolve*.

The implication of this co-evolution is largely left up to the reader to incorporate within his or her favoured paradigm for galaxy evolution. However, the author suggests that this leads most naturally towards a formation route whereby supermassive black holes are formed very early in the history of the Universe, and then grow through a mix of gas accretion (which we witness directly through X-ray emissions) and black hole merging (which most probably occurs in line with galaxy merging).

Furthermore, we discover in Chapter 4 (and Bluck et al. 2010a) that at least 40 % of all massive galaxies will reach Seyfert level luminosities (with hard band X-ray luminosities of $L_X > 2.35 \times 10^{43} \text{ erg s}^{-1}$) through gas accretion onto their central supermassive black holes over the past 12 billion years. This corresponds to a total energy output, due to Seyfert luminosity AGN, of *at least* 35 times the average binding energy of a massive galaxy. Thus, supermassive black holes have the means, through their colossal energy outpourings, to strip apart each massive galaxy in the Universe 35 times over. Therefore, we conclude that supermassive black holes most likely have a powerful influence over the galaxies they inhabit through shutting off star formation. Also this can lead to scenarios which are conducive for growing the sizes of massive galaxies as well (see e.g. Fan et al. 2008). However, a crucial question still remains unanswered in this work: what fraction of this energy actually couples to the host galaxies, leading to feedback on star formation and possibly size evolution?

5.2 Summary

In this thesis, the role of major and minor merging has been explored as a mechanism for the formation and evolution of massive galaxies. We conclude that major merging dominates over minor merging for the mass increase of massive galaxies, and, furthermore, note that the total merger fraction and major merger fraction increase dramatically with redshift, suggesting that massive galaxies start to form early in the history of the Universe. In total we estimate that these massive ($M_* > 10^{11} M_\odot$) galaxies experience ~ 4.5 mergers with $M_* > 10^9 M_\odot$ galaxies, which gives rise to a total mass increase of $\sim 3 \times 10^{11} M_\odot$ from $z = 3$ to $z = 0$. We also conclude that merging is perhaps the most likely cause of galactic size evolution, although acknowledge that there is still a potential role for AGN feedback here also. We go on to probe the co-evolution of massive galaxies and their supermassive black holes and compute that at least 40 % of all massive galaxies will contain Seyfert luminosity AGN at some point over the past 12 billion years, with typical lifetimes of ~ 1 Gyrs for these bright systems. The total energy released from this will be sufficient to strip apart every massive galaxy in the Universe at least 35 times over, and this potentially provides a huge reservoir of energy to tap in explaining size evolution and the shutting off of star formation in

many massive galaxies by current times.

By way of conclusion, we have witnessed that massive galaxies form early, grow in mass and size, become more regular and symmetric, have fewer close pairs, frequently form powerful and short lived AGN, and eventually grow passive and redder over the past 12 billion years. Therefore, not unlike humans, galaxies are formed from matter created in the Big Bang, grow in size and mass throughout their lifetimes, and eventually, of course, die, in the sense that they will in the future run out entirely of fuel from cool gas to form new stars, grow red, faint, and ultimately disappear as the Universe accelerates forever onwards into darkness. Or so our current best favoured paradigm (Λ CDM) suggests, which has phenomenal support from observations, including those presented in this thesis.

5.3 Future Work

The author has been offered, and accepted, a three year position as a Science Fellow at Gemini North Observatory in Hilo, Hawaii, beginning in November 2010, and will thus be able to continue research into the formation and evolution of massive galaxies and their supermassive black holes personally. What follows in this section are a few examples of unanswered questions posed by the research presented in this thesis, and some preliminary ideas for how to tackle them.

5.3.1 Massive Galaxy Formation and Evolution

Perhaps the most important outstanding question in the field of extra-galactic observational astrophysics is: how do galaxies form? Throughout this thesis I have presented numerous investigations broadly motivated by this question, in particular, looking at the minor and major merger histories of massive galaxies (see Chapters 2 and 3). Although we have made considerable progress in cataloguing the number of mergers massive galaxies experience and the stellar mass increase they cause, we have not begun to categorise gas rich (wet) and gas poor (dry) mergers. Since, for example, many of the theoretical merger driven models for size evolution are sensitive to these distinc-

tions, this becomes an important addition to attempt. The use of infrared spectroscopy (possibly through the use of FLAMINGOS-2 and GNIRS at Gemini) in addition to other measures (such as sub-millimetre approaches) can be utilised to begin to ascertain the gas fraction of high redshift massive galaxies. Furthermore, the use of infrared spectroscopy of massive galaxies can be used reliably to compute un-obscured star formation rates which give a direct insight into when galaxies build up the bulk of their stellar mass. Eventually, with deeper surveys and superior instruments, we may be able to distinguish once and for all between models of monolithic collapse and more gradual hierarchical assembly models.

Other approaches to distinguishing between these two competing models for galaxy formation will utilise morphology (as in many parts of this thesis). The use of superior adaptive optics (AO) technology on 8 metre class telescopes, the newly updated WFC3 on the HST, and the next generation of space telescopes (such as the JWST) will give unprecedented clarity, resolution and depth to the imaging of extremely distant galaxies. From this, measures of the morphological disturbance will give a clear indication of whether these galaxies can be forming gradually (via hierarchical assembly) or rapidly (via monolithic collapse), as, e.g., finding a high population of morphologically smooth and symmetric galaxies at $z \sim 4 - 6$ would highly disfavour hierarchical assembly. I will become involved in using AO on Gemini for NIR imaging of high redshift galaxies, as well as joining the CANDELS consortium to utilise the extraordinarily deep new WFC3 data from the HST covering all of the great extra-galactic deep fields in the NIR. The wider areas covered by CANDELS will finally allow for environment to be factored in to the evolution of massive galaxies from high redshifts. Differential environmental effects are well established at relatively low redshifts, but at higher redshifts (due to the exposure times necessary) this is almost entirely unexplored. The next ten years should see a revolution in this as CANDELS data becomes available, and then the JWST becomes operational.

To end this section, I feel it is paramount to make some mention of the hotly debated size evolution of massive galaxies. Most approaches to measuring the size of massive galaxies utilise some form of surface brightness profile fitting, such as GALFIT Sersic index fitting. However, some of the biases and degeneracies inherent in these ap-

proaches can be assuaged if one measures the actual velocity dispersion of the galaxy in question. This has already been attempted (see van Dokkum et al. 2009) but for only one galaxy, with disputable results. It would be particularly interesting to apply for time on 8 metre class telescopes such as Gemini, the VLT and Keck to utilise their NIR spectrographs to gain empirical measures of the velocity dispersion of a sizeable population of very high redshift massive galaxies. Combining measures of stellar mass to the velocity dispersion and estimated sizes will go a long way towards solving the question of whether or not size evolution is an artifact of surface brightness dimming and poor signal-to-noise ratios in current deep surveys. This will also allow the community to probe how mass-to-light ratios change over cosmic time, and understand the build up of dark matter potential wells, not just stellar matter. For all of these activities, I feel I will be ideally positioned at Gemini observatory to take part in this research.

5.3.2 Supermassive Black Holes

The most sophisticated and challenging research performed in this thesis all primarily resides in the examination of the role of supermassive black holes in galaxy evolution (see Chapter 4). One of the principal reasons for this is the degeneracy between black hole mass (M_{BH}) and Eddington ratio (μ) from Eddington limit methods. As such, in Chapter 4, we retained the degeneracies in all calculations and ended up discussing the evolution, or lack thereof, of the minimum, Eddington, mass of black hole ($M_E = \mu M_{BH}$) with redshift. Although this proved sufficient to glean many interesting discoveries about the co-evolution of supermassive black holes and their host galaxies, it is still a degeneracy which must be broken to truly answer the question of what drives the $M_{BH} - \sigma$ relation.

New instruments, such as the near infrared integral field unit spectrograph (NIFS) on Gemini North, have exceptional spacial resolution for near infrared spectroscopy. These can in principle be used to probe the velocity dispersions of the innermost regions of AGN, and from this be converted to black hole masses via virial estimator techniques. This could prove a way to compute actual black hole masses and, hence, Eddington ratios for intermediate redshift objects (as is indeed beginning to be done at low redshifts by e.g. McDermid et al. 2006). I have already approached the team

here and hope to become more involved in future applications for time to do this at higher redshifts. Moreover, to directly probe the $M_{BH} - \sigma$ relation at high redshifts, one must also compute σ as well as M_{BH} , and this can again be achieved via near infrared spectroscopy, using e.g. GNIRS on Gemini North. In a sense the past decade in extra-galactic astronomy has been given over to near infrared imaging, and I suggest that the next decade should go to near infrared spectroscopy, as this has the potential to break many of the current degeneracies in the field and truly propel our knowledge of galaxy formation and evolution forwards.

The question of AGN feedback on star formation still remains an open question in the field. This is not because there is any doubt about whether there is enough energy to make a difference (there clearly is, see Chapter 4 where we conclude that there is enough energy released by AGN to strip apart every massive galaxy at least 35 times over). Conversely, the reason the question is still open, is simply that no one has a clear idea of how much energy actually couples to the galaxy, and how much is simply lost to the intergalactic medium and the Universe at large. There are also theoretical disputes concerning the causal nature of this coupling, i.e.: by what mechanism can the energy released by AGN heat up (radiative driven AGN gas depletion) or push out (momentum driven AGN gas depletion) the cool gas used as fuel by supermassive black holes? Christopher Conselice and I are currently working towards an empirical approach to solve this question, which is not unduly model (or theory) dependent. For the purpose of this thesis it should suffice to state that this is work in progress, and at an early state of development, although we are quietly confident that in the not too distant future the question of AGN released energy coupling to galaxies will become an observationally determinable question.

5.3.3 Final Suggestions

During the course of the Viva Voce examination many interesting and valuable suggestions were made on how to expand or improve the work presented in this thesis. Although many of these ideas have now been investigated and implemented within the thesis, inevitably due to time, data and space constraints some have not been. In the final paragraph I list a few of these for future reference.

The need to test statistical measures of the pair fraction of galaxies with real world spectroscopic data at high redshifts as well as with model data (as performed towards the end of Chapter 2) is evident. This would come to establish once and for all the validity, or possible caveats applicable to the method. Further, testing the efficacy of the close pair method presented in this thesis with minor mergers as well as major mergers would be interesting to perform both for model and real world galaxies. Although this is beyond the scope of the thesis, the author hopes to look into these issues in the future. Moreover, a full comparison between the techniques of Lopez-Sanjuan and his collaborators in maximum likelihood methods with the ones presented in this thesis on more conventional pair fraction statistics would doubtless provide new insights which both groups could learn from. Finally, an even greater use of the multi-wavelength GOODS data (from radio to X-ray) to further establish the reliability of photometric redshifts, stellar masses, morphological estimates, star formation rates and global SED profiles as computed and utilised throughout this work would be of much future interest. As the data begins to come in from the HST WFPC3 CANDELS project, it is the author's hope that some of the original techniques and analyses presented here, as well as error considerations and qualifications, may be of immediate use to the astronomical community.

Appendices

Appendix A

CAS Structural Analysis

The following is adapted from text in Conselice, Yang and Bluck (2009) describing the formal procedures for deducing the CAS parameters:

We use the CAS (concentration, asymmetry, clumpiness) parameters to measure the structures of our $z < 3$ galaxies quantitatively. The CAS parameters are a non-parametric method for measuring the forms and structures of galaxies in resolved CCD images (e.g., Conselice et al. 2000; Bershady et al. 2000; Conselice et al. 2002; Conselice 2003). The basic idea behind these parameters is that galaxies have light distributions that reveal their past and present formation modes (Conselice 2003). Furthermore, well-known galaxy types in the nearby universe fall in well defined regions of the CAS parameter space. For example, the selection $A > 0.35$ locates systems which are nearly all major galaxy mergers in the nearby universe (e.g. Conselice et al. 2000; Conselice 2003; Hernandez-Toledo et al. 2005; Conselice 2007).

The way we measure structural parameters on our Hubble images varies slightly from what has been done earlier in the Hubble Deep Field, and GOODS imaging (e.g. Conselice et al. 2003; Conselice et al. 2004). The basic measurement procedure, after cutting out the galaxy into a smaller image, is to first measure the radius in which the parameters are computed. The radius we use for all our indices is defined by the Petrosian radii, which is the radius where the surface brightness at a given radius is 20% of the surface brightness within that radius (e.g., Bershady et al. 2000; Conselice 2003).

We use circular apertures for our Petrosian radii and quantitative parameter estimation. We begin our estimates of the galaxy centre for the radius measurement at the centroid of the galaxy's light distribution. Through modelling and various tests, it can be shown that the resulting radii do not depend critically on the exact centre, although the CAS and other parameters do (Conselice et al. 2000; Lotz et al. 2004). The exact Petrosian radius we use to measure our parameters is

$$R_{\text{Petr}} = 1.5 \times r(\eta = 0.2),$$

where $r(\eta = 0.2)$ is the radius where the surface brightness is 20% of the surface brightness within that radius.

A very important issue, especially for faint galaxies, is how to account for background light and noise. For faint galaxies there is a considerable amount of noise added due to the sky, which must be corrected. Through various test, outlined in detail in Conselice et al. (2008), we conclude that the proper way to correct parameters for the background requires that the selected background area be close to the object of interest. This is only an issue for faint galaxies, and for galaxies imaged on large mosaics which have a non-uniform weight map, and whose noise characteristics vary across the field. By using a background near each object we alleviate these issues as the noise properties do not vary significantly over $\sim 0.5 - 1$ arcmin, where the galaxy and the background area are selected. We review below how the CAS parameters are measured. For more detail see Bershady et al. (2000), Conselice et al. (2000), Conselice (2003).

A.1 Asymmetry

The asymmetry of a galaxy is measured by taking an original galaxy image and rotating it 180 degrees about its centre, and then subtracting the two images (e.g. Conselice et al. 2000). There are corrections done for background, and radius (explained in detail in Conselice et al. 2000). Most importantly, the centre for rotation is decided by an iterative process which finds the location of the minimum asymmetry. The formula for calculating the asymmetry is given by:

$$A = \min \left(\frac{\Sigma |I_0 - I_{180}|}{\Sigma |I_0|} \right) - \min \left(\frac{\Sigma |B_0 - B_{180}|}{\Sigma |I_0|} \right) \quad (\text{A.1})$$

Where I_0 is the original image pixels, I_{180} is the image after rotating by 180 degrees. The background subtraction using light from a blank sky area, called B_0 , are critical for this process, and must be minimised in the same way as the original galaxy itself. A lower value of A means that a galaxy has a higher degree of rotational symmetry which tends to be found in elliptical galaxies. Higher values of A indicate an asymmetric light distribution, which are usually found in spiral galaxies, or in the more extreme case, merger candidates.

A.2 Concentration

Concentration is a measure of the intensity of light contained within a central region in comparison to a larger region in the outer-parts of a galaxy. The exact definition is the ratio of two circular radii which contain 20% and 80% (r_{20}, r_{80}) of the total galaxy flux,

$$C = 5 \times \log \left(\frac{r_{80}}{r_{20}} \right). \quad (\text{A.2})$$

This index is sometimes called C_{28} . A higher value of C indicates that a larger amount of light in a galaxy is contained within a central region. This particular measurement of the concentration correlates well with the mass and halo properties of galaxies in the nearby universe (e.g., Bershady et al. 2000; Conselice 2003).

A.3 Clumpiness

The clumpiness (S) parameter is used to describe the fraction of light in a galaxy which is contained in clumpy distributions. Clumpy galaxies have a relatively large amount of light at high spatial frequencies, whereas smooth systems, such as elliptical galaxies contain light at low spatial frequencies. Galaxies which are undergoing star formation tend to have very clumpy structures, and high S values. Clumpiness can be measured

in a number of ways, the most common method used, as described in Conselice (2003) is,

$$S = 10 \times \left[\left(\frac{\Sigma(I_{x,y} - I_{x,y}^\sigma)}{\Sigma I_{x,y}} \right) - \left(\frac{\Sigma(B_{x,y} - B_{x,y}^\sigma)}{\Sigma I_{x,y}} \right) \right], \quad (\text{A.3})$$

where, the original image $I_{x,y}$ is blurred to produce a secondary image, $I_{x,y}^\sigma$. This blurred image is then subtracted from the original image leaving a residual map, containing only high frequency structures in the galaxy (Conselice 2003). To quantify this, we normalise the summation of these residuals by the original galaxy's total light, and subtract from this the residual amount of sky after smoothing and subtracting it in the same way. The size of the smoothing kernel σ is determined by the radius of the galaxy, and is $\sigma = 0.2 \cdot 1.5 \times r(\eta = 0.2)$ (Conselice 2003). Note that the centres of galaxies are removed when this procedure is carried out.

Appendix B

Data Tables

Full tables concerning all characteristics and derived properties of the HST GOODS NICMOS Survey galaxies are provided at: <http://www.nottingham.ac.uk/~ppzgns/index.html>.

This link is now available to the public - and our data is freely available for others to use.

The best guide to the GNS and available data is Conselice, Bluck et al. (2010), now accepted for publication in MNRAS, and currently available in draft version on the ArXiv.

Table B.1: Photometric Pair - Statistical Pair Comparison

z-range	N_{Gal}	f_m (stats)	f_m (1σ)	f_m (2σ)	f_m (3σ)	f_m (4σ)
2.3 - 3.0	37	0.38+/-0.06	0.27+/-0.04	0.35+/-0.04	0.43+/-0.07	0.62+/-0.10
1.7 - 2.3	44	0.20+/-0.03	0.05+/-0.01	0.09+/-0.02	0.25+/-0.04	0.30+/-0.04
All (1.7 - 3.0)	81	0.29+/-0.04	0.15+/-0.02	0.21+/-0.02	0.33+/-0.04	0.44+/-0.05

The above table shows close pair fractions for the massive GNS galaxies. These are computed statistically and via proximity of photometric redshifts, from 1 - 4 σ closeness. Effectively the photometric pair fractions may be interpreted as upper limits to the true pair fraction at the given confidence level stated. Errors presented here are Poisson counting errors only, and are not representative of the final error on the pair fraction.

Table B.2: Comparisons of Statistical and Photometric Close Pair Numbers, Asymmetry and Star Formation Rates

GNS ID	RA	Dec	z_{phot}	$\text{Log}(M_* [M_\odot])$	H_{AB}	N_p	$N_{p,corr}$	$N_{p,phot}$	A	$\text{SFR}_{UV,corr}$	$\text{SFR}_{24\mu m}$
21	189.1354	62.1172	2.70	11.05	23.75	0	0.00	0	0.263	20	178
43	189.1254	62.1155	2.20	11.08	22.75	0	0.00	0	0.352	88	000
77	189.1326	62.1121	1.91	11.41	21.99	0	0.00	0	0.192	158	2220
227	189.1198	62.1355	2.07	11.20	21.85	0	0.00	0	0.268	14	000
373	189.0587	62.1635	2.51	11.06	22.70	2	1.39	2	0.243	9	000
552	189.0772	62.1510	1.93	11.33	20.89	0	0.00	0	0.202	10	122
730	189.2512	62.1527	2.47	11.09	22.80	0	0.00	0	0.306	22	000
840	189.1737	62.1673	1.93	11.30	22.05	0	0.00	0	0.165	54	000
856	189.1788	62.1663	1.74	11.38	21.65	0	0.00	0	0.374	78	000
999	189.1430	62.2335	1.98	11.17	21.49	0	0.00	0	0.271	569	319
1129	189.5074	62.2717	2.37	11.19	23.14	0	0.00	0	0.396	67	120
1144	189.5035	62.2700	2.07	11.13	22.13	0	0.00	0	0.246	19	000
1257	189.2264	62.2922	2.02	11.00	22.76	0	0.00	0	0.303	77	000
1394	189.3997	62.3453	2.04	11.36	22.18	0	0.00	0	0.201	82	290

Table B.2 –Continued

GNS ID	RA	Dec	z_{phot}	$\text{Log}(M_* [M_\odot])$	H_{AB}	N_p	$N_{p,corr}$	$N_{p,phot} [3\sigma]$	A	$\text{SFR}_{UV,corr}$	$\text{SFR}_{24\mu m}$
1533	189.3058	62.1791	2.56	11.13	24.14	3	1.75	2	0.272	54	000
1666	189.2567	62.1962	2.36	11.38	21.47	1	0.73	0	0.240	217	1520
1769	189.2737	62.1871	1.95	11.32	22.20	2	1.59	2	0.445	9	000
1826	189.0732	62.2613	2.20	11.28	22.39	1	0.51	0	0.323	4	11
1942	189.2777	62.2546	2.51	11.03	21.83	2	1.65	0	0.319	49	000
2066	189.3002	62.2034	2.80	11.35	23.07	2	1.21	0	0.297	115	1230
2083	189.3122	62.2016	2.72	11.28	22.48	1	0.44	1	0.375	64	000
2282	189.3069	62.2626	2.30	11.13	23.36	0	0.00	0	0.402	21	679
2411	189.0479	62.1761	2.10	11.17	22.58	0	0.00	0	0.148	106	61
2564	189.2110	62.2488	1.83	11.13	22.18	0	0.00	0	0.434	119	000
2678	189.0475	62.1486	2.50	11.53	22.10	1	0.58	0	0.420	12	000
2734	189.0423	62.1463	2.60	11.03	23.60	1	0.00	1	0.138	38	000
2764	189.0525	62.1433	2.20	11.15	22.85	0	0.00	0	0.264	32	216
2837	189.0944	62.2750	2.30	11.39	22.83	1	0.37	1	0.269	30	131
2902	189.0913	62.2677	2.00	11.22	22.99	0	0.00	0	0.344	265	399
2965	189.0799	62.2449	2.80	11.13	22.97	1	0.25	0	0.286	50	472

Table B.2 –Continued

GNS ID	RA	Dec	z_{phot}	$\text{Log}(M_* [M_\odot])$	H_{AB}	N_p	$N_{p,corr}$	$N_{p,phot} [3\sigma]$	A	$\text{SFR}_{UV,corr}$	$\text{SFR}_{24\mu m}$
3036	189.0869	62.2377	2.10	11.11	22.24	1	0.57	1	0.476	4	000
3126	189.1304	62.1661	2.10	11.09	23.05	0	0.00	0	0.362	45	511
3250	189.2291	62.1385	2.30	11.12	23.14	0	0.00	0	0.287	52	424
3387	189.2942	62.3472	1.83	11.01	22.62	1	0.47	0	0.411	97	000
3422	189.2808	62.3442	2.80	11.09	23.63	0	0.00	0	0.268	45	484
3582	189.0987	62.1693	2.40	11.18	23.51	0	0.00	0	0.354	14	22
3629	189.1829	62.2725	2.10	11.28	21.73	2	1.69	2	0.249	98	153
3766	189.2056	62.3226	2.10	11.19	21.96	0	0.00	0	0.291	53	197
3818	189.2022	62.3171	1.75	11.41	21.33	1	0.77	0	0.270	227	000
3822	189.2198	62.3169	2.20	11.06	23.31	0	0.00	0	0.163	19	132
3970	189.3319	62.2059	2.34	11.16	22.72	1	0.40	1	0.326	72	000
3988	189.3130	62.2047	2.40	11.21	23.09	2	1.25	1	0.336	60	1130
4033	189.4641	62.2440	2.07	11.04	21.46	1	0.74	0	0.299	30	542
4121	189.4564	62.2332	1.92	11.20	21.72	0	0.00	0	0.598	148	000
4239	188.9812	62.1738	2.20	11.17	22.89	0	0.00	0	0.234	97	592
4282	53.0938	-27.8013	2.60	11.08	23.79	1	0.00	1	0.350	61	15

Table B.2 –Continued

GNS ID	RA	Dec	z_{phot}	$\text{Log}(M_* [M_\odot])$	H_{AB}	N_p	$N_{p,corr}$	$N_{p,phot} [3\sigma]$	A	$\text{SFR}_{UV,corr}$	$\text{SFR}_{24\mu m}$
4301	53.0923	-27.8031	2.40	11.33	23.54	0	0.00	0	0.207	51	65
4353	53.1011	-27.8086	1.97	11.21	23.29	0	0.00	0	0.216	155	000
4400	53.1013	-27.7117	2.30	11.10	24.30	2	0.73	1	0.234	10	000
4434	53.0976	-27.7153	2.14	11.06	22.30	1	0.54	1	0.300	32	53
4557	53.0892	-27.7601	2.27	11.21	21.87	1	0.65	1	0.271	109	25
4706	53.1231	-27.8033	2.35	11.10	21.96	0	0.00	0	0.311	150	000
4754	53.1200	-27.8082	2.00	11.50	22.61	0	0.00	0	0.196	109	126
4882	53.1718	-27.8257	1.74	11.10	21.88	0	0.00	0	0.325	309	000
4941	53.2300	-27.8508	1.83	11.01	21.68	0	0.00	0	-1.580	11	000
5171	53.0632	-27.6997	2.40	11.01	22.84	0	0.00	0	0.357	86	36
5282	53.0860	-27.7096	2.10	11.09	21.92	0	0.00	0	0.236	238	86
5372	53.1255	-27.8864	2.90	11.08	23.52	0	0.00	0	0.372	26	000
5445	53.1245	-27.8932	2.50	11.45	23.41	1	0.10	1	0.345	3	000
5524	53.1333	-27.9029	2.58	11.17	21.90	0	0.00	0	0.403	39	000
5533	53.1289	-27.9037	2.79	11.10	23.40	0	0.00	0	0.268	21	000
5764	53.2252	-27.8738	2.65	11.27	22.55	0	0.00	0	0.398	47	000

Table B.2 –Continued

GNS ID	RA	Dec	z_{phot}	$\text{Log}(M_* [M_\odot])$	H_{AB}	N_p	$N_{p,corr}$	$N_{p,phot}$ [3σ]	A	$\text{SFR}_{UV,corr}$	$\text{SFR}_{24\mu m}$
5853	53.0507	-27.7138	2.41	11.44	23.44	3	2.10	1	0.117	160	35
5933	53.0542	-27.7217	2.30	11.26	23.00	1	0.30	1	0.431	54	77
6035	53.0555	-27.8739	1.90	11.32	21.65	0	0.00	0	0.309	67	17
6114	53.0656	-27.8788	2.24	11.11	21.70	1	0.69	1	0.222	76	000
6220	53.0716	-27.8436	1.90	11.01	22.33	1	0.55	0	0.156	309	36
6352	53.0773	-27.8596	1.96	11.08	22.08	0	0.00	0	0.142	67	858
6468	53.1385	-27.6718	2.80	11.45	22.69	1	0.36	0	0.161	24	35
6575	53.0355	-27.6901	2.50	11.41	22.50	0	0.00	0	0.293	144	51
6584	53.0260	-27.6909	2.20	11.52	21.94	0	0.00	0	0.273	134	17
6876	53.0400	-27.6852	2.50	11.45	22.85	1	0.34	1	0.289	9	54
7090	53.0578	-27.8335	2.70	11.68	22.07	0	0.00	0	0.243	24	000
7156	53.1178	-27.9109	2.69	11.17	22.34	0	0.00	0	0.128	96	000
7321	53.1161	-27.8719	2.07	11.00	22.38	0	0.00	0	0.312	23	000
7425	53.1272	-27.8345	1.81	11.22	21.47	0	0.00	0	0.270	73	000
7677	53.1830	-27.7090	1.76	11.57	20.54	0	0.00	0	0.341	4	000
7970	53.0282	-27.7788	2.30	11.15	22.59	0	0.00	0	0.238	389	101

Table B.2 –Continued

GNS ID	RA	Dec	z_{phot}	$\text{Log}(M_* [M_\odot])$	H_{AB}	N_p	$N_{p,corr}$	$N_{p,phot}$ [3σ]	A	$\text{SFR}_{UV,corr}$	$\text{SFR}_{24\mu m}$
8140	53.1410	-27.7667	1.91	11.22	21.38	0	0.00	0	0.260	231	000
8214	53.1623	-27.7121	2.14	11.16	21.97	1	0.64	1	0.312	201	20

In the above table we compare statistical close pair numbers to photometric close pair numbers (those with companions with photometric redshifts within 3σ of the host). Those galaxies with high (non-zero) values of both may be worth considering for spectroscopic follow up in the future. Tables B.3 and B.4 present the 1st and 2nd potential true pairs respectively. We also add here CAS asymmetry and UV and 24 μm deduced SFRs. Full data catalogs are available at <http://www.nottingham.ac.uk/~ppzgn/index.html>, where all computed values and initial error estimations are publically available. Errors are omitted here due to space limitations. All star formation rates are given in solar units per year ($M_\odot \text{yr}^{-1}$).

Table B.3: List of Potential Close Pairs - 1

Host GNS ID	RA	Dec	z_{phot}	$\text{Log}(M_* [M_\odot])$	H_{AB}	Pair GNS ID	RA	Dec	z_{phot}	H_{AB}	$N_p [< 3\sigma]$
373	189.0587	62.1635	2.51	11.06	22.70	362	189.0594	62.1643	1.10	23.34	2
1533	189.3058	62.1791	2.56	11.13	24.14	1548	189.3076	62.1786	2.36	23.12	2
1769	189.2737	62.1871	1.95	11.32	22.20	1775	189.2730	62.1862	0.65	23.09	2
2083	189.3122	62.2016	2.72	11.28	22.48	2076	189.3126	62.2022	2.38	23.90	1
2734	189.0423	62.1463	2.60	11.03	23.60	2741	189.0417	62.1457	2.48	24.09	1
2837	189.0944	62.2750	2.30	11.39	22.83	2853	189.0938	62.2748	1.60	23.90	1
3036	189.0869	62.2377	2.10	11.11	22.24	3039	189.0874	62.2368	0.98	22.74	1
3629	189.1829	62.2725	2.10	11.28	21.73	3630	189.1826	62.2720	0.94	22.60	2
3970	189.3319	62.2059	2.34	11.16	22.72	3966	189.3336	62.2064	2.19	22.36	1
3988	189.3130	62.2047	2.40	11.21	23.09	3981	189.3142	62.2051	1.75	22.12	1
4282	53.0938	-27.8013	2.60	11.08	23.79	4280	53.0928	-27.8012	2.45	24.26	1
4434	53.0976	-27.7153	2.14	11.06	22.30	4442	53.0978	-27.7161	0.96	23.64	1
4400	53.1013	-27.7117	2.30	11.10	24.30	4399	53.1008	-27.7118	2.44	24.71	1
4557	53.0892	-27.7601	2.27	11.21	21.87	4559	53.0885	-27.7600	1.68	23.34	1
5445	53.1245	-27.8932	2.50	11.45	23.41	5455	53.1251	-27.8940	2.34	24.14	1

Table B.3 –Continued

Host GNS ID	RA	Dec	z_{phot}	$\text{Log}(M_* [M_\odot])$	H_{AB}	Pair GNS ID	RA	Dec	z_{phot}	H_{AB}	$N_p [< 3\sigma]$
5853	53.0507	-27.7138	2.41	11.44	23.44	5867	53.0503	-27.7146	2.81	24.48	1
5933	53.0542	-27.7217	2.30	11.26	23.00	5934	53.0545	-27.7217	1.71	24.47	1
6114	53.0656	-27.8788	2.24	11.11	21.70	6115	53.0654	-27.8786	1.25	22.78	1
6876	53.0400	-27.6852	2.50	11.45	22.85	6879	53.0394	-27.6861	3.74	24.09	1
8214	53.1623	-27.7121	2.14	11.16	21.97	8213	53.1629	-27.7123	0.90	21.97	1

This table presents a list of massive galaxies with possible companions with H-band magnitudes between ± 1.5 of the host, within a 30 Kpc (physical) catchment radius, and with photometric redshifts within 3σ of the host. A list of useful quantities is provided for each host and companion. For those objects with more than one companion please see Table B.4 for the second object.

Table B.4: List of Potential Close Pairs - 2

Host GNS ID	RA	Dec	z_{phot}	$\text{Log}(M_* [M_\odot])$	H_{AB}	Pair GNS ID	RA	Dec	z_{phot}	H_{AB}
373	189.0587	62.1635	2.51	11.06	22.70	385	189.0577	62.1629	0.94	23.42
1533	189.3058	62.1791	2.56	11.13	24.14	1534	189.3066	62.1789	2.61	23.91
1769	189.2737	62.1871	1.95	11.32	22.20	1774	189.2728	62.1865	1.45	22.40
3629	189.1829	62.2725	2.10	11.28	21.73	3614	189.1821	62.2730	0.80	22.72

This table presents a list of massive galaxies with possible companions with H-band magnitudes between ± 1.5 of the host, within a 30 Kpc (physical) catchment radius, and with photometric redshifts within 3σ of the host. In particular, this table lists for those primary targets with two possible companions, the second companion's derived properties.

Table B.5: Close Pair Method Test: Spectroscopy form the Millennium Simulation

Run ID	N_{hosts}	N_{total}	f_m (stats)	f_m (< 500 km/s)	f_m (< 1000 km/s)	f_m (< 1500 km/s)
1	44	30738	0.149+/-0.022	0.068+/-0.010	0.114+/-0.017	0.159+/-0.024
2	43	31295	0.247+/-0.038	0.210+/-0.032	0.233+/-0.036	0.280+/-0.043
3	82	31921	0.110+/-0.012	0.061+/-0.007	0.098+/-0.010	0.146+/-0.016
4	49	32501	0.161+/-0.023	0.121+/-0.017	0.167+/-0.024	0.198+/-0.028
5	62	33770	0.152+/-0.019	0.097+/-0.012	0.113+/-0.014	0.168+/-0.021
6	84	31948	0.189+/-0.020	0.123+/-0.013	0.166+/-0.018	0.221+/-0.024
7	54	34376	0.161+/-0.022	0.019+/-0.003	0.093+/-0.013	0.167+/-0.023
8	65	31727	0.191+/-0.024	0.070+/-0.009	0.142+/-0.018	0.161+/-0.020
mean	60	32285	0.170+/-0.040	0.095+/-0.050	0.142+/-0.045	0.188+/-0.044

This table presents the results from a series of eight Millennium Simulation run tests on the efficacy of the Close Pair method presented in Chapters 2 and 3. Presented are close pair fractions deduced statistically, and through a spectroscopic-like method for comparison. The final row presents the mean properties across the varying tests. The models used were taken from the Kitzbichler et al. (2006) view of the De Lucia et al. (2006) semianalytic galaxy catalog for the Millennium simulation. Please see <http://www.g-vo.org/Millennium> for full details and to access the mock catalogs used here for further investigation. The errors on individually calculated merger fractions are simple Poisson counting errors, with the errors presented for the mean values being the standard deviation about the mean across the eight runs performed here.

Table B.6: AGN Data Source Summary

Field	Waveband(s)	A_{Tot} [deg ²]	$A_{vol.lim.}$ [deg ²]	Depth	M_{*Lim} [M_{\odot}]	z Range
EGS (POWIR + CFHT)	BRIJK	1.5200	0.3466	23.0 (AB: K)	$10^{10.5}$	0.4 - 1.5
GOODS (GNS + ACS)	BViZH	0.0120	0.0079	26.5 (AB: H)	10^{10}	1.5 - 3.0
AEGIS-X	0.5-2, 2-10 KeV	0.6419	0.3466	3.8×10^{-16} erg cm ⁻² s ⁻¹	...	0.4 - 1.5
CDF-N	0.5-2, 2-8 KeV	0.1211	0.0044	2.5×10^{-17} erg cm ⁻² s ⁻¹	...	1.5 - 3.0
CDF-S	0.5-2, 2-8 KeV	0.1212	0.0035	1.9×10^{-17} erg cm ⁻² s ⁻¹	...	1.5 - 3.0

Table B.7: Average Properties of the AGN Samples

Sample	N_{Gal}	$\langle z \rangle$	$\langle \text{Log}(M_* [M_\odot]) \rangle$	$\langle \text{Log}(L_{2-10\text{Kev}} [\text{ergs}^{-1}]) \rangle$	$\langle \text{Log}(M_{Edd} [M_\odot]) \rangle$
Vol. Lim. ('Seyfert')	85	1.239	11.02	43.76	6.755
Total (All AGN)	508	1.343	10.90	43.29	6.285

Table B.8: Volume Limited Sample of Active Massive Galaxies at $0.4 < z < 3$

ID	RA	Dec	z_{phot}	$\text{Log}(M_* [M_\odot])$	$\text{Log}(L_{2-10\text{keV}} [\text{erg s}^{-1}])$	$\text{Log}(M_{Edd} [M_\odot])$	Hardness (H)
1	189.1483	62.2400	1.550	10.84	43.42	6.42	0.85
2	189.0489	62.1708	1.550	10.72	43.46	6.46	0.95
3	189.0659	62.2544	2.745	11.25	43.85	6.85	0.95
4	189.0912	62.2677	2.235	10.75	43.51	6.51	1.00
5	189.0798	62.2449	2.945	10.76	43.95	6.95	0.28
6	189.0944	62.1747	2.385	10.61	43.91	6.91	0.30
7	53.1070	-27.7182	2.410	11.27	44.17	7.17	0.59
8	53.0764	-27.8486	1.570	11.42	43.74	6.74	0.93
9	53.0393	-27.8018	2.705	11.37	44.34	7.34	0.67
10	213.8910	52.0994	0.986	11.06	44.18	7.18	0.17
11	213.9490	52.1455	0.619	11.33	43.44	6.44	0.77
12	213.7360	52.1612	0.992	11.32	43.77	6.76	0.42
13	213.9640	52.2279	0.752	10.95	43.43	6.42	0.45
14	214.2080	52.3026	0.808	11.17	43.41	6.41	0.97
15	214.2220	52.3511	0.982	11.06	43.37	6.37	0.16
16	214.4410	52.5090	0.985	11.34	43.85	6.85	0.70

Table B.8 –Continued

ID	RA	Dec	z_{phot}	$\text{Log}(M_* [M_\odot])$	$\text{Log}(L_{2-10\text{keV}} [\text{erg s}^{-1}])$	$\text{Log}(M_{Edd} [M_\odot])$	Hardness (H)
17	214.3860	52.5342	0.986	11.34	43.59	6.59	0.48
18	214.4790	52.6956	0.464	10.52	43.82	6.82	0.85
19	214.9280	52.7771	0.784	10.92	43.73	6.73	0.35
20	214.7950	52.7839	0.820	11.15	43.60	6.59	0.51
21	215.1170	52.9782	0.871	10.62	43.56	6.55	0.37
22	213.7870	52.1117	0.837	11.09	43.65	6.65	0.54
23	213.7930	52.1086	0.931	10.85	43.60	6.60	0.42
24	214.2680	52.3611	0.859	11.17	43.77	6.77	0.89
25	214.2140	52.3462	0.981	11.35	43.92	6.92	0.15
26	214.0950	52.3212	0.826	11.35	44.47	7.47	0.42
27	214.1440	52.3775	0.885	10.88	43.56	6.56	0.50
28	214.4960	52.5275	0.938	11.02	43.46	6.46	0.51
29	215.5220	53.1810	0.995	10.88	43.66	6.65	0.46
30	215.5000	53.2119	0.780	11.51	43.92	6.91	0.51
31	215.2640	53.3062	0.873	10.96	43.42	6.42	0.20
32	215.7650	53.4468	0.866	10.50	43.66	6.66	0.46
33	213.8120	52.1602	1.296	11.33	43.61	6.61	0.31

Table B.8 –Continued

ID	RA	Dec	z_{phot}	$\text{Log}(M_* [M_\odot])$	$\text{Log}(L_{2-10\text{keV}} [\text{erg s}^{-1}])$	$\text{Log}(M_{Edd} [M_\odot])$	Hardness (H)
34	214.2120	52.2579	1.034	10.89	44.24	7.23	0.35
35	214.1370	52.3172	1.028	11.12	44.15	7.15	0.97
36	214.0270	52.4165	1.313	11.37	44.34	7.34	0.60
37	214.4240	52.4732	1.148	11.93	44.37	7.37	0.53
38	214.3910	52.5637	1.083	11.43	43.40	6.40	0.66
39	214.5230	52.6757	1.413	10.79	44.08	7.07	0.54
40	214.9170	52.8274	1.232	11.32	43.42	6.42	0.69
41	214.7870	52.9436	1.392	10.69	44.22	7.22	0.40
42	215.4250	53.1798	1.418	11.26	43.60	6.59	0.30
43	213.9240	52.1551	1.343	10.51	43.46	6.45	0.45
44	213.6690	52.1407	1.017	11.02	43.59	6.59	0.50
45	214.1800	52.2433	1.069	11.54	45.03	8.03	0.35
46	214.2360	52.2577	1.033	11.49	43.44	6.44	0.19
47	213.9910	52.2502	1.060	10.81	43.39	6.39	1.00
48	213.9520	52.2691	1.033	10.93	43.91	6.90	0.44
49	214.1500	52.3201	1.180	10.98	43.38	6.38	0.50
50	214.4120	52.3925	1.138	10.68	43.91	6.90	0.35

Table B.8 –Continued

ID	RA	Dec	z_{phot}	$\text{Log}(M_* [M_\odot])$	$\text{Log}(L_{2-10\text{keV}} [\text{erg s}^{-1}])$	$\text{Log}(M_{Edd} [M_\odot])$	Hardness (H)
51	213.9730	52.3799	1.405	10.70	43.47	6.47	0.58
52	214.1240	52.3926	1.044	11.49	43.47	6.47	0.97
53	214.5000	52.3732	1.240	11.09	43.99	6.99	0.69
54	214.4550	52.4699	1.064	11.07	43.62	6.62	0.62
55	214.5860	52.5842	1.488	10.87	43.43	6.43	1.00
56	214.5190	52.6092	1.223	11.15	43.88	6.88	0.30
57	214.6920	52.6866	1.492	10.90	43.90	6.90	0.39
58	214.5590	52.7224	1.206	10.88	43.55	6.55	0.90
59	214.5770	52.7322	1.148	10.54	44.00	7.00	0.36
60	214.4680	52.7154	1.239	10.91	43.52	6.52	0.69
61	214.7520	52.7618	1.460	10.65	43.42	6.42	0.75
62	215.0280	52.8236	1.443	10.67	43.64	6.63	0.21
63	214.9480	52.8407	1.336	11.45	43.40	6.39	1.00
64	215.2690	52.9748	1.322	11.03	43.77	6.77	0.88
65	215.2820	53.0550	1.052	10.70	43.74	6.73	0.52
66	214.9760	53.0463	1.419	10.97	43.70	6.70	0.28
67	214.9720	53.0349	1.362	10.83	44.15	7.14	0.45

Table B.8 –Continued

ID	RA	Dec	z_{phot}	$\text{Log}(M_* [M_\odot])$	$\text{Log}(L_{2-10\text{keV}} [\text{erg s}^{-1}])$	$\text{Log}(M_{Edd} [M_\odot])$	Hardness (H)
68	215.0970	53.0865	1.078	11.43	43.55	6.55	0.89
69	215.0850	53.1205	1.309	11.08	43.58	6.58	0.35
70	215.4300	53.1478	1.200	10.95	43.61	6.61	0.59
71	215.4930	53.1347	1.043	10.77	43.47	6.47	0.46
72	215.0710	53.1338	1.038	11.18	43.68	6.68	0.34
73	215.5000	53.2149	1.309	10.62	43.56	6.56	0.69
74	215.3970	53.2262	1.150	11.17	43.74	6.73	0.33
75	215.2950	53.1810	1.206	10.81	43.71	6.70	0.45
76	215.4800	53.2373	1.226	10.83	43.80	6.80	0.38
77	215.7630	53.3735	1.405	11.44	44.27	7.27	0.67
78	215.6570	53.3620	1.272	11.05	43.96	6.96	0.43
79	215.5830	53.3306	1.240	11.13	43.71	6.71	0.43
80	215.4020	53.3373	1.466	11.08	43.88	6.88	0.18
81	215.5160	53.4142	1.082	11.13	44.11	7.11	0.37
82	215.8490	53.4718	1.460	10.90	44.19	7.18	0.91
83	215.7700	53.5167	1.281	10.67	43.41	6.40	0.20
84	215.7770	53.5192	1.281	10.69	44.22	7.21	0.91

Table B.8 –Continued

ID	RA	Dec	z_{phot}	$\text{Log}(M_* [M_\odot])$	$\text{Log}(L_{2-10\text{keV}} [\text{erg s}^{-1}])$	$\text{Log}(M_{Edd} [M_\odot])$	Hardness (H)
85	215.6980	53.5342	1.157	10.78	43.56	6.56	0.63

In the above table we restrict the full AGN matched list of 508 secure AGN detections (provided by matching within a 1.5'' radius GOODS and EGS galaxy catalogs with the extensive deep Chandra imaging in the same fields), by highlighting only those AGN with host galaxy stellar masses $M_* > 10^{10.5} M_\odot$ and with hard band X-ray luminosities $L_{2-10\text{keV}} > 2.35 \times 10^{43} \text{ erg s}^{-1}$, where we are complete for restricted areas of the EGS sample to $z = 1.5$, and for the GNS sub-sample to $z = 3$. M_* is the stellar mass of the AGN host galaxy, M_{Edd} is the Eddington limited (minimum) mass of the SMBH (see §4.4.3 for definition), and H is the hardness ratio (see §4.5.5 for definition). A detailed discussion of the errors on these quantities from both random and possible systematic sources is provided throughout Chapter 4 (see §4.3 in particular).

Bibliography

- Abraham R. G., Tanvir N. R., Santiago B. X., Ellis R. S., Glazebrook K.,
van den Bergh S., 1996, MNRAS, 279L, 47
- Aird J. et al., 2010, MNRAS, 401, 2531
- Alexander D. M. et al., 2003, AJ, 126, 539
- Alexander D. M. et al., 2008, AJ, 135, 1968
- Aragon-Salamanca A., Ellis R. S., Couch W. J., Carter D., 1993, MNRAS, 262, 764
- Baade W. & Zwicky F., 1934, Proceedings of the National Academy of Sciences,
20, 254
- Babic A., Miller L., Jarvis M. J., Turner T. J., Alexander D. M., Croom S. M.,
2007, A&A, 474, 755
- Barger A. J., Cowie L. L., Mushotzky R. F., Yang, Y., Wang, W. H., Steffen A. T.,
Capak P., 2005, ApJ, 129, 578
- Bauer A. E., Conselice C. J., Gruetzbauch R., Bluck A. F. L., Buitrago F., Mortlock
A., 2010, submitted to MNRAS
- Begelman M. C. et al., 2006, MNRAS, 370, 289
- Bell E. F., McIntosh D. H., Katz N., Weinberg, M. D., 2003, ApJS, 149, 289
- Bell E. F. et al., 2004, ApJ, 608, 752
- Bell E. F. et al., 2006, ApJ, 652, 270
- Benitez N., 2000, ApJ, 536, 571
- Bennett C. et al., 2003, ApJ, 583, 1
- Bershady M. A., Jangren A. & Conselice C. J., 2000, AJ, 119, 2645
- Bertin E. & Arnouts S., 1996, A&AS, 117, 393
- Bertone S. & Conselice C. J., 2009, MNRAS, 396, 2345
- Bett P. et al., 2007, MNRAS, 376, 215

- Blakeslee J. P. et al., 2006, *ApJ*, 644, 30
- Bluck A. F. L., Conselice C. J., Bouwens R. J., Daddi E., Dickinson M., Papovich C., Yan H., 2009, *MNRAS*, 394L, 51
- Bluck A. F. L., Conselice C. J., Almaini O., Laird E., Nandra K., and Gruetzbauch R., 2010a, accepted for publication in *MNRAS* [arXiv:1008.2162]
- Bluck A. F. L., Buitrago F., Conselice C. J., Gruetzbauch R., Hoyos C., Bauer A., Mortlock A., 2010b, in prep.
- Bolzonella M., Miralles J. M. & Pello R., 2000, *A&A*, 363, 476
- Borys C., Smail I., Chapman S. C., Blain A. W., Alexander D. M., Ivison R. J., 2005, *ApJ*, 635, 853
- Bower S., Byram E. T., Chubb T. A., Friedman H., 1965, *Science*, 147, 394
- Brighenti F. & Mathews W. G., 2003, *ApJ*, 587, 580
- Bruzual G. & Charlot S., 2003, *MNRAS*, 344, 1000
- Buitrago F., Trujillo I., Conselice C. J., Bouwens R. J., Dickinson M. & Yan H., 2008, *ApJ*, 687, 61
- Bundy K. et al., 2004, *ApJL*, 601, L123
- Bundy K. et al., 2006, *ApJ*, 651, 120
- Bundy K. et al., 2008, *ApJ*, 681, 931
- Butcher H. & Oemler A., 1984, *ApJ*, 285, 426
- Carlberg R., 1990, *ApJ*, 359, L1
- Carrasco E. R., Conselice C. J. & Trujillo, I., 2010, *MNRAS*, 405, 2253
- Chandrasekhar S., 1931, *MNRAS*, 91, 456
- Chandrasekhar S., 1935, *MNRAS*, 95, 207
- Chapman S. C., Blain A. W., Ivison R. J., Smail I. R., 2003, *Nature*, 422, 695
- Cimatti A. et al., 2008, *A&A*, 482, 21
- Ciotti L. & Ostriker J. P., 2001, *ApJ*, 551, 131
- Cole S., Aragon-Salamanca A., Frenk C. S., Navarro J. F., Zepf S. E., 1994, *MNRAS*, 271, 781
- Cole S. et al., 2005, *MNRAS*, 362, 505
- Collister A. A. & Lahav O., 2004, *PASP*, 116, 345
- Conroy C., Gunn J. E. & White M., 2009, *ApJ*, 699, 486
- Conselice C. J., 2003, *ApJS*, 147, 1

- Conselice C. J., 2006, *ApJ*, 639, 120
- Conselice C. J. & Arnold J., 2009, *MNRAS*, 397, 208
- Conselice C. J., Bershadsky M. A. & Jangren A., 2000, *ApJ*, 529, 886
- Conselice C. J., Gallagher J. S. III & Wyse R. F. G., 2002, *AJ*, 123, 2246
- Conselice C. J. et al., 2003, *AJ*, 126, 1183
- Conselice C. J. et al., 2007, *MNRAS*, 381, 962
- Conselice C. J. et al., 2008a, *MNRAS*, 386, 909
- Conselice, C. J., Bundy, K., U, Vivian, Eisenhardt, P., Lotz, J., Newman, J., 2008b, *MNRAS*, 383, 1366
- Conselice C. J., Yang C. & Bluck A. F. L., 2009, *MNRAS*, 394, 1956
- Conselice C. J., Bluck A. F. L., Buitrago F., Bauer A. E., + GNS Team, 2010, accepted for publication in *MNRAS* [arXiv:1010.1164]
- Couchman H. M. P. & Rees M. J., 1986, *MNRAS*, 221, 53
- Cowley A. p., Schmidtke P. C., Crampton D. & Hutchings J. B., 1990, *ApJ*, 350, 288
- Daddi E. et al., 2007, *ApJ*, 670, 156
- Damjanov I. et al., 2009, *ApJ*, 695, 101
- Davis et al. 2007, *ApJ*, 660, 1L
- De Propris et al., 2007, *ApJ*, 666, 212D
- De Vaucouleurs G., 1948, *AnAp*, 11, 247
- Declari R., Falomo R., Treves A., Labita M., Kotilainen K., Scarpa R., 2010, *MNRAS*, 402, 2453
- Declari R., Falomo R., Treves A., Labita M., Kotilainen K., Scarpa R., 2010, *MNRAS*, 402, 2441
- De Lucia G. & Blaizot J., 2007, *MNRAS*, 375, 2
- Dickinson M., papovich C., Ferguson H. C., Budavari T., 2003, *ApJ*, 587, 25
- Dickinson M., Giavalisco M & GOODS Team, 2003, Proceedings of the ESO workshop held in Venice, Italy, 24-26 October 2001; ed. R. Bender, p.324
- Dickinson M. et al., 2004, 600, 99L
- Diehl et al., 2006, *Nature*, 439, 45
- D'Onofrio M., Valentinuzzi T., Secco L., Caimmi R., Bindoni D., 2006, *New Astronomy Reviews*, 50, 447
- Dressler A., 1980, *ApJ*, 236, 351

- Drory N., 2005, *ApJ*, 619, L131
- Dyson F. W., Eddington A.S. & Davidson C.R., 1920, *Phil. Trans. Roy. Soc. A* 220, 291
- Elvis M. et al., 1994, *ApJS*, 95, 1
- Elvis M., Risaliti G. & Zamorani G., 2002, *ApJ*, 565, 75L
- Fabian A. C., 1999, *MNRAS*, 308, 39L
- Ferrarese L. & Merritt D., 2000, *ApJ*, 593L, 9
- Fontana A. et al., 2006, *AA*, 5474
- Gamow G., 1948, *Nature*, 162, 680
- Gebhardt K. et al., 2000, *ApJ*, 539, 13L
- Giacconi R. et al., 2000, *AAS*, 197, 9001
- Giavalisco, M., Ferguson, H. C., Koekemoer, A. M. et al., 2004, *ApJ*, 600, L93
- Green P. J. et al., 2009, *ApJ*, 690, 644
- Grogin N. A. et al., 2003, *ApJ*, 595, 685
- Gnedin O. Y. & Ostriker J. P., 1997, *ApJ*, 474, 223
- Grutzbauch R., Chuter R. W., Conselice C. J., Bauer A. E., Bluck, A. F. L., Buitrago F., Mortlock A., 2010, accepted for publication in *MNRAS* [arXiv:1011.4846]
- Gunn J.E. & Gott III J. S., 1972, *ApJ*, 176, 1
- Guth A. H., 1981, *Phys. Rev. D*, 23, 347
- Haehnelt, M., Natarajan, P., & Rees, M. J., 1998, *MNRAS*, 300, 817
- Hamabe M. & Kormendy J., 1987, *AUS*, 127, 379
- Haring N. & Rix H., 2004, *ApJL*, 604, 89
- Harker G. et al., 2006, *MNRAS*, 367, 1039
- Hasinger G., Miyaji T. & Schmit M., 2005, *A&A*, 441, 417
- Hernandez-Toledo H. M., Avila-Reese V., Conselice C. J., Puerari I., 2005, *AJ*, 129, 682
- Heusler M., 1998, *Living Rev. Relativity* 1, 6
- Hinshaw G. et al., 2009, *ApJ*, 180, 225
- Hopkins P. F., Richards, G. T. & Helmquist, L., 2007, *ApJ*, 654, 731
- Hoyos C. et al., 2010, *MNRAS*, submitted
- Hubble E., 1922, *ApJ*, 56, 162
- Hubble E., 1925, *ApJ*, 62, 409

- Hubble E., 1926, *ApJ*, 63, 321
- Ibata R., Irwin M., Lewis G. F. & Stolte A., 2001, *ApJ*, 547, 133L
- Jahnke K. et al., 2009, *ApJ*, 706, 215
- Juneau S. et al., 2005, *ApJ*, 619, 135
- Kauffmann, G. & Haehnelt, M., 2000, *MNRAS*, 311, 576
- Kaufmann T., Mayer L., Wadsley J., Stadel J. & Moore B., 2006, *MNRAS*, 370, 1612
- Kessler R. et al., 2009, *ApJS*, 185, 32
- Khochfar S. & Silk J., 2006, *ApJ*, 648, 21L
- King A., 2003, *ApJ*, 596, 27L
- Kitzbichler M. G. & White S. D. M., 2007, *MNRAS*, 376, 2
- Kormendy J., 1977a, *ApJ*, 214, 359
- Kormendy J., 1977b, *ApJ*, 217, 406
- Kormendy J., 1977c, *ApJ*, 218, 333
- Kormendy J. & Richstone D., 1995, *A&A*, 33, 581
- Krolik J. H., 1999, Princeton University Press, 'Active Galactic Nuclei'
- Krumholz M. R., McKee C. F., 2005, *ApJ*, 630, 250
- Laird E. S. et al., 2009, *ApJS*, 180, 102L
- Le Verrier U., 1859, (in French), *Comptes rendus hebdomadaires des sances de l'Academie des sciences (Paris)*, vol. 49, pp.379383
- Lin L. et al., 2004, *ApJL*, 617, L9
- Lin L. et al., 2008, *ApJ*, 681, 232
- Longhetti M. et al., 2007, 374, 614
- Lopez-Sanjuan C., Balcells M., Perez-Gonzalez P. G., Barro G., Garcia-Dabo C. E., Gallego J., Zamorano J., 2009a, *A&A*, 501, 505
- Lopez-Sanjuan C. et al., 2009b, *ApJ*, 649, 643
- Lopez-Sanjuan C. et al., 2010, *ApJ*, 710, 1170L
- Lotz J. M. et al., 2008a, *ApJ* 672, 177
- Lotz J. M., Jonsson P., Cox T. J., Primack J. R., 2008b, *MNRAS*, 391, 1137L
- Lotz J. M., Jonsson P., Cox T. J. & Primack J. R., 2010, *MNRAS*, 404, 575L
- Luo, F. E. et al., 2008, *ApJ*, 179, 19
- Madau P., Pozzetti L. & Dickinson M., 1998, *ApJ*, 498, 106
- Magee D. K., Bouwens R., Illingworth G. D., 2007, *ASPC*, 376, 261

- Magorrian J. et al., 1998, *AJ*, 115, 2285
- Marconi A. & Hunt L. K., 2003, *ApJ*, 589L, 21
- Marconi A. et al., 2004, *MNRAS*, 351, 169
- Marconi A. et al., 2009, *ApJ*, 698L, 103
- Markevitch M. et al., 2004, *ApJ*, 606, 819
- Martini P., 2003, review, [arXiv:astro-ph/0304009]
- Mathis H. et al., 2005, *MNRAS*, 365, 385
- McClintock J. E. & Remillard R. A., 1986, *ApJ*, 308, 110
- McKernan B., Ford K. E. & Reynolds C., 2010, arXiv:1005.4907
- McLure R. J. & Dunlop J. S., 2002, *MNRAS*, 331, 759
- McLure R. J. & Dunlop J. S., 2004, *MNRAS*, 352, 1390
- McLure R. J. & Jarvis M. J., 2002, *MNRAS*, 337, 109
- Merloni A. et al., 2010, *ApJ*, 708, 137
- Meszáros P., 1975, *A&A*, 44, 59
- Michell J., 1784, *Phil. Trans. of the R.S.*, 35-57
- Misner W., Thorne K. S. & Wheeler J. A., 1973, 'Gravitation', ISBN 0-7167-0334-3
- Moore B., Lake G. & Katz N., 1998, *ApJ*, 495, 139
- Moore B., Quinn T., Governato F., Stadel J., Lake G., 1999, *MNRAS*, 310, 1147
- Mushotzky R. F., Winter L. M., McIntosh D. H., Tueller, J., 2008, *ApJ*, 684L, 65
- Naab T., Johansson P. H. & Ostriker J. P., 2009, *ApJ*, 699, 178L
- Narayanan D, Cox T., Hayward C. C., Younger J. D., Hernquist L., 2009, *MNRAS*, 400, 1919
- Nigoche-Netro A., Ruelas-Mayorga A. & Franco-Balderas A., 2008, *A&A*, 491, 731
- O'Neil P. M., Nandra K., Iossif E. P., Turner T. J., 2005, *MNRAS*, 358, 1405
- Oemler A. J., 1974, *ApJ*, 701, 787
- Oda M., 1977, *SSRv*, 20, 757
- Oppenheimer J. R. & Volkoff G. M., 1939, *Phys. Rev.*, 55, 374
- Pipino A. & Matteucci F., 2008, *A&A*, 486, 763
- Popesso P. et al., 2008, *A&A*, 494, 443
- Papovich C. et al., 2006, *ApJ*, 640, 92
- Panessa, F. et al., 2006, *A&A*, 455, 173
- Patton D. R. et al., 2000, *ApJ*, 536, 153

- Peng C. Y., Ho L. C., Impey C. D. & Rix H., 2002, *AJ*, 124, 266
- Rawat A., Hammer F., Kembhavi A. K., Flores H., 2008, *ApJ*, 681, 1089
- Reddish V. C., 1975, *MNRAS*, 225, 795
- Reddy N. A., Erb D. K., Steidel C. C., Shapley A. E., Adelberger K. L., Pettini M., 2005, *ApJ*, 633, 478
- Retzlaff J. et al., 2010, *A&A*, 511, 50
- Roediger E. & Hensler G., 2005, *A&A*, 433, 875
- Romano-Daz E., Shlosman I., Heller C., Hoffman Y., 2009, *ApJ*, 702, 1250
- Rubin V., Thornnard N. & Ford Jr. W. K., 1980, *ApJ*, 238, 471
- Schade D., Lilly S. J., Crampton D., Hammer F., Le Fevre O., Tresse L., 1995, *ApJ*, 451, 1
- Schodel R et al., 2002, *Nature*, 419, 694
- Schreier E. J. et al., *ApJ*, 2001, 560, 127
- Schwarzschild K., 1916, *Sitzungsberichte der Deutschen Akademie der Wissenschaften zu Berlin, Klasse für Mathematik, Physik, und Technik*, 189
- Silk J. & Rees M. J., 1998, *A&A*, 331, 1
- Sparke L. S. & Gallagher III J. S., 2000, 'Galaxies in the Universe', ISBN 978-0-85593-8
- Steffen A. T., Barger A. J., Cowie L. L., Mushotzky R. F., Yang Y, 2003, *ApJ*, 596L, 23
- Suess H. & Urey H., 1956, *Reviews of Modern Physics*, 28, 53
- Sugerman B., Summers F. J., Kaminonkowski M., 2000, *MNRAS*, 311, 762
- Suyu S. H. et al., 2010, *ApJ*, 711, 201
- Taylor A. N., Dye S., Broadhurst T. J., Benitez N. & van Kampen E., 1998, *ApJ*, 501, 539
- Thaker R. J. & Couchmann H. M. P., 2001, *ApJ*, 555L, 17
- Thomas P. A. & Fabian A. C., 1990, *MNRAS*, 246, 156
- Thorne K. S., 1974, *ApJ*, 191, 507
- Tolman R. C., 1939, *Phys. Rev.*, 55, 364
- Townsley L. K. et al., 2003, *ApJ*, 593, 874
- Treu T., Woo J., Malkan M., Blandford R. D., 2007, *ApJ*, 667, 117
- Trujillo I., Conselice C. J., Bundy K., Cooper M. C., Eisenhardt P. & Ellis R. S., 2007,

- MNRAS, 382, 109
- Trujillo I., Cenarro A. J., de Lorenzo-Cceres A., Vazdekis, A., de la Rosa I. G., Cava A., 2009, ApJ, 692, 118L
- Ueda, Y., Akiyama, M., Ohta, K. & Miyaji, T., 2003, ApJ, 598, 886
- van Dokkum P. G. et al., 2010, ApJ, 709, 1018
- van Dokkum P. G., Kriek M., Franx M., 2009, Nature, 460, 717
- Vasudevan R. V. & Fabian A. C., 2007, MNRAS, 381, 1235
- Vasudevan R. V. & Fabian A. C., 2009, MNRAS, 392, 1124
- Vasudevan R. V., Fabian A. C., Gandhi P., Winter L. M., Mushotzky R. F., 2009, MNRAS, 402, 1081
- Vikhlini et al., 2006, ApJ, 640, 691
- Voit M. G., 2004, Rev. Mod. Phys., 77, 207
- Waddington I. et al., 2002, MNRAS, 336, 1342
- Williams R. E., 1996, AJ, 112, 1335
- Willet C. J., McLure M. A. & Jarvis M. J., 2003, ApJ, 587, 15
- Woo J., Treu T., Malkan M. A., Blanford R. D., 2008, ApJ, 681, 925
- Wuyts S. et al., 2008, ApJ, 682, 985
- Wetzel A. R., 2008, ApJ, 683, 1
- Willet C. J., McLure R. J. & Jarvis M. J., 2003, ApJ, 587, 15
- Woo J., Treu T., Malkan M. A., Blanford R. D., 2008, ApJ, 681, 925
- Yamada T. et al., 2009, ApJ, 699, 1354
- Yan H. et al., 2004, ApJ, 616, 63
- Yu Q. & Tremaine S., 2002, ApJ, 335, 965
- Ziegler B. L., Saglia R. P., Bender R., Belloni P., Greggio L., Seitz S., 1999, A&A, 346, 13
- Zwicky F., 1933, ApJ, 86, 217